RECENT ADVANCES IN FLUORESCENT PROBES FOR SUPER-RESOLUTION MICROSCOPY

EDITED BY: Chayan Kanti Nandi, Fan Wang, Xusan Yang and Qiuqiang Zhan
PUBLISHED IN: Frontiers in Chemistry and Frontiers in Physics

frontiers Research Topics

ISSN 1664-8714
ISBN 978-2-88971-071-3
DOI 10.3389/978-2-88971-071-3

About Frontiers

Frontiers is more than just an open-access publisher of scholarly articles: it is a pioneering approach to the world of academia, radically improving the way scholarly research is managed. The grand vision of Frontiers is a world where all people have an equal opportunity to seek, share and generate knowledge. Frontiers provides immediate and permanent online open access to all its publications, but this alone is not enough to realize our grand goals.

Frontiers Journal Series

The Frontiers Journal Series is a multi-tier and interdisciplinary set of open-access, online journals, promising a paradigm shift from the current review, selection and dissemination processes in academic publishing. All Frontiers journals are driven by researchers for researchers; therefore, they constitute a service to the scholarly community. At the same time, the Frontiers Journal Series operates on a revolutionary invention, the tiered publishing system, initially addressing specific communities of scholars, and gradually climbing up to broader public understanding, thus serving the interests of the lay society, too.

Dedication to Quality

Each Frontiers article is a landmark of the highest quality, thanks to genuinely collaborative interactions between authors and review editors, who include some of the world's best academicians. Research must be certified by peers before entering a stream of knowledge that may eventually reach the public - and shape society; therefore, Frontiers only applies the most rigorous and unbiased reviews.
Frontiers revolutionizes research publishing by freely delivering the most outstanding research, evaluated with no bias from both the academic and social point of view. By applying the most advanced information technologies, Frontiers is catapulting scholarly publishing into a new generation.

What are Frontiers Research Topics?

Frontiers Research Topics are very popular trademarks of the Frontiers Journals Series: they are collections of at least ten articles, all centered on a particular subject. With their unique mix of varied contributions from Original Research to Review Articles, Frontiers Research Topics unify the most influential researchers, the latest key findings and historical advances in a hot research area! Find out more on how to host your own Frontiers Research Topic or contribute to one as an author by contacting the Frontiers Editorial Office: frontiersin.org/about/contact

RECENT ADVANCES IN FLUORESCENT PROBES FOR SUPER-RESOLUTION MICROSCOPY

Topic Editors:
Chayan Kanti Nandi, Indian Institute of Technology Mandi, India
Fan Wang, University of Technology Sydney, Australia
Xusan Yang, Cornell University, United States
Qiuqiang Zhan, South China Normal University, China

Citation: Nandi, C. K., Wang, F., Yang, X., Zhan, Q., eds. (2021). Recent Advances in Fluorescent Probes for Super-Resolution Microscopy. Lausanne: Frontiers Media SA. doi: 10.3389/978-2-88971-071-3

Table of Contents

frontiers in Chemistry

EDITORIAL
published: 11 June 2021
doi: 10.3389/fchem.2021.698531

Editorial: Recent Advances in Fluorescent Probes for Super-Resolution Microscopy

Fan Wang[1], Xusan Yang[2]*, Qiuqiang Zhan[3]* and Chayan K. Nandi[4,5,6]**

[1]School of Electrical and Data Engineering, University of Technology Sydney, Sydney, NSW, Australia, [2]School of Applied and Engineering Physics, Cornell University, Ithaca, NY, United States, [3]South China Academy of Advanced Optoelectronics, South China Normal University, Guangzhou, China, [4]School of Basic Sciences, Indian Institute of Technology, Mandi, India, [5]Advanced Materials Research Centre, Indian Institute of Technology, Mandi, India, [6]BioX Centre, Indian Institute of Technology, Mandi, India

Keywords: super resolution, fluorescent probe, nanodots, localization microscopy, optical bioimaging

Editorial on the Research Topic

Recent Advances in Fluorescent Probes for Super-Resolution Microscopy

Super-resolution microscopy (SRM) has become an indispensable tool for monitoring cytoskeleton dynamics as well as the imaging, detection, and tracing of functional biomolecules in living cells. It overcomes the barrier of diffraction limit and allows for the visualization of sub-cellular structures down to the sub-10 nm level. Several types of SRM techniques are available, with a vast number of applications in interdisciplinary research fields. To date, many fluorescent probes such as fluorescent proteins, organic dyes, nanomaterials, quantum dots, polymer dots, organic dots, carbon dots, and upconversion nanomaterials have been employed for SRM. Each has its own limitations, and, as such, in order to obtain a better-resolved structure, improving the efficiency of these probes is of great importance.

The performance of fluorescent probes in super-resolution microscopy is dependent on several important photo-physical parameters. Organic molecules, with their smaller size, have excellent blinking properties, but they are often dim and undergo rapid photobleaching. Photoactivable or photoswitchable fluorescent proteins suffer from poor localization precision due to their low photon counts. Nanomaterials, quantum dots, carbon dots, polymers dots, etc. have shown promising results due to their high brightness and photostability, but their large size compared to organic molecules limits their potential applications.

In this research topic, we present a collection of original research, mini review, perspective, and review articles touching upon different aspects of new fluorescent probe materials that advance the SRM techniques one step ahead to the current state of the art in the field. We also provide a new labeling strategy of the fluorescent probe in the live cell SRM imaging.

Han et al., in their research article on "a labeling strategy for living specimens in long term super resolution fluorescence imaging", showed the capability of many fluorescent dyes to stain various types of subcellular structures in living specimens with high brightness and photostability. They used several known dyes, such as Atto 495, Atto 565, Atto 590, Atto 647N, BODIPY, Alexa fluoro 647, Cy3B, and Cy5, for their study. They have shown their results in mitochondria, endoplasmic reticulum, endocytic vesicles, and the plasma membrane. The new strategy required only specific incubation conditions without any chemical modification or physical penetration, minimizing the damages and artifacts induced during the sample preparation. Among all, ATTO-647N dye exhibited extraordinary brightness and photostability in live cell mitochondrial labeling. Their strategy could be a future toolbox for understanding the dynamics and interactions of subcellular structures in living specimens.

OPEN ACCESS

Edited and reviewed by:
Paolo Oliveri,
University of Genoa, Italy

****Correspondence:***
Fan Wang
Fan.Wang@uts.edu.au
Xusan Yang
xy389@cornell.edu
Qiuqiang Zhan
zhanqiuqiang@m.scnu.edu.cn
Chayan K. Nandi
chayan@iitmandi.ac.in

Specialty section:
This article was submitted to Analytical Chemistry, a section of the journal Frontiers in Chemistry

Received: *21 April 2021*
Accepted: *03 May 2021*
Published: *11 June 2021*

Citation:
Wang F, Yang X, Zhan Q and Nandi CK (2021) Editorial: Recent Advances in Fluorescent Probes for Super-Resolution Microscopy. Front. Chem. 9:698531. doi: 10.3389/fchem.2021.698531

Yao et al., showed the efficient application of SNAP-tag in the expansion-SRM technique using DNA oligostrands. Expansion-SRM is a new technology that anchors the dye to the hydrogel, and the dye expands with the expansion of the hydrogel so that an SRM map can be obtained under an ordinary microscope. By labeling the target protein with a first antibody and secondary antibody, the distance between the fluorescent group and the actual target protein is greatly increased. Instead of using the fluorescent proteins, which can be destroyed during sample preparation of the measurement, DNA oligostrand-linked fluorescent dye was used as an efficient probe in the expansion-SRM. The DNA oligostrand is brought to the vicinity of the target protein by specific binding technology with the SNAP. This protocol greatly reduced the error between the position of the fluorescent group and the actual target protein, and it also reduced the loss of the fluorescent group during sample preparation.

Laxman et al. showed the benefits of unnatural amino acid incorporation as protein labels for single-molecule localization microscopy (SMLM) such as stochastic optical reconstruction microscopy (STORM) and photoactivated localization microscopy (PALM). In the context of proteins, a large component of successful SMLM imaging is the choice of fluorescent probe used as a label for the protein of interest. The ideal fluorescent tag candidate for SMLM should aim for photostability during activation and deactivation cycles, be small in size, and have high levels of photon emission for better single-molecule detection by the microscope. Here, they have used protein labeling by incorporating unnatural amino acids with an attached fluorescent dye for precise localization and visualization of individual molecules. A detailed understanding and comparison of the unnatural amino acid labeling with other commonly used protein-based labeling methods, such as fluorescent proteins (FPs) or self-labeling tags like Halotag, SNAP-tags, and CLIP-tags, both highlight the benefits and shortcomings of the site-specific incorporation of unnatural amino acids coupled with fluorescent dyes in SMLM.

In another interesting article by Zhuang et al., the photobleaching imprinting technique has been utilized to reject background light and improve contrast by fully using line-scanning temporal focusing microscopy. With the removal of the background light, the method could achieve high contrast imaging both in the transparent and scattering medium.

More than 50% of total background light rejection was achieved, providing a higher signal to background ratio images of the MCF-10A samples and mouse brains. This photobleaching imprinting technology can be easily adapted to other fluorescence dyes or proteins, which may have application in studies involving relatively large and nontransparent organisms.

In this collection, the mini review, perspective, and review articles summarize the detailed information on the fluorescent nanoprobes, such lanthanide-doped upconversion nanoparticle by Dong et al., quantum, dots, carbon dots, polymer dots, and aggregation-induced emissive dots by Liu et al., and the hexagonal boron nitrides by Bradac et al. On the other hand, Cheng et al. have provided a new avenue on the biosensing interfaces with SMLM. They have given an update on the progress of using SMLM in characterizing nanostructured biointerfaces, focusing on practical aspects, recent advances, and emerging opportunities from an analytical science perspective.

In summary, the editors hope that the collection presented in this research topic, "Recent Advances in Fluorescent Probes for Super-Resolution Microscopy", will contribute to the progress of research and development activities in the field.

AUTHOR CONTRIBUTIONS

All authors listed have made a substantial, direct, and intellectual contribution to the work and approved it for publication.

ACKNOWLEDGMENTS

CN thank the kind support received from the Science and Engineering Board (SERB) Core Research Grant (CRG) India for the financial support with the project number CRG/2020/000268. The editors are grateful to the authors for submitting their valuable work and to all the reviewers who contributed to this effort by thoroughly evaluating the submitted articles and providing thoughtful advice on how these can be improved.

Conflict of Interest: The authors declare that the research was conducted in the absence of any commercial or financial relationships that could be construed as a potential conflict of interest.

frontiers in Chemistry

ORIGINAL RESEARCH
published: 17 December 2020
doi: 10.3389/fchem.2020.618131

Photobleaching Imprinting Enhanced Background Rejection in Line-Scanning Temporal Focusing Microscopy

Chaowei Zhuang[1], *Xinyang Li*[1], *Yuanlong Zhang*[1], *Lingjie Kong*[2], *Hao Xie*[1]* and *Qionghai Dai*[1,3,4,5]*

[1] Department of Automation, Tsinghua University, Beijing, China, [2] Department of Precision Instrument, Tsinghua University, Beijing, China, [3] Beijing National Research Center for Information Science and Technology, Beijing, China, [4] Institute for Brain and Cognitive Science, Tsinghua University, Beijing, China, [5] Beijing Laboratory of Brain and Cognitive Intelligence, Beijing Municipal Education Commission, Beijing, China

Compared with two-photon point-scanning microscopy, two-photon temporal focusing microscopy (2pTFM) provides a parallel high-speed imaging strategy with optical sectioning capability. Owing to out-of-focus fluorescence induced by scattering, 2pTFM suffers deteriorated signal-to-background ratio (SBR) for deep imaging in turbid tissue, Here, we utilized the photobleaching property of fluorophore to eliminate out-of-focus fluorescence. According to different decay rates in different focal depth, we extract the in-focus signals out of backgrounds through time-lapse images. We analyzed the theoretical foundations of photobleaching imprinting of the line-scanning temporal focusing microscopy, simulated implementation for background rejection, and demonstrated the contrast enhancement in MCF-10A human mammary epithelial cells and cleared Thy1-YFP mouse brains. More than 50% of total background light rejection was achieved, providing higher SBR images of the MCF-10A samples and mouse brains. The photobleaching imprinting method can be easily adapted to other fluorescence dyes or proteins, which may have application in studies involving relatively large and nontransparent organisms.

Keywords: temporal focusing microscope, photobleaching imprinting, background rejection, biomedical imaging, two-photon effect

OPEN ACCESS

Edited by:
Xusan Yang,
Cornell University, United States

Reviewed by:
Yan-Kai Tzeng,
Stanford University, United States
Zhigang Yang,
Shenzhen University, China
Chenshuo Ma,
Duke University, United States

***Correspondence:**
Hao Xie
xiehao@tsinghua.edu.cn
Qionghai Dai
qhdai@tsinghua.edu.cn

Specialty section:
This article was submitted to Analytical Chemistry, a section of the journal Frontiers in Chemistry

Received: *16 October 2020*
Accepted: *20 November 2020*
Published: *17 December 2020*

Citation:
Zhuang C, Li X, Zhang Y, Kong L, Xie H and Dai Q (2020) Photobleaching Imprinting Enhanced Background Rejection in Line-Scanning Temporal Focusing Microscopy. Front. Chem. 8:618131. doi: 10.3389/fchem.2020.618131

INTRODUCTION

Two-photon fluorescence microscopy has become a powerful tool in biomedical deep-tissue imaging for its advantages in high spatial resolution, deep penetration, and optical sectioning capability (Denk et al., 1990; Zipfel et al., 2003; Helmchen and Denk, 2005). In biological two-photon microscopy, the fluorophore absorbs two infrared photons simultaneously to generate an emission photon in the visible spectrum. Conventional two-photon fluorescence microscopy employs the point-scanning scheme, in which all the voxels are excited sequentially and the fluorescence is detected by bulk semiconductor photodetectors. The two-photon excitation intensity is a quadratic function of the excitation radiance, so fluorescence is effectively excited only in the perifocal region (Zipfel et al., 2003). Besides, tissue scattering decrease monotonically as the wavelength decreases in 350–2,000 nm. As a result, two-photon laser scanning microscopy processes high signal-to-background ratio (SBR), which is vital in biological fluorescence imaging.

Due to the point scanning strategy, the imaging speed of the two-photon microscopy is limited by the inertia of mechanical scanners and the laser repetition rate (Kong et al., 2015). To solve this problem, temporal focusing microscopy (TFM) has reportedly achieved parallel excitation in samples. Different from spatially focusing to generate high peak intensity at the focus in the two-photon microscopy, the TFM controls the temporal profile of the pulse, whose width is minimal at the focal plane and stretches out of the focal plane. Because the excited fluorescence is inversely proportional to the pulse width in two-photon excitation process, the fluorescence intensity reaches its peak value at the focal plane (Oron et al., 2005; Durst et al., 2008; Dana and Shoham, 2011; Oron and Silberberg, 2015). Therefore, TFM achieves optical sectioning capability and, in a parallel manner, excites the full region of interest simultaneously.

According to the shape of the focus, TFM is classified into two categories: wide-field temporal focusing microscopy (WTFM) illuminates the whole 2D plane simultaneously (Papagiakoumou et al., 2010; Cheng et al., 2012; Rowlands et al., 2017); line-scanning temporal focusing microscopy (LTFM) produces a linear focus and sweeps this line in the focal plane (Tal et al., 2005; Dana et al., 2014; Lou et al., 2018). Although WTFM has a larger illuminated area, the two-photon excitation efficiency is decreased severely, according to power-law dependence on light intensity in multiphoton processes (Dana et al., 2013). Benefiting from both spatial focusing and pulse width modulation, LTFM has superior performance in imaging speed, field-of-view, depth, and axial confinement, so it has been shown to have wide applications in large-scale imaging of biological dynamics (Li et al., 2017; Park et al., 2017).

Unfortunately, as the imaging depth increases, tissue scattering distorts the excitation focus of LTFM. In turbid specimens, the power of ballistic photons P_b is characterized by Beer's law $P_{\mathrm{b}} = P_0 \exp\left(-z/l_{\mathrm{s}}\right)$, where l_s is the effective attenuation length (EAL) and z is the depth (Wang et al., 2018). As the axial confinement of LTFM is corrupted in deep tissues, the out-of-focus fluorescence at different depth contributes to an intensified image background on the sCMOS detector. To solve this problem, structured illumination microscopy (SIM) enhances axial confinement and suppresses background noise by synthesizing several images illuminated by different patterns (Therrien et al., 2011; Cheng et al., 2014; Meng et al., 2017). The structured illumination pattern is only the sharpest at the focal plane, so the signal at the focal plane is extracted by reconstruction. Previous studies have reported that LTFM combined with SIM is effective to suppress the background for imaging C. elegans (Li et al., 2017). Focal modulation microscopy (FMM) can also be applied to LTFM for enhancing the SBR by subtracting an aberrated point-spread-function (PSF) image from the origin image. The background intensity is estimated from the aberrated PSF image, in which the focal intensity is decreased but out-of-focus light intensity remains. Then the background is to improve the signal to background ratio (Leray and Mertz, 2006; Zhang et al., 2018). Nevertheless, these methods need extra phase modulation devices, such as a spatial light modulator (SLM), digital micromirror device (DMD), and deformable mirror (DM), which increase the system complexity and cause laser power loss. TFM combined with sum-frequency generation also improves the axial confinement effectively but suffers from relatively low excitation power because of the partially blocking excitation beam (Durst et al., 2009).

In this paper, we proposed a novel method termed LTFM-PIM, which combines photobleaching imprinting microscopy (PIM) with LTFM to enhance axial confinement and reject the background (Li et al., 2013; Gao et al., 2014a). PIM extracts high-order fluorescence signals from photobleaching-induced fluorescence decay, and no extra device is required. We first describe the proposed method through formulations and then simulate our implementation for demonstrating background rejection improvements by LTFM-PIM. To further demonstrate the improvement of LTFM-PIM, we show imaging results of MCF-10A human mammary epithelial cells and clear Thy1-YFP mouse brains.

METHODS AND MATERIALS

Our optical system is a standard LTFM, illustrated in **Figure 1**. The 80 MHz Chameleon Discovery (Coherent) is a laser source for two-photon excitation whose central wavelength is at 920 nm with pulse duration ∼100 fs. The laser power was controlled by an electro-optical modulator with the polarization modulated by a half-wave plate. A beam expander (BE05-10-B, Thorlabs) was utilized to expand the laser beam to 8 mm. After this expansion, the beam was scanned by a one-dimensional galvanometer (GVS211, Thorlabs) vertically and then formed a line on the surface of the grating (830 lines/mm, Edmund Optics) after the use of a cylindrical lens ($f = 400$ mm). A half-wave plate was placed in front of the galvanometer to maximize the efficiency of grating diffraction. To ensure that the central wavelength of the 1st diffraction light is perpendicular to the grating surface, the incident beam was directed at a ∼50° angle by a reflective mirror. A collimation lens ($f = 200$ mm) and an objective with NA 1.05 (XLPLN25XWMP2, Olympus), forming a 4f configuration, refocused the beam to a line-shape pattern on the specimen. For each scanning period, we captured a fluorescence image using an epifluorescence setup including a dichroic mirror (DMSP750B, Thorlabs), a bandpass filter (E510/80, Chroma), a 200-mm tube lens (TTL200-A, Thorlabs) and sCMOS (pixel size 6.50 μm, Andor Zyla 5.5 plus). Hardware synchronization was realized using a multi-functional DAQ (USB-6363, NI Instrument), with three voltage output channels controlling the response of the electro-optical modulator, galvanometer scanner, and camera acquisition respectively.

Photobleaching Imprinting of LTFM

In LTFM combined with a wide-field detection strategy, the background light consists of two parts: one part is the excited fluorescence out of the focal plane (E_{exc}), and the other part is the scattered fluorescence from the focal plane (E_{det}). Here, we show that the PIM can suppress the out-of-focus fluorescence (E_{exc}) and enhance the signal-to-noise ratio.

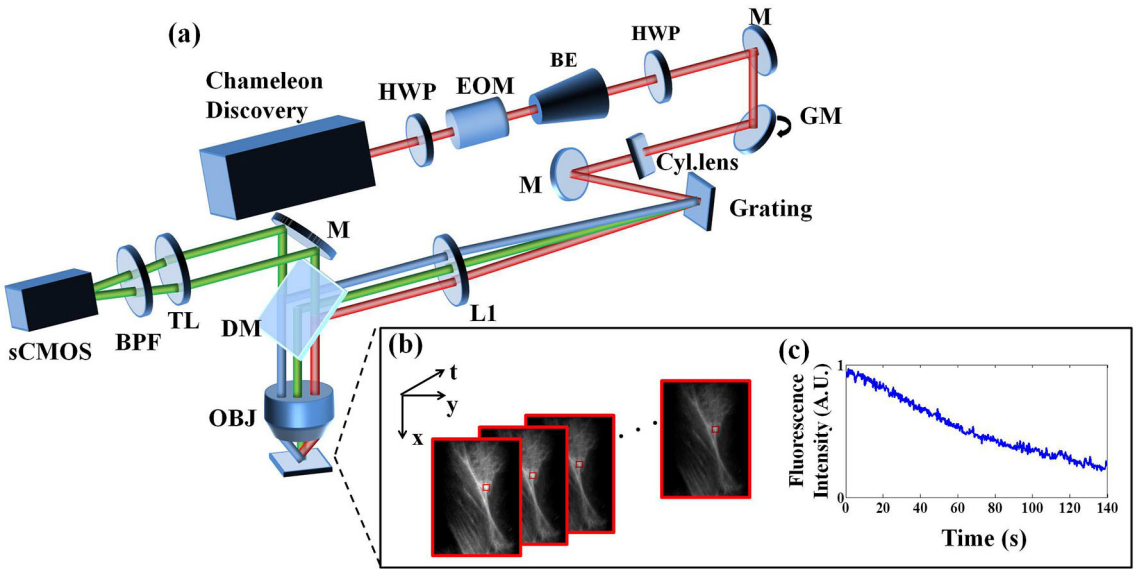

FIGURE 1 | (a) Line-scanning temporal focusing system. The ultrashort pulsed laser was modulated in intensity by an electro-optical modulator (EOM) and formed a line-shape focus on the grating after passing through a cylinder lens (Cyl.lens). The temporal chirp induced by the grating was first broadened then compressed to the minimum at the objective focus to form axial confinement. The fluorescence image was captured by an sCMOS camera in the epidetection scheme. **(b)** A sequence of images from photobleaching imprinting microscopy (PIM). **(c)** The fluorescence polynomial decay of the subregion marked by the red box in **(b)**. Symbols: HWP, half-wave plate; BE, beam expander; M, reflective mirror; GM, galvanometer mirror; L, lens; DM, dichroic mirror; TL, tube lens; BPF, bandpass filter; OBJ, objective.

Based on LTFM, the time-averaged fluorescence photon flux $<F>$, measured by a wide-field microscope, is the integration of the fluorescence emitted from all depths (Gao et al., 2014a):

$$\langle F(x,y)\rangle = C\int \left\{\mu_a(x,y,z)I^2(x,y,z)\right\} * \mathrm{PSF}_z(x,y)\mathrm{d}z \quad (1)$$

where C is a constant, μ_a is the two-photon absorption coefficient of the fluorophore, and PSF_z is the PSF of the fluorescence imaging system at depth z. I is the equivalent excitation fluence: $I(x,y,z) = \sqrt{\left\langle\left[I_b(x,y,z,t)+I_s(x,y,z,t)\right]^2\right\rangle}$, which consists of the ballistic excitation intensity I_b and scattered excitation intensity I_s. The operator $*$ represents 2D convolution and $<\cdot>$ represents time average.

In fluorescence microscopy, photobleaching occurs when the fluorochrome molecules are exposed to excitation light. Fluorophores irreversibly lose their ability to fluorescence due to the photon-induced chemical damage and covalent modification. The photobleaching obeys an empirical exponential temporal decay law (Gao et al., 2014b) (shown in **Figure 2A**) and in the Nth frame captured at time t_n, the absorption rate μ is also a function of t_n, written as:

$$\mu_a(x,y,z,t_n) = \mu_0(x,y,z)\exp(-kI^m t_n) \quad (2)$$

where μ_0 is the initial absorption coefficient and k is a constant. In the case of two-photon excitation, the photobleaching rate increases rapidly with $m \geq 3$ (Patterson and Piston, 2000; Gao et al., 2014a). Combining Equations (1) and (2) after Taylor expansion

$$\langle F(x,y,t_n)\rangle = C\sum_{l=0}^{\infty} t_n^l \frac{(-\mathrm{k})^l}{l!}\int_{-\infty}^{\infty}\mu_0(x,y,z)\,I^{ml+2}(x,y,z) * \mathrm{PSF}_z(x,y)\,\mathrm{d}z = \sum_{l=0}^{\infty}\langle F_l(x,y)\rangle t_n^l \quad (3)$$

where

$$\langle F_l(x,y)\rangle = D_l\int_{-\infty}^{\infty}\mu_0(x,y,z)\,I^{ml+2}(x,y,z) * \mathrm{PSF}_z(x,y)\mathrm{d}z = D_l I^{ml+2}(x,y,z_0)\int\mu_0(x,y,z)\left(\frac{I(x,y,z)}{I(x,y,z_0)}\right)^{ml+2} * \mathrm{PSF}_z(x,y)\,\mathrm{d}z \quad (4)$$

and $D_l = C(-\mathrm{k})l/l!$. In Equation (4), $F(t_n)$ is a polynomial function associated with t_n and $<F_l>$ is the coefficient for t_n^l depicted. $<F_l>$ can be derived from the polynomial fitting of $F(t_n)$. To solve $<F_l>$ in practice, a sequence of images is required (**Figure 1B**) to analyze intensity associated with time (**Figure 1C**).

In general, $I(x, y, z_0)$ is the maximum intensity of all depth in the sample, where z_0 is the imaging depth. When a 3D fluorescent sample is excited by LTFM along the depth axis, the photobleached fluorophores on the focal plane decay faster than

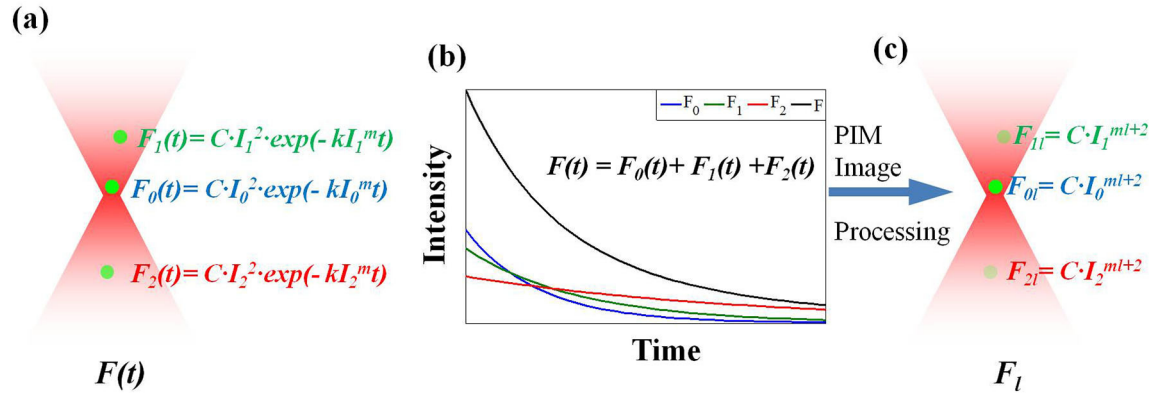

FIGURE 2 | The operating principle of LTFM-PIM. **(a)** The fluorophore sample is excited by an LTFM light along the depth axis. The photobleaching rate depends on the high order of excitation intensity *I*. **(b)** In the detection process, the total fluorescence of each fluorophore is detected. **(c)** High-order PIM component F_l, which is dependent on the $ml + 2$ order intensity distribution, is yielded by polynomial fitting of fluorescence decay.

those out of focus, which are dependent on *I* (**Figure 2A**). The polynomial fitting of fluorescent decay yields the PIM component $<F_l>$, which contains the higher order term *I*. Therefore, when $ml + 2 >> 1$, the excited fluorescence light of the focal plane can be suppressed by the higher order PIM component (**Figures 2B,C**).

Simulation of LTFM-PIM

To further demonstrate the effect of eliminating the out-of-focus fluorescence light by PIM, we assume that the spatial focus of the LTFM is same as in two-photon line-scanning microscopy, while the pulse widths were stretched by the effect of temporal focusing. Thus, we simplified the line-shaped focus model of the ballistic excitation distribution by the 1D Gaussian function shown below (Theer and Denk, 2006):

$$I_b(x,y,z,t) \propto \frac{2P_b(z,t)}{\omega_b(z_f)} \exp\left(-\frac{x^2}{\omega_b^2(z_f)}\right) \quad (5)$$

$$P_b(z,t) = \sqrt{\frac{2}{\pi}} \frac{E}{\tau_b(z)} \exp\left(-\frac{2t^2}{\tau_b^2(z)}\right) e^{-z/l_s} \quad (6)$$

where P_b is the ballistic optical power through a transverse plane, z_0 is imaging depth and $z_f = z - z_0$, l_s is the effective attenuation length of the excitation light. The variable $\omega_b(z)$ is the beam's half-width of the ballistic light at depth z and shown as follows (Theer and Denk, 2006): $\omega_b(z) = 2\sqrt{\lambda\left(z_f^2 + z_r^2\right)/\left(4\pi n z_r + \lambda z_f/l_s\right)}$. The Rayleigh range ($z_r$) is related to the beam's far-field angular spread θ_0: $z_r = \lambda/\left(n\pi\theta_0^2\right)$.

Then, the scattering excitation distribution was drawn from two-photon scanning microscopy as follows (Theer, 2004):

$$I_s(x,y,z,t) \propto \frac{2P_s(z,t)}{\omega_s(z_f)} \exp\left(-\frac{x^2}{\omega_s^2(z_f)}\right) \quad (7)$$

$$P_s(z,t) = \sqrt{\frac{2}{\pi}} \frac{E}{\tau_s(z)} \exp\left(-\frac{2t^2}{\tau_s^2(z)}\right)\left(1 - e^{-z/l_s}\right) \quad (8)$$

where P_s is the scattering optical power through a transverse plane. The beam width and pulse width of the scattering light at a different depth are $\omega_s(z) = \sqrt{\omega_b^2(z-z_0) + 4z^3(1-g)/(3l_s)}$ and $\tau_s(z) = \sqrt{\tau_b^2(z) + 8z^3(g-2)(g-1)/(9c^2 l_s) + 2z^4(1-g)^2/(3c^2 l_s^2)}$, where g is the anisotropy factor and c is the velocity of light. If we consider that the pulse width widens from temporal focusing, the Gaussian temporal profile at a different depth is estimated from wide-filed temporal focusing as $\tau_b(z) = \tau_0\left[1 + \frac{z_M}{z_b}\frac{(z_0-z)^2}{(z_0-z)^2 + z_M z_R}\right]^{\frac{1}{2}}$ and $z_M = \frac{2f^2}{ks^2}$, $z_R = \frac{2f^2/k}{s^2+\alpha^2\Omega^2}$, $z_B = \frac{2f^2}{k\alpha^2\Omega^2}$ (Durst et al., 2008).

In our system, the focal length of the objective f is 7.2 mm, and the pulse width at focal plane τ_0 is ~130 fs. The FWHM of each monochromatic beam $\sqrt{2\ln 2}s$ in space and the spatially-chirped beam $\alpha\Omega$ on the back aperture of the objective are 30 μm and 3.32 mm, respectively. The effective excitation NA for spatial focusing is ~0.5, and we set the anisotropy factor g is 0.9. The photobleaching rate is $m = 3$, and the imaging depth is 400 μm.

To evaluate the sectioning capability of the LTFM-PIM, we simulated a uniform fluorophore slice (5 nm thickness) at a different focal depth and calculated the total fluorescence of each slice $E(z)$ by integrating the fluorescence radially. Considering that the depth of field (DOF) in our system is approximate, $D = 2n\lambda_{flu}/NA_{det}^2 \approx 1.25\ \mu m$, by applying the collection numerical aperture $NA_{det} = 1.05$, and the wavelength of the fluorescence λ_{flu} is 520 nm, we define the energy of the signal fluorescence S and background light B as $S = \int_{z_0-0.5D}^{z_0+0.5D} E(z)\,dz$, $B = \int_{-\infty}^{z_0-0.5D} E(z)\,dz + \int_{z_0+0.5D}^{+\infty} E(z)\,dz$. We analyze the fluorescence in the scattering medium ($l_s = 400\,\mu m$). We integrate the intensity in each fluorescent slice and the results indicate that the SBR of the LTFM and LTFM-PIM are obtained 0.4 for LTFM and 2.3 for LTFM-PIM, demonstrates that the LTFM-PIM ($l = 1$) could suppress nearly five times the out-of-focus fluorescence (**Figure 3**).

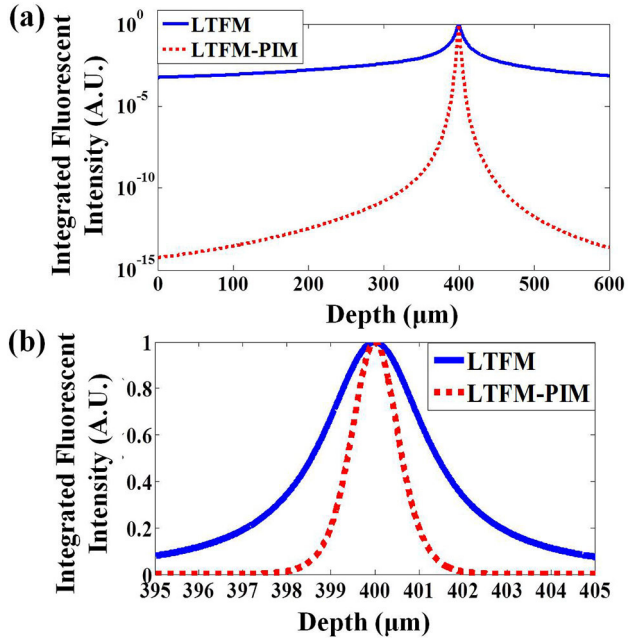

FIGURE 3 | (a) Radially integrated fluorescence vs. depth for the LTFM and LTFM-PIM ($l = 1$). **(b)** Radially integrated fluorescence for the LTFM and LTFM-PIM ($l = 1$) near the focus. The focal depth is 400 μm, the EAL (l_s) are 800 μm.

The results demonstrate that the out-of-focus fluorescence is almost eliminated by the PIM technology, improving the SBR effectively.

Experimental Data Processing

For practical implementation, the LTFM-PIM image was obtained by processing time-lapse images with the following steps (Xiong et al., 2020):

1. Take M time-lapsed LTFM images with the same exposure time: $F_1, F_2 \ldots F_M$;
2. For each pixel (x, y) in an image, we extract an intensity curve with time $F_N(x, y)$;
3. Following Equations (1) and (4), we apply the exponential decay function to fit the intensity curve $F_N(x, y)$. To solve the intensity curve simply, we use the logarithmic operation to get: $\ln\left(F_N\left(x,y\right)\right) = \ln\left(a\left(x,y\right)\right) - b\left(x,y\right)N$. Then, we can do a linear fit on the intensity $F_1(x, y)$, $F_2(x, y) \ldots F_M(x, y)$ to get $\ln[a(x, y)]$ and $b(x, y)$ of each pixel;
4. For the lth order PIM component, we generate the LTFM-PIM image$F_l\left(x,y\right) = a\left(x,y\right)\cdot b^{l}\left(x,y\right)$.

Sample Preparation

MCF-10A Cells

MCF-10A cells (ATCC CRL-10317) were maintained and subcultured in MEBM basal medium supplemented with bullet kits (CC-3150, Lonza). 1.00×10^4 cells were seeded on Φ12 mm circular coverslips (0.17 mm thickness, Fisher Brand), then fixed by 4% paraformaldehyde in the phosphate buffered saline (PBS) after overnight incubation at 37°C 5% CO_2 incubator. Cells were permeated by 0.2% TritonX-100 for 15 min, blocked in 3% BSA in PBS for 1 h at the room temperature, and incubated with Tom20 antibody (sc11415, Santa Cruz) overnight at 4°C. The next day, cells were washed with PBS and stained with Alexa Fluor 488 labeled goat-anti-rabbit IgG (ab150077, Abcam) for 2 h at the room temperature.

Cleared Mouse Brain

After deeply anesthetized and perfused with phosphate buffered saline, we remove the brain from the mouse and cut it to 1 mm transverse slices after fixation. The slices are sequentially dehydrated in a series of tert-butanol (30, 50, 70, 80, 90, 96, and 100%, 2 h each step) at room temperature. The dehydrated slices are incubated in BABB-D4 (BABB: benzyl alcohol/benzyl benzonate = 1/2, BABB-D4: BABB/diphenyl ether = 4/1) for more than 1 h at room temperature until they became optically transparent. The EAL (l_s) of the brainslice is approximate 800 μm.

RESULTS

Imaging of the MCF-10A Sample

We first validated the contrast enhancement on biological samples by imaging MCF-10A human mammary epithelial cells, whose F-actin is stained with Alexa Fluor 488. The photobleaching rate m of Alexa Fluor 488 in cells is $2 < m < 4$ (Chen et al., 2001). The imaging depth was ~100 μm. Fluorescence images obtained by LTFM and LTFM-PIM ($l = 1$) were presented in **Figures 4a,b**, respectively. The power after the objective was 200 mW. Due to the scattering light and relatively thick optical section, the in-focus structure was obscured by out-of-focus fluorescent light so that the image was blurred. By contrast, LTFM-PIM image, which was calculated by 100 time-lapse LTFM images with 0.3 s frame integration time, had a significant signal-to-background ratio (SBR) compared with the original one. We measured the intensity fluctuations alone the yellow line in **Figures 4a,b**, indicating that the structures were shaper in the LTFM-PIM image due to the decreased background. The SBR level of the microtubule labeled by the yellow line, labeled by (c), decreased from 0.6 to 0.2, shown in **Figure 4c**, owing to the elimination of the background around the microtubule. Furthermore, comparing intensity fluctuations alone the red line, labeled by (d) in each image, the signals of the microtubules were almost submerged in the background so that the closely distanced microtubules could be distinguished—see the blue solid curve in **Figure 4d**. After using PIM computation, we found that closely distanced microtubules were distinguished clearly with our LTFM-PIM. The background levels between the microtubules are decreased from 0.9 to 0.6 by our method—see the green dashed curve plotted in **Figure 4d**.

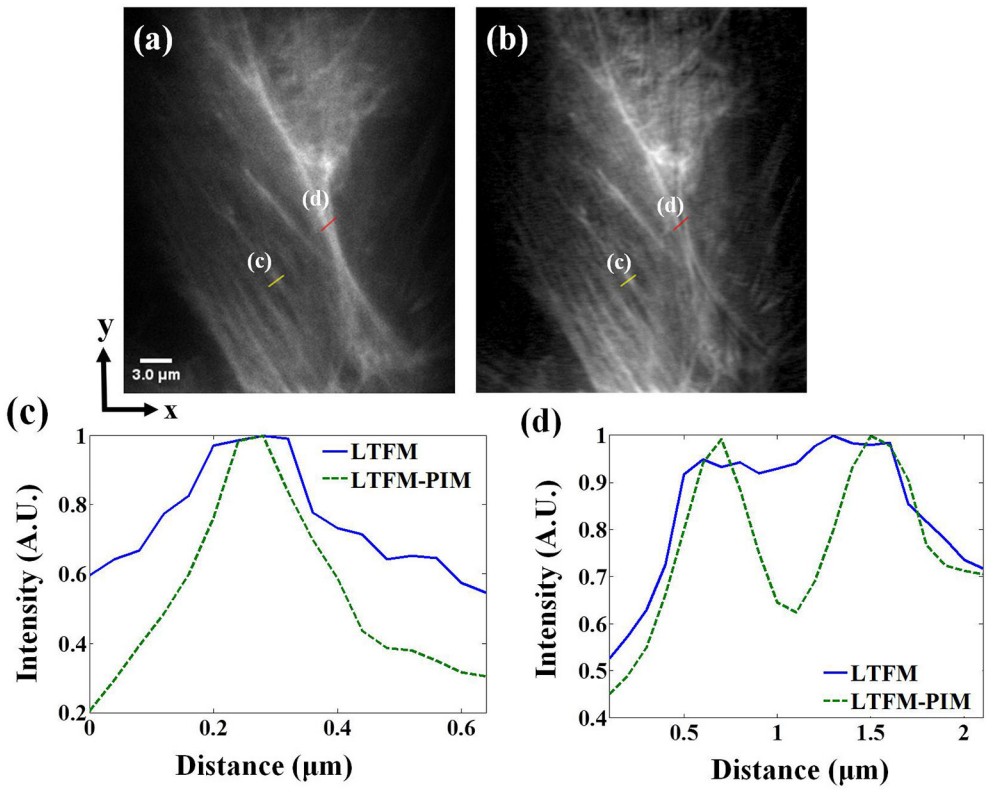

FIGURE 4 | (a,b) LTFM and LTFM-PIM images of an MCF-10A human mammary epithelial cell, respectively. **(c,d)** Comparison of signal intensities along the yellow and red solid lines in **(a,b)**. Gamma correction 0.5 was applied to enhance the visibility of mitochondria structures.

Imaging of the Cleared Thy1-YFP Brainslice

Next, we imaged the cleared brainslice of Thy1-YFP-H mice (JAX No. 003782) to further demonstrate the contrast-enhanced performance of our technique for deep imaging. The photobleaching rate m of YFP in cells is >3.5 (Chen et al., 2001). The power after the objective was 250 mW. At ∼300 μm under the surface of the brainslice, the fluorescence signals of the dendritic spines were almost submerged in background light because of scattering, as shown in **Figure 5a**. Especially in the subregion marked in the yellow box in **Figure 5a**, the dendritic spines were hardly distinguishable, as shown in the upper image in **Figure 5c**. The minimal background noise between the two spines was about 0.6—see the blue solid line in **Figure 5d**. By contrast, in the corresponding LTFM-PIM image ($l = 1$) which was calculated by 250 time-lapse LTFM images with 0.3 s frame integration time, the dendritic spines were visible clearly, and most out-of-focus light was suppressed. Also, compared with the same region marked by a yellow box in **Figure 5b**, LTFM-PIM provided a higher contrast image, allowing clear visualization of dendritic spines. The minimal background noise between the two spines was <0.2, shown by the green dashed curve in **Figure 5d**. The result indicated that LTFM failed to provide enough contrast, while the LTFM-PIM improved contrast approximately five times so that dendritic spines were distinguishable. Therefore, LTFM-PIM showed superior contrast-enhanced ability in the scattering medium.

DISCUSSION

Tissue scattering deteriorates image quality from two aspects: out-of-focus light contributes to the majority of background, while in-focus fluorescence induces image blur. We had validated the fact that the PIM could effectively eliminate fluorescence out of the focal plane (E_{exc}), while the fluorescence crosstalk between neighboring pixels from the focal plane (E_{det}) could be further alleviated by deconvolution algorithms (Zhang et al., 2019). In our experiment, we record photobleaching decay of the samples for tens of seconds to achieve better restriction results. To record biological dynamics such as neural activity in cells, this method could be optimized with a higher pulse energy laser and combined with novel fluorescence proteins like GFP with reversible photobleaching (Sinnecker et al., 2005; Gao et al., 2016; Niu et al., 2019).

CONCLUSION

In summary, we utilized the photobleaching imprinting technique to reject background light and improved contrast

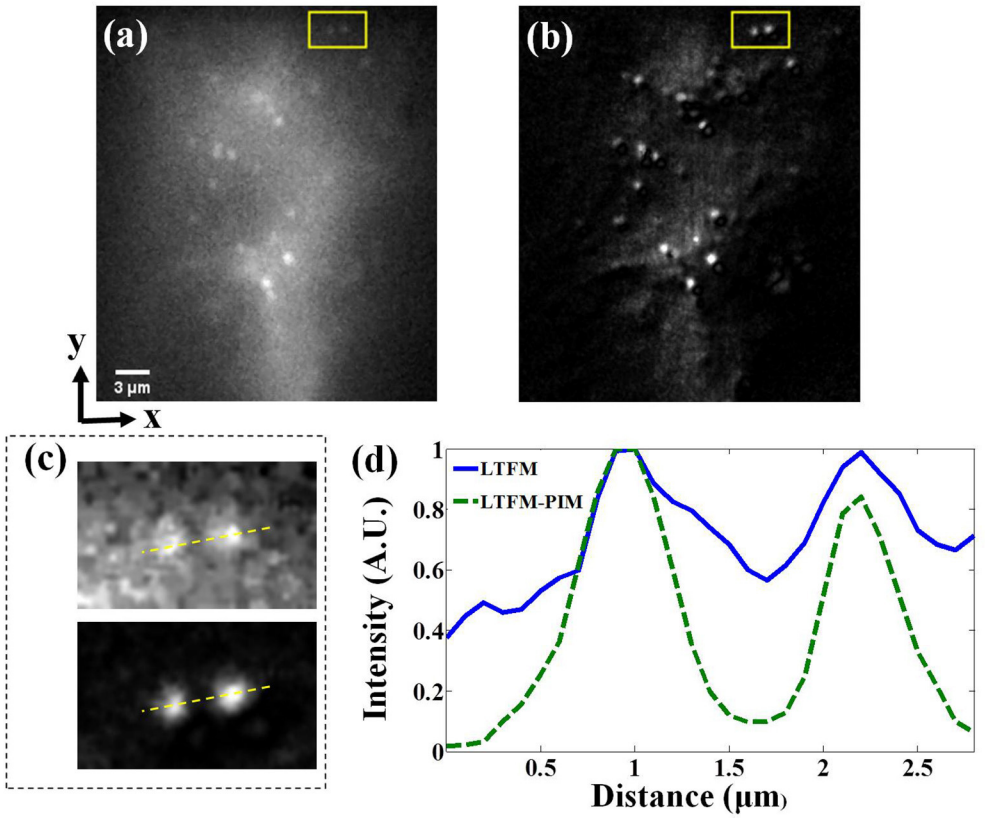

FIGURE 5 | (a,b) LTFM and LTFM-PIM image of a cleared brainslice of the Thy1-YFP mice, respectively (about 300 μm under the surface of the slices). **(c)** Magnified view of the subregion marked by the yellow box—upper image for **(a)** and lower for **(b)**. **(d)** Signal intensity along the yellow dash lines in **(c)**.

by fully using the properties of line-scanning temporal focusing microscopy. With the removal of the background light, the proposed method could achieve high contrast imaging both in the transparent and scattering medium. We analyzed our method numerically by simulation and validated the performance improvement in imaging MCF-10A human mammary epithelial cells and cleared mouse brainslices.

DATA AVAILABILITY STATEMENT

The original contributions generated for the study are included in the article/supplementary materials, further inquiries can be directed to the corresponding author/s.

ETHICS STATEMENT

The animal study was reviewed and approved by the Animal Care and Use Committees of Tsinghua University.

AUTHOR CONTRIBUTIONS

CZ performed the experiments, analyzed the results, made the simulations, and drafted the manuscript. XL and YZ built the imaging setup and assisted with taking the fluorescence images. LK supervised the biological experiments. HX and QD conceived the original idea and supervised the project. All authors contributed to the article and approved the submitted version.

FUNDING

This work was supported by Natural Science Foundation of Beijing Municipal Science & Technology Commission (BMSTC) (No. Z181100003118014) and National Natural Science Foundation of China (NSFC) (Nos. 61327902, 61971256, and 62088102). This is a project of the National Key Research and Development Program of China (No. 2020AA0105500s).

ACKNOWLEDGMENTS

CZ thanks Xu Zhang for help in sample preparation and Xiaofei Han for valuable discussions.

REFERENCES

Chen, T., Zeng, S., Luo, Q., Zhou, W., and Zhang, Z. (2001). "Novel photobleaching model in living cells," in *Paper Presented at the Proceedings of SPIE - The International Society for Optical Engineering, Russian, Federation.*

Cheng, L. C., Chang, C. Y., Lin, C. Y., Cho, K. C., Yen, W. C., Chang, N. S., et al. (2012). Spatiotemporal focusing-based widefield multiphoton microscopy for fast optical sectioning. *Opt. Exp.* 20, 8939–8948. doi: 10.1364/OE.20.008939

Cheng, L. C., Lien, C. H., Da Sie, Y., Hu, Y. Y., Lin, C. Y., Chien, F. C., et al. (2014). Nonlinear structured-illumination enhanced temporal focusing multiphoton excitation microscopy with a digital micromirror device. *Biomed. Opt. Exp.* 5, 2526–2536. doi: 10.1364/BOE.5.002526

Dana, H., Kruger, N., Ellman, A., and Shoham, S. (2013). Line temporal focusing characteristics in transparent and scattering media. *Opt. Exp.* 21, 5677–5687. doi: 10.1364/OE.21.005677

Dana, H., Marom, A., Paluch, S., Dvorkin, R., Brosh, I., and Shoham, S. (2014). Hybrid multiphoton volumetric functional imaging of large-scale bioengineered neuronal networks. *Nat. Commun.* 5:3997. doi: 10.1038/ncomms4997

Dana, H., and Shoham, S. (2011). Numerical evaluation of temporal focusing characteristics in transparent and scattering media. *Opt. Exp.* 19, 4937–4948. doi: 10.1364/OE.19.004937

Denk, W., Strickler, J. H., and Webb, W. W. (1990). Two-photon laser scanning fluorescence microscopy. *Science* 248, 73–76. doi: 10.1126/science.2321027

Durst, M., Straub, A., and Xu, C. (2009). Enhanced axial confinement of sum-frequency generation in a temporal focusing setup. *Opt. Lett.* 34, 1786–1788. doi: 10.1364/OL.34.001786

Durst, M. E., Zhu, G., and Xu, C. (2008). Simultaneous spatial and temporal focusing in nonlinear microscopy. *Opt. Commun.* 281, 1796–1805. doi: 10.1016/j.optcom.2007.05.071

Gao, J., Yang, X., Djekidel, M. N., Wang, Y., Xi, P. Zhang, Michael. (2016). Developing bioimaging and quantitative methods to study 3D genome. *Quantitative Biology*, 4, 129–147. doi: 10.1007/s40484-016-0065-2

Gao, L., Garcia-Uribe, A., Liu, Y., Li, C., and Wang, L. V. (2014a). Photobleaching imprinting microscopy: seeing clearer and deeper. *J. Cell. Sci.* 127, 288–294. doi: 10.1242/jcs.142943

Gao, L., Zhu, L., Li, C., and Wang, L. V. (2014b). Nonlinear light-sheet fluorescence microscopy by photobleaching imprinting. *J. R. Soc. Interface* 11:20130851. doi: 10.1098/rsif.2013.0851

Helmchen, F., and Denk, W. (2005). Deep tissue two-photon microscopy. *Nat. Methods* 2, 932–940. doi: 10.1038/nmeth818

Kong, L., Tang, J., Little, J. P., Yu, Y., Lammermann, T., Lin, C. P., et al. (2015). Continuous volumetric imaging via an optical phase-locked ultrasound lens. *Nat. Methods* 12, 759–762. doi: 10.1038/nmeth.3476

Leray, A., and Mertz, J. (2006). Rejection of two-photon fluorescence background in thick tissue by differential aberration imaging. *Opt. Exp.* 14, 10565–10573. doi: 10.1364/OE.14.010565

Li, C., Gao, L., Liu, Y., and Wang, L. V. (2013). Optical sectioning by wide-field photobleaching imprinting microscopy. *Appl. Phys. Lett.* 103:183703. doi: 10.1063/1.4827535

Li, Z. W., Hou, J., Suo, J. L., Qiao, C., Kong, L. J., and Dai, Q. H. (2017). Contrast and resolution enhanced optical sectioning in scattering tissue using line-scanning two-photon structured illumination microscopy. *Opt. Exp.* 25, 32010–32020. doi: 10.1364/OE.25.032010

Lou, K., Wang, B., Jee, A. Y., Granick, S., and Amblard, F. (2018). Deep line-temporal focusing with high axial resolution and a large field-of-view using intracavity control and incoherent pulse shaping. *Opt. Lett.* 43, 4919–4922. doi: 10.1364/OL.43.004919

Meng, Y., Lin, W., Li, C., and Chen, S. C. (2017). Fast two-snapshot structured illumination for temporal focusing microscopy with enhanced axial resolution. *Opt. Exp.* 25, 23109–23121. doi: 10.1364/OE.25.023109

Niu, F., Wu, R., Wu, D., Gou, D., Feng, L., Chen, L., et al. (2019). Photobleaching of ultrashort pulses with different repetition rates in two-photon excitation microscopy. *Laser Phys.* 29, 288–294. doi: 10.1088/1555-6611/ab036a

Oron, D., and Silberberg, Y. (2015). Temporal focusing microscopy. *Cold Spring Harb Protoc.* 2015, 145–151. doi: 10.1101/pdb.top085928

Oron, D., Tal, E., and Silberberg, Y. (2005). Scanningless depth-resolved microscopy. *Opt. Exp.* 13, 1468–1476. doi: 10.1364/OPEX.13.001468

Papagiakoumou, E., Anselmi, F., Begue, A., de Sars, V., Gluckstad, J., Isacoff, E. Y., et al. (2010). Scanless two-photon excitation of channelrhodopsin-2. *Nat. Methods* 7, 848–854. doi: 10.1038/nmeth.1505

Park, J. K., Rowlands, C. J., and So, P. T. C. (2017). Enhanced axial resolution of wide-field two-photon excitation microscopy by line scanning using a digital micromirror device. *Micromachines* 8:85. doi: 10.3390/mi8030085

Patterson, G. H., and Piston, D. W. (2000). Photobleaching in two-photon excitation microscopy. *Biophys. J.* 78, 2159–2162. doi: 10.1016/S0006-3495(00)76762-2

Rowlands, C. J., Park, D., Bruns, O. T., Piatkevich, K. D., Fukumura, D., Jain, R. K., et al. (2017). Wide-field three-photon excitation in biological samples. *Light Sci. Appl.* 6:e16255. doi: 10.1038/lsa.2016.255

Sinnecker, D., Voigt, P., Hellwig, N., and Schaefer, M. (2005). Reversible photobleaching of enhanced green fluorescent proteins. *Biochemistry* 44, 7085–7094. doi: 10.1021/bi047881x

Tal, E., Oron, D., and Silberberg, Y. (2005). Improved depth resolution in video-rate line-scanning multiphoton microscopy using temporal focusing. *Opt. Lett.* 30, 1686–1688. doi: 10.1364/OL.30.001686

Theer, P. (2004). *On the Fundamental Imaging-Depth Limit in Two-Photon Microscopy* (Doctoral dissertation). Ruperto-Carola University of Heidelberg, Germany.

Theer, P., and Denk, W. (2006). On the fundamental imaging-depth limit in two-photon microscopy. *J. Opt. Soc. Am. A Opt. Image Sci. Vis.* 23, 3139–3149. doi: 10.1364/JOSAA.23.003139

Therrien, O. D., Aube, B., Pages, S., Koninck, P. D., and Cote, D. (2011). Wide-field multiphoton imaging of cellular dynamics in thick tissue by temporal focusing and patterned illumination. *Biomed. Opt. Exp.* 2, 696–704. doi: 10.1364/BOE.2.000696

Wang, M., Wu, C., Sinefeld, D., Li, B., Xia, F., and Xu, C. (2018). Comparing the effective attenuation lengths for long wavelength *in vivo* imaging of the mouse brain. *Biomed. Opt. Exp.* 9, 3534–3543. doi: 10.1364/BOE.9.003534

Xiong, B., Han, X., Wu, J., Xie, H., and Dai, Q. (2020). Improving axial resolution of Bessel beam light-sheet fluorescence microscopy by photobleaching imprinting. *Opt. Exp.* 28, 9464–9476. doi: 10.1364/OE.388808

Zhang, Y., Kong, L., Xie, H., Han, X., and Dai, Q. (2018). Enhancing axial resolution and background rejection in line-scanning temporal focusing microscopy by focal modulation. *Opt. Exp.* 26, 21518–21526. doi: 10.1364/OE.26.021518

Zhang, Y., Zhou, T., Hu, X., Li, X., Xie, H., Fang, L., et al. (2019). Overcoming tissue scattering in wide-field two-photon imaging by extended detection and computational reconstruction. *Opt. Exp.* 27, 20117–20132. doi: 10.1364/OE.27.020117

Zipfel, W. R., Williams, R. M., and Webb, W. W. (2003). Nonlinear magic: multiphoton microscopy in the biosciences. *Nat. Biotechnol.* 21, 1368–1376. doi: 10.1038/nbt899

Conflict of Interest: The authors declare that the research was conducted in the absence of any commercial or financial relationships that could be construed as a potential conflict of interest.

frontiers in Chemistry

ORIGINAL RESEARCH
published: 15 January 2021
doi: 10.3389/fchem.2020.601436

A Labeling Strategy for Living Specimens in Long-Term/Super-Resolution Fluorescence Imaging

*Yubing Han[1], Zhimin Zhang[1], Wenjie Liu[1], Yuanfa Yao[2], Yingke Xu[2], Xu Liu[1,3,4], Cuifang Kuang[1,3,4] and Xiang Hao[1]**

[1] State Key Laboratory of Modern Optical Instrumentation, College of Optical Science and Engineering, Zhejiang University, Hangzhou, China, [2] Department of Biomedical Engineering, Key Laboratory of Biomedical Engineering of Ministry of Education, Zhejiang Provincial Key Laboratory of Cardio-Cerebral Vascular Detection Technology and Medicinal Effectiveness Appraisal, Zhejiang University, Hangzhou, China, [3] Ningbo Research Institute, Zhejiang University, Ningbo, China, [4] Collaborative Innovation Center of Extreme Optics, Shanxi University, Taiyuan, China

OPEN ACCESS

Edited by:
Fan Wang,
University of Technology Sydney, Australia

Reviewed by:
Karl Zhanghao,
Southern University of Science and Technology, China
Hao Xie,
Tsinghua University, China
Chaohao Chen,
ETH Zürich, Switzerland

***Correspondence:**
Xiang Hao
haox@zju.edu.cn

Specialty section:
This article was submitted to Analytical Chemistry, a section of the journal Frontiers in Chemistry

Received: 01 September 2020
Accepted: 14 December 2020
Published: 15 January 2021

Citation:
Han Y, Zhang Z, Liu W, Yao Y, Xu Y, Liu X, Kuang C and Hao X (2021) A Labeling Strategy for Living Specimens in Long-Term/Super-Resolution Fluorescence Imaging. Front. Chem. 8:601436. doi: 10.3389/fchem.2020.601436

Despite the urgent need to image living specimens for cutting-edge biological research, most existing fluorescent labeling methods suffer from either poor optical properties or complicated operations required to realize cell-permeability and specificity. In this study, we introduce a method to overcome these limits—taking advantage of the intrinsic affinity of bright and photostable fluorophores, no matter if they are supposed to be live-cell incompatible or not. Incubated with living cells and tissues in particular conditions (concentration and temperature), some Atto and BODIPY dyes show live-cell labeling capability for specific organelles without physical cell-penetration or chemical modifications. Notably, by using Atto 647N as a live-cell mitochondrial marker, we obtain 2.5-time enhancement of brightness and photostability compared with the most commonly used SiR dye in long-term imaging. Our strategy has expanded the scientist's toolbox for understanding the dynamics and interactions of subcellular structures in living specimens.

Keywords: super-resolution microscopy, organic fluorescent dye, long-term imaging, living specimens, subcellular structures

INTRODUCTION

Biologists rely on an array of fluorescent microscopy to observe morphologies and dynamics in living cells, which is crucial in interpreting vital physiological and pathological activities. However, although dramatic improvements have been implemented since the seminal discovery of fluorophores and their applications in microscopy (Miyawaki et al., 2003; Specht et al., 2017), it is still quite challenging to achieve live-cell specific staining simultaneously with high brightness and photostability.

In fact, most live-cell labeling methods, including fluorescent proteins (Mishin et al., 2015), chemical tag techniques using cell-permeable fluorescent dyes [e.g., SNAP-Cell 647-SiR (Lukinavičius et al., 2015)], and live-cell organic fluorescent probes [e.g., MitoTracker dyes (Chazotte, 2011)], suffer from relatively low brightness and photostability (Fernandez-Suarez and Ting, 2008; Han et al., 2017). Low optical properties of the fluorescent probes may

lead to low signal-to-noise ratios (SNR) and fast photobleaching, while low SNR reduces the quality of the microscope images or may even introduce artifacts. Worse still, is that the photobleaching is undesirable in long-term experiments. A dosage increase can partially remedy this problem, but it may also lead to non-specific labeling (Han et al., 2017; Shen et al., 2018). Another option is to increase the illumination laser power, but it, in turn, further accelerates the photobleaching and introduces stronger phototoxicity. This issue stands out especially in imaging methods for more information in multiple dimensions (e.g., high spatiotemporal resolution, long acquisition times, and large volume imaging) (Jaiswal et al., 2003; Fernandez-Suarez and Ting, 2008; Ji et al., 2016).

In the past few decades, various types of commercially available dyes, with exceptionally excellent brightness and photostability, have been developed and are widely used in cells and organisms (Chazotte, 2011; Sigal et al., 2018). Although several dyes have been proven to be efficient in live-cell super-resolution imaging (Lukinavicius et al., 2014; Yang et al., 2020), most of these fluorophores were supposed to be "live-cell incompatible" (Mao et al., 2020). Their intracellular cytosolic delivery and labeling specifically, rely heavily on specific physical or chemical methods, such as microinjection, encapsulating vesicles, or chemical modifications using cell-penetrating peptides (Erazo-Oliveras et al., 2014; Hennig et al., 2015; Han et al., 2017).

Following our previous work, which demonstrated the live-cell mitochondrial labeling capacity of Atto 647N (Han et al., 2017), here we prove that Atto 647N is not an individual case and that there is a general pattern behind it. We present a strategy to label living cells and tissues using commercially available dyes that were supposed to be "incompatible" for live-cell labeling (von Provazek, 1914; Bosch et al., 2014). The transition from "incompatible" to "compatible" is based on discovering and utilizing the intrinsic affinity of the dyes to subcellular structures in living cells when working at micromolar-level concentrations. Specifically, by incubating with living specimens at 1.5–15 μM for 30 min at 37°C or 20°C, the "live-cell incompatible" dyes can also be used for live-cell labeling, without needing complicated chemical modifications or physical operations during the entire process. Using our labeling strategy, these commercially available dyes, especially Atto 647N NHS ester, shows great potential as a live-cell mitochondrial marker in long-term, three-dimensional (3D), and super-resolution imaging.

MATERIALS AND METHODS

Primary Cultural Astrocytes

Primary cultural astrocytes were obtained from Sprague-Dawley (SD) rat brains (1 day old). The rats were bought from the Zhejiang Research Center of Laboratory Animals, China, sterilized with 75% ethanol, and sacrificed by decapitation. The following steps were all done on ice. The scalps and skulls were incised, and the brains were taken out and placed into pre-cooling Phosphate buffered saline (PBS; Thermo Fisher Scientific, Inc.). The cortex was then isolated, cut into pieces using knives, and incubated with pre-warmed Trypsin-EDTA (Thermo Fisher Scientific, Inc.) at 37°C for 20 min. The mixture was centrifuged for 5 min at 1,000 rpm, and the supernatant was removed. The cells were then dissociated by adding 5 mL of pre-warmed growth medium (DMEM, high glucose + 10% fetal bovine serum (FBS); Thermo Fisher Scientific, Inc.), followed by vigorous pipetting. Finally, the cell suspension was incubated in a T25 flask (Thermo Fisher Scientific, Inc.) at 37°C in a humidified 5% CO_2 environment. The medium was changed every 2 days, and after 7 ∼ 8 days, the culture flask was shaken manually for 30 min to remove the overlaying microglia exposed on the astrocyte layer. The supernatant containing microglia was discarded, and 5 mL of culture medium was added into the flask. This step was repeated once to remove oligodendrocyte precursor cells.

Cell Culture

HeLa (human adenocarcinoma cell line), HEK293 (human embryonic kidney epithelial cell line), NIH/3T3 (mouse embryonic fibroblast cell line), and U2OS (human osteosarcoma cell line) cells were purchased from the American Type Culture Collection. HeLa, HEK293, and NIH/3T3 cells were cultured in the DMEM medium (Thermo Fisher Scientific, Inc.). U2OS cells were cultured in McCoy's 5A medium (Thermo Fisher Scientific, Inc.). All media were supplemented with 10% (v/v) FBS, and the cultures were maintained at 37°C in a humidified 5% CO_2 environment.

Transfection

Cells were grown overnight in 24-well plates at 37°C in a 5% CO_2 atmosphere. After reaching over 80% confluence, the plasmids mRuby-Clathrin (Addgene #55852), pEGFP-Sec23A (Addgene #66609), ZsGreen-Rab5 (custom synthesized by Genomeditech (Shanghai, China) Co., Ltd.), EGFP-Rab7A (Addgene #28047), GFP-LAMP1 (Addgene #16290), EMTB-3XGFP (Addgene #26741), pSNAPf-Cox8A (Addgene #101129), or pSNAPf-TOMM20 (custom synthesized by Genomeditech (Shanghai, China) Co., Ltd.) was transfected into the cells using Lipofectamine 3000 (Thermo Fisher Scientific, Inc.) according to the manufacturer's instructions. After 24 h, the transfected cells were digested with trypsin-EDTA and seeded into Nunc Glass Bottom Dishes (Φ 12 mm, Thermo Fisher Scientific, Inc.) at a density of 1.5 ∼ 2.0 × 10^4 per well in growth medium (150 μL). The cells were grown for an additional 12 ∼ 24 h before incubation with the indicated probes.

Live-Cell Labeling With Commercially Available Probes

Before staining, the indicated cells were seeded in Nunc Glass Bottom Dishes at a density of 1.5 ∼ 2.0 × 10^4 per well in growth medium (150 μL). After overnight incubation, the cells were washed three times with PBS. Working solutions of the indicated probes at different concentrations were prepared with phenol red-free DMEM (Thermo Fisher Scientific, Inc.). The cells were then incubated with MitoTracker Deep Red FM (200–500 nM, 100 μL; Thermo Fisher Scientific, Inc.), MitoTracker Green FM (1,000 nM, 100 μL; Thermo Fisher Scientific, Inc.), SiR-actin (Cytoskeleton, Inc.), and DiO (5 μM, 100 μL; Beyotime Biotechnology) in a 5% CO_2 atmosphere at

37°C for 30 min. For SNAP-Cell 647-SiR (New England Biolabs, Inc.) dye labeling, transfection of pSNAPf-Cox8A or pSNAPf-TOMM20 was performed before incubation of SNAP-Cell 647-SiR (3 μM) at 37°C for 30 min. After incubation, the supernatant was discarded, and a solution of Trypan blue (TB, 100 μL, 1 mg mL^{-1}; Sigma-Aldrich Co., LLC) in PBS was added to exclude the dead cells and quench the extracellular fluorescence from the probes bound to either the cell membrane or the dish surface (Manceur et al., 2007; Cottet-Rousselle et al., 2011; Han et al., 2017). After 1 min, TB was removed, and the cells were washed twice gently with PBS. Cells were immersed in Live Cell Imaging Solution (Thermo Fisher Scientific, Inc.) before imaging. ProLong Live Antifade Reagent (Thermo Fisher Scientific, Inc.) was added to this solution according to the manufacturer's instructions when required.

Live-Cell Labeling With Fluorescent Dyes

Before staining, the indicated cells were seeded in Nunc Glass Bottom Dishes at a density of $1.5 \sim 2.0 \times 10^4$ per well in growth medium (150 μL). After overnight incubation, the cells were washed three times with PBS. Aliquots of Atto 495, Atto 565, Atto 590, Atto 647N (Sigma-Aldrich Co., LLC), BODIPY 650/665, Alexa Fluor 647 (Thermo Fisher Scientific, Inc.), Cy3B, and Cy5 (GE Healthcare Co., Ltd) NHS esters were dissolved in Dimethyl sulfoxide (DMSO; Sigma-Aldrich Co., LLC) to make 3-mM stock solutions at −20°C. Stock solutions were diluted with phenol red-free DMEM to work solutions at different concentrations before use. The cells were incubated with these dyes either at 37°C in a 5% CO_2 atmosphere or at 20°C for 30 min. The post-incubation treatment was the same as that of the commercially available probes above.

The organic probes Dye-Lyso, Dye-Tubulin, and Dye-Actin were constructed in two parts. One part contains the recognition unit (epoxysuccinyl scaffold (Han et al., 2017), docetaxel (Lukinavicius et al., 2018), and Lifeact (Han et al., 2019), the cell-penetrating peptide $(rR)_3R_2$, and a short peptide GKGKGK (in which lysine offers free active amino groups available to conjugate with commercially available dyes via an NHS group). The other part is a commercially available fluorescent dye containing an NHS group. Covalent bonds link these two parts to form an entire probe. The first part was later purified by preparative high-performance liquid chromatography (HPLC) to >95% after being prepared by solid-phase peptide synthesis. Its mass was confirmed by electrospray ionization mass spectrometry (EI-MS). Before being conjugated to the dyes, the peptide part was dissolved in bicarbonate buffer (0.1 M, pH 8.3) at a 1 mM concentration and stored at 4°C. For the conjugation, an aliquot of each dye was dissolved with 10–20 μL of DMSO added to 14 μL of the peptide part solution and mixed thoroughly. The mixture was allowed to react at room temperature overnight with constant shaking. The mixture was then purified using Pierce C18 Spin columns (Thermo Fisher Scientific, Inc.) according to the manufacturer's instructions. After purification, the supernatant was evaporated to dryness in a vacuum centrifuge, and the residue was dissolved in 200 μL of Phosphate Buffered Saline (PBS, pH 7.4; Thermo Fisher Scientific, Inc.) to generate a stock solution of the indicated probes.

Filipin (Meilunbio) and Cytochalasin D (Aladdin) were dissolved in DMSO to make 1-mM stock solutions, which were diluted with phenol red-free DMEM to working solutions at different concentrations before use. The cells were incubated with the drug solutions for 30 min at 37°C in a 5% CO_2 atmosphere before Atto 565 labeling.

Labeling Living Tissue Slices With Fluorescent Probes

All animal procedures were conducted in compliance with the guidelines for animal care and use of Zhejiang University and conformed to the Guide for the Care and Use of Laboratory Animals published by the National Academy Press (Washington, DC, 1996). The 12-week-old Institute of Cancer Research (ICR) mice were obtained from Zhejiang Academy of Medical Sciences [License Number: SCXK (Zhe) 2014001] and housed in cages under a standard condition of temperature (23 ± 2°C), relative humidity (55 ± 5%), and a light 12/12 h light/dark cycle. The mice had free access to food and water. Before the experiment, the mice were sacrificed by euthanasia. The brains were separated and washed with cold PBS buffer. The brains were then cut into slices from different orientations and incubated with Atto 647N (15 μM) for 30 min at 37°C. After incubation, the supernatant was discarded, and the tissue slices were washed twice gently with PBS. The tissue slices were then put on the Nunc Glass Bottom Dishes with the wound surface toward the glass bottom.

Cell Viability

The Atto dyes' cytotoxicity on different cell lines was tested using the 3-(4,5-dimethylthiazol-2-yl)-5-(3-carboxymethoxyphenyl)-2-(4-sulfophenyl)-2H-tetrazolium (MTS) assay (Cory et al., 1991). Cells ($3–4 \times 10^3$ cells per well) were seeded into a 96-well plate and cultured in the growth medium for 24 h. The cells were incubated with the dyes (1.5 μM or 15 μM) in a 5% CO_2 atmosphere at 20°C or 37°C for 30 min, washed twice gently with PBS, and incubated in the growth medium for 3 h at 37°C. The cells were then immersed in 100 μL of growth medium and 20 μL of CellTiter 96 AQueousOne Solution Reagent (Promega Co.) for another 1 h at 37°C, and the absorbance was recorded at 492 nm using a TECAN GENios Plus ELISA reader (Tecan, Inc.). The cell viabilities were expressed as the percentage of the A492 of the dye-treated cells to the untreated controls. The A492 of the dyes themselves, tested in cells without MTS treats, were subtracted in the treated cells. All the measurements were performed in triplicate.

pH Sensitivity of Atto 565

Solutions of Atto 565 at different pH were diluted from the stock solution (see Section Live-cell labeling with fluorescent dyes) with citric acid or sodium hydroxide solutions at certain concentrations (Sigma-Aldrich Co., LLC). The fluorescence intensity was recorded ($\lambda_{ex} = 563$ nm) using a SpectraMax M2e (Molecular Devices, LLC.).

Confocal Laser Scanning Microscopy

The confocal images were obtained using a C2 confocal laser scanning microscope (Nikon, Inc.) equipped with a 100×/1.49

numerical aperture (NA) oil immersion objective lens and were analyzed with NIS-elements (Nikon, Inc.) and ImageJ software (National Institutes of Health).

STED Microscopy

The STED images were obtained using a STEDYCON microscope (Abberior, GmbH.) equipped with a 100×/1.49 NA oil immersion objective lens. A 40-MHz pulsed laser (775 nm) was used for depletion. The depletion laser intensity on the back-pupil plane was measured as about 80 mW. The depletion time was set as 1.2 ns, and the time gating was set as 1–7 ns. The resolution was calculated with the system's built-in software as 37 nm, using 40-nm red fluorescent beads (Abberior, GmbH.). Pinhole: 64 μm. For **Figure 4B**, the pixel size is 50 nm, and the pixel dwell time is 4 μs; for **Figures 4C,E**, the pixel size is 20 nm, and the pixel dwell time is 10 μs (STED) and 10 μs (Confocal).

RESULTS

Evaluation of Atto Dyes for Labeling Living Cells

Several types of fluorescent dyes were characterized according to their structure series.

Many cell-permeable cationic dyes (e.g., Rhodamine and Carbocyanine derivates) have been developed as mitochondrial probes, as they tend to accumulate in the mitochondrial matrix driven by the potential gradient in mitochondria at about 100-nM concentrations (Chazotte, 2011; Cottet-Rousselle et al., 2011; Xu et al., 2016). Endoplasmic reticulum (ER) staining can also be realized by raising the dosages of these dyes (Han et al., 2017). However, for the "live-cell compatible" dyes, concentrations at the 100-nM level are not enough.

Four Rhodamine derivatives, i.e., Atto 495, Atto 565, Atto 590, and Atto 647N N-Hydroxysuccinimide (NHS) esters, were investigated due to their relatively good optical properties in the corresponding spectral bands (**Figure 1**; **Supplementary Figures 1–6**). When incubated at 37°C, which is the optimal temperature for cell cultures, both mitochondria-like and bright dot signals inside the cells were observed (**Supplementary Figure 1B**); whereas when the incubation temperature was set to 20°C (room temperature), the dot signals were dramatically reduced (**Supplementary Figure 1C**).

For the mitochondria-like signals, colocalization experiments using MitoTracker probes were performed to verify the mitochondrial staining, and the Pearson correlation coefficients for Atto 495, Atto 590, and Atto 647N were 0.70, 0.57, and 0.82, respectively (**Figures 1A–C**; **Supplementary Figure 2**). The results indicate the mitochondrial labeling of Atto 495 and Atto647N.

Furthermore, the dot signals of Atto 565 were partially colocalized with endocytic-associated vesicles (i.e., early endosomes, late endosomes, and lysosomes; **Figures 1D,F** and **Supplementary Figures 3–5**), while no macroscopic colocalization was found with endocytic-unassociated vesicular structures (**Supplementary Figure 6**). After the cells were treated with Filipin and Cytochalasin D, which are known as endocytosis inhibitors (Rodal et al., 1999; Fujimoto et al., 2000; Dutta and Donaldson, 2012), the fluorescence intensity of Atto 565 labeling decreased to 36 ∼ 68% (**Supplementary Figure 7**). These results suggest the dependence of the dot signals on endocytosis to some extent (**Figure 1G**). The pH sensitivity of Atto 565 was also investigated since most of its signals were discovered in vesicles with an acidic environment (Yamashiro et al., 1983). The results showed that the fluorescence intensity of Atto 565 decreases as the pH values decline, suggesting that its brightness is limited when caught in endocytic vesicles (**Supplementary Figure 8**).

Staining Mechanism of Atto 647N and 565 NHS Ester

For Atto 647N NHS ester, which contains two parts (i.e., the cationic dye Atto 647N and the NHS moiety), we further investigated its mitochondrial labeling mechanism. Various recognition units (Han et al., 2017) were conjugated to Atto 647N to verify the dye's affinity to mitochondria. Probes were named as Atto 647N -Lyso, Atto 647N -Tubulin, and Atto 647N -Actin according to the recognition units they contain (**Figure 2A**). Atto 647N NHS ester was taken as a control group. The results showed that the conjugated units did not work, and all the probes labeled mitochondria or ER. Similar tests were performed for Atto 565, too. The results showed that only Atto 565-Actin partially marked actin filaments, and the other Atto 565-probes only labeled vesicle structures (**Figure 2B**). These results suggest that the affinity competition occurs between the dyes and their conjugated groups, and there is a strong tendency for mitochondria in Atto 647N itself, no matter what ligands were bound to it.

Fluorescent cationic dyes that tend to accumulate in mitochondria can be divided into two categories. Without any other active groups (e.g., Rhodamine 123), dyes may fail to stain mitochondria after fixation due to the loss of membrane potential, while with active groups (e.g., MitoTracker probes), dyes can form covalent bonds with mitochondrial membrane proteins (Poot et al., 1996). In our previous tests (Han et al., 2017), Atto 647N NHS ester kept its labeling pattern after fixation, indicating that the NHS ester contributes to the labeling by covalently binding to mitochondrial membrane proteins. The colocalization study employing MitoTracker Green by super-resolution imaging, which showed a high fluorescent signal in both inner and outer mitochondrial membranes, further proved this (Han et al., 2017). A recent labeling method, named FLARE also utilizes Atto 647N NHS ester as a mitochondrial marker in fixed cells by the reaction with amines (Mao et al., 2020).

The above results indicate that both the cationic charge of Atto 647N and the covalent bonds from the NHS ester contribute to the mitochondrial affinity of Atto 647N NHS ester.

Evaluation of the Dyes From Other Series for Live-Cell Labeling

Then, as Carbocyanine dyes, anionic Alexa Fluor (AF) 647, zwitterionic Cy3B, and cationic Cy5 were chosen as representative research objects (**Supplementary Figures 9A–C**).

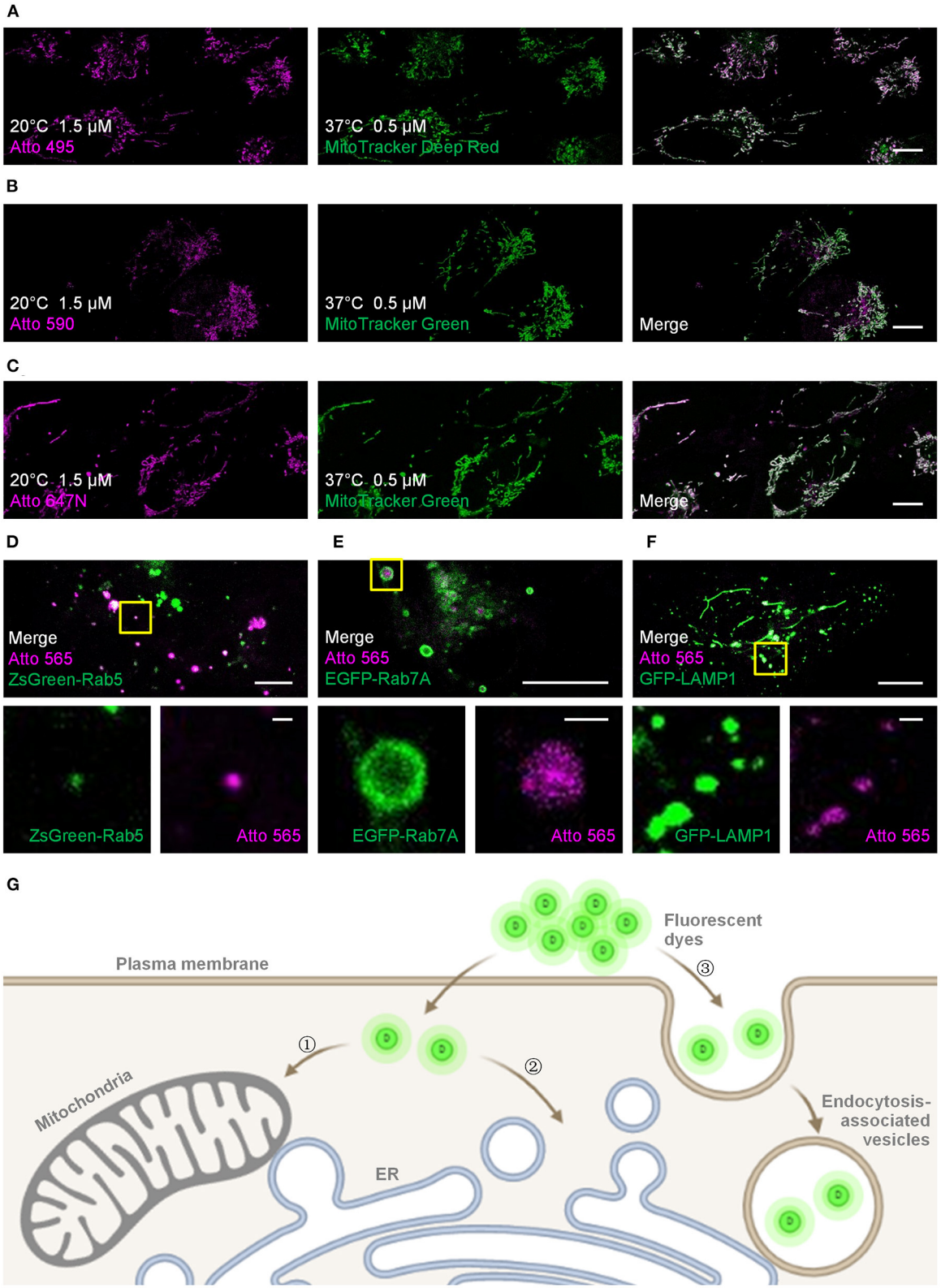

FIGURE 1 | Live-cell labeling of the Atto dyes. Colocalization studies employing different fluorescent probes and proteins as the standard mitochondrial markers. **(A)** Living U2OS cells were incubated with Atto 495 (magenta, 1.5 μM) for 30 min at 20°C and then with MitoTracker Deep Red (green, 0.5 μM) for 30 min at 37°C before imaging. Living U2OS cells were incubated with **(B)** Atto 590 or **(C)** Atto 647N (magenta, 1.5 μM) for 30 min at 20°C and then with MitoTracker Green (green, 0.5 μM)

(Continued)

FIGURE 1 | for 30 min at 37°C before imaging. Pearson correlation coefficient: 0.70, 0.57, and 0.82 for Atto 495, Atto 590, and Atto 647N, respectively. Living U2OS cells transiently transfected by **(D)** ZsGreen-Rab5 (green; early endosomes), **(E)** EGFP-Rab7A (green; late endosomes), and **(F)** GFP-LAMP1 (green; lysosomes) were stained with Atto 565 (magenta, 6 μM) for 30 min at 37°C and imaged by confocal microscope. Top panels: merged channels; bottom panels: enlarged single-channel images from the yellow boxed regions in the top panels, revealing colocalization of Atto 565 and specific endocytic vesicles. **(G)** The dyes enter living cells through ①, ② concentration-dependent free diffusion (e.g., Atto 647N), or ③ endocytosis (e.g., Atto 565). Scale bars, (**A–C**, upper panels of **D–F**) 10 μm, and (lower panels of **D–F**) 1 μm.

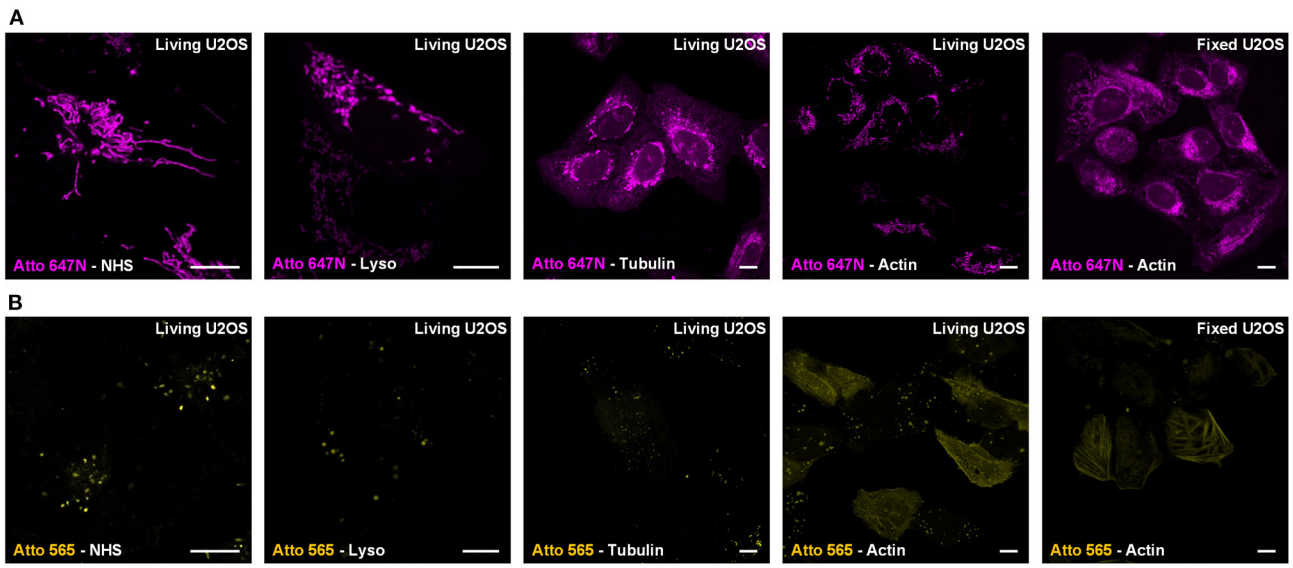

FIGURE 2 | Live-cell labeling mechanism of Atto 647N and Atto 565. The dyes were conjugated with either NHS ester (Dye-NHS) or different recognition units targeting lysosomes (Dye-Lyso), microtubules (Dye-Tubulin), and actin filaments (Dye-Actin). Confocal images show the intracellular distribution of probes containing **(A)** Atto 647N and **(B)** Atto 565 in living or fixed U2OS cells.

No mitochondrial staining was found after the incubation at either 37°C or 20°C. For AF 647 and Cy3B, the introduction of sulfonic acid groups improves fluorescence and solubility in water but adds negative charges, preventing their affinity for mitochondria (Wories et al., 1985). For Cy5, the high hydrophobicity leads to a certain degree of affinity for the plasma membrane (Pearson correlation coefficient: 0.52; **Supplementary Figures 9B, 10A**), preventing its permeation into living cells (Simons et al., 2009).

Unexpectedly, zwitterionic BODIPY 650/665 showed an affinity for mitochondria at a low concentration (300 nM, Pearson correlation coefficient: 0.52; **Supplementary Figures 9D, 10B**) while labeled ER at a relatively high concentration (15 μM, Pearson correlation coefficient: 0.82; **Supplementary Figures 9D, 10C**) was shown, suggesting its potential as a live-cell ER marker. Our results also indicate the mitochondrial affinity of BODIPY 650/665, breaking through the earlier conclusion (Xu et al., 2016) that this purpose can only be achieved using cationic dyes.

In view of the above observations, we hypothesize that without additional vector reagents and physical penetration, a group of fluorescent dyes, no matter if they were initially considered live-cell compatible or not, can mark subcellular structures in living cells using our labeling strategy (**Supplementary Table 1**).

Labeling in Various Types of Living Cells

We also used the living HeLa (human adenocarcinoma cell line), HEK293 (human embryonic kidney epithelial cell line), NIH/3T3 (mouse embryonic fibroblast cell line) cells, and primary cultural astrocytes from 1-day-old Sprague-Dawley (SD) rats (**Figure 3**; **Supplementary Figure 11**) to demonstrate the universality of our strategy. Notably, while the transfection in primary cultural astrocytes is challenging to achieve, the incubation with fluorescent probes is quite efficient and straightforward.

Compared with the above-mentioned fluorescent probes containing fluorescent dyes, recognition units, and cell-permeable peptides, which also work at the micromolar level (Han et al., 2017), the cytotoxicity of our method here mainly comes from the dyes themselves and the organic solvent in the incubation buffer (e.g., DMSO). To further confirm that our approach is compatible with the living specimens, the cytotoxicity of this method was then investigated by a 3-(4,5-dimethylthiazol-2-yl)-5-(3-carboxymethoxyphenyl)-2-(4-sulfophenyl)-2H-tetrazolium (MTS) assay (Cory et al., 1991). The cell viabilities were expressed as the percentage of the dye-treated cells' absorbance to the untreated controls. All the measurements were performed in triplicate. The results showed that after being treated with the indicated dyes, the cell viabilities usually exceeded 80% when incubated at 37°C and between

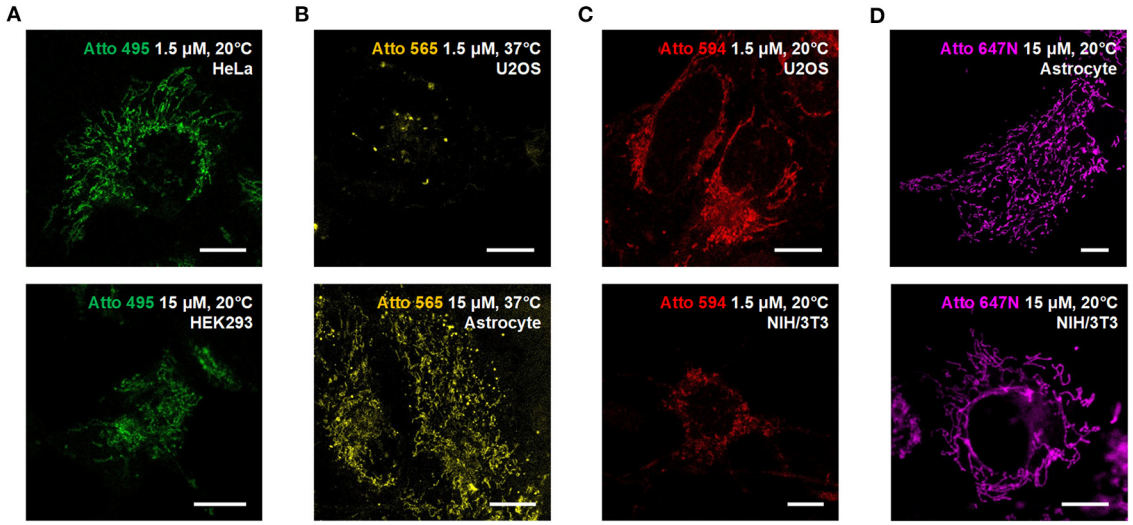

FIGURE 3 | Compatibility of the Atto dyes to various types of living cells. Confocal images of living U2OS, Astrocyte, H3K293, HeLa, and NIH/3T3 cells incubated with **(A)** Atto 495, **(B)** Atto 565, **(C)** Atto 590, and **(D)** Atto 647N at either 37°C or 20°C. Scale bars, 10 μm.

60 and 90% when incubated at 20°C, except in isolated cases (**Supplementary Figure 12**).

Photostability of Atto 647N

We quantitatively compared the optical properties of the frequently-used red-absorbing fluorophores. For photostability evaluation, fluorescence intensity curves were extracted from 20-min confocal imaging of U2OS cells (**Figure 4A**; **Supplementary Figure 13**), where all the imaging settings (e.g., laser power, size of field-of-view, imaging speed) were retained to control variables (**Supplementary Table 2**). The power density on the sample was adjusted to ∼1.25 kW cm^{-2} to ensure that all the probes were bright enough in the first frame. For Atto 647N, whose brightness is 2.50 times that of the SiR dye (Mishin et al., 2015) according to the manufacturers (**Supplementary Table 3**), the laser power used can be reduced by at least an order of a magnitude. The results showed that: (i) Atto 647N kept more than 88% of its intensity after 20-min of imaging (**Supplementary Figure 13A**); (ii) incubation of MitoTracker Deep Red at 200 nM (recommended concentration according to the manufacturer's instructions) already exhibited intense non-specific labeling of ER, while the signal intensity of both mitochondria and ER declined rapidly with only 19% left in the end (**Supplementary Figure 13B**); (iii) SNAP-Cell 647-SiR kept more than 70% of the intensity in the last frame. However, the cells stained with SNAP-Cox8A-SiR exhibited strong background in the cytosols (**Supplementary Figures 13C,D**); (iv) SiR-Actin were bleached very quickly, indicating the insufficient anti-bleaching property of SiR dye itself (**Supplementary Figure 13E**). The excess over-expression level of the SNAP- protein, which is relatively challenging to control in normal cancer cells and to realize in primary cultural cells, may result in the low image quality in the SNAP-tag technique (**Supplementary Figures 13C,D**). However, fluorescent probes are easy to control by simply changing the incubation concentration. The results suggest that Atto 647N exhibited the best photostability (4.66 times the value of MitoTracker Deep Red, and 2.58 times that of SiR dye itself; **Figure 3A**; **Supplementary Figure 13A**). By adding antioxidant reagent Prolong Live (Westbrook et al., 2018), all the bleaching speeds of these dyes decelerated to some extent. However, the difference between the dyes remained unchanged (**Figure 4A**; **Supplementary Figure 13**).

The performance of Atto 647N was further investigated using stimulated emission depletion (STED) microscopy (**Figures 4B–E**). The distance of mitochondrial outer membranes was resolved as 116 nm in STED mode, while the confocal image showed blurred structures (**Figures 4C,D**). Besides, structures of folded inner membranes, cristae, which were arranged in groups, and the voids between them were visible in the STED image (white arrows in **Figure 4E**) (Han et al., 2017; Huang et al., 2018; Stephan et al., 2019). Therefore, these results indicate that by applying our method in live-cell mitochondrial staining, especially in long-term or super-resolution imaging, Atto 647N can substitute SiR dye (Stephan et al., 2019) by offering better optical properties.

Dual-Color Applications

Dual-color staining combined with either fluorescent proteins (EMTB-3XGFP (Guo et al., 2018); **Figure 5A**) or other probes (ER-Tracker Green; **Figures 5B–D** and **Supplementary Figure 14**) were performed, suggesting the compatibility of our method with other labeling strategies. Long-term dual-color confocal imaging (20-min imaging duration at 2.4-s intervals) was performed in living Astrocytes, based on the excellent optical properties of Atto 647N (**Figures 5B–D** and **Supplementary Figure 14**). Interestingly, the results in astrocytes indicate that some of the ER substructures

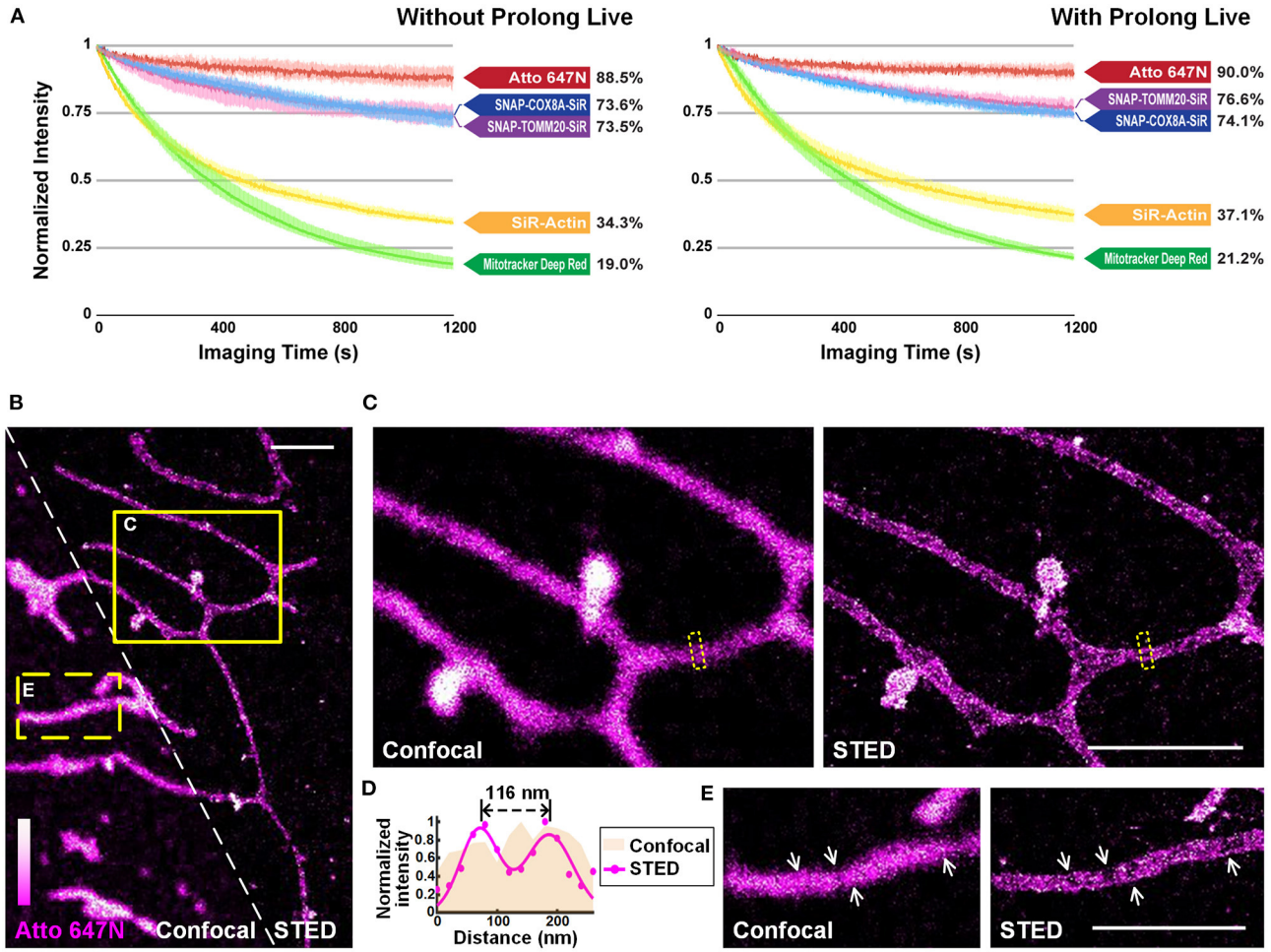

FIGURE 4 | Atto 647N for live-cell imaging applications with high demand for optical properties. **(A)** Curves of intensity decay of the indicated dyes without (left) or with (right) the addition of Prolong Live under the same confocal imaging condition. Consecutive frames spaced at 1-s intervals were recorded. Error bars represent the standard deviations of triplicate experiments. **(B)** Living U2OS cells were incubated with Atto 647N for 30 min at 20°C. Enlarged confocal and STED images from the **(C)** solid or **(E)** dashed yellow boxes shown in **(B)**. **(D)** Intensity profiles at the positions within the dashed boxes in **(C)** (pink area for the confocal image, and magenta dots and Gaussian fitting curve for STED image). Scale bars, 2 μm.

colocalized with mitochondria over time (the white and yellow arrowheads in **Figure 5B**; **Supplementary Figure 14A**). The possibility of crosstalk between channels was ruled out since there were some places with no overlap of the two channels (highlighted with the yellow arrows in **Figure 5B**). Moreover, hitchhiking interactions (Guo et al., 2018) between ER-mitochondria (**Figures 5C,D**), ER-vesicles (white arrowheads in **Supplementary Figure 14C**), and ER themselves (magenta arrowheads in **Supplementary Figure 14C**) were observed in our experiments.

Labeling Living Tissues

Compared with typical mammalian cells cultured on coverslips, labeling living tissue samples usually harbor a more significant challenge. Tissues *in vitro* die soon after losing blood flow support, resulting in mitochondrial potential gradient loss. As a consequence, the cationic dyes cannot affine to mitochondria. To permit sufficient staining deep into the living tissue, the fluorescent probes should permeate through the tissues fast enough so that they can bind to mitochondria before the gradient is lost. Specifically, the brain slices were incubated with Atto 647N immediately after the mice were sacrificed. Our results suggest that 0.5-h incubation was sufficient for the dye to permeate for at least 20-μm thickness, indicating its excellent permeability through tissues (**Figure 5E**; **Supplementary Figures 15A–C**). In contrast, MitoTracker Green failed to stain the brain sample (**Figure 5F**), which suggests the abilities of Atto 647N to substitute MitoTracker probes in staining living tissues. Notably, our approach is highly versatile. Besides the brain slices, adipose tissues (**Supplementary Figure 15D**), blood cells (**Supplementary Figure 15E**), cardiac and skeletal muscle fibers (**Supplementary Figures 15F,G**), and embryo slices (**Supplementary Figure 15H**) were also successfully stained. Compared with the immunofluorescence techniques in previous

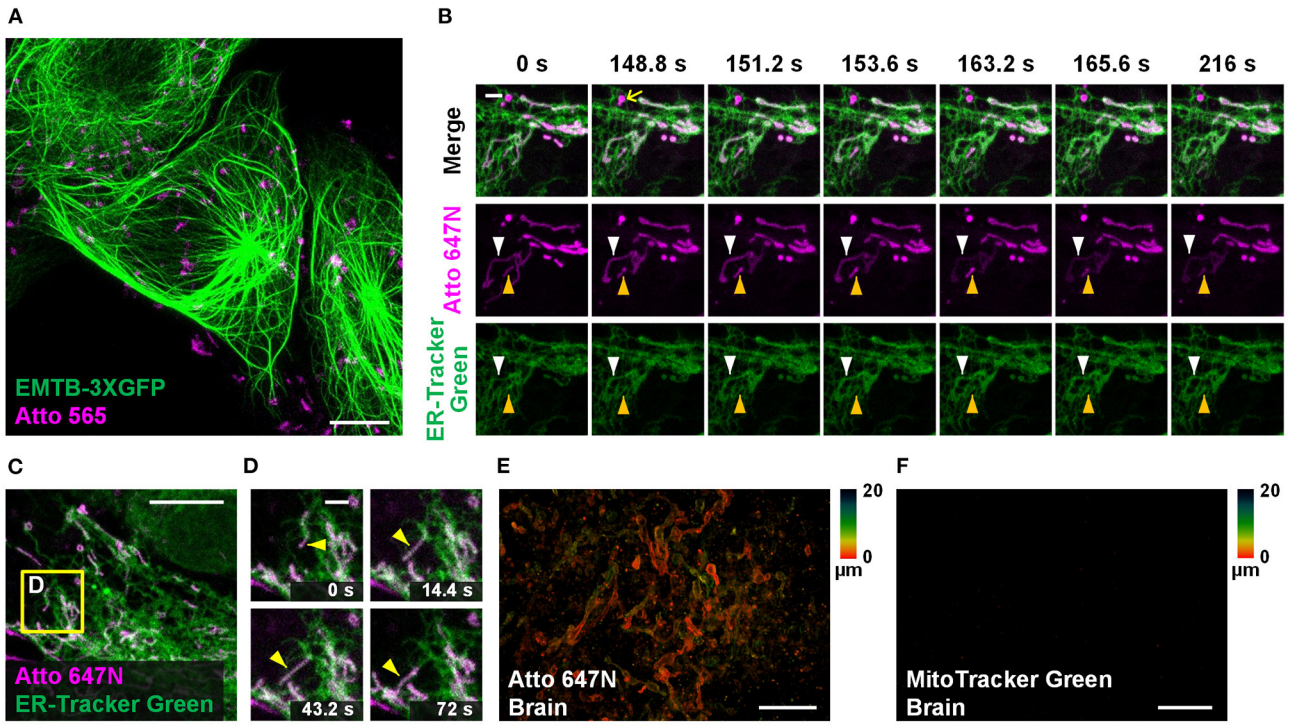

FIGURE 5 | Other applications in living cells and tissues. **(A)** Dual-color confocal image (maximum intensity projection) of living U2OS cells labeled with EMTB-3XGFP (green) and Atto 565 (magenta; 3 μM). **(B,C)** Dual-color confocal image of living Astrocytes labeled with Atto 647N (magenta; 15 μM, middle row) and ER-Tracker Green (green; 2 μM, bottom row) for 30 min at 20°C. **(D)** Mitochondria move along ER tubules. No deconvolution or bleaching compensation procedure was applied during the figure rendering. For the time-lapse images, consecutive frames spaced at 2.4-s intervals were recorded; representative images of consecutive frames are displayed. Brain slices incubated with **(E)** Atto 647N and **(F)** MitoTracker Green. Color bars on the right of **(E)** and **(F)** indicate the imaging depth. Scale bars, **(A,C)** 10 μm, **(B,D)** 2 μm, and **(E,F)** 20 μm.

works (Schneider Gasser et al., 2006; Chakrabarty et al., 2018), our method requires convenient and straightforward protocol steps, and direct incubation used here avoids the structural change caused by fixation. Therefore, our method is advantageous for many applications that expect instant actions, such as the rapid medical diagnoses of biospecimen *in vitro* and assessment for some mitochondrial diseases (Lee et al., 2019).

CONCLUSION

In summary, the capability of many fluorescent dyes, which was ignored to some extent before, to stain various types of subcellular structures in living specimens with high brightness and photostability is confirmed. Potential targets include mitochondria, ER, endocytic vesicles, and the plasma membrane. The implementation requires only specific incubation conditions without any chemical modification or physical penetration, minimizing the damages and artifacts induced during the sample preparation. Moreover, Atto 647N exhibited extraordinary brightness and photostability in live-cell mitochondrial labeling, which can substitute SiR dye in long-term imaging or super-resolution microscopy.

Due to the limits from objective conditions, especially considering that the structures of many of the commercially available fluorescent dyes are a trade secret, not all of them are tested in this paper. It is worth noting that micromolar-level concentrations of some fluorophores may lead to a potential cytotoxicity to some sensitive cell lines. The organic solvent (e.g., DMSO) in the incubation solutions should also be controlled carefully to balance the dye dissolution and the toxicity to living cells when using new fluorophores. However, the hypothesis that was built in this work provides a guideline to elucidating these candidates and to broaden the applications of existing dyes. Moreover, the phenomena observed here show their great potential in answering a wide range of biological questions in living cells and tissues.

DATA AVAILABILITY STATEMENT

The raw data supporting the conclusions of this article will be made available by the authors, without undue reservation.

ETHICS STATEMENT

The animal study was reviewed and approved by Zhejiang University.

AUTHOR CONTRIBUTIONS

XH, YH, CK, and XL conceived the project. Experiments were performed primarily by YH. ZZ and WL set up the system and contributed to the imaging. YH and YY prepared the samples. YH and XH drafted the manuscript. All authors contributed to the manuscript polish. All authors contributed to the article and approved the submitted version.

FUNDING

This work was financially sponsored by the grants from the National Key R&D Program of China (2018YFA0701400 and 2018YFE0119000), the National Natural Science Foundation of China (61827825, 61735017, and 31901059), Fundamental Research Funds for the Central Universities (2019XZZX003-06 and 2019QNA5006), China Postdoctoral Science Foundation (2019M662042), Natural Science Foundation of Zhejiang province (LR16F050001), Zhejiang Lab (2018EB0ZX01), and ZJU-Sunny Photonics Innovation Center (2019-01).

ACKNOWLEDGMENTS

We thank Mr. Yisheng Wu from SRstar Instruments Ltd., Shanghai, China, for operating the Abberior STEDYCON. This manuscript has been released as a pre-print at bioRxiv (Han et al., 2020).

SUPPLEMENTARY MATERIAL

The Supplementary Material for this article can be found online at: https://www.frontiersin.org/articles/10.3389/fchem.2020.601436/full#supplementary-material

REFERENCES

Bosch, P. J., Correa, I. R. Jr., Sonntag, M. H., Ibach, J., Brunsveld, L., Kanger, J. S., et al. (2014). Evaluation of fluorophores to label SNAP-tag fused proteins for multicolor single-molecule tracking microscopy in live cells. *Biophys. J.* 107, 803–814. doi: 10.1016/j.bpj.2014.06.040

Chakrabarty, S., Kabekkodu, S. P., Singh, R. P., Thangaraj, K., Singh, K. K., and Satyamoorthy, K. (2018). Mitochondria in health and disease. *Mitochondrion* 43, 25–29. doi: 10.1016/j.mito.2018.06.006

Chazotte, B. (2011). Labeling mitochondria with MitoTracker dyes. *Cold Spring Harb. Protoc.* 2011, 990–992. doi: 10.1101/pdb.prot5648

Cory, A. H., Owen, T. C., Barltrop, J. A., and Cory, J. G. (1991). Use of an aqueous soluble tetrazolium formazan assay for cell-growth assays in culture. *Cancer Commun.* 3, 207–212. doi: 10.3727/095535491820873191

Cottet-Rousselle, C., Ronot, X., Leverve, X., and Mayol, J. F. (2011). Cytometric assessment of mitochondria using fluorescent probes. *Cytometry A* 79, 405–425. doi: 10.1002/cyto.a.21061

Dutta, D., and Donaldson, J. G. (2012). Search for inhibitors of endocytosis: intended specificity and unintended consequences. *Cell. Logist.* 2, 203–208. doi: 10.4161/cl.23967

Erazo-Oliveras, A., Najjar, K., Dayani, L., Wang, T. Y., Johnson, G. A., and Pellois, J. P. (2014). Protein delivery into live cells by incubation with an endosomolytic agent. *Nat. Methods* 11, 861–867. doi: 10.1038/nmeth.2998

Fernandez-Suarez, M., and Ting, A. Y. (2008). Fluorescent probes for super-resolution imaging in living cells. *Nat. Rev. Mol. Cell Biol.* 9, 929–943. doi: 10.1038/nrm2531

Fujimoto, L. M., Roth, R., Heuser, J. E., and Schmid, S. L. (2000). Actin assembly plays a variable, but not obligatory role in receptor-mediated endocytosis in mammalian cells. *Traffic* 1, 161–171. doi: 10.1034/j.1600-0854.2000.010208.x

Guo, Y., Li, D., Zhang, S., Yang, Y., Liu, J. J., Wang, X., et al. (2018). Visualizing intracellular organelle and cytoskeletal interactions at nanoscale resolution on millisecond timescales. *Cell* 175, 1430–1442. doi: 10.1016/j.cell.2018.09.057

Han, Y., Li, M., Qiu, F., Zhang, M., and Zhang, Y. H. (2017). Cell-permeable organic fluorescent probes for live-cell long-term super-resolution imaging reveal lysosome-mitochondrion interactions. *Nat. Commun.* 8:1307. doi: 10.1038/s41467-017-01503-6

Han, Y., Li, M., Zhang, M., Huang, X., Chen, L., Hao, X., et al. (2019). Cell-permeable organic fluorescent probes for live-cell super-resolution imaging of actin filaments. *J. Chem. Technol. Biot.* 94, 2040–2046. doi: 10.1002/jctb.5990

Han, Y., Zhang, Z., Liu, W., Yao, Y., Chen, Y., Luo, X., et al. (2020). Labeling subcellular structures in living specimens using live-cell incompatible dyes with excellent optical properties. *bioRxiv [Preprint]* 2020.2005.2010.086538. doi: 10.1101/2020.05.10.086538

Hennig, S., van de Linde, S., Lummer, M., Simonis, M., Huser, T., and Sauer, M. (2015). Instant live-cell super-resolution imaging of cellular structures by nanoinjection of fluorescent probes. *Nano Lett.* 15, 1374–1381. doi: 10.1021/nl504660t

Huang, X., Fan, J., Li, L., Liu, H., Wu, R., Wu, Y., et al. (2018). Fast, long-term, super-resolution imaging with Hessian structured illumination microscopy. *Nat. Biotechnol.* 36, 451–459. doi: 10.1038/nbt.4115

Jaiswal, J. K., Mattoussi, H., Mauro, J. M., and Simon, S. M. (2003). Long-term multiple color imaging of live cells using quantum dot bioconjugates. *Nat. Biotechnol.* 21, 47–51. doi: 10.1038/nbt767

Ji, N., Freeman, J., and Smith, S. L. (2016). Technologies for imaging neural activity in large volumes. *Nat. Neurosci.* 19, 1154–1164. doi: 10.1038/nn.4358

Lee, J. H., Park, A., Oh, K. J., Lee, S. C., Kim, W. K., and Bae, K. H. (2019). The role of adipose tissue mitochondria: regulation of mitochondrial function for the treatment of metabolic diseases. *Int. J. Mol. Sci.* 20:4924. doi: 10.3390/ijms20194924

Lukinavicius, G., Mitronova, G. Y., Schnorrenberg, S., Butkevich, A. N., Barthel, H., Belov, V. N., et al. (2018). Fluorescent dyes and probes for super-resolution microscopy of microtubules and tracheoles in living cells and tissues. *Chem. Sci.* 9, 3324–3334. doi: 10.1039/C7SC05334G

Lukinavicius, G., Reymond, L., D'Este, E., Masharina, A., Gottfert, F., Ta, H., et al. (2014). Fluorogenic probes for live-cell imaging of the cytoskeleton. *Nat. Methods* 11, 731–733. doi: 10.1038/nmeth.2972

Lukinavičius, G., Reymond, L., and Johnsson, K. (2015). *Site-specific Protein Labeling: Methods and Protocols*. New York, NY: Humana Press.

Manceur, A., Wu, A., and Audet, J. (2007). Flow cytometric screening of cell-penetrating peptides for their uptake into embryonic and adult stem cells. *Anal. Biochem.* 364, 51–59. doi: 10.1016/j.ab.2007.02.015

Mao, C., Lee, M. Y., Jhan, J. R., Halpern, A. R., Woodworth, M. A., Glaser, A. K., et al. (2020). Feature-rich covalent stains for super-resolution and cleared tissue fluorescence microscopy. *Sci. Adv.* 6:eaba4542. doi: 10.1126/sciadv.aba4542

Mishin, A. S., Belousov, V. V., Solntsev, K. M., and Lukyanov, K. A. (2015). Novel uses of fluorescent proteins. *Curr. Opin. Chem. Biol.* 27, 1–9. doi: 10.1016/j.cbpa.2015.05.002

Miyawaki, A., Sawano, A., and Kogure, T. (2003). Lighting up cells: labelling proteins with fluorophores. *Nat. Cell Biol.* 5, 1–2. doi: 10.1038/ncb0103-1

Poot, M., Zhang, Y. Z., Kramer, J. A., Wells, K. S., Jones, L. J., Hanzel, D. K., et al. (1996). Analysis of mitochondrial morphology and function with novel fixable fluorescent stains. *J. Histochem. Cytochem.* 44, 1363–1372. doi: 10.1177/44.12.8985128

Rodal, S. K., Skretting, G., Garred, O., Vilhardt, F., van Deurs, B., and Sandvig, K. (1999). Extraction of cholesterol with methyl-beta-cyclodextrin perturbs formation of clathrin-coated endocytic vesicles. *Mol. Biol. Cell* 10, 961–974. doi: 10.1091/mbc.10.4.961

Schneider Gasser, E. M., Straub, C. J., Panzanelli, P., Weinmann, O., Sassoe-Pognetto, M., and Fritschy, J. M. (2006). Immunofluorescence in brain sections: simultaneous detection of presynaptic and postsynaptic proteins in identified neurons. *Nat. Protoc.* 1, 1887–1897. doi: 10.1038/nprot.2006.265

Shen, S. L., Zhang, X. F., Ge, Y. Q., Zhu, Y., Lang, X. Q., and Cao, X. Q. (2018). A near-infrared lysosomal pH probe based on rhodamine derivative. *Sensor Actuat. B-Chem.* 256, 261–267. doi: 10.1016/j.snb.2017.10.103

Sigal, Y. M., Zhou, R., and Zhuang, X. (2018). Visualizing and discovering cellular structures with super-resolution microscopy. *Science* 361, 880–887. doi: 10.1126/science.aau1044

Simons, M., Gault, W. J., Gotthardt, D., Rohatgi, R., Klein, T. J., Shao, Y., et al. (2009). Electrochemical cues regulate assembly of the Frizzled/Dishevelled complex at the plasma membrane during planar epithelial polarization. *Nat. Cell Biol.* 11, 286–294. doi: 10.1038/ncb1836

Specht, E. A., Braselmann, E., and Palmer, A. E. (2017). A critical and comparative review of fluorescent tools for live-cell imaging. *Annu. Rev. Physiol.* 79, 93–117. doi: 10.1146/annurev-physiol-022516-034055

Stephan, T., Roesch, A., Riedel, D., and Jakobs, S. (2019). Live-cell STED nanoscopy of mitochondrial cristae. *Sci. Rep.* 9:12419. doi: 10.1038/s41598-019-48838-2

von Provazek, S. (1914). Uber fluoreszenz der zellen. *Kleinwelt* 6 30.

Westbrook, A. W., Ren, X., Moo-Young, M., and Chou, C. P. (2018). Engineering of cell membrane to enhance heterologous production of hyaluronic acid in Bacillus subtilis. *Biotechnol. Bioeng.* 115, 216–231. doi: 10.1002/bit.26459

Wories, H. J., Koek, J. H., Lodder, G., Lugtenburg, J., Fokkens, R., Driessen, O., et al. (1985). A novel water-soluble fluorescent-probe - synthesis, luminescence and biological properties of the sodium-salt of the 4-sulfonato-3,3′,5,5′-tetramethyl-2,2′-pyrromethen-1,1′-bf2 complex. *Recl. Trav. Chim. Pay B* 104, 288–291. doi: 10.1002/recl.19851041104

Xu, W., Zeng, Z., Jiang, J. H., Chang, Y. T., and Yuan, L. (2016). Discerning the chemistry in individual organelles with small-molecule fluorescent probes. *Angew. Chem. Int. Ed Engl.* 55, 13658–13699. doi: 10.1002/anie.201510721

Yamashiro, D. J., Fluss, S. R., and Maxfield, F. R. (1983). Acidification of endocytic vesicles by an ATP-dependent proton pump. *J. Cell Biol.* 97, 929–934. doi: 10.1083/jcb.97.3.929

Yang, X., Yang, Z., Wu, Z., He, Y., Shan, C., Chai, P., et al. (2020). Mitochondrial dynamics quantitatively revealed by STED nanoscopy with an enhanced squaraine variant probe. *Nat. Commun.* 11:3699. doi: 10.1038/s41467-020-17546-1

Conflict of Interest: The authors declare that the research was conducted in the absence of any commercial or financial relationships that could be construed as a potential conflict of interest.

frontiers in Chemistry

PERSPECTIVE
published: 15 January 2021
doi: 10.3389/fchem.2020.619377

Lanthanide-Doped Upconversion Nanoparticles for Super-Resolution Microscopy

Hao Dong[1], *Ling-Dong Sun*[1]* *and Chun-Hua Yan*[1,2]*

[1] *Beijing National Laboratory for Molecular Sciences, State Key Laboratory of Rare Earth Materials Chemistry and Applications, PKU-HKU Joint Laboratory in Rare Earth Materials and Bioinorganic Chemistry, College of Chemistry and Molecular Engineering, Peking University, Beijing, China,* [2] *College of Chemistry and Chemical Engineering, Lanzhou University, Lanzhou, China*

Super-resolution microscopy offers a non-invasive and real-time tool for probing the subcellular structures and activities on nanometer precision. Exploring adequate luminescent probes is a great concern for acquiring higher-resolution image. Benefiting from the atomic-like transitions among real energy levels, lanthanide-doped upconversion nanoparticles are featured by unique optical properties including excellent photostability, large anti-Stokes shifts, multicolor narrowband emissions, tunable emission lifetimes, etc. The past few years have witnessed the development of upconversion nanoparticles as probes for super-resolution imaging studies. To date, the optimal resolution reached 28 nm (λ/36) for single nanoparticles and 82 nm (λ/12) for cytoskeleton structures with upconversion nanoparticles. Compared with conventional probes such as organic dyes and quantum dots, upconversion nanoparticle-related super-resolution microscopy is still in the preliminary stage, and both opportunities and challenges exist. In this perspective article, we summarized the recent advances of upconversion nanoparticles for super-resolution microscopy and projected the future directions of this emerging field. This perspective article should be enlightening for designing efficient upconversion nanoprobes for super-resolution imaging and promote the development of upconversion nanoprobes for cell biology applications.

Keywords: upconversion nanoparticle, super-resolution microscopy, lanthanide, STED, multiphoton imaging

OPEN ACCESS

Edited by:
Qiuqiang Zhan,
South China Normal University, China

Reviewed by:
Haichun Liu,
Royal Institute of Technology, Sweden
Juan Manuel Lázaro-Martínez,
University of Buenos Aires, Argentina

***Correspondence:**
Ling-Dong Sun
sun@pku.edu.cn
Chun-Hua Yan
yan@pku.edu.cn

Specialty section:
This article was submitted to Analytical Chemistry, a section of the journal Frontiers in Chemistry

Received: *20 October 2020*
Accepted: *07 December 2020*
Published: *15 January 2021*

Citation:
Dong H, Sun L-D and Yan C-H (2021) Lanthanide-Doped Upconversion Nanoparticles for Super-Resolution Microscopy. Front. Chem. 8:619377. doi: 10.3389/fchem.2020.619377

INTRODUCTION

Optical microscopy that can visualize the morphological and physiological details of biological samples with high sensitivity as well as non-invasive and real-time capability has become an important part for diagnosis (Biffi et al., 2013; Chen et al., 2013; Tang et al., 2013). Nonetheless, the Abbe's diffraction limit constrains the imaging resolution in hundreds of nanometers (*ca.* λ/2) and makes it impossible to access the subcellular organelles' detection (Abbe, 1873). With the development of super-resolution microscopy since the 1990's, the optical diffraction limit has been circumvented or even broken, leading to the unprecedented observation of nanoscale subcellular structures and dynamics of cells and tissues (Hell and Wichmann, 1994; Betzig et al., 2006; Rust et al., 2006).

In super-resolution imaging, luminescent probes are key components for labeling and disclosing the structure and activities of target molecules in nanometer precision. An ideal probe should have adequate brightness, excellent photostability, good biocompatibility, etc (Sahl et al., 2017). In recent years, lanthanide-doped upconversion nanoparticles (UCNPs) that can transduce near-infrared (NIR) photons to visible emissions have been emerging as a new kind of probe for super-resolution microscopy (Dong et al., 2020). The atomic-like transitions among real 4*f* energy levels endow UCNPs with unique optical properties, including vigorous resistance to photobleaching and photoblinking, efficient anti-Stokes emission efficiency, and being free of autofluorescence interference, which are not inherent in conventional probes such as organic dyes and quantum dots (Chan et al., 2015; Dong et al., 2015a; Zheng et al., 2015). UCNPs with high monodispersity, uniform shape, and phase structure can be produced by well-developed approaches such as high-temperature thermal decomposition (Mai et al., 2006) and coprecipitation (Li and Zhang, 2008). The size of UCNPs can be controlled from sub-5 nm to super-100 nm with narrow distribution. The physical characters including size, hydrodynamic diameter, and concentration can be obtained with transmission electron microscopy (TEM), dynamic light scattering (DLS), and inductively coupled plasma-atomic emission spectroscopy (ICP-AES), respectively. Moreover, with proper surface modification (Muhr et al., 2014), UCNPs can well be internalized by cells through endocytosis and show no obvious toxic effect on cell proliferation and viability (Gnach et al., 2015). These merits make UCNPs greatly promising for long-term and real-time observations.

To date, UCNPs have been implanted in diverse super-resolution imaging techniques, including ion beam excitation (Mi et al., 2015), stimulated emission depletion (STED) microscopy (Kolesov et al., 2011), fluorescence emission difference (FED) microscopy (Wu et al., 2017), and structured illumination microscopy (SIM) (Liu et al., 2020). The spatial resolution of 28 nm (λ/36) and 82 nm (λ/12) has been achieved for single UCNPs (Liu et al., 2017) and UCNPs-labeled cytoskeleton proteins (Zhan et al., 2017), respectively, which is greatly improved than the λ/2 resolution in conventional confocal imaging. Despite these achievements, great challenges still exist for the super-resolution imaging with UCNPs. On one hand, the 4*f* intra-configurational transitions of lanthanides are shielded by $5s^2 5p^6$ shells; thus, the energy level position as well as the excitation/emission wavelengths are almost invariable (Dong et al., 2015b). This actually poses a challenge for tuning the luminescence properties of UCNPs, which are not as flexible as that of organic dyes and quantum dots. On the other hand, the stimulated emission cross-section of UCNPs is quite small because of the parity-forbidden nature (Sun et al., 2019), which makes it difficult to achieve stimulated emission for STED microscopy. In this perspective article, we firstly summarized the recent advances in UCNPs-based super-resolution microscopy and then discussed the future directions in aspects of UCNPs design and cellular biological applications.

RECENT ADVANCES IN UCNPS-BASED SUPER-RESOLUTION IMAGING

UCNPs in Ion Beam Excitation

According to Abbe's diffraction limit, the spatial resolution is proportional to the excitation wavelength. Therefore, excitation with charged particles such as electron or ion beams that have much shorter de Broglie wavelength can accomplish much better resolution than that with usual UV-vis-NIR lasers (Prigozhin et al., 2019). This approach has no specific requirements for the composition of UCNPs, yet more sensitizers are beneficial for the increased absorption of excitation energy. Bettiol et al. presented a paradigmatic example by using MeV focused helium ions to excite $NaYF_4$:Yb,Tm UCNPs (**Figure 1A**), in which Yb^{3+} and Tm^{3+} ions can directly harvest the energy of helium ions and stably generate upconversion emissions over hours period (Mi et al., 2015). Compared with 980-nm laser excitation, the helium ion beam excitation enabled greatly improved resolution from 253 to 28 nm. Moreover, an areal density map of the distribution of individual UCNPs within a whole HeLa cell as well as the 3D cellular structure can be revealed at ultrahigh spatial resolution. Although the ion beam excitation can generate super-resolution imaging, the special imaging setups, especially the high-energy ion beams, are not easily accessible. Moreover, the high-energy ion beam may induce irreversible damage to living biological samples, which thus should have certain limitations in practical use.

UCNPs in Stimulated Emission Depletion Microscopy

In the 1990's, STED microscopy was theoretically proposed (Hell and Wichmann, 1994) and experimentally validated (Klar and Hell, 1999) to break the diffraction barrier by reducing the point spread function (PSF) with two concentrical laser beams, namely, an excitation laser and a depletion laser (**Figure 1B**). The advantage of STED microscopy lies in the direct acquisition of a super-resolved image without image post-processing. A qualified STED probe should exhibit fluorescence and stimulated emission under excitations of excitation laser and depletion laser, respectively. In this way, the undesired fluorescence can be erased, leading to shrunk effective PSF. The excitation-correlated emission property is easy to be implemented for organic dyes (Willig et al., 2006) and quantum dots (Hanne et al., 2015), which however is a daunting challenge for lanthanide-doped UCNPs. This can be ascribed to the two following aspects: (I) Stimulated emission is quite difficult to be generated from single UCNPs because of the small stimulated emission cross-section. (II) The co-illumination of excitation and depletion lasers is much likely to match the abundant energy levels of lanthanides, which is deleterious to erasing process. To circumvent the two aforementioned challenges, the UCNPs for STED microscopy are designed to show depleted upconversion emissions through cross-relaxations under the co-illumination of excitation and depletion lasers. Therefore, there are strict requirements for the composition and excitation conditions of UCNPs in STED microscopy, and only few types of UCNPs have been developed.

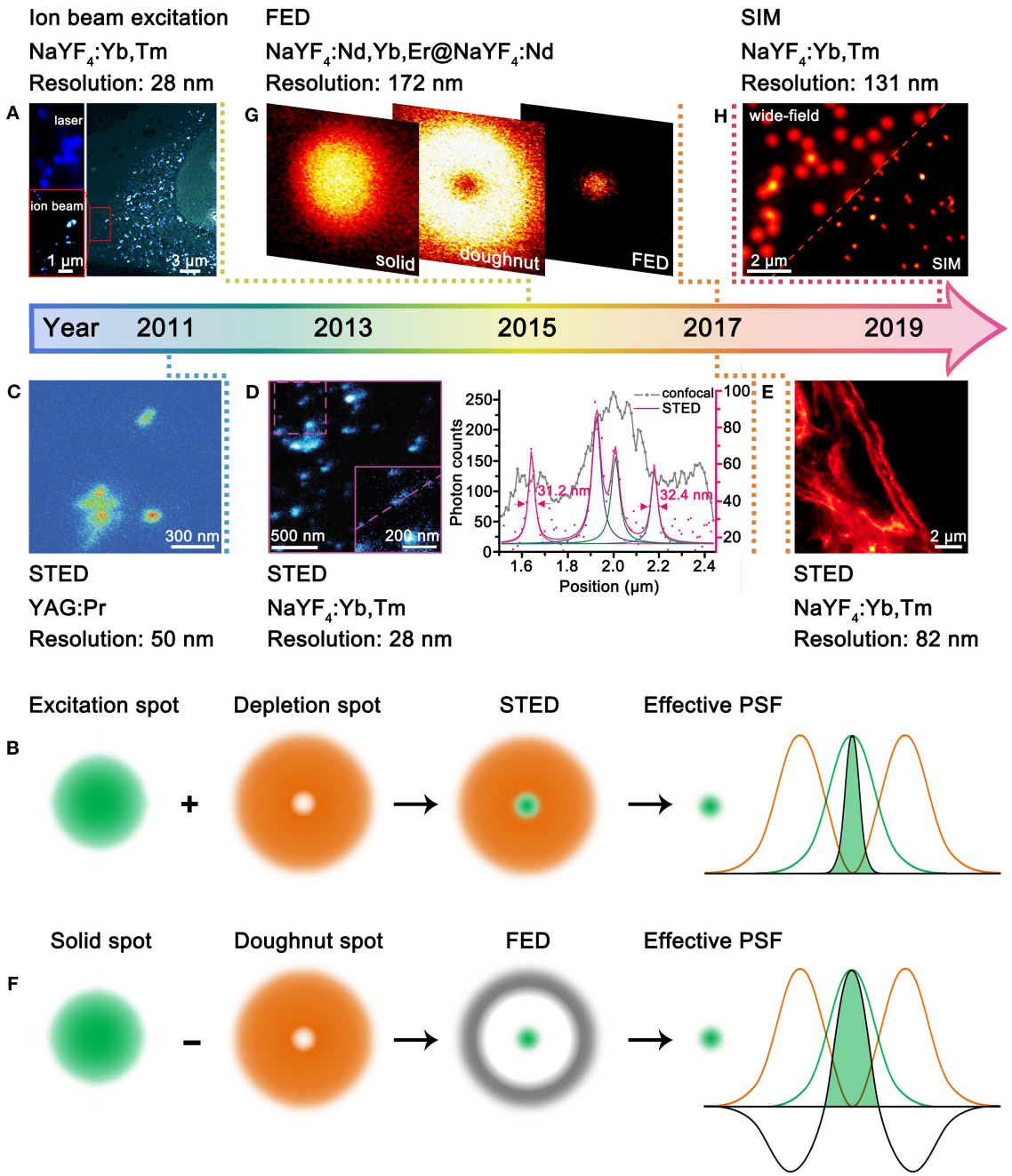

FIGURE 1 | Development of UCNPs for super-resolution microscopy. **(A)** Comparative photoluminescence imaging under 980-nm excitation (top left) and ionoluminescence imaging under helium ion beam excitation (bottom left) of $NaYF_4$:Yb,Tm UCNPs in a HeLa cell (right). Reproduced with permission from Mi et al. (2015). Copyright 2015 Springer Nature Publishing Group. **(B)** Schematic illustration for STED microscopy. **(C)** STED imaging of YAG:Pr nanoparticle clusters. Reproduced with permission from Kolesov et al. (2011). Copyright 2011 American Physical Society. **(D)** STED imaging of *ca*. 13 nm $NaYF_4$:Yb,Tm UCNPs (left) and the intensity profiles along the dashed line (right). Reproduced with permission from Liu et al. (2017). Copyright 2017 Springer Nature Publishing Group. **(E)** STED imaging of cytoskeleton structures and desmin proteins in HeLa cancer cells with $NaYF_4$:Yb,Tm UCNPs. Reproduced with permission from Zhan et al. (2017). Copyright 2017 Springer Nature Publishing Group. **(F)** Schematic illustration for FED microscopy. **(G)** FED imaging of a single $NaYF_4$:Nd,Yb,Er@$NaYF_4$:Nd UCNPs. Reproduced with permission from Wu et al. (2017). Copyright 2017 The Optical Society. **(H)** Comparative wide-field and SIM imaging of $NaYF_4$:Yb,Tm UCNPs. Reproduced with permission from Liu et al. (2020). Copyright 2020 American Chemical Society.

In 2011, Kolesov et al. employed UCNPs for STED microscopy for the first time (**Figure 1C**) (Kolesov et al., 2011). The upconversion emission properties of YAG:Pr nanoparticles were modulated by three lasers, including pulsed excitation, continuous depletion, and pulsed readout. The accomplishment of super-resolution was based on the longer lifetime of the

intermediate state (*ca*. 150–200 μs) than that of the excited state (*ca*. 18 ns). Although the resolution was improved from *ca*. 400 nm to *ca*. 50 nm, the imaging wavelength was concentrated at the UV region (300–450 nm), which is deleterious to detection and bioapplications (Idris et al., 2015). In 2017, Jin et al. made a significant promotion of upconversion STED microscopy with $NaYF_4$:Yb,Tm UCNPs (**Figure 1D**) (Liu et al., 2017). A 980-nm excitation laser (*ca*. 10^4-10^5 W/cm^2) and an 808-nm depletion laser (*ca*. 10^6-10^7 W/cm^2) were used to activate and quench the blue upconversion emissions of Tm^{3+}, respectively, which is much easier to operate. Heavy doping of Tm^{3+} was found crucial to depopulate the blue-emitting energy level (455 nm) through cross-relaxation. The imaging resolution of a single $NaYF_4$:Yb,Tm UCNP, which has a physical size of 13 nm, reached *ca*. 28 nm. Almost simultaneously, Zhan et al. reported the STED imaging with heavily doped $NaYF_4$:Yb,Tm UCNPs (Zhan et al., 2017). Importantly, the authors realized blue (Tm^{3+}) and green (Tb^{3+}) bi-color STED imaging with core/shell structured $NaGdF_4$:Yb,Tm@$NaGdF_4$:Tb UCNPs. Moreover, STED imaging of cytoskeleton structures and desmin proteins in HeLa cells was realized with antibody modification, and the optimal resolution was down to 82 nm (**Figure 1E**). A recent study shows that the doping ratio of Tm^{3+} in $NaYF_4$:Yb,Tm can be increased from 8 to 20% with no influence on the STED imaging performance (Camillis et al., 2020). Meanwhile, the content of Yb^{3+} can be enriched to *ca*. 90% by forming $NaYbF_4$:Tm. The prominent increase in Yb^{3+} content also benefits to accelerate emission kinetics of Tm^{3+}, which enables fast STED imaging capability. The pixel dwell time for the STED imaging of $NaYbF_4$:Tm UCNPs can be shortened from a few milliseconds to 10 μs (Peng et al., 2019), which is close to that for organic dyes. The simultaneous improvement in spatial and temporal resolution benefits to visualize the dynamics of cells and tissues.

Till now, UCNP-based probes for STED microscopy still concentrate on Yb^{3+}-Tm^{3+}-activated nanoparticles, suggesting the difficulty in modulating the upconversion emission properties of lanthanide ions under the STED mode. In addition, the blue emissions of Tm^{3+} still face the obstacle from limited penetration and potential photodamage; thus, exploring novel UCNP-based STED probes with longer working wavelength is desirable.

UCNPs in Fluorescence Emission Difference Microscopy

FED microscopy relies on the subtraction of two distinct images taken under excitations of a solid laser and a doughnut-shaped laser, respectively (**Figure 1F**) (Kuang et al., 2013). The super-resolved FED image is obtained by setting the negative values to zero with the equation $I_{FED} = I_{solid} - r \times I_{doughnut}$, in which the I_{FED}, I_{solid}, $I_{doughnut}$, and r represent the normalized FED intensity profile, solid laser scanning profile, doughnut-shaped laser scanning profile, and subtractive factor, respectively. The more intense the doughnut-shaped laser is, the better the imaging resolution will be. In principle, there is no specific requirement for the composition of UCNPs. Nonetheless, because of the requirement of image processing, FED is not advantageous in temporal resolution. In 2017, Zhan et al. described the first UCNP-based FED microscopy (**Figure 1G**) (Wu et al., 2017). $NaYF_4$:Nd,Yb,Er@$NaYF_4$:Nd UCNPs were excited by 808-nm solid and doughnut-shaped lasers, respectively, with a power density of 10^7 W/cm^2. The resolution was improved from 440 to 170 nm for single UCNPs. In a typical FED imaging, two separate scans are required to acquire the solid and doughnut-shaped images. Recently, Zhan et al. achieved one-scan FED microscopy with $NaYF_4$:Er@$NaYF_4$@$NaYF_4$:Yb,Tm UCNPs (Huang et al., 2018). The UCNPs show blue emissions of Tm^{3+} under 940-nm solid laser excitation while green emissions of Er^{3+} under 808-nm doughnut-shaped laser excitation. With the orthogonally luminescent UCNPs, a resolution of 54 nm was obtained. Aiming at achieving deep penetration, Jin et al. investigated the FED imaging on the basis of the NIR emission of $NaYF_4$:Yb,Tm UCNPs (Chen et al., 2018). They obtained a resolution of sub-50 nm in imaging single UCNPs through 93-μm-thick liver tissue.

UCNPs in Structured Illumination Microscopy

SIM refers to the wide-field illumination of samples with light that has closely packed periodic patterns (Gustafsson, 2000). Upon interference with samples, Moiré patterns that contain high spatial frequency information of samples are obtained, from which the super-resolved image can be reconstructed through deconvolution algorithm. However, the strong extinction of light by biological tissues, which are deleterious to imaging depth and resolution, restricts further bioapplications of SIM microscopy. This problem can be conquered by using UCNPs as the SIM probes. Very recently, Jin et al. employed $NaYF_4$:Yb,Tm UCNPs as SIM probes and achieved a resolution below 131 nm and an imaging rate of 1 Hz (**Figure 1H**) (Liu et al., 2020). The authors show that the non-linear photoresponses of UCNPs can produce high-frequency harmonics in the Fourier domain of the imaging plane, enabling non-linear SIM under mild excitation conditions (10^3 W/cm^2). Moreover, Tm^{3+}-activated NIR-emissive UCNPs are found superior to visible-emissive counterparts in preserving the structured spatial information through thick tissue. It is noteworthy that the non-linear SIM can generate improved resolution compared to the linear SIM; thus, the doping ratio of lanthanide ions, which can influence both the non-linearity and intensity of upconversion emissions, should be carefully optimized.

PERSPECTIVES OF UCNPs-BASED SUPER-RESOLUTION IMAGING

Small-Sized UCNPs With Bright Emissions

The parity-forbidden nature of 4*f* intra-configurational transitions makes lanthanide upconversion a low-efficiency process. Deleterious coupling with surface defects, ligands, and solvent molecules would further aggravate the upconversion brightness (Dong et al., 2015b). To obtain adequate luminescence

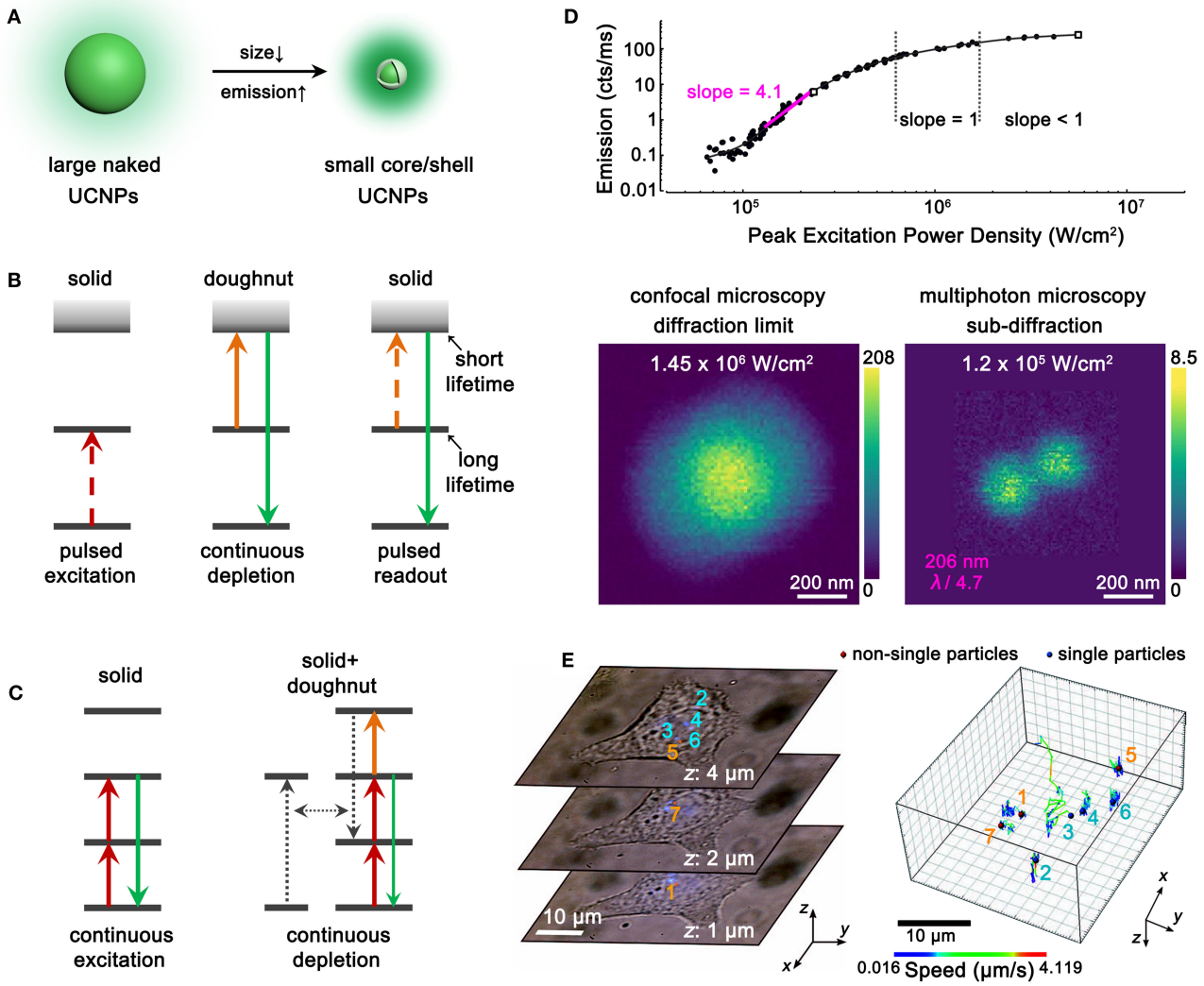

FIGURE 2 | Perspectives of UCNPs-based Super-Resolution Imaging. **(A)** Schematic illustration showing the requirement of size decrease and emission enhancement with core/shell UCNPs. **(B)** Schematic illustration showing the UCNPs with long intermediate-level lifetime and short excited-state lifetime for STED microscopy. **(C)** Schematic illustration showing the combination of excitation and non-radiative cross-relaxation in UCNPs for STED microscopy. **(D)** Non-linear photoresponses of $NaYF_4$:Yb,Tm UCNPs at 455 nm under 980-nm excitation (top) and comparative imaging of two adjacent UCNPs under 980-nm excitation with different power densities (bottom). Reproduced with permission from Denkova et al. (2019). Copyright 2019 Springer Nature Publishing Group. **(E)** Three representative single-cell images containing seven UCNP spots (left) and the 3D trajectories of the UCNPs (right). Reproduced with permission from Wang et al. (2018). Copyright 2018 Springer Nature Publishing Group.

from single UCNPs, large-sized nanoparticles (larger than 20 nm) and high pump power (more than 10^4 W/cm^2) are usually required in super-resolution microscopy. However, both the size effect (Albanese et al., 2012) of UCNPs and the heating effect (Peña et al., 2012) of high pump power may interfere with the intrinsic activities of as-labeled biomolecules or the whole cells, leading to misapprehensive observations. Moreover, the imaging resolution is limited by the physical size of UCNPs to some extent; thus, the ultimate resolution is larger than 20 nm in current studies. To improve the application performance of UCNPs and avoid interference with cellular activities, small-sized UCNPs with bright emissions should be developed. It has been reported that sub-5 nm $NaLnF_4$ UCNPs can be obtained with co-precipitation synthesis (Xing et al., 2014; Zheng et al., 2017), and an epitaxial shell can greatly enhance the upconversion emissions of core nanoparticles by orders of magnitudes (Dong et al., 2017). Therefore, sub-10-nm bright UCNPs are expected to be prepared with the sub-5-nm core and an epitaxial shell (**Figure 2A**). The decrease in nanoparticle size should facilitate both the efficient labeling of biomolecules and improved imaging resolution.

Tailoring Upconversion for Novel Super-Resolution Probes

As discussed above, the as-developed UCNPs probes for super-resolution microscopy are mainly focused on Yb^{3+}-Tm^{3+} co-doped nanoparticles. Generally, there are no rigid restrictions on the types of luminescent centers for ion beam excitation, FED and SIM. UCNPs doped with other lanthanide ions such as Er^{3+}, Ho^{3+}, Nd^{3+}, etc. can be examined. In comparison, STED microscopy strictly requires depleted upconversion emission under co-illumination of excitation and depletion lasers, which is indeed challenging for lanthanide ions with ladder-like energy levels. Adequate cross-relaxation pairs that can depopulate the emissive levels under STED mode should be explored. It can be referred to the example that takes advantage of lifetime difference in YAG:Pr UCNPs (Kolesov et al., 2011), in which long and short lifetimes are preferred for the intermediate and excited states, respectively (**Figure 2B**). Moreover, the combination of excitation and non-radiative relaxation/cross-relaxation can be considered as a new depletion approach for STED microscopy (**Figure 2C**) (Wu et al., 2015). Besides, probes for photoactivated localization microscopy (PALM) (Betzig et al., 2006), stochastic optical reconstruction microscopy (STORM) (Rust et al., 2006), and super-resolution optical fluctuation imaging (SOFI) (Dertinger et al., 2009) are desired to be explored with the composites of UCNPs and fluorescent proteins, organic dyes, and quantum dots, respectively. Meanwhile, fast decay rates of UCNPs are preferred for real-time imaging with high temporal resolution (Peng et al., 2019). Thus, rational screening of the host matrices, doping types, and concentrations of lanthanide ions should also be considered for exploring novel UCNP probes for super-resolution microscopy.

Exploiting High-Order Non-linearity of UCNPs for High-/Super-Resolution Microscopy

Except for the canonical super-resolution techniques, multiphoton probes with high order of non-linearity favors higher spatial resolution (Yu et al., 2013; Bednarkiewicz et al., 2019). In multiphoton imaging, the imaging resolution approximately equals to $\lambda/(2\times\sqrt{N})$, where λ and N denote the excitation wavelength and the order of non-linearity, respectively. Importantly, the high-resolved image can be directly achieved on a laser-scanning confocal microscopy without the requirements of complex systems and image post-processing. This is ascribed to the fact that only the central and most intense region of the excitation beam can induce adequate emissions from multiphoton probes, while the periphery of the beam barely excites the probes. To some extent, imaging with multiphoton probes also alleviates the requirement of the pinhole because of less interference from out-of-focus light. Therefore, exploring UCNPs with highly non-linear photoresponses are greatly desirable. The four-photon 455-nm emission of Tm^{3+} is a good paradigm for achieving high-resolution imaging. Denkova (Denkova et al., 2019) and Zvyagin (Kostyuk et al., 2019) et al. realized a *ca*. 200-nm resolution in heavily doped $NaYF_4$:Yb,Tm UCNPs under 980-nm excitation (**Figure 2D**). Zhan and coworkers improved the resolution to 161 nm by blue-shifting the excitation wavelength to 730 nm with $Nd^{3+}/Yb^{3+}/Tm^{3+}$ tri-doped UCNPs (Wang et al., 2016). UCNPs with higher non-linearity and longer emission wavelength are preferred to achieve higher/super resolution and improved tissue penetration. Very recently, Schuck et al. developed Tm^{3+}-activated photon avalanching UCNPs with giant non-linear photoresponses (N up to 26) for the 800-nm NIR emissions and achieved a resolution of *ca*. 70 nm (Lee et al., 2020). With the unique advantage of rich energy levels, more intriguing multiphoton upconversion processes in lanthanide-doped UCNPs are desired for high-/super-resolution microscopy.

Applying UCNPs for Cellular Biology

The super-resolved cellular biology application of UCNPs is still in the preliminary stage compared with that of conventional probes (Jin et al., 2018). Great efforts should be devoted to resolve the morphological and physiological characters of living cells, subcellular organelles, proteins, etc., such as the structure and communications of neuron cells (Xu et al., 2013; Tang et al., 2016) as well as the translational and rotational movements of motor proteins (Ohmachi et al., 2012). Labeling of targeted biomolecules precisely requires solid foundation on the surface modification of UCNPs; thus, the effective loading of DNA strands, peptides, antibodies, etc. that have targeting ability should be addressed.

Each super-resolution microscopy has its unique advantages and limitations, yet the combination of the techniques might generate further improved performance. For example, the implantation of multiphoton probes with large non-linearity into STED/FED/SIM should result in higher resolution. The conjunction of SIM and STED should enable video-rate and large-view super-resolution imaging. In this way, the interactions between UCNPs and cells can be disclosed in nanoscale accuracy, including the internalization and externalization of UCNPs by cells as well as the subcellular trajectories of UCNPs (**Figure 2E**). The size-, morphology-, and surface charge-dependent interactions can also be studied. Moreover, the subcellular microenvironments including the viscosity (Wang et al., 2018) and temperature (Rodríguez-Sevilla et al., 2016) can be unraveled by the super-resolved upconversion images with UCNPs.

DISCUSSION

Lanthanide-doped UCNPs are being developed as probes for diverse super-resolution microscopy. The excellent photostability, adequate multiphoton emission efficiency, and tunable emission colors and lifetimes make UCNPs stand out among various as-developed super-resolution probes, especially in long-term and real-time imaging applications. Nonetheless, the complex energy levels and the small stimulated emission cross-section of lanthanide ions are still considerable challenges for flexible design of UCNPs for super-resolution techniques such as STED microscopy. Moreover, the particle size should be reduced and the heating effects should be avoided by exploring small-sized and bright UCNPs. With the development

of UCNP probes, the super-resolved cellular biology applications of UCNPs are ready to be implemented. There is still plenty of room for UCNP-based super-resolution microscopy, and it is believed that UCNPs would attract great concern as probes for super-resolution microscopy in the near future.

DATA AVAILABILITY STATEMENT

The original contributions presented in the study are included in the article/supplementary material, further inquiries can be directed to the corresponding author.

AUTHOR CONTRIBUTIONS

All authors listed have made a substantial, direct and intellectual contribution to the work, and approved it for publication.

FUNDING

This work was supported by the China Postdoctoral Science Foundation (2018T110004), NSFC (Nos. 21590791, 21771005, and 21931001), and MOST of China (2017YFA0205101 and 2017YFA0205104).

REFERENCES

Abbe, E. (1873). Beiträge zur theorie des mikroskops und der micrkoskopischen wahrnehmung. *Arch. Mikrosk. Anat*. 9, 413–468. doi: 10.1007/BF02956173

Albanese, A., Tang, P. S., and Chan, W. C. W. (2012). The effect of nanoparticle size, shape, and surface chemistry on biological systems. *Annu. Rev. Biomed. Eng*. 14, 1–16. doi: 10.1146/annurev-bioeng-071811-150124

Bednarkiewicz, A., Chan, E. M., Kotulska, A., Marciniak, L., and Prorok, K. (2019). Photon avalanche in lanthanide doped nanoparticles for biomedical applications: super-resolution imaging. *Nanoscale Horiz*. 4, 881–889. doi: 10.1039/C9NH00089E

Betzig, E., Patternson, G. H., Sougrat, R., Lindwasser, O. W., Olenych, S., Bonifacino, J. S., et al. (2006). Imaging intracellular fluorescent proteins at nanometer resolution. *Science* 313, 1642–1645. doi: 10.1126/science.1127344

Biffi, G., Tannahill, D., McCafferty, J., and Balasubranmanian, S. (2013). Quantitative visualization of DNA G-quadruplex structures in human cells. *Nat. Chem*. 5, 182–186. doi: 10.1038/nchem.1548

Camillis, S. D., Ren, P., Cao, Y., Plöschner, M., Denkova, D., Zheng, X., et al. (2020). Controlling the non-linear emission of upconversion nanoparticles to enhance super-resolution imaging performance. *Nanoscale* 12, 20347–20355. doi: 10.1039/D0NR04809G

Chan, E. M., Levy, E. S., and Cohen, B. E. (2015). Rationally designed energy transfer in upconverting nanoparticles. *Adv. Mater.* 27, 5753–5761. doi: 10.1002/adma.201500248

Chen, C., Wang, F., Wen, S., Su, Q. P., Wu, M. C. L., Liu, Y., et al. (2018). Multi-photon near-infrared emission saturation nanoscopy using upconversion nanoparticles. *Nat. Commun*. 9:3290. doi: 10.1038/s41467-018-05842-w

Chen, T.-W., Wardill, T. J., Sun, Y., Pulver, S. R., Renninger, S. L., Baohan, A., et al. (2013). Ultrasensitive fluorescent proteins for imaging neuronal activity. *Nature* 499, 295–300. doi: 10.1038/nature12354

Denkova, D., Ploschner, M., Das, M., Parker, L. M., Zheng, X., Lu, Y., et al. (2019). 3D sub-diffraction imaging in a conventional confocal configuration by exploiting super-linear emitters. *Nat. Commun*. 10:3695. doi: 10.1038/s41467-019-11603-0

Dertinger, T., Colyer, R., Iyer, G., Weiss, S., and Enderlein, J. (2009). Fast, background-free, 3D super-resolution optical fluctuation imaging (SOFI). *Proc. Natl. Acad. Sci. U.S.A*. 106, 22287–22292. doi: 10.1073/pnas.0907866106

Dong, H., Du, S. R., Zheng, X. Y., Lyu, G. M., Sun, L. D., Li, L. D., et al. (2015b). Lanthanide nanoparticles: from design toward bioimaging and therapy. *Chem. Rev*. 115, 10725–10815. doi: 10.1021/acs.chemrev.5b00091

Dong, H., Sun, L. D., Li, L. D., Si, R., Liu, R., and Yan, C. H. (2017). Selective cation exchange enabled growth of lanthanide core/shell nanoparticles with dissimilar structure. *J. Am. Chem. Soc*. 139, 18492–18495. doi: 10.1021/jacs.7b11836

Dong, H., Sun, L. D., and Yan, C. H. (2015a). Energy transfer in lanthanide upconversion studies for extended optical applications. *Chem. Soc. Rev*. 44, 1608–1634. doi: 10.1039/C4CS00188E

Dong, H., Sun, L. D., and Yan, C. H. (2020). Upconversion emission studies of single particles. *Nano Today* 35:100956. doi: 10.1016/j.nantod.2020.100956

Gnach, A., Lipinski, T., Bednarkiewicz, A., Rybka, J., and Capobianco, J. A. (2015). Upconverting nanoparticles: assessing the toxicity. *Chem. Soc. Rev*. 44, 1561–1584. doi: 10.1039/C4CS00177J

Gustafsson, M. G. L. (2000). Surpassing the lateral resolution limit by a factor of two using structured illumination microscopy. *J. Microsc*. 198, 82–87. doi: 10.1046/j.1365-2818.2000.00710.x

Hanne, J., Falk, H. J., Görlitz, F., Hoyer, P., Engelhardt, J., Sahl, S. J., et al. (2015). STED nanoscopy with fluorescent quantum dots. *Nat. Commun*. 6:7127. doi: 10.1038/ncomms8127

Hell, S. W., and Wichmann, J. (1994). Breaking the diffraction resolution limit by stimulated emission: stimulated-emission-depletion fluorescence microscopy. *Opt. Lett*. 19, 780–782. doi: 10.1364/OL.19.000780

Huang, B., Wu, Q., Peng, X., Yao, L., Peng, D., and Zhan, Q. (2018). One-scan fluorescence emission difference nanoscopy developed with excitation orthogonalized upconversion nanoparticles. *Nanoscale* 10, 21025–21030. doi: 10.1039/C8NR07017B

Idris, N. M., Jayakumar, M. K. G., Bansal, A., and Zhang, Y. (2015). Upconversion nanoparticles as versatile light nanotransducers for photoactivation applications. *Chem. Soc. Rev*. 44, 1449–1478. doi: 10.1039/C4CS00158C

Jin, D., Xi, P., Wang, B., Zhang, L., Enderlein, J., and van Oijen, A. M. (2018). Nanoparticles for super-resolution microscopy and single-molecule tracking. *Nat. Methods* 15, 415–423. doi: 10.1038/s41592-018-0012-4

Klar, T. A., and Hell, S. W. (1999). Subdiffraction resolution in far-field fluorescence microscopy. *Opt. Lett*. 24, 954–956. doi: 10.1364/OL.24.000954

Kolesov, R., Reuter, R., Xia, K., Stöhr, R., Zappe, A., and Wrachtrup, J. (2011). Super-resolution upconversion microscopy of praseodymium-doped yttrium aluminum garnet nanoparticles. *Phys. Rev. B* 84:153413. doi: 10.1103/PhysRevB.84.153413

Kostyuk, A. B., Vorotnov, A. D., Ivanov, A. V., Volovetskiy, A. B., Kruglov, A. V., Sencha, L. M., et al. (2019). Resolution and contrast enhancement of laser-scanning multiphoton microscopy using thulium-doped upconversion nanoparticles. *Nano Res*. 12, 2933–2940. doi: 10.1007/s12274-019-2527-0

Kuang, C., Li, S., Liu, W., Hao, X., Gu, Z., Wang, Y., et al. (2013). Breaking the diffraction barrier using fluorescence emission difference microscopy. *Sci. Rep*. 3:1441. doi: 10.1038/srep01441

Lee, C., Xu, E., Liu, Y., Teitelboim, A., Yao, K., Fernandez-Bravo, A., et al. (2020). Giant nonlinear optical responses from photon avalanching nanoparticles. *arXiv [Preprint]. arXiv:2007.10551*.

Li, Z., and Zhang, Y. (2008). An efficient and user-friendly method for the synthesis of hexagonal-phase $NaYF_4$:Yb, Er/Tm nanocrystals with controllable shape and upconversion fluorescence. *Nanotechnology* 19:345606. doi: 10.1088/0957-4484/19/34/345606

Liu, B., Chen, C., Di, X., Liao, J., Wen, S., Su, Q. P., et al. (2020). Upconversion nonlinear structured illumination microscopy. *Nano Lett*. 20, 4775–4781. doi: 10.1021/acs.nanolett.0c00448

Liu, Y., Lu, Y., Yang, X., Zheng, X., Wen, S., Wang, F., et al. (2017). Amplified stimulated emission in upconversion nanoparticles for super-resolution nanoscopy. *Nature* 543, 229–233. doi: 10.1038/nature21366

Mai, H. X., Zhang, Y. W., Si, R., Yan, Z. G., Sun, L. D., You, L. P., et al. (2006). High-quality sodium rare-earth fluoride nanocrystals: controlled synthesis and optical properties. *J. Am. Chem. Soc*. 128, 6426–6436. doi: 10.1021/ja060212h

Mi, Z., Zhang, Y., Vanga, S. K., Chen, C.-B., Tan, H. Q., Watt, F., et al. (2015). Subwavelength imaging through ion-beam-induced upconversion. *Nat. Commun*. 6:8832. doi: 10.1038/ncomms9832

Muhr, V., Wilhelm, S., Hirsch, T., and Wolfbeis, O. S. (2014). Upconversion nanoparticles: from hydrophobic to hydrophilic surfaces. *Acc. Chem. Res.* 47, 3481–3493. doi: 10.1021/ar500253g

Ohmachi, M., Komori, Y., Iwane, A. H., Fujii, F., Jin, T., and Yanagida, T. (2012). Fluorescence microscopy for simultaneous observation of 3D orientation and movement and its application to quantum rod-tagged myosin V. *Proc. Natl. Acad. Sci. U.S.A.* 109, 5294–5298. doi: 10.1073/pnas.1118472109

Peña, Á. B., Kemper, B., Woerdemann, M., Vollmer, A., Ketelhut, S., von Bally, G., et al. (2012). Optical tweezers induced photodamage in living cells quantified with digital holographic phase microscopy. *Proc. SPIE* 8427, 1–7. doi: 10.1117/12.922456

Peng, X., Huang, B., Pu, R., Liu, H., Zhang, T., Widengren, J., et al. (2019). Fast upconversion super-resolution microscopy with 10 μs per pixel dwell times. *Nanoscale* 11, 1563–1569. doi: 10.1039/C8NR08986H

Prigozhin, M. B., Maurer, P. C., Courtis, A. M., Liu, N., Wisser, M. D., Siefe, C., et al. (2019). Bright sub-20-nm cathodoluminescent nanoprobes for electron microscopy. *Nat. Nanotechnol.* 14, 420–425. doi: 10.1038/s41565-019-0395-0

Rodríguez-Sevilla, P., Zhang, Y., Haro-González, P., Sanz-Rodríguez, F., Jaque, F., Solé, J. G., et al. (2016). Thermal scanning at the cellular level by an optically trapped upconverting fluorescent particle. *Adv. Mater.* 28, 2421–2426. doi: 10.1002/adma.201505020

Rust, M. J., Bates, M., and Zhuang, X. (2006). Sub-diffraction-limit imaging by stochastic optical reconstruction microscopy (STORM). *Nat. Methods* 3, 793–795. doi: 10.1038/nmeth929

Sahl, S. J., Hell, S. W., and Jakobs, S. (2017). Fluorescence nanoscopy in cell biology. *Nat. Rev. Mol. Cell Bio.* 18, 685–701. doi: 10.1038/nrm.2017.71

Sun, T., Li, Y., Ho, W. L., Zhu, Q., Chen, X., Jin, L., et al. (2019). Integrating temporal and spatial control of electronic transitions for bright multiphoton upconversion. *Nat. Commun.* 10:1811. doi: 10.1038/s41467-019-09850-2

Tang, A.-H., Chen, H., Li, T. P., Metzbower, S. R., MacGillavry, H. D., and Blanpied, T. (2016). A trans-synaptic nanocolumn aligns neurotransmitter release to receptors. *Nature* 536, 210–214. doi: 10.1038/nature19058

Tang, J., Kong, B., Wu, H., Xu, M., Wang, Y., Wang, Y., et al. (2013). Carbon nanodots featuring efficient FRET for real-time monitoring of drug delivery and two-photon imaging. *Adv. Mater.* 25, 6569–6574. doi: 10.1002/adma.201303124

Wang, B., Zhan, Q., Zhao, Y., Wu, R., Liu, J., and He, S. (2016). Visible-to-visible four-photon ultrahigh resolution microscopic imaging with 730-nm diode laser excited nanocrystals. *Opt. Express* 24, A302–A311. doi: 10.1364/OE.24.00A302

Wang, F., Wen, S., He, H., Wang, B., Zhou, Z., Shimoni, O., et al. (2018). Microscopic inspection and tracking of single upconversion nanoparticles in living cells. *Light: Sci. Appl.* 7:18007. doi: 10.1038/lsa.2018.7

Willig, K. I., Rizzoli, S. O., Westphal, V., Jahn, R., and Hell, S. W. (2006). STED microscopy reveals that synaptotagmin remains clustered after synaptic vesicle exocytosis. *Nature* 440, 935–939. doi: 10.1038/nature04592

Wu, Q., Huang, B., Peng, X., He, S., and Zhan, Q. (2017). Non-bleaching fluorescence emission difference microscopy using single 808-nm laser excited red upconversion emission. *Opt. Express* 25, 30885–30894. doi: 10.1364/OE.25.030885

Wu, R., Zhan, Q., Liu, H., Wen, X., Wang, B., and He, S. (2015). Optical depletion mechanism of upconverting luminescence and its potential for multi-photon STED-like microscopy. *Opt. Express* 23, 32401–32412. doi: 10.1364/OE.23.032401

Xing, H., Zhang, S., Bu, W., Zheng, X., Wang, L., Xiao, Q., et al. (2014). Ultrasmall $NaGdF_4$ nanodots for efficient MR angiography and atherosclerotic plaque imaging. *Adv. Mater.* 26, 3867–3872. doi: 10.1002/adma.201305222

Xu, K., Zhong, G., and Zhuang, X. (2013). Actin, spectrin, and associated proteins form a periodic cytoskeletal structure in axons. *Science* 339, 452–456. doi: 10.1126/science.1232251

Yu, J. H., Kwon, S.-H., Petrášek, Z., Park, O. K., Jun, S. W., Shin, K., et al. (2013). High-resolution three-photon biomedical imaging using doped ZnS nanocrystals. *Nat. Mater.* 12, 359–366. doi: 10.1038/nmat3565

Zhan, Q., Liu, H., Wang, B., Wu, Q., Pu, R., Zhou, C., et al. (2017). Achieving high-efficiency emission depletion nanoscopy by employing cross relaxation in upconversion nanoparticles. *Nat. Commun.* 8:1058. doi: 10.1038/s41467-017-01141-y

Zheng, W., Huang, P., Tu, D., Ma, E., Zhu, H., and Chen, X. (2015). Lanthanide-doped upconversion nano-bioprobes: electronic structures, optical properties, and biodetection. *Chem. Soc. Rev.* 44, 1379–1415. doi: 10.1039/C4CS00178H

Zheng, X., Zhao, K., Tang, J., Wang, X. Y., Li, L. D., Chen, N. X., et al. (2017). Gd-Dots with strong ligand–water interaction for ultrasensitive magnetic resonance renography. *ACS Nano* 11, 3642–3650. doi: 10.1021/acsnano.6b07959

Conflict of Interest: The authors declare that the research was conducted in the absence of any commercial or financial relationships that could be construed as a potential conflict of interest.

frontiers in Chemistry

MINI REVIEW
published: 25 March 2021
doi: 10.3389/fchem.2021.641355

The Benefits of Unnatural Amino Acid Incorporation as Protein Labels for Single Molecule Localization Microscopy

*Pooja Laxman, Shirin Ansari, Katharina Gaus and Jesse Goyette**

European Molecular Biology Laboratory (EMBL) Australia Node in Single Molecule Sciences, School of Medical Sciences, University of New South Wales, Sydney, NSW, Australia

Single Molecule Localization Microscopy (SMLM) is an imaging method that allows for the visualization of structures smaller than the diffraction limit of light (~200 nm). This is achieved through techniques such as stochastic optical reconstruction microscopy (STORM) and photoactivated localization microscopy (PALM). A large part of obtaining ideal imaging of single molecules is the choice of the right fluorescent label. An upcoming field of protein labeling is incorporating unnatural amino acids (UAAs) with an attached fluorescent dye for precise localization and visualization of individual molecules. For this technique, fluorescent probes are conjugated to UAAs and are introduced into the protein of interest (POI) as a label. Here we contrast this labeling method with other commonly used protein-based labeling methods such as fluorescent proteins (FPs) or self-labeling tags such as Halotag, SNAP-tags, and CLIP-tags, and highlight the benefits and shortcomings of the site-specific incorporation of UAAs coupled with fluorescent dyes in SMLM.

Keywords: unnatural (non-canonical) amino acids, single molecule localization microscopy, fluorescent protein, unnatural amino acid incorporation, stochastic optical reconstruction microscopy, photo-activated localization microscopy, self-labeling protein tag

OPEN ACCESS

Edited by:
Qiuqiang Zhan,
South China Normal University, China

Reviewed by:
Lingxin Chen,
Yantai Chinese Academy of Sciences (CAS), China
Qian Peter Su,
University of Technology Sydney, Australia

****Correspondence:***
Jesse Goyette
j.goyette@unsw.edu.au

Specialty section:
This article was submitted to Analytical Chemistry, a section of the journal Frontiers in Chemistry

Received: *14 December 2020*
Accepted: *26 February 2021*
Published: *25 March 2021*

Citation:
Laxman P, Ansari S, Gaus K and Goyette J (2021) The Benefits of Unnatural Amino Acid Incorporation as Protein Labels for Single Molecule Localization Microscopy. Front. Chem. 9:641355. doi: 10.3389/fchem.2021.641355

INTRODUCTION

Advances in fluorescence microscopy have now allowed researchers to investigate the intricate details behind subcellular protein localization and organization. However, these methods were limited in optical resolution due to the diffraction limit of light microscopy (Adhikari et al., 2019). Single Molecule Localization Microscopy (SMLM) belongs to the subset of super-resolution imaging and has positively impacted the ways in which cell architecture (Jimenez et al., 2020). In conventional microscopy the ability to resolve fluorescent signals arising from molecules in close proximity is limited by the diffraction of photons as they emanate from the point source, pass through the microscope, and are detected by the camera. The point spread function (PSF) of a microscope refers to this "blurring" effect, which limits the ability to distinguish structures on the scale of half the wavelength of the photons that are detected. In a sample with densely packed molecules that are fluorescently tagged, differentiating two molecules that overlap in each other's PSF would render it impossible to resolve through regular light microscopy (Jradi and Lavis, 2019).

Single Molecule Localization Microscopy is able to bypass the resolution limit through the precise localization of individual fluorophores to increase the spatial resolution of single molecules (Xu et al., 2017). This super-resolution is largely achieved through stochastically activating a small subset of fluorophores at any given time. This factor differentiates the technique from regular fluorescence microscopy which do not involve selectively turning the probes "on" and "off" (Hess et al., 2006). The ability to map out detailed images beyond the distances provided by the diffraction limit makes this advantageous over light microscopy techniques to visualize key cellular structures. Through the use of the various SMLM techniques, it is able to detect structures as small as 20 nm in size (Fürstenberg and Heilemann, 2013).

While several techniques are used in SMLM imaging, two primary approaches include Direct Stochastic Optical Reconstruction Microscopy (dSTORM) and Photoactivated Localization Microscopy (PALM) (Almada et al., 2015). These involve the use of reversibly photoswitchable fluorophores that can activate and deactivate periodically (Jimenez et al., 2020). The use of these techniques can allow for the localization of these individual fluorophores with a much higher precision in contrast to regular fluorescence microscopy techniques. Once all the fluorophore points have been collected, single molecule localization can then be achieved through computational analysis (Babcock and Zhuang, 2017). The PSF of each fluorophore is fitted onto a 2D Gaussian curve function that is then used to estimate the exact coordinates of each individual fluorophore (Huang et al., 2008). This together can generate the super-resolution image required to visualize nanoscopic structures and protein-protein interactions (as seen in **Figure 1**).

In a standard stochastic optical reconstruction microscopy (STORM) experiment, the vital elements required include the use of fluorescent probes to be fused to the target of interest, the separation, and stochastic activation of the individual fluorophores to ensure the proper imaging of single molecules and the localization precision of the fluorophores (Endesfelder and Heilemann, 2015; Xu et al., 2017). The spatial separation of active fluorophores in STORM ensures the activated fluorophores do not overlap their point-spread functions (Adhikari et al., 2019). Photoactivated Localization Microscopy (PALM) similarly shares these features with STORM. What differs the two techniques are the type of fluorescent labels used. Unlike STORM that requires fluorescent probes, PALM makes use of photoactivatable fluorescent proteins (FPs) as the labeling technique (Almada et al., 2015). To control the selective activation of the fluorophores, STORM uses specialized buffers to trap fluorophores in the dark state and low levels of UV light to stochastically photo convert a small subset into the fluorescent state (Betzig et al., 2006). In PALM photoactivatable FPs are stochastically converted from a dark state, or spectral properties of photoswitchable FPs stochastically shifted, by the use of UV light, thereby allowing a subset to be imaged and bleached with high laser power before the next subset is converted (Betzig et al., 2006).

In the context of proteins, a large component of successful SMLM imaging is the choice of fluorescent probe used as a label for the protein of interest (POI). The ideal fluorescent tag candidate for SMLM should aim for photostability during activation and deactivation cycles, be small in size, have high levels of photon emission for better single-molecule detection by the microscope and must not perturb the functionality of the intrinsic interactions of the POI and the other proteins in the environment (Hirabayashi et al., 2011; Toseland, 2013). Various approaches have been developed over the years and have seen great advancement in the creation of photoswitchable fluorophores (Zessin et al., 2012). Types of protein labeling tags include the use of FPs, self-labeling enzymes, and unnatural amino acids (UAAs) (Cranfill et al., 2016; Freidel et al., 2016; Saal et al., 2018). Other forms of labeling such as antibodies are used extensively but have already shown to have come with its own limitations such as the requirement for antibodies with high affinity and high specificity with the target protein. Secondary antibodies are also often used to attach the desired fluorescent dye and can increase technical artifacts in the final image (Li and Vaughan, 2018).

Protein labeling methods that have seen more success and are also used more in recent years include the use of photoswitchable proteins/enzymes that can be genetically fused to the POI (Moerner et al., 2015). This includes the use of naturally FPs (such as GFPs) and self-labeling enzyme tags which aid in attaching the POI with the fluorescent dye for imaging. While several issues come with the use of these labels such as their larger size, the one major limitation that they share is the lack of site-specific tagging (Lee et al., 2019). Therefore, the use of UAAs tagged with a small organic fluorophore can be seen as an attractive alternative approach. The use of gene expansion technology has led to many potential biological applications as the limits to which a gene sequence can be manipulated are theoretically infinite (Ambrogelly et al., 2007). One aspect of this is the use of UAAs as fluorescent markers for SMLM imaging. Through the comparison of the characteristics of all three different types of labeling methods, it is possible to determine that UAA labeling can be a good alternative to the other more commonly used fluorophores (Vreja et al., 2015).

TYPES OF LABELING STRATEGIES

Photoswitchable Fluorescent Proteins

In order for particular fluorophores to be utilized in SMLM, a series of reversible photoswitching mechanism is required in order to switch between the fluorescent state and a non-fluorescent state (Li and Vaughan, 2018). Unlike photoactivable FPs which irreversibly shift from an "off" state to an "on" state and are deactivated through photobleaching, photoswitchable FPs provide the ability to shift between two fluorescent states with different excitation and emission profiles over the course of an experiment (Chozinski et al., 2014). Photo-convertible fluorophores could also be a potential alternative as they provide the ability to change their emission spectrum when exposed to UV (Bek et al., 2020). Amongst the choices, reversibly photoswitchable FPs are one of the most common choices for SMLM as the desired fluorophore largely for its efficacy and reliability (Zhou and Lin, 2013). Fluorescent proteins are shown to be useful in discovering the molecular interactions

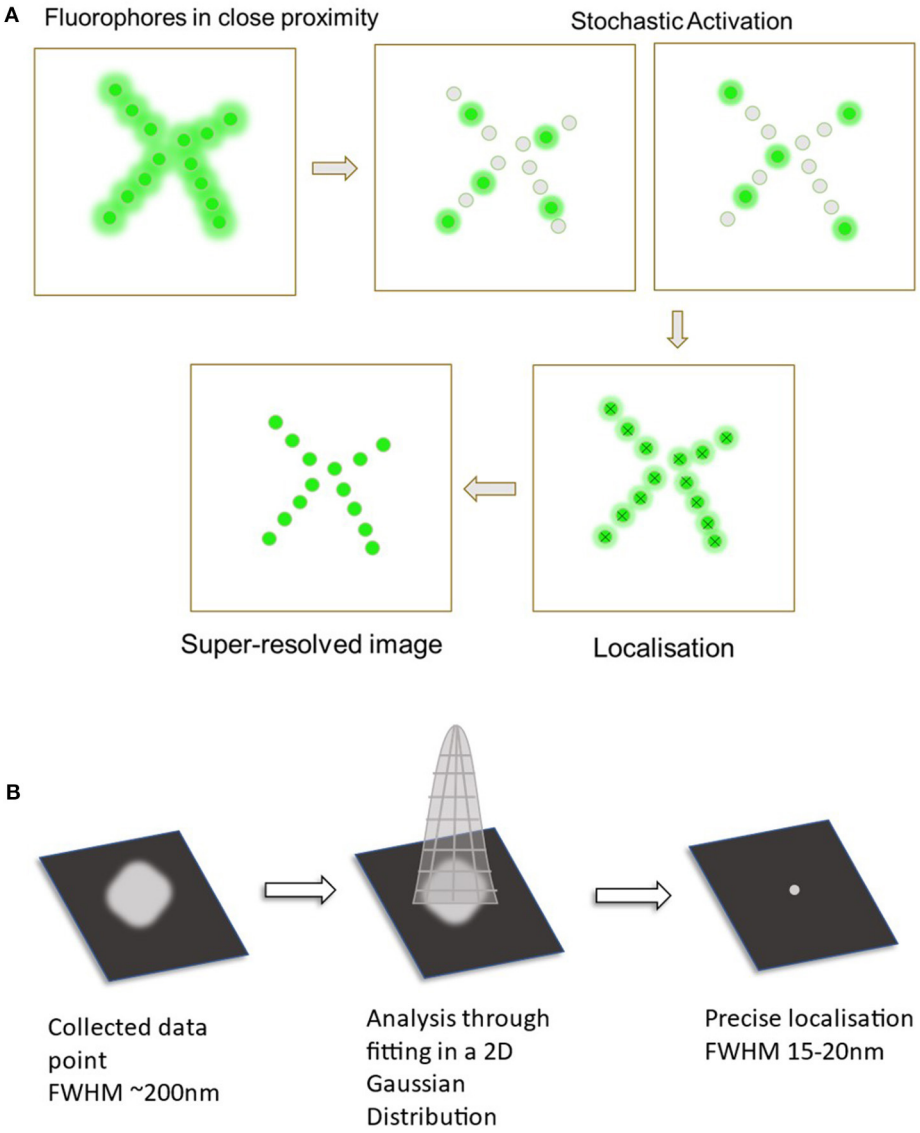

FIGURE 1 | Diagram displaying the process of single molecule localization microscopy (SMLM). **(A)** The primary steps in SMLM starts off with the fluorophores in a densely packed area. These are then stochastically activated to spatially separate the fluorophores. Data from all of the probes are collected and analyzed to localize all the points. This now creates the final super-resolved image. **(B)** Analysis through fitting to a 2D Gaussian distribution. Collected fluorescent signal (Full width at half maximum ~200 nm).

between two species particularly regarding proteins. They can provide further information regarding enzyme activity, protein localization, conformation changes, and many other structural and spatial movements (Toseland, 2013). The photoswitching capability of FPs needed for SMLM can be achieved through the use of specialized buffers or using various levels of UV light (Stiel et al., 2007; Xu et al., 2017). However, despite its widespread usage, it comes with its own disadvantages that can hinder the understanding behind the POI.

Most types of FPs range from 25 to 35 kDa in size and around 4–5 nm in diameter (Crivat and Taraska, 2012). Compared with the localization precision of PALM (<20 nm) this can be seen as bulky and adds to the imprecision of localizing the POI. Furthermore, larger fluorophores could potentially disrupt the natural protein–protein interactions and their general intrinsic activity (Prescher and Bertozzi, 2005). Thus, alternative methods can address this concern by the use of smaller fluorophores to minimize this perturbation. Additionally, due to its size being comparatively larger than other fluorophores, FPs are normally required to be attached to the N or C terminus of the POI to avoid large disruptions of the protein structure or folding behavior (Crivat and Taraska, 2012). Fluorescent proteins additionally do not offer a wide spectral coverage as options for the far-red side of the spectrum become limited (Cranfill et al., 2016).

The structure of a FP consists of a β-sheet barrel that encloses a helix structure containing the central chromophore (Shaner, 2014). While FPs are generally resistant to denaturing, high temperatures and proteolysis, there is variability in the speed of chromophore maturation and in the aggregation of POI-FP fusions (Cranfill et al., 2016). The folding of a FP is essential in maintaining the stability of the chromophore as the β-sheet barrel acts as a protector to the internal chromophore. Perturbation to this structure can cause the loss of the chromophore formation and therefore fluorescence efficiency (Kremers et al., 2011). Finally, FP are typically less bright than organic fluorophores that can be specifically engineered to emit higher levels of fluorescence (Lavis and Raines, 2008).

Fluorescent proteins have been observed to be good candidates as fluorescent tags. However, as it comes with limitations that can alter the results of the finalized super-resolved image, researchers have looked into alternative approaches of labeling.

Self-Labeling Tags

Self-labeling tags are engineered enzymes that react covalently with their substrates. These substrates can be linked to useful chemical moieties, such as biotin or in the case of SMLM imaging, an organic fluorophore (Liss et al., 2015). Due to the flexibility offered by the available labeled substrates, these tags have been in more common use over the years (Hansen et al., 2016). Examples of some of the most common self-labeling tags include SNAP-tag, Halo-tag, and CLIP-tag.

Unlike FPs, self-labeling enzymes are not naturally fluorescent and therefore must be linked to a fluorescent dye (Stagge et al., 2013). This is achieved through the use of a substrate linker. Firstly, the POI is genetically fused to the self-labeling tag. As each of the enzymes binds to a fluorescently conjugated substrate, this substrate can then covalently react, successfully tagging the POI for fluorescence microscopy (Keppler et al., 2003).

The Halo-tag originates from the bacterial enzyme haloalkane dehalogenase and is modified to ensure it can covalently bond to synthetic ligands. The enzyme can be conjugated with the POI through the substrate linker chloroalkane (Los et al., 2008). The Halo-tag is able to fuse with the chloroalkane linker through the removal of the chlorine atom through a nucleophilic displacement mechanism (England et al., 2015). Similarly, the SNAP-tag and CLIP-tag are both modified forms of the human enzyme O^6-alkylguanine-DNA alkyltransferase (hAGT) with the former covalently interacting with O^6-benzylguanine derivatives and the latter so with the O^2-benzylcytosine derivatives (Stagge et al., 2013). Both of these compounds act as substrates to their respective mutant hAGT enzymes (Hoehnel and Lutolf, 2015). These tags similarly form an irreversible covalent bond with their substrate that links the fluorophore.

Factors that make self-labeling tags advantageous over FPs are prolonged observation time through limiting photobleaching and the ability to emit more photons in blinking periods and therefore providing improved brightness of the fluorophore (Li and Vaughan, 2018; Banaz et al., 2019). Furthermore, the tags are also more open to modification without the loss of fluorescence when compared to FPs. Therefore, the features of these tags are aimed to improve upon the limitations presented by FPs (Yan and Bruchez, 2015).

However, despite improvements in flexibility and brightness, self-labeling tags continue to present disadvantages in SMLM. Like FPs, self-labeling tags require the enzymes to be genetically fused to the POI. This can similarly cause perturbations to protein-protein interactions due to its larger size (Fernández-Suárez and Ting, 2008). It also lacks the capability of site-specific protein tagging which can be beneficial when wanting to image specific regions of the POI (Lee et al., 2019). Therefore, for finding an appropriate fluorescent label for SMLM, it could be beneficial to find alternatives in using genetic in-fusion proteins.

UNNATURAL AMINO ACIDS AS A VIABLE ALTERNATIVE

Unnatural Amino Acids

The limitations presented by the use of FPs and other fluorophore labeling strategies have influenced the search for more ideal candidates for fluorescent tagging. Amongst the labeling strategies in practice for SMLM imaging, an upcoming technique is the use of fluorescently labeled UAAs, also referred to as the expanded genetic code (Saal et al., 2018). The genetic code is made up of 20 standard amino acids which make up the natural building blocks of life, however, hundreds of amino acids outside of this have been discovered in nature (Brown et al., 2018). Unnatural amino acids (UAAs) thus are structures that are not found in natural proteins but can be found in other parts of nature or can be chemically synthesized (Wiltschi, 2016).

The expansion of the genetic code through the use of UAAs have become a common practice in many biomolecular applications as it continues to show they aid in the better understanding in the functioning of proteins and other biomolecules (Stevenazzi et al., 2014). Unnatural amino acids (UAAs) have also been found to be advantageous in many biological/chemical applications such as drug discovery and protein labeling (Narancic et al., 2019). Along with the standard amino acids, two additional amino acids have been incorporated into biological systems which are selenocysteine (Sec) and pyrrolysine (Pyl) and these are at times referred to as the 21^{st} and 22^{nd} amino acids (Ambrogelly et al., 2007) (**Figure 2**).

UAA Incorporation

The site-specific incorporation began through the discovery that the two extra amino acids Sec and Pyl that correspond to the opal (TGA) and amber (TAG) codons, respectively (Böck et al., 1991; Krzycki, 2005). This is done through the aid of a corresponding amino acid insertion sequence that is able to suppress the stop codon and subsequently add the amino acid (Xue et al., 2015). Through this discovery, it could be shown that the natural translational mechanism can incorporate UAAs into a POI. This therefore led to the discovery of the insertion of other UAAs through the use of orthogonal aminoacyl-tRNA synthetase/tRNA pairs (Schmied et al., 2014). Various forms of the orthogonal pairs have been created depending on the choice of amino acid that would be

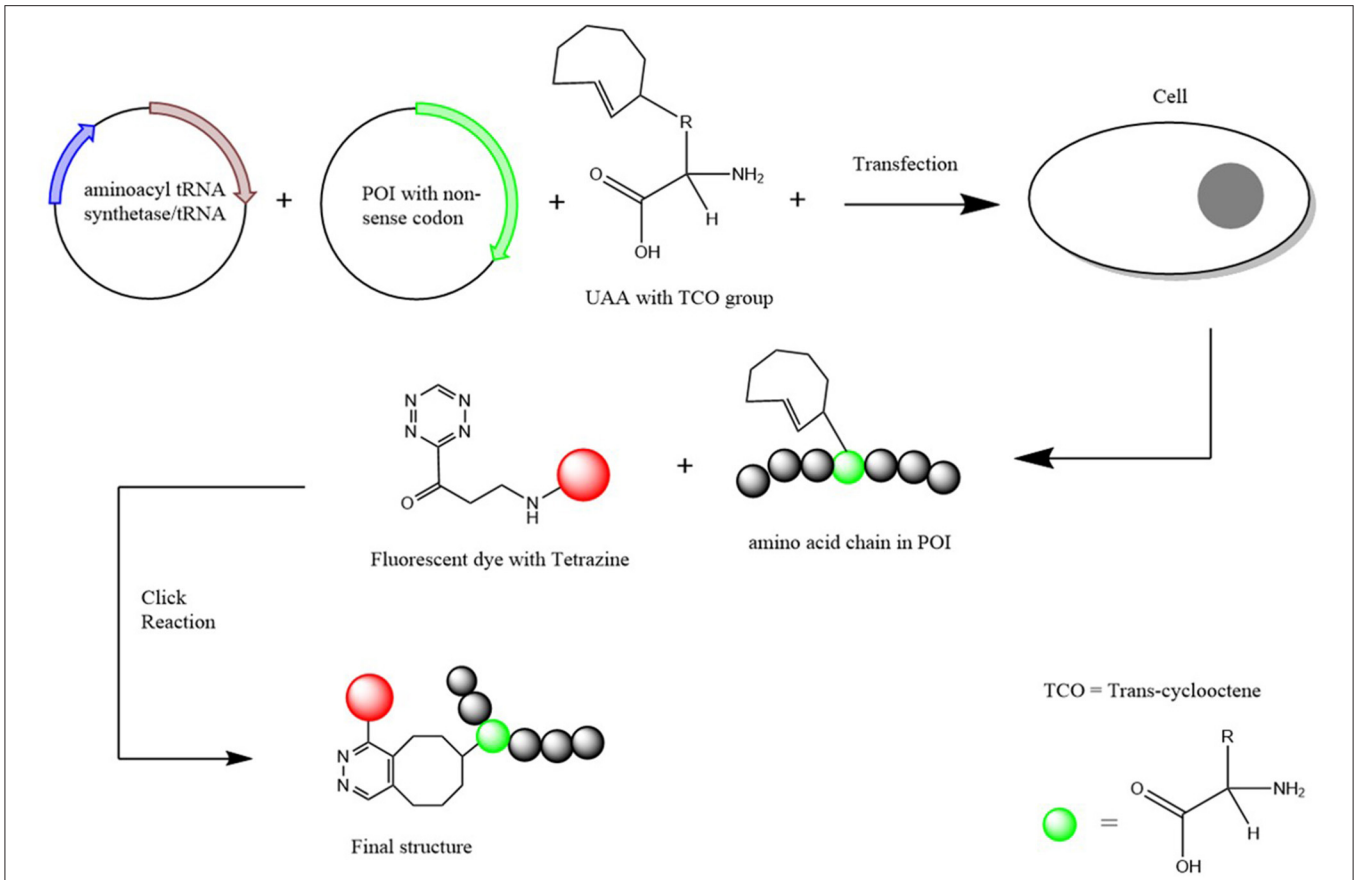

FIGURE 2 | Schematic Diagram of how an UAA is incorporated into a protein of interest. Two plasmids (one containing the aminoacyl-tRNA synthetase and the other the POI with the non-sense codon inserted) and the UAA with a TCO group attached are transfected into the chosen cells. Once incorporated, a fluorescent dye with a tetrazine group is added for the click chemical reaction to result in a structure that attaches the POI with the fluorescent dye together. Scheme based on Nikić et al. (2016).

incorporated (Cervettini et al., 2020). Through the use of a non-sense codon and the orthogonal pair selective to the fluorescent UAA, hundreds of UAAs can now be incorporated into a particular protein/polypeptide chain (Jakob et al., 2019). This method of UAA incorporation is known to be highly selective and kinetically fast so therefore has potential to be the most preferred method of UAA incorporation over other biochemical strategies (Pantoja et al., 2009).

Once incorporated into the POI, the UAA is then fluorescently labeled for SMLM imaging. Labeling is achieved by the addition of chemical handles to the amino acid through a bio-orthogonal "click" reaction (Courtney and Deiters, 2018). This can be done through an azide-alkyne cycloaddition with Copper [Cu (I)] as the needed catalyst. The Cu(I) catalyzed reaction provides the benefits of kinetically fast reaction times, great regioselectivity and high yields, however, poses a threat to cells due to the toxic nature of the copper catalyst (Baskin et al., 2007). To overcome the toxic nature of the copper catalyst, an alternative copper free reaction is used for the click reaction (Gutmann et al., 2016). However, the alternative reaction does come with its own issues regarding efficacy causing the yield to potentially be a lot lower than its catalytic version. Therefore, while the alternative copper free reaction is a preferred method to overcome toxicity, reaction times may need to be extended to ensure more complete conjugation of the fluorescent label to the UAA (Li and Zhang, 2016).

UAAs as Fluorescent Tags

One primary benefit of the usage of UAAs include the site-specific placement of the fluorescent tag unlike the usage of other labeling techniques. This can allow for the monitoring of protein interactions at the desired location producing more localized data for single molecules as FPs and other similar fluorophores are required to be genetically fused to the C or N terminus (Summerer et al., 2006). Unnatural amino acids (UAAs) are often also easier to tag onto the gene/POI due to its significantly smaller size when compared to larger FPs (Neumann-Staubitz and Neumann, 2016).

Choosing the appropriate amino acid to incorporate in SMLM would be based on a synergy of fluorescence levels, ease of insertion and its ability in reversibly photoswitching. A popular strategy is incorporating the desired amino acid with a plasmid containing the GFP gene. These along with the plasmid for the orthogonal tRNA synthetase pair can provide the necessary fluorescence for imaging (Schmied et al., 2014). Other examples of this technique used with many various types of UAAs have been used and have shown high fluorescence and efficiency (Hino et al., 2005; Nikić et al., 2016; Hilaire et al., 2017). This can be compared with studies using different fusion proteins to highlight the subtle improved quality of fluorescently tagged UAA and the disadvantages posed with the use of the bulky fluorophores (Cinelli et al., 2000; Snapp et al., 2003; Wang et al., 2014). As the field continues to advance, different types of UAAs are continuing to be successfully developed in an effort to achieve the ideal imaging of biomolecule constructs.

The first reported single-molecule imaging of a fluorescently labeled UAA was done by Pantoja et al. (2009). In this report total internal reflection fluorescence microscopy was used to image individual molecules of a fluorescent lysine conjugate UAA incorporated into muscle nicotinic acetylcholine receptor in *Xenopus* oocytes. This report provided the first proof of concept which has been applied to other microscopy methods including super resolution techniques. Uttamapinant et al. (2015) utilized the incorporation of fluorescently labeled UAAs in observing live cells through the use of STORM imaging. The study managed to visualize structures beyond the diffraction limit and have successfully generated precise images of the biomolecules. Similar super-resolution techniques that utilize UAA incorporation (Sakin et al., 2017; Schvartz et al., 2017; Neubert et al., 2018) also demonstrate the benefits of their use. However, as the area remains relatively new and up and coming, the number of successful studies using SMLM to visualize nanoscopic biomolecules remains limited.

CONCLUSION

Single Molecule Localization Microscopy has revolutionized the field of biomolecule imaging due to its ability to investigate cellular and protein structures that go beyond the diffraction limit that regular light microscopy lacks to do. However, the most successful experiments involve the use of the best type of fluorophores labeled to the molecules. While many common fluorescent tags have been used in the past such as FPs and self-labeling tags, these come with their own limitations. In an attempt to combat these, UAA can be incorporated into the gene/POI to provide better fluorescence and therefore more precise imaging in SMLM. The use of UAAs as tags in SMLM have shown to have several benefits such as site-specific incorporation and the lower likelihood of the hinderance of intrinsic protein–protein interactions due to its much smaller size. Despite these benefits, due to the limited number of studies available, the practical aspects of UAAs as probes needs further study. For example, the efficacy of certain reactions used such as the copper-based cycloaddition or in the transfection process involving the UAA and target constructs may vary between cells of interest. Despite these technical challenges, the added benefits of targeted, site specific labeling with UAA promises to unlock the full potential of super-resolution microscopy.

AUTHOR CONTRIBUTIONS

PL has first authorship while authors SA, KG, and JG all share senior authorship. All authors contributed to the article and approved the submitted version.

FUNDING

The authors would like to acknowledge funding from the Australian Research Council (ARC) (CE140100011 to KG) and the National Health and Medical Research Council of Australia (APP1163814 to JG and APP1183588 to KG and JG).

REFERENCES

Adhikari, S., Moscatelli, J., Smith, E. M., Banerjee, C., and Puchner, E. M. (2019). Single-molecule localization microscopy and tracking with red-shifted states of conventional BODIPY conjugates in living cells. *Nat. Commun.* 10:3400. doi: 10.1038/s41467-019-11384-6

Almada, P., Culley, S., and Henriques, R. (2015). PALM and STORM: into large fields and high-throughput microscopy with sCMOS detectors. *Methods* 88, 109–121. doi: 10.1016/j.ymeth.2015.06.004

Ambrogelly, A., Palioura, S., and Söll, D. (2007). Natural expansion of the genetic code. *Nat. Chem. Biol.* 3, 29–35. doi: 10.1038/nchembio847

Babcock, H. P., and Zhuang, X. (2017). Analyzing single molecule localization microscopy data using cubic splines. *Sci. Rep.* 7, 552–552. doi: 10.1038/s41598-017-00622-w

Banaz, N., Mäkelä, J., and Uphoff, S. (2019). Choosing the right label for single-molecule tracking in live bacteria: side-by-side comparison of photoactivatable fluorescent protein and Halo tag dyes. *J. Phys. D Appl. Phys.* 52:064002. doi: 10.1088/1361-6463/aaf255

Baskin, J. M., Prescher, J. A., Laughlin, S. T., Agard, N. J., Chang, P. V., Miller, I. A., et al. (2007). Copper-free click chemistry for dynamic *in vivo* imaging. *Proc. Natl. Acad. Sci. U.S.A.* 104, 16793–16797. doi: 10.1073/pnas.0707090104

Bek, J. W., De Clercq, A., De Saffel, H., Soenens, M., Huysseune, A., Witten, P. E., et al. (2020). Photoconvertible fluorescent proteins: a versatile tool in zebrafish skeletal imaging. *J. Fish Biol.* doi: 10.1111/jfb.14335. [Epub ahead of print].

Betzig, E., Patterson, G. H., Sougrat, R., Lindwasser, O. W., Olenych, S., Bonifacino, J. S., et al. (2006). Imaging intracellular fluorescent proteins at nanometer resolution. *Science* 313, 1642–1645. doi: 10.1126/science.1127344

Böck, A., Forchhammer, K., Heider, J., Leinfelder, W., Sawers, G., Veprek, B., et al. (1991). Selenocysteine: the 21st amino acid. *Mol. Microbiol.* 5, 515–520. doi: 10.1111/j.1365-2958.1991.tb00722.x

Brown, W., Liu, J., and Deiters, A. (2018). Genetic code expansion in animals. *ACS Chem. Biol.* 13, 2375–2386. doi: 10.1021/acschembio.8b00520

Cervettini, D., Tang, S., Fried, S. D., Willis, J. C. W., Funke, L. F. H., Colwell, L. J., et al. (2020). Rapid discovery and evolution of orthogonal aminoacyl-tRNA synthetase–tRNA pairs. *Nat. Biotechnol.* 38, 989–999. doi: 10.1038/s41587-020-0479-2

Chozinski, T. J., Gagnon, L. A., and Vaughan, J. C. (2014). Twinkle, twinkle little star: photoswitchable fluorophores for super-resolution imaging. *FEBS Lett.* 588, 3603–3612. doi: 10.1016/j.febslet.2014.06.043

Cinelli, R. A., Ferrari, A., Pellegrini, V., Tyagi, M., Giacca, M., and Beltram, F. (2000). The enhanced green fluorescent protein as a tool for the analysis of protein dynamics and localization: local fluorescence study at the single-molecule level. *Photochem. Photobiol.* 71, 771–776. doi: 10.1562/0031-8655(2000)0710771TEGFPA2.0.CO2

Courtney, T., and Deiters, A. (2018). Recent advances in the optical control of protein function through genetic code expansion. *Curr. Opin. Chem. Biol.* 46, 99–107. doi: 10.1016/j.cbpa.2018.07.011

Cranfill, P. J., Sell, B. R., Baird, M. A., Allen, J. R., Lavagnino, Z., de Gruiter, H. M., et al. (2016). Quantitative assessment of fluorescent proteins. *Nat. Methods* 13, 557–562. doi: 10.1038/nmeth.3891

Crivat, G., and Taraska, J. W. (2012). Imaging proteins inside cells with fluorescent tags. *Trends Biotechnol.* 30, 8–16. doi: 10.1016/j.tibtech.2011.08.002

Endesfelder, U., and Heilemann, M. (2015). "Direct Stochastic Optical Reconstruction Microscopy (dSTORM)," in *Advanced Fluorescence Microscopy: Methods and Protocols,* ed P. J. Verveer (New York, NY: Springer New York), 263–276. doi: 10.1007/978-1-4939-2080-8_14

England, C. G., Luo, H., and Cai, W. (2015). HaloTag technology: a versatile platform for biomedical applications. *Bioconjugate Chem.* 26, 975–986. doi: 10.1021/acs.bioconjchem.5b00191

Fernández-Suárez, M., and Ting, A. Y. (2008). Fluorescent probes for super-resolution imaging in living cells. *Nat. Rev. Mol. Cell Biol.* 9, 929–943. doi: 10.1038/nrm2531

Freidel, C., Kaloyanova, S., and Peneva, K. (2016). Chemical tags for site-specific fluorescent labeling of biomolecules. *Amino Acids* 48, 1357–1372. doi: 10.1007/s00726-016-2204-5

Fürstenberg, A., and Heilemann, M. (2013). Single-molecule localization microscopy-near-molecular spatial resolution in light microscopy with photoswitchable fluorophores. *Phys. Chem. Chem. Phys.* 15, 14919–14930. doi: 10.1039/c3cp52289j

Gutmann, M., Memmel, E., Braun, A. C., Seibel, J., Meinel, L., and Lühmann, T. (2016). Biocompatible azide–alkyne "click" reactions for surface decoration of glyco-engineered cells. *ChemBioChem* 17, 866–875. doi: 10.1002/cbic.201500582

Hansen, S. R., Rodgers, M. L., and Hoskins, A. A. (2016). "Fluorescent labeling of proteins in whole cell extracts for single-molecule imaging, Chapter 4," in *Methods in Enzymology*, eds M. Spies and Y. R. Chemla (Madison, WI: Academic Press), 83–104. doi: 10.1016/bs.mie.2016.08.018

Hess, S. T., Girirajan, T. P. K., and Mason, M. D. (2006). Ultra-high resolution imaging by fluorescence photoactivation localization microscopy. *Biophys. J.* 91, 4258–4272. doi: 10.1529/biophysj.106.091116

Hilaire, M. R., Ahmed, I. A., Lin, C.-W., Jo, H., DeGrado, W. F., and Gai, F. (2017). Blue fluorescent amino acid for biological spectroscopy and microscopy. *Proc. Natl. Acad. Sci. U. S. A.* 114, 6005–6009. doi: 10.1073/pnas.17055 86114

Hino, N., Okazaki, Y., Kobayashi, T., Hayashi, A., Sakamoto, K., and Yokoyama, S. (2005). Protein photo-cross-linking in mammalian cells by site-specific incorporation of a photoreactive amino acid. *Nat. Methods* 2, 201–206. doi: 10.1038/nmeth739

Hirabayashi, K., Hanaoka, K., Shimonishi, M., Terai, T., Komatsu, T., Ueno, T., et al. (2011). Selective two-step labeling of proteins with an off/on fluorescent probe. *Chemistry* 17, 14763–14771. doi: 10.1002/chem.201102664

Hoehnel, S., and Lutolf, M. P. (2015). Capturing cell–cell interactions via SNAP-tag and CLIP-tag technology. *Bioconjugate Chem.* 26, 1678–1686. doi: 10.1021/acs.bioconjchem.5b00268

Huang, B., Wang, W., Bates, M., and Zhuang, X. (2008). Three-dimensional super-resolution imaging by stochastic optical reconstruction microscopy. *Science* 319, 810–813. doi: 10.1126/science.1153529

Jakob, L., Gust, A., and Grohmann, D. (2019). Evaluation and optimisation of unnatural amino acid incorporation and bioorthogonal bioconjugation for site-specific fluorescent labelling of proteins expressed in mammalian cells. *Biochem. Biophys. Rep.* 17, 1–9. doi: 10.1016/j.bbrep.2018.10.011

Jimenez, A., Friedl, K., and Leterrier, C. (2020). About samples, giving examples: optimized single molecule localization microscopy. *Methods* 174, 100–114. doi: 10.1016/j.ymeth.2019.05.008

Jradi, F. M., and Lavis, L. D. (2019). Chemistry of photosensitive fluorophores for single-molecule localization microscopy. *ACS Chem. Biol.* 14, 1077–1090. doi: 10.1021/acschembio.9b00197

Keppler, A., Gendreizig, S., Gronemeyer, T., Pick, H., Vogel, H., and Johnsson, K. (2003). A general method for the covalent labeling of fusion proteins with small molecules *in vivo*. *Nat. Biotechnol.* 21, 86–89. doi: 10.1038/nbt765

Kremers, G.-J., Gilbert, S. G., Cranfill, P. J., Davidson, M. W., and Piston, D. W. (2011). Fluorescent proteins at a glance. *J. Cell Sci.* 124, 157–160. doi: 10.1242/jcs.072744

Krzycki, J. A. (2005). The direct genetic encoding of pyrrolysine. *Curr. Opin. Microbiol.* 8, 706–712. doi: 10.1016/j.mib.2005.10.009

Lavis, L. D., and Raines, R. T. (2008). Bright ideas for chemical biology. *ACS Chem. Biol.* 3, 142–155. doi: 10.1021/cb700248m

Lee, K. J., Kang, D., and Park, H.-S. (2019). Site-specific labeling of proteins using unnatural amino acids. *Mol. Cells* 42, 386–396. doi: 10.14348/molcells.2019.0078

Li, H., and Vaughan, J. C. (2018). Switchable fluorophores for single-molecule localization microscopy. *Chem. Rev.* 118, 9412–9454. doi: 10.1021/acs.chemrev.7b00767

Li, L., and Zhang, Z. (2016). Development and applications of the Copper-Catalyzed Azide-Alkyne Cycloaddition (CuAAC) as a bioorthogonal reaction. *Molecules* 21:1393. doi: 10.3390/molecules21101393

Liss, V., Barlag, B., Nietschke, M., and Hensel, M. (2015). Self-labelling enzymes as universal tags for fluorescence microscopy, super-resolution microscopy and electron microscopy. *Sci. Rep.* 5:17740. doi: 10.1038/srep17740

Los, G. V., Encell, L. P., McDougall, M. G., Hartzell, D. D., Karassina, N., Zimprich, C., et al. (2008). HaloTag: a novel protein labeling technology for cell imaging and protein analysis. *ACS Chem. Biol.* 3, 373–382. doi: 10.1021/cb8 00025k

Moerner, W. E., Shechtman, Y., and Wang, Q. (2015). Single-molecule spectroscopy and imaging over the decades. *Faraday Discuss.* 184, 9–36. doi: 10.1039/C5FD00149H

Narancic, T., Almahboub, S. A., and O'Connor, K. E. (2019). Unnatural amino acids: production and biotechnological potential. *World J. Microbiol. Biotechnol.* 35:67. doi: 10.1007/s11274-019-2642-9

Neubert, F., Beliu, G., Terpitz, U., Werner, C., Geis, C., Sauer, M., et al. (2018). Bioorthogonal click chemistry enables site-specific fluorescence labeling of functional NMDA receptors for super-resolution imaging. *Angew. Chem. Int. Ed.* 57, 16364–16369. doi: 10.1002/anie.201808951

Neumann-Staubitz, P., and Neumann, H. (2016). The use of unnatural amino acids to study and engineer protein function. *Curr. Opin. Struct. Biol.* 38, 119–128. doi: 10.1016/j.sbi.2016.06.006

Nikić, I., Estrada Girona, G., Kang, J. H., Paci, G., Mikhaleva, S., Koehler, C., (2016). Debugging eukaryotic genetic code expansion for site-specific click-PAINT super-resolution microscopy. *Angew. Chem. Int. Ed. Engl.* 55, 16172–16176. doi: 10.1002/anie.201608284

Pantoja, R., Rodriguez, E. A., Dibas, M. I., Dougherty, D. A., and Lester, H. A. (2009). Single-molecule imaging of a fluorescent unnatural amino acid incorporated into nicotinic receptors. *Biophys. J.* 96, 226–237. doi: 10.1016/j.bpj.2008.09.034

Prescher, J. A., and Bertozzi, C. R. (2005). Chemistry in living systems. *Nat. Chem. Biol.* 1, 13–21. doi: 10.1038/nchembio0605-13

Saal, K.-A., Richter, F., Rehling, P., and Rizzoli, S. O. (2018). Combined use of unnatural amino acids enables dual-color super-resolution imaging of proteins via click chemistry. *ACS Nano* 12, 12247–12254. doi: 10.1021/acsnano. 8b06047

Sakin, V., Hanne, J., Dunder, J., Anders-Össwein, M., Laketa, V., Nikić, I., et al. (2017). A versatile tool for live-cell imaging and super-resolution nanoscopy studies of HIV-1 Env distribution and mobility. *Cell Chem. Biol.* 24, 635.e635–645.e635. doi: 10.1016/j.chembiol.2017.04.007

Schmied, W. H., Elsässer, S. J., Uttamapinant, C., and Chin, J. W. (2014). Efficient multisite unnatural amino acid incorporation in mammalian cells via optimized pyrrolysyl tRNA synthetase/tRNA expression and engineered eRF1. *J. Am. Chem. Soc.* 136, 15577–15583. doi: 10.1021/ja5069728

Schvartz, T., Aloush, N., Goliand, I., Segal, I., Nachmias, D., Arbely, E., et al. (2017). Direct fluorescent-dye labeling of alpha-tubulin in mammalian cells for live cell and superresolution imaging. *Mol. Biol. Cell.* 28, 2747–2756. doi: 10.1091/mbc.e17-03-0161

Shaner, N. C. (2014). "Green Fluorescent Protein (GFP)," in *eLS*, ed John Wiley and Sons, Ltd. (John Wiley and Sons, Ltd). doi: 10.1002/9780470015902.a0002663.pub3

Snapp, E. L., Altan, N., and Lippincott-Schwartz, J. (2003). Measuring protein mobility by photobleaching GFP chimeras in living cells. *Curr. Protoc. Cell Biol.* 19, 21.21.21–21.21.24. doi: 10.1002/0471143030.cb2101s19

Stagge, F., Mitronova, G. Y., Belov, V. N., Wurm, C. A., and Jakobs, S. (2013). SNAP-, CLIP- and Halo-tag labelling of budding yeast cells. *PLoS ONE* 8:e78745. doi: 10.1371/journal.pone.0078745

Stevenazzi, A., Marchini, M., Sandrone, G., Vergani, B., and Lattanzio, M. (2014). Amino acidic scaffolds bearing unnatural side chains: an old idea generates new and versatile tools for the life sciences. *Bioorg. Med. Chem. Lett.* 24, 5349–5356. doi: 10.1016/j.bmcl.2014.10.016

Stiel, A. C., Trowitzsch, S., Weber, G., Andresen, M., Eggeling, C., Hell, S. W., et al. (2007). 1.8 A bright-state structure of the reversibly switchable fluorescent protein Dronpa guides the generation of fast switching variants. *Biochem. J.* 402, 35–42. doi: 10.1042/BJ20061401

Summerer, D., Chen, S., Wu, N., Deiters, A., Chin, J. W., and Schultz, P. G. (2006). A genetically encoded fluorescent amino acid. *Proc. Natl. Acad. Sci. U.S.A.* 103, 9785–9789. doi: 10.1073/pnas.0603965103

Toseland, C. P. (2013). Fluorescent labeling and modification of proteins. *J. Chem. Biol.* 6, 85–95. doi: 10.1007/s12154-013-0094-5

Uttamapinant, C., Howe, J. D., Lang, K., Beránek, V., Davis, L., Mahesh, M., et al. (2015). Genetic code expansion enables live-cell and super-resolution imaging of site-specifically labeled cellular proteins. *J. Am. Chem. Soc.* 137, 4602–4605. doi: 10.1021/ja512838z

Vreja, I. C., Nikić, I., Göttfert, F., Bates, M., Kröhnert, K., Outeiro, T. F., et al. (2015). Super-resolution microscopy of clickable amino acids reveals the effects of fluorescent protein tagging on protein assemblies. *ACS Nano* 9, 11034–11041. doi: 10.1021/acsnano.5b04434

Wang, S., Moffitt, J. R., Dempsey, G. T., Xie, X. S., and Zhuang, X. (2014). Characterization and development of photoactivatable fluorescent proteins for single-molecule-based superresolution imaging. *Proc. Natl. Acad. Sci. U.S.A.* 111, 8452–8457. doi: 10.1073/pnas.1406593111

Wiltschi, B. (2016). Incorporation of non-canonical amino acids into proteins in yeast. *Fungal Genet. Biol.* 89, 137–156. doi: 10.1016/j.fgb.2016.02.002

Xu, J., Ma, H., and Liu, Y. (2017). Stochastic Optical Reconstruction Microscopy (STORM). *Curr. Protoc. Cytometry* 81, 12.46.11–12.46.27. doi: 10.1002/cpcy.23

Xue, L., Karpenko, I. A., Hiblot, J., and Johnsson, K. (2015). Imaging and manipulating proteins in live cells through covalent labeling. *Nat. Chem. Biol.* 11, 917–923. doi: 10.1038/nchembio.1959

Yan, Q., and Bruchez, M. P. (2015). Advances in chemical labeling of proteins in living cells. *Cell Tissue Res.* 360, 179–194. doi: 10.1007/s00441-015-2145-4

Zessin, P. J., Finan, K., and Heilemann, M. (2012). Super-resolution fluorescence imaging of chromosomal DNA. *J. Struct. Biol.* 177, 344–348. doi: 10.1016/j.jsb.2011.12.015

Zhou, X. X., and Lin, M. Z. (2013). Photoswitchable fluorescent proteins: ten years of colorful chemistry and exciting applications. *Curr. Opin. Chem. Biol.* 17, 682–690. doi: 10.1016/j.cbpa.2013.05.031

Conflict of Interest: The authors declare that the research was conducted in the absence of any commercial or financial relationships that could be construed as a potential conflict of interest.

frontiers in Chemistry

ORIGINAL RESEARCH
published: 12 April 2021
doi: 10.3389/fchem.2021.641670

Detection and Classification of Multi-Type Cells by Using Confocal Raman Spectroscopy

Jing Wen[1], Tianchen Tang[1], Saima Kanwal[1], Yongzheng Lu[1], Chunxian Tao[1], Lulu Zheng[1], Dawei Zhang[1] and Zhengqin Gu[2]**

[1]Engineering Research Center of Optical Instrument and Systems, Ministry of Education and Shanghai Key Lab of Modern Optical System, University of Shanghai for Science and Technology, Shanghai, China, [2]Department of Urology, Xinhua Hospital, School of Medicine, Shanghai Jiao Tong University, Shanghai, China

Tumor cells circulating in the peripheral blood are the prime cause of cancer metastasis and death, thus the identification and discrimination of these rare cells are crucial in the diagnostic of cancer. As a label-free detection method without invasion, Raman spectroscopy has already been indicated as a promising method for cell identification. This study uses a confocal Raman spectrometer with 532 nm laser excitation to obtain the Raman spectrum of living cells from the kidney, liver, lung, skin, and breast. Multivariate statistical methods are applied to classify the Raman spectra of these cells. The results validate that these cells can be distinguished from each other. Among the models built to predict unknown cell types, the quadratic discriminant analysis model had the highest accuracy. The demonstrated analysis model, based on the Raman spectrum of cells, is propitious and has great potential in the field of biomedical for classifying circulating tumor cells in the future.

Keywords: Raman spectroscopy, cancer cells, SVM, LDA, QDA

OPEN ACCESS

Edited by:
Xusan Yang,
Cornell University, United States

Reviewed by:
Chenshuo Ma,
Duke University, United States
Yiqing Lu,
Macquarie University, Australia
Hugh Byrne,
Dublin Institute of Technology, Ireland

****Correspondence:***
Dawei Zhang
dwzhang@usst.edu.cn
Zhengqin Gu
guzhengqin@xinhuamed.com.cn

Specialty section:
This article was submitted to Analytical Chemistry, a section of the journal Frontiers in Chemistry

Received: *14 December 2020*
Accepted: *19 February 2021*
Published: *12 April 2021*

Citation:
Wen J, Tang T, Kanwal S, Lu Y, Tao C, Zheng L, Zhang D and Gu Z (2021) Detection and Classification of Multi-Type Cells by Using Confocal Raman Spectroscopy. Front. Chem. 9:641670. doi: 10.3389/fchem.2021.641670

INTRODUCTION

Over the past few years, there has been a gradual increase in the number of cancer deaths (Jemal et al., 2010; Ferlay et al., 2015). It be known that human organs can produce cancer cells at any stage. In fewer cases, cancer cells may develop into tumors when they accumulate to a certain extent. Circulating tumor cells (CTCs) shed from the primary tumor and spread to the peripheral blood or lymph. These CTCs are the major cause of cancer metastases and death (Fidler, 1995; Mocellin et al., 2006). Thus, it is essential to distinguish these tumor cells. Nowadays, immunocytological is still the golden standard and specific biomarkers remain the main screening method for tumor cell examination (Oosterwijk-Wakka et al., 2013; Alix-Panabières and Pantel, 2014; Bhana et al., 2015). However, some cancer cells may exhibit inadequate or vague expression of bio-markers probably by completing the epithelial-mesenchymal transition (Choueiri et al., 2013; Zerati et al., 2013; Alix-Panabières and Pantel, 2014). Besides, the use of fluorescent probes often has the disadvantage of spectral overlap and the binding of fluorescent molecules is based on the specific binding of antigen and antibody, which may change the structure of the cell molecules. It is not conducive to the follow-up of other detection experiments (Chan et al., 2008; Jones et al., 2015). Therefore, a highly sensitive, label-free, cost-efficient CTCs detection method that can accurately identify cancer cells is a pressing need.

Raman spectroscopy is a rapid and non-destructive technique for studying a biological system based on detecting molecular vibration and rotation (Krafft, 2012; Krafft et al., 2016; Popp et al.,

TABLE 1 | Names of cell lines and cell numbers.

Cell lines	Cell names	Total number	Calibration	Prediction
786-O	Human clear cell renal cancer cells	52	40	12
HKC	Human kidney tubular epithelial cells	52	40	12
HepG-2	Human hepatoblastoma cells	38	29	9
A549	Human non-small cell lung cancer cells	57	45	12
A375	Human malignant melanoma cells	56	44	12
4T1	Mouse breast cancer cells	50	38	12

2016; Wang et al., 2020). Numerous biochemical components can be identified by Raman spectra, for instance, genetic material, protein, and lipid, all have their unique peaks in the Raman spectrum (Stone et al., 2004; Brauchle et al., 2014; Fang et al., 2019). As a well-known fact, mutations in cancer cells are always accompanied by wireless proliferation, which leads to a huge increase of genes in the nucleus. Some cancer cells also suffer protein changes on the cell membrane or accumulate large amounts of lipids in the cytoplasm (Abramczyk et al., 2009; Yue et al., 2014; Surmacki et al., 2015). At present, there have been many studies reporting the use of Raman microspectroscopy combined with multivariate statistical analysis methods to distinguish and classify cell types (Kong et al., 2015). Machine learning-based analysis methods such as support vector machine (SVM), principal component analysis (PCA), linear discriminant analysis (LDA), and quadratic discriminant analysis (QDA) were introduced in combination with Raman spectroscopy which has successfully attained the identification of many cells and tissues in the declining years (Dixon and Brereton, 2009; Neugebauer et al., 2010; Pudlas et al., 2011; Zhang et al., 2016; Siqueira et al., 2017). However, these research only compare tumor cells with normal cells produced by the same organ, the differences between tumor cells from different organs are not clear (Crow et al., 2005; Krishna et al., 2005; Chan et al., 2008; Pijanka et al., 2013). We expect to get a broader spectrum of cancer cells in order to recognize CTCs at an early stage, which will help to identify the diseased organs in advance, allowing cancer patients to avoid mortality outcomes. The accuracy and classification characteristics using the statistical analysis methods for cell samples also need to be verified by comparison.

In this article, we chose the cell samples from kidney, lung, liver, breast, and skin as the research object, and explore the process of living cell detection by confocal Raman spectroscopy. With the combination of multivariate statistical methods, Raman spectra of various types of cells are classified based on three models i.e. SVM, LDA, and QDA, the accuracy of classifying the accurate cell types is above 95%. In order to verify the feasibility of the model, the results validate that high sensitivity is realized to predict the unknown cell types. Furthermore, the comparison of the pros and cons of the three models is also discussed. The flexible combination of Raman spectroscopy and various modeling methods can immediately identify a variety of cells at a high accuracy which will provide potential applications in CTCs detection.

METHODS AND EXPERIMENTS

Cell Culture and Sample Preparation

Cells in this study are obtained from the American Type Culture Collection (ATCC), which is listed in **Table 1**. All the cells were grown in Dulbecco's Modified Eagle's Medium (DMEM) with 10% fetal bovine serum (FBS) and antibiotics (penicillin and streptomycin) at 37°C in a humidified atmosphere of 5% CO_2. Cells in the logarithmic phase were taken to harvest with Trypsin-EDTA and suspended in phosphate-buffered saline (PBS 1×) before Raman measurement. All cells were collected under the same condition. About 2 ml of the cell suspension was added into a culture dish with a quartz glass bottom. Approximately three-quarters of the cells were used as training and validation, while another quarter was for the prediction set.

Raman Spectroscopy Measurement

Raman spectra of living cells were obtained from a laser confocal Raman spectrometer (RAMANtouch, Japan) with 532 nm laser excitation. Before the Raman test, a CCD detector must be cooled to −70°C, and the system was calibrated by using silicon with its peak at 520.5 cm^{-1}. The laser was focused by a ×60 water immersion objective lens (NA = 1.0, Nikon, Japan) onto the sample. To ensure an appropriate signal-to-noise ratio without damaging the samples, the laser power was controlled at about 10 mW. Single point measurement mode was used and the laser spot size on the sample was about 0.65 μm. The exposure time for each cell was kept at 8 s for each time and tested three times. Subsequently, the spectrometer automatically took the averaged spectra. The test range was in the Raman low wavenumber region and a minimum of 35 spectra were obtained from each kind of cell. Regions of each cell's nucleus were preferentially sampled. The measurements of all cells were worked out under the same conditions.

Data Processing and Analysis

Raman spectral data were pre-processed using WiRE 4.2 (Renishaw, United Kingdom), with baseline corrected and smoothed, and cosmic rays were removed if existing. Before analysis, the Raman shift in each spectrum was cut into the 'fingerprint' region from 600 to 1800 cm^{-1}, which removed the Raman peak of the quartz glass substrate. The Raman intensity was normalized and unified as the relative intensity of arbitrary unit (a.u.) using OriginPro 9.1. (OriginLab Corp., Northampton, MA, United States) (Zhao et al., 2007; Zhang et al., 2010a; Zhang

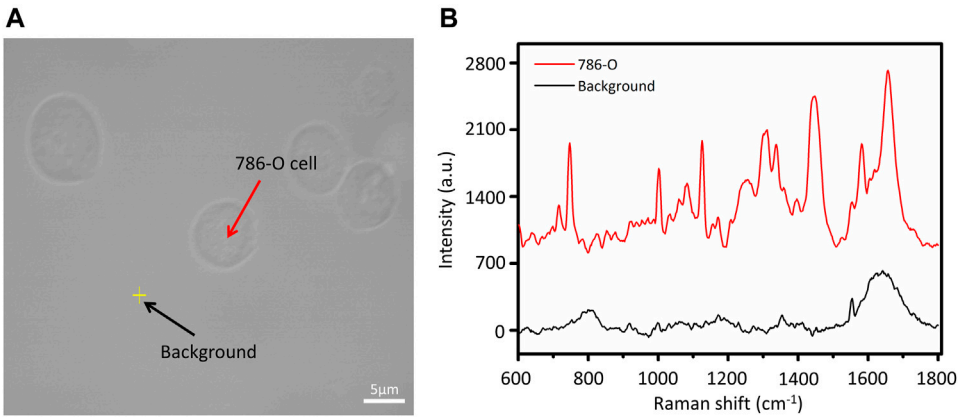

FIGURE 1 | (A) Bright field image of 786-O cells and **(B)** Raman spectrum of background and cell.

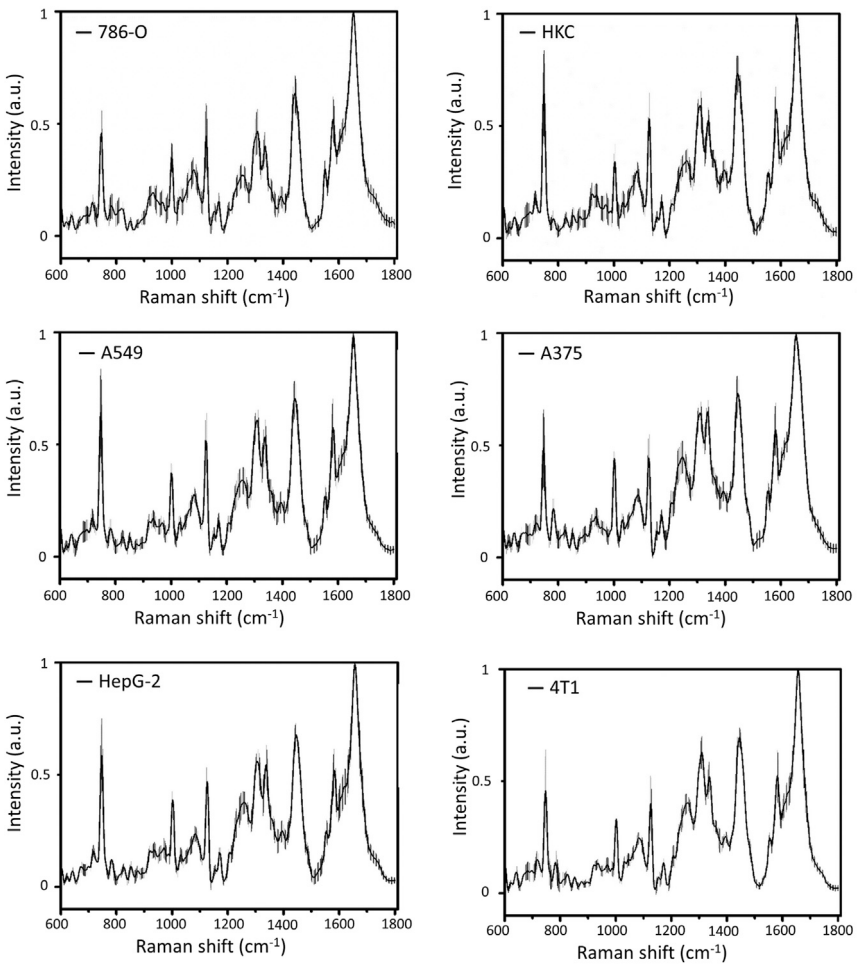

FIGURE 2 | The average Raman spectra of 6 kinds of cells with error bars.

et al., 2010b). All spectral data were corrected for baseline translation and shift phenomena using the EMSC (extended multiplicative signal correction) algorithm, assuming the average of all spectral data as the ideal spectrum(Popp et al., 2018). Multivariate statistical analysis methods i.e. SVM, PCA, LDA, QDA were carried out with MATLAB R2016b

TABLE 2 | The representative peak assignments in cell Raman spectra (Stone et al., 2004; Notingher and Hench, 2006; Wood et al., 2007; Surmacki et al., 2015).

Raman shift (cm^{-1})	DNA	Protein	Lipid
642		Tyrosine (C–C)	
747	Thymine		
831/851		Tyrosine	
1003		Phenylalanine	
1124			C–C stretching mode
1176	Cytosine, guanine	Tyrosine	
1208		Tyrosine	
1252		Amide III	=CH in-plane bending
1311	Adenine		
1337	Adenine, guanine	Tryptophan	
1445			CH2 deformation
1581	Pyrimidine ring		
1604		Tyrosine	
1620		Tyrosine	
1655		Amide I	

TABLE 3 | Prediction result of cancer cells/normal cells with SVM classification.

	Actual set	
Prediction set	786-O	HKC
786-O	12	0
HKC	0	12

TABLE 4 | Confusion matrix of five cancer cell lines using the SVM classification model.

		Actual sets				
		A549	A375	HepG-2	4T1	786-O
Prediction set	A549	45	0	0	0	0
	A375	0	44	0	0	0
	HepG-2	0	0	29	0	0
	4T1	0	0	0	38	0
	786-O	0	0	0	0	40

(MathWorks, Inc., United States) and The Unscramble@10.4 (CAMO, Oslo, Norway).

RESULTS AND DISCUSSION

To determine whether the spectral data obtained from the measurement were Raman signals of cells, we checked the signals around the cells, the laser point was slightly above the bottom to focus on the cells. **Figure 1A** shows the bright field image of a typical 786-O cell and the blank background near the cells, while **Figure 1B** shows the Raman spectra of the two corresponding points. Unlike the cell curve, deprived of a large number of sharp Raman peaks, the background curve is relatively smoother. The only background peak displayed in the spectrum was at about 1554 cm^{-1}. It demonstrates that the Raman signal in quartz glass background exhibited extremely low interference which is consistent with the description in the previous report (Palonpon et al., 2013).

Figure 2 manifests the average Raman spectrum curves of six types of cells. The shadow area is the error bars which represent the standard deviation of the mean value. The main common Raman peaks at 642, 831, 851, 1171, 1208, 1604, 1620 cm^{-1} (tyrosine), 1003 cm^{-1} (phenylalanine), 1246 cm^{-1} (Amide III), 1337 cm^{-1} (tryptophan), 1655 cm^{-1} (Amide I) are assigned to proteins. Strong and wide peaks are corresponding with lipid at 1124 cm^{-1} (C–C stretching mode), 1252 cm^{-1} (=CH in-plane bending), and 1445 cm^{-1} (CH2 deformation). Other bands at around 747 cm^{-1} (thymine), 1176 cm^{-1} (cytosine, guanine), 1311 cm^{-1} (adenine), 1581 cm^{-1} (pyrimidine ring of nucleic acids) are assigned to DNA and RNA. Details of Raman peaks assignment to cell spectrum are presented in **Table 2** (Stone et al., 2004; Notingher and Hench, 2006; Wood et al., 2007; Surmacki et al., 2015). Various cells have quite comparable Raman spectra due to the similar biochemical components (as shown in **Figure 2**). But there are also a few Raman peaks that are different, such as distinct peaks at 831 and 850 cm^{-1}, which represent tyrosine residue conformations (Zhuang et al., 2013). These spectral peaks distinguished by the human eye may not be sufficient to accurately identify different cells. Herein, we used a multivariate statistical analysis algorithm (SVM, PCA, LDA) to process the data set and analyze the subtle differences of the Raman spectrum among different cells.

SVM is a supervised learning method for the binary classification of data. It finds the maximum geometric margin hyperplane between two kinds of learning data sets and using the optimal hyperplane to distinct the two data sets into two sides to complete the classification (Dixon and Brereton, 2009; Zhang et al., 2016). In this paper, we use an SVM with a linear kernel function to realize the discriminative classification of prediction samples. To prevent overfitting, while ensuring the classification accuracy, the penalty factor C selection was set to 1. Each spectrum was cross-validated with 10 segments. Initially, we performed a feasibility validation using cancer and normal cells derived from the same organ which had an apparent difference of biochemical components. 40 cancer cells (786-O) and 40 normal cells (HKC) were used to construct the SVM model. Meanwhile, to verify the accuracy of the SVM model for predicting unknown cells, a set containing 24 new cells (12 786-O, 12 HKC) was used. The prediction accuracy was 100% so that the cancer cells and normal cells could be distinguished from each other. The details of predicting results are shown in **Table 3**. Using the same SVM method could additionally construct a classification model among five different cancer cells. 196 cancer cells are used to form a training set (including 40 786-O, 29 HepG-2, 45 A549, 44 A375, 38 4T1) to construct the model. **Table 4** shows the details in a confusion matrix of the SVM classification model and the validation accuracy in the training set was 100%. However, the predictive performance needs to be tested. The prediction rate of these SVM models is verified by a prediction set of 57 new 'unknown' cells (actually already known

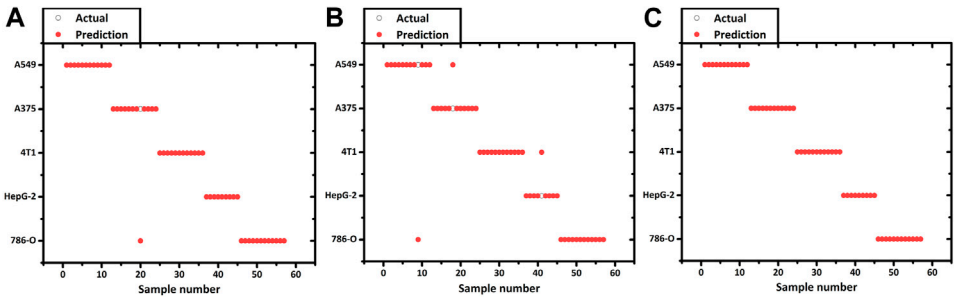

FIGURE 3 | Prediction result of 5 kinds of cancer cell lines using the **(A)** SVM, **(B)** LDA and **(C)** QDA model.

but not included in the training set, including 12 786-O, 9 HepG-2, 12 A549, 12 A375, 12 4T1). The result is shown in **Figure 3A** and the prediction of accuracy is 98.25%.

Although SVM had successfully established the classification among different cancer cells, it has the drawbacks of a complex and time-consuming model. SVM is a binary classifier, seeking the optimal hyperplane between the two data sets. While dealing with the problem of multi-sample classification, SVM models should be constructed between every two samples. As for N different types of cells, at least $N \times (N\text{-}1)/2$ decision values should be considered. While dealing with two distinct cell types (cancer cell 786-O and normal cells HKC, the N is not too large), the training speed is relatively swift. However, to deal with the classification of multiple cancer cells, the number of binary classifiers increases as a quadratic function concerning N, which significantly increases the amount of training operation and reduces the training speed (Dixon and Brereton, 2009). Therefore, we employ an LDA method to predict and classify various cancer cells. LDA is a classical linear supervised learning method to reduce the dimension and classify, which has been reported in classification of cancer Raman spectra(Dochow et al., 2011; Pijanka et al., 2013). Given a labeled set of training samples, LDA tries to project the samples into low-dimensional space, so that the projection points of the same samples are as close as possible and the projection points of the heterogeneous samples are as far as possible. After projection, the different types of the sample will be distributed in different regions of the lower dimensional space, and the prediction sets will also be projected in the space according to the previously calculated dimensionality reduction rules. Afterward, the category of the new sample is determined based on the location of the projection point (Dixon and Brereton, 2009; Siqueira et al., 2017).

Before constructing the LDA and QDA classification model the Raman spectral data needs further process due to a large number of variables arrays. PCA is introduced to eliminate any overlapped information in the spectrum through a multivariate linear transformation which extracts the eigenvalues of the data matrix and then reconstructs a basic eigenvector to form a new data set (Dixon and Brereton, 2009). Through the transformation, PCA could also classify some simple data sets. However, in this study, PCA is not implemented with the SVM model. Various studies have directly used the SVM method to analyze the Raman spectrum. We suppose that this is because the SVM method can better solve the problem of classification of high-dimensional data and there is no need of reducing the dimension of the data in advance. According to the validation on our spectrum dataset, the accuracy of PCA + SVM trained and predicted is indeed lower than the method that uses SVM directly. In this contribution, Raman shift in the spectrum was including 683 variables evenly distributed over the region of 600–1800 cm^{-1}. The 197 cancer cell spectrum, previously used to build SVM models, is still used as the verification set here. **Figure 4** shows the result of three dimensions of the first principal component (PC1, PC2, and PC3). The five groups of cells were spatially clustered but could not be well separated. This shows that the classification effect of PCA is not ideal when dealing with high-dimensional data with complex and fuzzy noise distribution. The comprehensive contribution rate of three PCs was 55.25%, which represented the main variances. Due to the more PC numbers retains more original Raman spectrum information (Tang et al., 2017), to improve the accuracy of subsequent predictions, we increased the number to the first 20 PCs, which described 85% of variables. Subsequently, the LDA

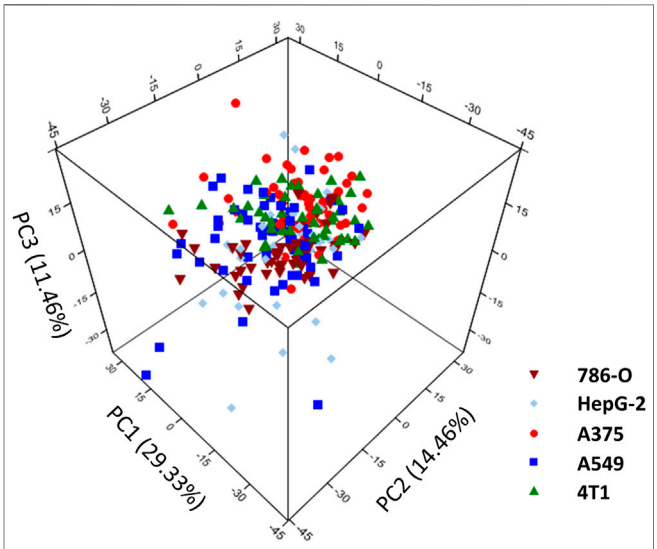

FIGURE 4 | The top three PCs' score plot of different cancer cells.

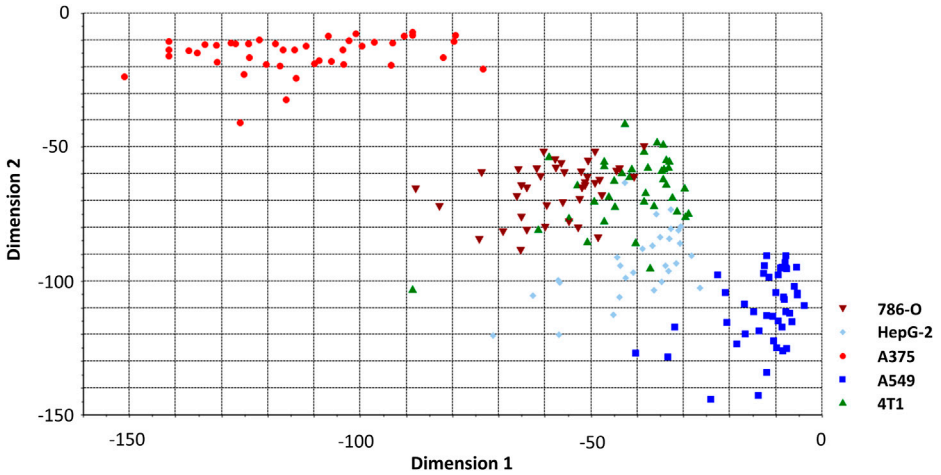

FIGURE 5 | LDA classification model classifying spectrum of cancer cell lines. Two of five dimensions are plotted.

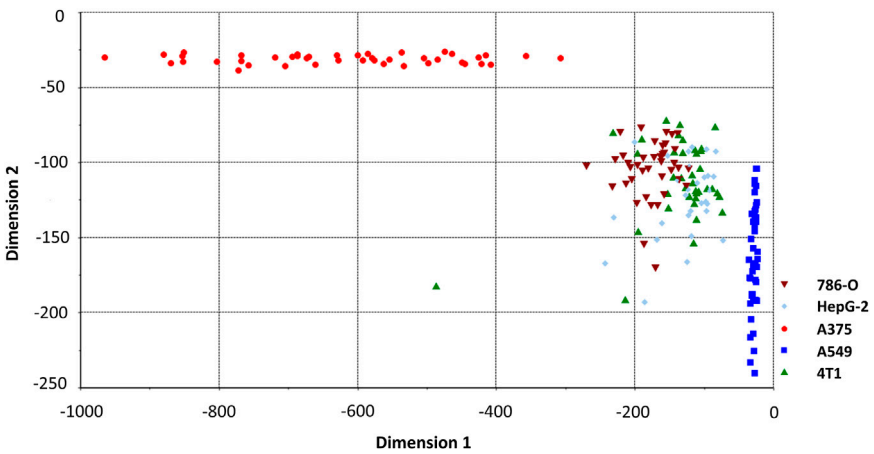

FIGURE 6 | QDA classification model classifying spectrum of cancer cell lines. Two of five dimensions are plotted.

model was constructed with these PCs. The prior probabilities were calculated from the training set. Cell spectral data was classified in fivefold dimensional space. **Figure 5** selects the projection of two dimensions to plot, which represents the division of A375 (red) and A549 (blue). Under the combination of any two different dimensions, the discrimination of the two types of cells can be found. The prediction result is indicated in **Figure 3B** with an accuracy of 94.73%, which is a little lower than the SVM model.

We perceived that some cell spectra were misclassified into the wrong category. It is due to the limitation of LDA which is linearly partitioned, while the boundary of the cell Raman spectrum is irregular. QDA is based on LDA which uses quadratic information and far higher complexity hypersurface to enhance the accuracy of classification (Dixon and Brereton, 2009; Tang et al., 2017). **Figure 6** shows a QDA analysis model using two of the five dimensions. Utilizing the verification set previously constructed, the 57 unknown cell spectrum were also used for QDA. **Figure 3C** presents the prediction detail. Each cell spectra had precisely predicted with a 100% prediction accuracy. Finally, we compared the efficiency of building these models. The computation time to construct the SVM model costs 0.47 s, while the LDA and QDA method was 0.014 and 0.018 s. SVM costs the longest time, which is consistent with the previous theory. Constructing the QDA model is slightly slower than LDA, but both are in the same order of magnitude. Consequently, the QDA model had the elite classification and prediction ability with relatively good efficiency.

In practical applications (such as CTC detection), besides the tumor cells, another cellular material is contained in the peripheral blood. Mainly including leukocytes, red blood cells et al. Since the supervised learning model is used, we need to know the extent possible about the cell types that may be contained in the samples. Relative to the multivariate cancer cells, these haemocytes have a greater difference in size, morphology, components, and are easier to distinguish. By the

existing devices, such as magnetic bead sorting or optical tweezers, the tumor cells can be preliminarily distinguished from these common haemocytes cells (Dochow et al., 2011; Rao et al., 2018; Chang et al., 2020). To avoid haemocytes, that are not completely excluded in the actual detection affecting the discrimination accuracy, the Raman spectrum of haemocytes could also be added to the training database. Some of the previous studies, for example, Zhang et al. successfully distinguished cancer cells from leukocytes using Raman spectroscopy(Zhang et al., 2016). For clinical applications, the analytical throughput of cells is also an important indicator. The time spent for each cell is 24 s. Considering a little more consumption of time by the spectrometer to automatically adjust the laser spot to switch to the other cells, the Raman test throughput was <150 cells/h. Usually, there are several CTCs out of 10^3–10^7 nucleated cells in a patient's blood sample (Pachmann et al., 2005). To meet the need for clinical application in the future, we can pre-dispose of tumor cells by magnetic bead enrichment before Raman spectroscopy measurement, with the number of tumor cells enriched being much smaller than this test throughput. Therefore, it is acceptable to measurement within an hour, which holds a great prospect for rapid detection in the future.

CONCLUSION

In this study, Raman spectra of six different cells were obtained from confocal Raman spectroscopy. Different cell lines had tiny different spectra. The Raman peaks of 831 and 850 cm^{-1} showed the tyrosine residue conformation, which revealed the difference of renal and breast cancer cells from the liver, lung, and skin cancer cells. By using multivariate statistical methods of SVM, LDA, and QDA, we further studied the spectral differences between various cancer cells. The identification accuracy and advantages were compared to discuss. The SVM and LDA model had identical specific accuracy of classifying and predicting cell spectrum, but LDA is more beneficial when the type and number of samples are vast. QDA is a variant of LDA and had a better sensitivity of 100% prediction accuracy in the analysis of cellular Raman spectra. In the follow-up study, we will accumulate more cell spectrum to improve the reliability of the calibration sample library and implement it to identify the circulating tumor cells in the peripheral blood of tumor patients. Raman spectroscopy is a powerful, rapid, and non-destructive means in the identification of biochemical components. It has the potential to play a substantial role in the detection of cancer metastasis in an early stage of cancer or after surgery in the future.

DATA AVAILABILITY STATEMENT

The raw data supporting the conclusion of this article will be made available by the authors, without undue reservation.

AUTHOR CONTRIBUTIONS

JW and TT contributed equally to this work. DZ and ZG designed the experiments. TT, CT, and YL conducted the experiments. TT, JW, SK, and LZ wrote this paper. All authors agreed to this manuscript.

FUNDING

This work was supported by the National Natural Science Foundation of China (Project No. 81701745) and the Interdisciplinary Program of Medicine and Engineering of USST.

REFERENCES

Abramczyk, H., Surmacki, J., Brożek-Płuska, B., Morawiec, Z., and Tazbir, M. (2009). The hallmarks of breast cancer by Raman spectroscopy. *J. Mol. Struct.* 924–926, 175–182. doi:10.1016/j.molstruc.2008.12.055

Alix-Panabières, C., and Pantel, K. (2014). Technologies for detection of circulating tumor cells: facts and vision. *Lab. Chip* 14, 57–62. doi:10.1039/c3lc50644d

Bhana, S., Wang, Y., and Huang, X. (2015). Nanotechnology for enrichment and detection of circulating tumor cells. *Nanomedicine* 10, 1973–1990. doi:10.2217/nnm.15.32

Brauchle, E., Thude, S., Brucker, S. Y., and Schenke-Layland, K. (2014). Cell death stages in single apoptotic and necrotic cells monitored by Raman microspectroscopy. *Sci. Rep.* 4, 4698–4699. doi:10.1038/srep04698

Chan, J., Fore, S., Wachsmann-hogiu, S., and Huser, T. (2008). Raman spectroscopy and microscopy of individual cells and cellular components. *Laser Photon. Rev.* 2, 325–349. doi:10.1002/lpor.200810012

Chang, Z., Zhang, R., Yang, C., Shao, D., Tang, Y., Dong, W., et al. (2020). Cancer-leukocyte hybrid membrane-cloaked magnetic beads for the ultrasensitive isolation, purification, and non-destructive release of circulating tumor cells. *Nanoscale* 12, 19121–19128. doi:10.1039/d0nr04097e

Choueiri, T. K., Cheng, S., Qu, A. Q., Pastorek, J., Atkins, M. B., and Signoretti, S. (2013). Carbonic anhydrase IX as a potential biomarker of efficacy in metastatic clear-cell renal cell carcinoma patients receiving sorafenib or placebo: analysis from the treatment approaches in renal cancer global evaluation trial (TARGET). *Urol. Oncol.* 31, 1788–1793. doi:10.1016/j.urolonc.2012.07.004

Crow, P., Barrass, B., Kendall, C., Hart-Prieto, M., Wright, M., and Persad, R. (2005). The use of Raman spectroscopy to differentiate between different prostatic adenocarcinoma cell lines. *Br. J. Cancer* 92, 2166. doi:10.1038/sj.bjc.6602638

Dixon, S. J., and Brereton, R. G. (2009). Comparison of performance of five common classifiers represented as boundary methods: euclidean distance to centroids, linear discriminant analysis, quadratic discriminant analysis, learning vector quantization and support vector machines, as dependent on data structure. *Chemom. Intell. Lab. Syst.* 95, 1–17. doi:10.1016/j.chemolab.2008.07.010

Dochow, S., Krafft, C., Neugebauer, U., Bocklitz, T., Henkel, T., and Mayer, G. (2011). Tumour cell identification by means of Raman spectroscopy in combination with optical traps and microfluidic environments. *Lab. Chip.* 11, 1484–149090. doi:10.1039/c0lc00612b

Fang, T., Shang, W., Liu, C., Xu, J., Zhao, D., Liu, Y., et al. (2019). Nondestructive identification and accurate isolation of single cells through a chip with Raman optical tweezers. *Anal. Chem.* 91, 9932–9939. doi:10.1021/acs.analchem.9b01604

Ferlay, J., Soerjomataram, I., Dikshit, R., Eser, S., Mathers, C., Rebelo, M., et al. (2015). Cancer incidence and mortality worldwide: sources, methods and major patterns in GLOBOCAN 2012. *Int. J. Cancer* 136, E359–E386. doi:10.1002/ijc.29210

Fidler, I. J. (1995). The pathogenesis of cancer metastasis: the 'seed and soil'hypothesis revisited. *Prod. Oper. Manag.* 4, 46–56. doi:10.1038/nrc1098

Jemal, A., Center, M. M., DeSantis, C., and Ward, E. M. (2010). Global patterns of cancer incidence and mortality rates and trends. *Cancer Epidemiol. Biomark. Prev.* 19, 1893–1907. doi:10.1158/1055-9965.EPI-10-0437

Jones, S., Anagnostou, V., Lytle, K., Parpart-Li, S., Nesselbush, M., Riley, D. R., et al. (2015). Personalized genomic analyses for cancer mutation discovery and interpretation. *Sci. Transl. Med.* 7, 283ra53. doi:10.1126/scitranslmed.aaa7161

Kong, K., Kendall, C., Stone, N., and Notingher, I. (2015). Raman spectroscopy for medical diagnostics—from *in-vitro* biofluid assays to *in-vivo* cancer detection. *Adv. Drug Deliv. Rev.* 89, 121. doi:10.1016/j.addr.2015.03.009

Krafft, C., Dietzek, B., Schmitt, M., and Popp, J. (2012). Raman and coherent anti-stokes Raman scattering microspectroscopy for biomedical applications. *J. Biomed. Opt.* 17, 040801. doi:10.1117/1.JBO.17.4.040801

Krafft, C., Schie, I. W., Meyer, T., Schmitt, M., and Popp, J. (2016). Developments in spontaneous and coherent Raman scattering microscopic imaging for biomedical applications. *Chem. Soc. Rev.* 45, 1819–1849. doi:10.1039/c5cs00564g

Krishna, C. M., Sockalingum, G. D., Kegelaer, G., Rubin, S., Kartha, V. B., and Manfait, M. (2005). Micro-Raman spectroscopy of mixed cancer cell populations. *Vib. Spectrosc.* 38, 95–100. doi:10.1016/j.vibspec.2005.02.018

Mocellin, S., Keilholz, U., Rossi, C. R., and Nitti, D. (2006). Circulating tumor cells: the 'leukemic phase' of solid cancers. *Trends Mol. Med.* 12, 130–139. doi:10.1016/j.molmed.2006.01.006

Neugebauer, U., Bocklitz, T., Clement, J. H., Krafft, C., and Popp, J. (2010). Towards detection and identification of circulating tumour cells using Raman spectroscopy. *Analyst* 135, 3178–3182. doi:10.1039/c0an00608d

Notingher, I., and Hench, L. L. (2006). Raman microspectroscopy: a noninvasive tool for studies of individual living cells *in vitro*. *Expert Rev. Med. Devices* 3, 215–234. doi:10.1586/17434440.3.2.215

Oosterwijk-Wakka, J. C., Boerman, O. C., Mulders, P. F. A., and Oosterwijk, E. (2013). Application of monoclonal antibody G250 recognizing carbonic anhydrase IX in renal cell carcinoma. *Int. J. Mol. Sci.* 14, 11402–11423. doi:10.3390/ijms140611402

Pachmann, K., Clement, J. H., Schneider, C., Willen, B., Camara, O., Pachmann, U., et al. (2005). Standardized quantification of circulating peripheral tumor cells from lung and breast cancer. *Clin. Chem. Lab. Med.* 43, 617–627. doi:10.1515/CCLM.2005.107

Palonpon, A. F., Ando, J., Yamakoshi, H., Dodo, K., Sodeoka, M., Kawata, S., et al. (2013). Raman and SERS microscopy for molecular imaging of live cells. *Nat. Protoc.* 8, 677–692. doi:10.1038/nprot.2013.030

Pijanka, J. K., Stone, N., Rutter, A. V., Forsyth, N., Sockalingum, G. D., Yang, Y., et al. (2013). Identification of different subsets of lung cells using Raman microspectroscopy and whole cell nucleus isolation. *Analyst* 138, 5052–5058. doi:10.1039/c3an00968h

Popp, J., Bocklitz, T., and Jena, D. (2018). Extended multiplicative signal correction based model transfer for Raman spectroscopy in biological applications. *Anal. Chem.* 90 (16), 9787–9795. doi:10.1021/acs.analchem.8b01536

Popp, J., Krafft, C., Schmitt, M., Schie, I., Cialla-May, D., Matthaeus, C., et al. (2016). Label-free molecular imaging of biological cells and tissues by linear and non-linear Raman spectroscopic approaches. *Angew. Chem. Int. Ed. Engl.* 56 (16),4392–4430. doi:10.1002/anie.201607604

Pudlas, M., Koch, S., Bolwien, C., Thude, S., Jenne, N., Hirth, T., et al. (2011). Raman spectroscopy: a noninvasive analysis tool for the discrimination of human skin cells. *Tissue Eng. Part C Methods* 17, 1027–1040. doi:10.1089/ten.tec.2011.0082

Rao, L., Meng, Q., Huang, Q., Wang, Z., Yu, G., Li, A., et al. (2018). Platelet–leukocyte hybrid membrane-coated immunomagnetic beads for highly efficient and highly specific isolation of circulating tumor cells. *Adv. Funct. Mater.* 22, 1803531. doi:10.1002/adfm.201803531

Siqueira, L. F. S., Araújo Júnior, R. F., de Araújo, A. A., Morais, C. L. M., and Lima, K. M. G. (2017). LDA vs. QDA for FT-MIR prostate cancer tissue classification. *Chemom. Intell. Lab. Syst.* 162, 123–129. doi:10.1016/j.chemolab.2017.01.021

Stone, N., Kendall, C., Smith, J., Crow, P., and Barr, H. (2004). Raman spectroscopy for identification of epithelial cancers. *Faraday Discuss* 126, 141–157. doi:10.1039/b304992b

Surmacki, J., Brozek-Pluska, B., Kordek, R., and Abramczyk, H. (2015). The lipid-reactive oxygen species phenotype of breast cancer. Raman spectroscopy and mapping, PCA and PLSDA for invasive ductal carcinoma and invasive lobular carcinoma. Molecular tumorigenic mechanisms beyond Warburg effect. *Analyst* 140, 2121–2133. doi:10.1039/c4an01876a

Tang, M., Xia, L., Wei, D., Yan, S., Du, C., and Cui, H. L. (2017). Distinguishing different cancerous human cells by Raman spectroscopy based on discriminant analysis methods. *Appl. Sci.* 7, 900. doi:10.3390/app7090900

Wang, Y., Xu, J., Kong, L., Li, B., Li, H., Huang, W. E., et al. (2020). Raman-activated sorting of antibiotic-resistant bacteria in human gut microbiota. *Environ. Microbiol.* 22, 2613–2624. doi:10.1111/1462-2920.14962

Wood, B. R., Caspers, P., Puppels, G. J., Pandiancherri, S., and McNaughton, D. (2007). Resonance Raman spectroscopy of red blood cells using near-infrared laser excitation. *Anal. Bioanal. Chem.* 387, 1691–1703. doi:10.1007/s00216-006-0881-8

Yue, S., Li, J., Lee, S. Y., Lee, H. J., Shao, T., Song, B., et al. (2014). Cholesteryl ester accumulation induced by PTEN loss and PI3K/AKT activation underlies human prostate cancer aggressiveness. *Cell Metab.* 19, 393–406. doi:10.1016/j.cmet.2014.01.019

Zerati, M., Leite, K. R., Pontes-Junior, J., Segre, C. C., Reis, S. T., Srougi, M., et al. (2013). Carbonic anhydrase IX is not a predictor of outcomes in non-metastatic clear cell renal cell carcinoma-a digital analysis of tissue microarray. *Int. Braz. J. Urol.* 39, 484–492. doi:10.1590/S1677-5538.IBJU.2013.04.05

Zhang, Y., Ye, X., Xu, G., Jin, X., Luan, M., Lou, J., et al. (2016). Identification and distinction of non-small-cell lung cancer cells by intracellular SERS nanoprobes. *RSC Adv.* 6, 5401–5407. doi:10.1039/c5ra21758j

Zhang, Z. M., Chen, S., and Liang, Y. Z. (2010a). Baseline correction using adaptive iteratively reweighted penalized least squares. *Analyst* 135, 1138–1146. doi:10.1039/b922045c

Zhang, Z. M., Chen, S., Liang, Y. Z., Liu, Z. X., Zhang, Q. M., Ding, L. X., et al. (2010b). An intelligent background-correction algorithm for highly fluorescent samples in Raman spectroscopy. *J. Raman Spectrosc.* 41, 659–669. doi:10.1002/jrs.2500

Zhao, J., Lui, H., Mclean, D. I., and Zeng, H. (2007). Automated autofluorescence background subtraction algorithm for biomedical Raman spectroscopy. *Appl. Spectrosc.* 61, 1225–1232. doi:10.1366/000370207782597003

Zhuang, Z., Li, N., Guo, Z., Zhu, M., Xiong, K., and Chen, S. (2013). Study of molecule variations in renal tumor based on confocal micro-Raman spectroscopy. *J. Biomed. Opt.* 18, 31103. doi:10.1117/1.JBO.18.3.031103

Conflict of Interest: The authors declare that the research was conducted in the absence of any commercial or financial relationships that could be construed as a potential conflict of interest.

frontiers in Physics

REVIEW
published: 15 April 2021
doi: 10.3389/fphy.2021.641341

High-Resolution Optical Imaging and Sensing Using Quantum Emitters in Hexagonal Boron-Nitride

Carlo Bradac *

Department of Physics and Astronomy, Trent University, Peterborough, ON, Canada

Super-resolution microscopy has allowed optical imaging to reach resolutions well beyond the limit imposed by the diffraction of light. The advancement of super-resolution techniques is often an application-driven endeavor. However, progress in material science plays a central role too, as it allows for the synthesis and engineering of nanomaterials with the unique chemical and physical properties required to realize super-resolution imaging strategies. This aspect is the focus of this review. We show that quantum emitters in two-dimensional hexagonal boron nitride are proving to be excellent candidate systems for the realization of advanced high-resolution imaging techniques, and spin-based quantum sensing applications.

Keywords: hexagonal boron-nitride, quantum emitters, super-resolution microscopy, quantum sensing, van der waals materials

OPEN ACCESS

Edited by:
Qiuqiang Zhan,
South China Normal University, China

Reviewed by:
Chaohao Chen,
University of Technology Sydney, Australia
Nirmal Mazumder,
Manipal Academy of Higher Education, India
Yan-Kai Tzeng,
Stanford University, United States

***Correspondence:**
Carlo Bradac
carlobradac@trentu.ca

Specialty section:
This article was submitted to Optics and Photonics, a section of the journal Frontiers in Physics

Received: *16 December 2020*
Accepted: *19 February 2021*
Published: *15 April 2021*

Citation:
Bradac C (2021) High-Resolution Optical Imaging and Sensing Using Quantum Emitters in Hexagonal Boron-Nitride. Front. Phys. 9:641341. doi: 10.3389/fphy.2021.641341

INTRODUCTION

Super-Resolution Microscopy

Super-resolution microscopy (SRM) has expanded optical imaging to resolutions well beyond the diffraction limit of light. While traditional microscopy techniques can resolve lateral spot sizes ~200–300 nm (and ~500–700 nm, axially), super-resolution fluorescence microscopy can achieve resolutions of the order of ~20–50 nm, and in some cases <10 nm [1–3]. The key of SRM is to render the fluorophores within the same diffraction region transiently discernible from one another for a short period of time. This is achieved through several strategies (briefly summarized below) that exploit the specific optical properties of photoluminescent materials, such as the non-linearity or stochastic nature of their emission.

Resolft

In reversible saturable/switchable optical linear fluorescence transitions (RESOLFT) microscopy, the super-resolved detection of individual emitters is achieved through non-linear optical excitation and emission schemes. RESOLFT microscopy generalizes the principles of techniques such as stimulated emission depletion (STED) and ground state depletion (GSD) microscopy [4, 5]. These usually involve point-scanning strategies where the laser excitation and photoluminescence collection are designed ad hoc. A standard approach is to co-excite the sample with a torus-shaped beam overlapped to a confocal one to selectively induce "off" and "on" states in the fluorophores, and separate them in time/space as the beam is scanned across the sample. RESOLFT approaches can routinely achieve lateral resolutions of ~40–80 nm.

Structured Illumination

In structured illumination microscopy (SIM) the sample is illuminated by high spatial-frequency patterns with a specific profile e.g., parallel lines [6]. Fluorophores are resolved beyond the diffraction limit as their emission combined with the patterned illumination generates large and detectable interference patterns. The incident pattern is applied in different orientations, and the super-resolution image is mathematically deconvolved from the interference signal. SIM methods can reach lateral and axial resolutions of ~125 nm and 350 nm, respectively. Higher lateral resolutions of ~50 nm can be achieved combining SIM with RESOLFT strategies, as for the case of nonlinear SIM [7] and instant SIM [8].

Stochastic Methods

Rather than through point-scanning or structured excitation, single-molecule localization microscopy (SMLM) achieves sub-diffraction resolution via wide-field illumination. The emission of the fluorophores is photo-controlled as these are switched "on" and "off" by the laser. This is the case, for instance, for stochastic optical reconstruction microscopy (STORM) [9] and photoactivated localization microscopy (PALM) [10, 11]. Different fluorophores within the (wide-field) excitation area are detected individually as their photo-blinking and/or -bleaching behavior render them optically active and inactive at different (random) times. Stochastic, state-switching detection is also the working principle of points accumulation for imaging in nanoscale topography (PAINT) [12]. PAINT exploits single fluorophores becoming optically "bright" as they (reversibly) bind to a target structure, which in turns makes them individually distinguishable from the "dark", unbound ones. Stochastic methods can generally achieve lateral resolutions of ~20–25 nm with advanced setups reaching the ~5 nm limit.

Off-State Microscopy

A particularly powerful SRM approach is minimal photon flux microscopy (MINFLUX) [3, 13]. The method can operate both with scanning beam and standing wave microscopy arrangements. It relies on detecting the position of single fluorophores at the deep intensity minimum of e.g., a torus-shaped excitation spot, as this is sequentially moved in space. The location of the emitter is inferred using a statistical maximum likelihood strategy that estimates the exact position based on where the fluorescence intensity is ~zero (i.e., where the emitter is minimally excited at the center of the torus beam). MINFLUX microscopy can achieve lateral resolutions of ~1–3 nm. Variants of MINFLUX include multiple off-state transitions for nanoscopy [14] and MINFIELD [15], which are designed to improve resolution, signal contrast and/or temporal sampling while reducing the light dose to the sample.

The Role of Material Science in SRM

Super resolution microscopy is an active field of research whose steady objective is to both develop new SRM approaches and design strategies to improve existing ones. Notably, this is not a mere application-driven endeavor. On one hand super-resolution microscopy has certainly being advanced as an indispensable characterization tool; for example in biology for monitoring cellular and subcellular processes [1], or in material science for studying complex materials [16]. On the other hand however, SRM has certainly been advanced by the progress made in material science and in the synthesis of nanomaterials with the unique chemical and physical properties required to realize super-resolution imaging strategies. This second aspect is the focus of this review. The goal is to present and discuss recent developments in high resolution imaging and sensing applications based on a specific two-dimensional material: hexagonal boron-nitride (hBN). We show that this material possesses distinctive physical and spin-optical properties that make it a desirable system for advanced realizations requiring the measurement of objects and quantities at the nanoscale.

This review is organized as per the following. The first part focuses on the hBN material and its properties. Emphasis is put on those most relevant for high resolution (bio)imaging and (bio) sensing such as the material's optical properties, the synthesis of hBN nanostructures as well as their toxicity, surface chemistry and functionalization. The second part discusses a selection of the most recent fundamental and practical realizations in super-resolution microscopy and spin sensing based on quantum emitters in hBN.

HEXAGONAL BORON-NITRIDE

Hexagonal boron-nitride (hBN) is a two-dimensional (2D) van der Waals (vdW) material. Two-dimensional materials which also include materials of the graphene family, 2D chalcogenides and 2D oxides are rapidly becoming one of the most studied subject in condensed matter physics [17]. Their low dimensionality confers them unique properties. For instance, they can be used to engineer heterostructure and hybrid devices consisting of ordered stacks of atom-thin layers, with designer properties [17, 18]. They are being widely utilized to explore characteristic physical phenomena [17, 19, 20] such as Moiré patterns [21], high-temperature quantum spin Hall effect [22] and interlayer excitons with valley-/spin-contrasting degrees of freedom [23–27]. Besides fundamental studies, vdW heterostructures are also largely investigated for technological realizations e.g., in electronic, opto-electronic and nanophotonic devices such as lasers [28], diodes [29], transistors [30–33], sensors [34, 35], photodetectors [36–38] and amplifiers [39].

Here, we focus specifically on hexagonal boron-nitride and its recent developments as a desirable material for high-resolution imaging and sensing. The material's properties are therefore presented with attention to the main key features required for ideal (bio)probes: 1) bright and photo-stable or controllable fluorescence, 2) small size (<10 nm), 3) non-toxicity, 4) room-temperature operation, water solubility and ability to withstand pH variability, 5) controllable chemistry and high binding-specificity.

Crystalline Structure

Two-dimensional hexagonal boron-nitride is a van der Waals material with a graphite-like crystalline structure where boron

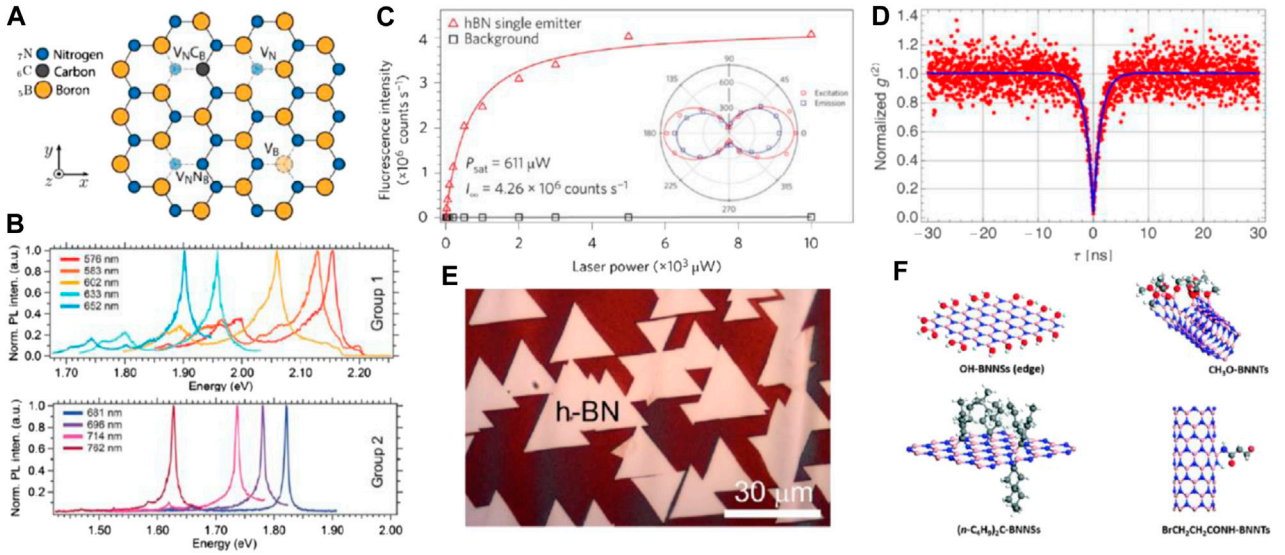

FIGURE 1 | Properties of hexagonal boron-nitride. **(A)** Crystalline structure of hBN and point defects consisting of (complexes of) vacancies and foreign atoms. **(B)** Multicolor photoluminescence from point defects in hBN. **(C)** Photoluminescence saturation curve from a single hBN defect (maximum emission rate 4.26×10^6 counts/s). Inset: excitation (red, circles) and emission (blue, squares) polarization curves from a single hBN defect. **(D)** Second-order autocorrelation measurement $g^{(2)}(\tau = 0) = 0.033\,(47)$ of a single hBN defect, indicating the quantum (single-photon emission) nature of the emitter (conventionally attributed for $g^{(2)}(0) < 0.5$). **(E)** Optical image of hBN grown for 10 min on copper foil by atmospheric pressure chemical vapor deposition (APCVD). **(F)** Schematics of a selection of functionalized boron-nitride nanosheets and nanotubes. Figures adapted and reprinted with permission: **(A)** [53] Copyright American Chemical Society 2018; **(B)** [54] Copyright American Chemical Society 2016; **(C)** [52] Copyright Springer Nature 2015; **(D)** [60] Copyright American Chemical Society 2018; **(E)** [140] Copyright WILEY-VCH Verlag GmbH & Co. KGaA, Weinheim 2019; **(F)** [111] Royal Society of Chemistry 2016.

and nitrogen atoms are organized in atom-thin layers stacked over one another (**Figure 1A**). Within each layer, B and N atoms are bound in a honeycomb hexagonal lattice (lattice constant 2.504 Å). The B–N bonds are *sp* [2]-hybridized, partially covalent and partially ionic, with the electron pairs more confined to the N atoms due to their high electronegativity.

The different atomic layers are instead connected (layer spacing 3.30–3.33 Å) mainly via weaker van der Waals forces [40]. This structure makes hBN a versatile material that can be produced using different methods and in a variety of nanostructures. The material has a large energy bandgap of ~5–6 eV [41], which is the basis of some of its optical properties (Note that values of the bandgap have been reported in the wider range 3.6–7.1 eV [42], with the variability depending on hBN being mono- or multi-layered and on the stacking arrangement of its layers [43, 44]).

Optical Properties

Hexagonal boron-nitride exhibits optical properties which are the foundations of several photoluminescence-based imaging and sensing applications. Being a wide-bandgap material, pristine hBN is nominally transparent in the visible spectral range (~390–700 nm). It displays absorption and emission in the deep ultraviolet (~210–220 nm) due to generation and recombination of free (~215 nm) and bound excitons (~227 nm) [45, 46].

However, hBN generally hosts various type of crystalline defects: dislocations, grain boundaries, edges, vacancies and interstitial atoms [47–53]. Amongst these, atom-like defects consisting of complexes of vacancies and/or foreign atoms are of particular interest, as they give rise to characteristic photoluminescence emission in the visible and near infrared spectral range (**Figures 1A,B**) [54, 55].

Besides a few exceptions [56–58], the exact chemical composition and structure of these defects are still unknown. Yet, these so-called color centers are widely utilized in both fundamental and practical realizations as they display properties that are ideal for photoluminescence-based applications (**Figures 1A–D**). These include bright, polarized [52], multi-wavelength [54], single-photon (quantum) emission [52], as well as chemical stability [59], high photon purity [58, 60, 61], large stark-shift wavelength tuning [62, 63], non-linear photo-physics compatible to super-resolution imaging [64, 65], and addressable spin-dependent photo-emission [56].

Note also that due to the 2D nature of the host hBN material, the photon extraction efficiency from these atom-like emitters is comparatively high (~10^6 counts/s at saturation)—as phenomena like Fresnel and total internal reflection, scattering and re-absorption are negligible [60]. This is ideal for photoluminescence-based applications as high collection efficiencies translate into high signal-to-noise ratio and thus better signal and/or temporal resolution.

Synthesis and Nanostructures

One of the key factors for practical high-resolution imaging and sensing applications is the ability to readily fabricate fluorescent nanoprobes. In this regard, hBN is an extremely versatile material as there are several methods available to synthesize 2D BN

nanostructures, either via bottom-up or top-down methods. Bottom-up techniques include synthesis by chemical vapor deposition (**Figure 1E**) [66–68], segregation [69] and by solid-state [70] or substitution reaction [71]. Top-down approaches include mechanical [72–75] or chemical exfoliation [76–79], as well as high-energy electron irradiation [80, 81].

Boron-nitride nanomaterials (BNNs) include zero-dimensional (0D) fullerenes and nanoparticles, one-dimensional (1D) nanotubes and nanoribbons, two-dimensional (2D) nanosheets and three-dimensional (3D) nanoporous BN. There are extensive reviews dedicated to the fabrication of BNNs [82, 83], here we briefly summarize the methods developed to fabricate fluorescent nanoparticle-like (0D) objects, which are used in some of the SRM applications described below. Common nanofabrication approaches include the breaking down of large hBN microscopic crystals into nanosized hBN particles e.g., via ball-milling [84] or acoustic cavitation [85, 86]. These methods can usually achieve high yields of hBN nanoparticles, but their size is relatively large (~tens or ~ hundreds of nm), especially for applications in bio-imaging and nanoscale sensing. Recently however, high yields of hBN nanoparticles less than 10 nm in size have been achieved via cryogenic-induced cracking of hBN [87, 88] and by hydrothermal synthesis [89]. It should be noted that at this size the photostability of the emitters can be compromised—giving rise to photo-blinking and -bleaching—due to interaction with surface states and fluctuations in the local electric field. These are associated, for instance, with dangling bonds, other point-defects, or trapped charges, whose effect becomes more prominent as the particle size reduces [90–93]. These effects can partially be reduced with surface passivation strategies [94–97], but must be taken into account for assessing the reliability of the probes. In some cases however, they are central to achieve super-resolution imaging and are therefore a desirable feature.

Non-toxicity

Boron-nitride is considered a suitable material for biological and medical applications. Boron-nitride nanomaterials (BNNs) possess good biocompatibility [98–101] and high chemical and mechanical stability [102, 103]. BNNs have been found not to inhibit cell growth or induce apostosis [104, 105] and they have been shown to be up-taken by cells [99, 106, 107]. In fact, they have been used in practical realizations including as drug and gene carriers [108] and in cancer treatment studies [109]. For completeness, it should be noted that time-, dose- and cell-dependent cytotoxicity of BNNs has been reported in a small number of studies [108, 110].

Functionalization

The chemical functionalization of boron-nitride nanomaterials (BNNs) is challenging as, in general, the network of B and N atom connected by *sp* [2]-hybridized bonds is highly stable and chemically inert. Nevertheless, several functionalization strategies have been proposed and realized, albeit with low overall yields (**Figure 1F**) [111]. Note that both N and B can be utilized for functionalization whenever they are at an edge or at a lattice defect, where they give rise to dangling bonds. Conversely, reactions on the basal plane require opening of the B–N bonds. Both B and N must be terminated either by multiple functional groups (to balance the overall charge) or via a bridging bond. The B–N bond is partly covalent and partly ionic, which makes the nitrogen and boron atoms partially negatively and positively charged, respectively, due to their different electronegativity. As a result, B tends to bind to nucleophile (electron-donating) groups while N to electrophile (electron-accepting) ones. The list of functional groups successfully conjugated to BN nanomaterials include hydroxyl (–OH), amino ($–NH_2$), ether (–OR), amine (–NHR), arcyl (–COR), alkyl (–R), and halogen (–X) groups. The relevant functionalization methods can be found in dedicated reviews [111–114] and are summarized here, briefly.

Hydroxyl groups. Hydroxyl groups (–OH) are amongst the most fundamental functionalization groups for BNNs both for direct applications (matrix filling and bio-applications) and as base for more complex conjugations. The functionalization of BNNs—in particular BN nanotubes and nanosheets—with–OH groups is generally achieved via covalent bonding to B sites and has been realized through a series of alternative approaches including plasma treatment, hydrothermal reactions with NaOH, NaOH-assisted ball-milling, and reactions with H_2O at a high temperature, or using reagents that can generate OH radicals [115–121].

Amino and amine groups. Analogously to hydroxyl (–OH) group, the electrophilic B centers can be functionalized with amino ($–NH_2$) and amine (–NHR) groups. This can be achieved for instance by plasma treatment, etched-assisted sonication and urea-assisted ball-milling [122–125].

Alkoxy groups. Alkoxy groups consisting of an alkyl group (carbon and hydrogen chain) bonded to an oxygen atom (–OR) can be functionalized directly onto BN surfaces e.g., by sonication in primary alcohols solvents [126]. Note that the–OR termination is advantageous for applications that require (alcoholysized) BN nanostructures to be readily dispersed in alcohol solvents.

Alkyl groups. Alkyl (–R) groups can attach to BN by forming B–C–N bridges or directly on B or N sites. This has been realized e.g., by carbene-assisted substitution and by reaction with a reductant solution and hexyl-containing compounds [127, 128].

Other groups. A whole suite of other groups has been successfully conjugated to BNNs. For instance, esterified (–OCOR), amidated (–NHCOR) and acylated (–COR) groups have been attached to BN nanostructures directly from their BN precursors or via their hydroxylated (OH-BN) and aminated (NH_2-BN) intermediates [116, 118, 124, 129–132]. Functionalization with hydrogen and fluorine, as well as other groups ($–CH_3$, –CHO, –CN, –OH, $–NH_2$, etc.), has been also largely investigated as these species can significantly affect the material properties such as the BNNs stability, bandgap energy and electronic properties [133–135].

It is important to note that the ability to readily functionalize BN nanostructures—e.g., for stability in physiological environments and for target-specific labelling of subcellular structures—is only one of the aspects that must be considered

TABLE 1 | Super-resolution imaging techniques based on hBN emitters.

System	Method	Mechanism	Resolution
SPEs in hBN flakes 64	RESOLFT, off-state microscopy	Non-linear excitation of SPEs with repumping from metastable state(s)	(63 ± 4) nm
SPEs (V_B) in hBN monolayers 141	SMLM	Stochastic on/off photo-blinking between charge states ($V_B^0 \leftrightarrow V_B^-$)	10.7 nm
SPEs in hBN nanoparticles (≥3 nm) 87	SMLM	Stochastic on/off photo-blinking	<10 nm
SPEs in monolayer/bulk hBN 65	SMLM	Stochastic on/off photo-blinking combined with spectral analysis	~10 nm
SPEs (V_B^-) in multilayer hBN 142	SMLM	Stochastic on/off photo-blinking due to protonation of SPEs ($V_B^- + H^+ \rightarrow V_BH$)	~5–40 nm

for super-resolution imaging and sensing. Another critical factor to take into account is determining whether the presence of functionalized groups on the surface of the BN nanostructures alters their optical properties, possibly hindering their suitability as super-resolution probes. When nanostructures are smaller than a few nanometers, surface effects become relevant and the fluorescence of the hosted emitter can undergo intensity fluctuations, spectral diffusion, photoluminescence intermittency ("blinking") or even cease all together. These effects are not unique to hBN but rather universal and are due to the presence of surface states (e.g., dangling bonds, point-defects, trapped charges and conjugated chemical species) which can drive the emitter in different charge states or generate random electric fields that destabilize the optical dipole moments of the emitters via spontaneous Stark shifts [93, 136, 137].

There are two main considerations to make in this regard. Firstly, these effects can be mitigated via specific surface passivation of the hBN nanoprobes. Suitable approaches are already available e.g., sol-gel coating via Stober reaction [138, 139]. Besides, establishing whether certain functionalization groups deteriorate the optical properties of the BN nanoprobes is both feasible and experimentally testable. Secondly, in some cases the photo-instability of the probes is a desirable—in fact, necessary—feature. It allows for super-resolution imaging schemes based on the stochastic intermittency of individual, and otherwise unresolvable, emitters between "on" and "off" states, over time.

SUPER-RESOLUTION IMAGING WITH HBN

Standard, diffraction-limited microscopy using hexagonal boron-nitride nanomaterials (BNNs) is well established. Yet, super-resolution imaging has been realized only recently, thanks to the discovery and control of specific optical properties associated with quantum emitters in hBN (**Table 1**) [64, 141].

Resolft

One of the first demonstration of super-resolution imaging in hBN was realized in 2018 [64]. The technique utilizes the non-linear behavior of a specific class of hBN single-photon emitters (SPEs). The exact nature and chemical structure of these hBN emitters is unknown—the emission is likely due to transition between energy states in the hBN bandgap associated to atom-like defects in the lattice. Regardless, the non-linear behavior is observed consistently for an entire family of them with zero-phonon line (ZPL) emission wavelengths >700 nm.

Upon excitation with a laser (at 675 nm or 708 nm in the study), the emitters produce a photoluminescence signal with a sharp ZPL (e.g., 785 nm). When co-excited with a second low-power (~30× less) laser at a shorter wavelength (532 nm), the emitters show a highly non-linear behavior characterized by an increase in photoluminescence (~2×) and lowering (~5×) of their saturation intensity. This non-linear behavior is attributed to the 532 nm laser repumping the system from a metastable "dark" state back to the excited "bright" state. The existence of photo-switchable dark/bright emission states is one of the main requirements for RESOLFT super-resolution microscopy. This unique photo-physical behavior can thus be harnessed to realize a variant of saturable, far-field, sub-diffraction fluorescence nanoscopy, which is what was done in the study.

The technique has two notable advantages. Hexagonal boron-nitride emitters are extremely robust against high-power illumination [143]. Whilst this is not a requirement for RESOLFT SRM, it is a desirable feature. For instance, both in STED and GSD the transition from the "bright" to the "dark" state is achieved by optical saturation—via stimulated emission depletion and ground-state depletion, respectively. This usually requires high excitation powers, which can lead to photo-bleaching of the emitters—a problem that has led to the development of off-state transitions nanoscopy methods. In addition, the issue of requiring high laser excitations for inducing saturation is further alleviated with this approach, as the second repumping laser effectively reduces the saturation intensity of the emitters. This is shown in the study where a negative-GSD-like scheme is utilized to assess the resolution of the technique (**Figure 2A**).

In the first experiment, a single torus beam (708 nm) is used as the excitation source. As the beam is scanned, the emitter is excited by a high–null–high intensity profile and produces a corresponding high–null–high emission pattern. In the confocal image, the emitter's location thus coincides with the center of the emission null (like in standard off-state transitions nanoscopy) and is readily extracted via mathematical deconvolution of the inverse image (**Figure 2A**, right). Sub-diffraction resolution is achieved as at higher excitation powers of the scanning torus beam, the high–null and null–high photoluminescence emission gradients become steeper. This effectively narrows the full width at half-maximum (FWHM) of the emission null according to the relation:

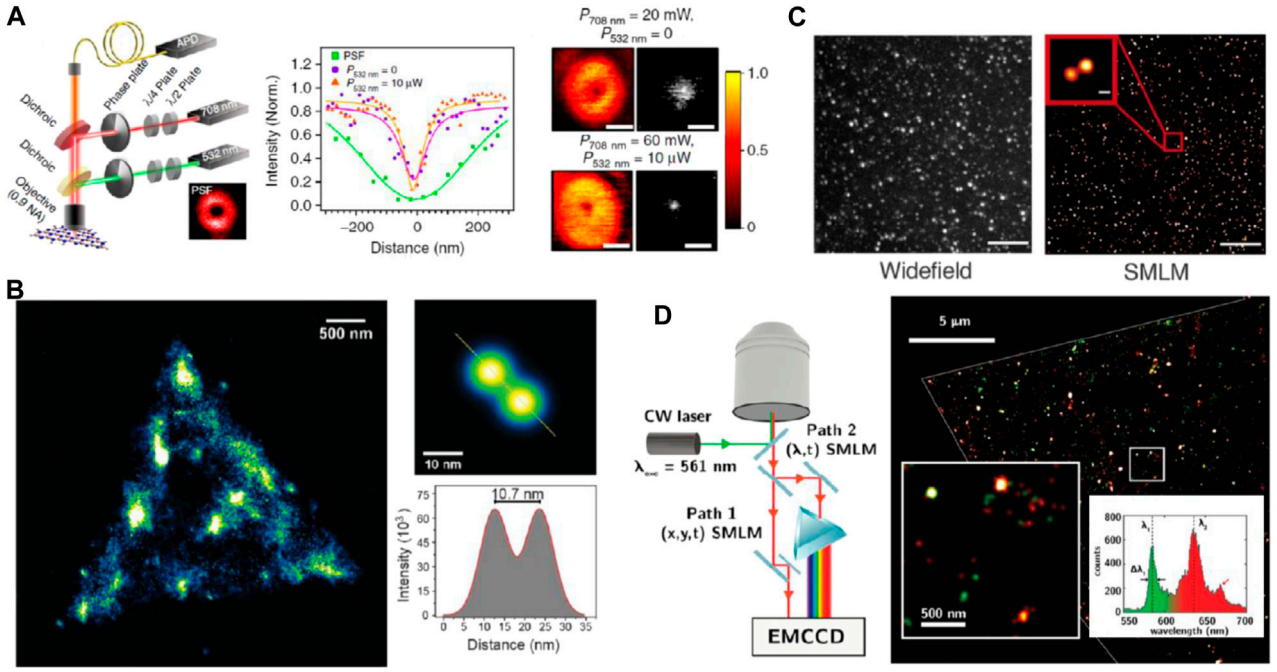

FIGURE 2 | RESOLFT and SMLM microscopy in hBN. **(A)** Super-resolution microscopy using dual torus-beam excitation. Left: schematics of the experiment. Center: point spread function of the confocal system (green), and resolutions obtained under 708 nm torus-beam laser excitation only (violet) and adding a second 532 nm torus-beam (orange). Right: the resolution increases upon increasing the intensity of both the 708 nm and the 532 nm lasers. **(B)** SMLM imaging of optically active defects in hBN reconstructed from an image sequence of 20,000 frames, display pixel size: 1 nm. With drift correction using fiducial markers, the method achieves a resolution of 10.7 nm **(C)** Widefield and SMLM reconstructed image (based on 6,000 frames) of an ensemble of hBN nanoparticles (average size (3.0 ± 0.7) nm), synthesized by cryo-exfoliation (scale bar: 5 µm). Inset: zoomed-in section showing two emitters in the super-resolved image (scale bar: 100 nm). **(D)** Multimodal SMLM. Left: schematics of the experiment showing dual spatial and spectral detection. Right: Spatial and spectral distribution of centers in a CVD-grown hBN flake. A dual spectral distribution is visible corresponding to green and red emitters with emission wavelength λ_1 and λ_2 (right inset). Figures adapted and reprinted with permission: **(A)** [64] Copyright Springer Nature 2018; **(B)** [141] Copyright American Chemical society 2018; **(C)** [87] Copyright American Chemical society 2019; **(D)** [65] Copyright American Chemical society 2019.

$$\Delta r \cong \lambda\left(\beta\pi n\right)^{-1}\sqrt{\varepsilon + \frac{I_s}{I_m}} \tag{1}$$

where Δr is the resolution; I_m is the maximum laser intensity in the periphery of the torus, and εI_m is the minimum (null) intensity in the center. The quantity I_s is the saturation intensity, while λ and n are the wavelength and the refractive index, respectively. The parameter β is the steepness of the point spread function which depends on the emitter's properties and on the periphery-to-minimum intensity gradient of the toroidal excitation beam.

Equation 1 shows that the resolution Δr improves (Δr becomes smaller) when the ratio I_s/I_m is minimized. Generally, in other RESOLFT approaches, this is done by increasing the excitation laser intensity I_m well above I_s. This method, however, also allows to directly reduce I_s via the re-pumping mechanism. This was demonstrated in a subsequent experiment of the study (**Figure 2A**, left and center panel), where a second torus beam (532 nm laser) was superimposed to the first one (708 nm laser). The addition of the 532 nm toroidal beam effectively reduces I_s minimizing the ratio I_s/I_m, for any given intensity I_m of the excitation torus at 708 nm. The highest resolution achieved using just the 708 nm excitation torus was (87 ± 10) nm, slightly worse than (63 ± 4) nm obtained with the two 708 nm and 532 nm torus beams overlapped. Both resolutions are far better than the ~460 nm value of the confocal setup used in the study.

As a final point, it should be noted that this variant of SRM developed using hBN emitters could be extended to other classes of fluorophores, provided that they possess an analogous behavior characterized by the ability of the system to be re-pumped from the ("dark") metastable state to the excited ("bright") state.

Single-Molecule Localization Microscopy (SMLM)

Simultaneously to the approach described in §3.1, SRM was also realized in hBN monolayers using single-molecule localization microscopy [141]. The method exploits the on/off photo-switching behavior (blinking) of hBN emitters, which allows for their temporal—and thus spatial—separation, by capturing them when they are "bright/dark" alternately, one at a time (**Figure 2B**).

Note that the photo-stability of hBN emitters depends on their local environment as, e.g., electric field fluctuations and nearby trap states can induce phenomena such as spectral diffusion and

blinking [144, 145]. In the case of hBN, photo-blinking is often more prominent for small (<10 nm) and thin (~monolayer) nanoparticles/nanoflakes as the proximity to the surface increases the probability of local perturbations.

In the study, the sample consisted of a hBN monolayer. The material shows optically active emitters which are attributed to boron monovacancies V_B (i.e., a missing B atom in the hBN lattice)—as deduced form transition electron microscopy (TEM) analysis. The blinking behavior of the emitters is attributed to photo-induced ionization and recombination between the neutral V_B^0 and negatively charged V_B^- states. For SMLM to work, the sample must be spatially fixed with no drift over time. This can be achieved either through the use of a closed-loop feedback-controlled stage or, like in this study, through post processing alignment using fiducial markers. The spatial resolution achieved in the study is 10.7 nm (**Figure 2B**, right panels).

The approach has a few desirable features. It utilizes wide-field illumination and detection of large sample areas (~up to tens of μm) with fast acquisition (~ms) and minimum damage to the sample thanks to the low power density (~100 kW/m^2) of the excitation laser, compared to e.g., STED microscopy. It also allows for probing the chemical reactivity of the emitters. In the study this was done by submerging the sample in solutions of different pH and monitoring differences in fluorescence behavior. To this end, the technique was combined with balanced super-resolution optical fluctuation imaging (bSOFI) [146], which utilizes higher-order statistics to increase resolution and image contrast—provided that the emitters display uncorrelated, stochastic fluctuations.

Almost at the same time, this SMLM technique developed for monolayer hBN was successfully implemented to investigate the optical properties of hBN nanoparticles as small as (3.0 ± 0.7) nm, produced by cryogenic exfoliation (**Figure 2C**) [87]. The merit of the work was to demonstrate that hBN nanoparticles/nanoflakes possess a combination of optical and size properties that make them desirable for (bio-)imaging and sensing applications, either via SMLM or RESOLFT microscopy.

In a follow-up study [65], this SMLM technique was further improved to include the ability to perform spectral analysis of the emitters and thus producing super-resolved images containing spatial, spectral and temporal dynamics of the emitters (**Figure 2D**). This was achieved by utilizing a calcium fluoride (CaF_2) filter in one of the detection paths (**Figure 2D**, left). This dispersive element allowed for the simultaneous correlation of spatial and spectral mapping of each emitter—showcased in the study by clearly distinguishing two families of hBN emitters one displaying photoluminescence at ~585 nm and the other at ~640 nm (**Figure 2D**, right panel).

A key feature of this multimodal SMLM method is the ability to correlate different characteristics and properties of the fluorophores, in time. For instance, the study shows the possibility to extract differences in blinking photo-kinetics for the two families of emitters and understand their physical origin (e.g., charge separation or ionization of the defects, as these follow different dynamics).

The versatility of this single-molecule localization microscopy technique was recently highlighted in a remarkable experiment that succeeded in imaging proton transfer phenomena in water, at an interface with single-charge resolution (**Figures 3A**,**B**) [142].

The basic SMLM scheme is analogous to the ones described above. Multilayer hBN flakes were irradiated in low-power oxygen plasma to create a high density of surface defects. These defects are hypothesized to be V_B^- and show a considerably different fluorescence behavior when exposed to air or submerged in aqueous solutions of different pH. Monitoring the photoluminescence at ~2 eV (~620 nm) reveals that only a few emitters are luminescent in air (~0.3 per 2 × 2 μm^2 area), while many more are when the sample is submerged in slightly acidic solutions (~70 per 2 × 2 μm^2 area, in a 3.4 pH solution). The proposed explanation is that the V_B^- defects are optically dark but become active (emitting photons at ~ 2 eV) as solvated protons H^+ compensate their charge through the reaction $V_B^- + H^+ \rightarrow V_BH$. The SMLM technique thus allows monitoring—with high resolution, and over time—the occurrence of this protonation reaction in solution, at each one of the hBN defect sites.

Notably, SMLM can capture the specific hopping of protons between adjacent sites as these sites undergo "dark/bright" switching events corresponding to their V_B^-/V_BH states. In the study, trajectories of single protons moving from site to site over distances up to ~1 μm (imaging resolution ~5–40 nm) were monitored over time (~180 s). Different behaviors were observed, and it was possible to extract parameters such as diffusion coefficients and mean square displacement of the moving protons (**Figure 3B**). The study was able to clearly show—at the single-molecule scale—the mechanism of desorption-limited transport of protons occurring in water at a solid/water interface between adjacent surface defects. It also underscores how the interface provides a preferential pathway for charge migration, which is relevant for several fields ranging from cellular transport and signaling, to catalysis and membrane dynamics. The study is a remarkable demonstration of the interfacial transport of protons in relation to the surrounding bulk water—a mechanism which, up to now, has been beyond reach due to the inability to measure directly the motion of single protons in water, with high-enough resolution.

Nonlinear Optical Microscopy

In the context of high-resolution imaging, nonlinear optical microscopy deserves a special mention as it has become a powerful tool not just for imaging but also for (2D) material characterization [147, 148]. Nonlinear microscopy relies on multi-photon excitation of the fluorophores via virtual states, which produces a set of inherent benefits compared to traditional single-photon excitation [149, 150]. These include better fluorophores-to-background contrast due to lower background autofluorescence [151], excitation through a favorable biological window (NIR wavelengths, 650–900 nm, characterized by lower absorption from hemoglobin and water) [152], as well as improved imaging resolution [153, 154].

Nonlinear optical excitation of single-photon emitters (SPEs) in hexagonal boron nitride has been demonstrated [143]. In the

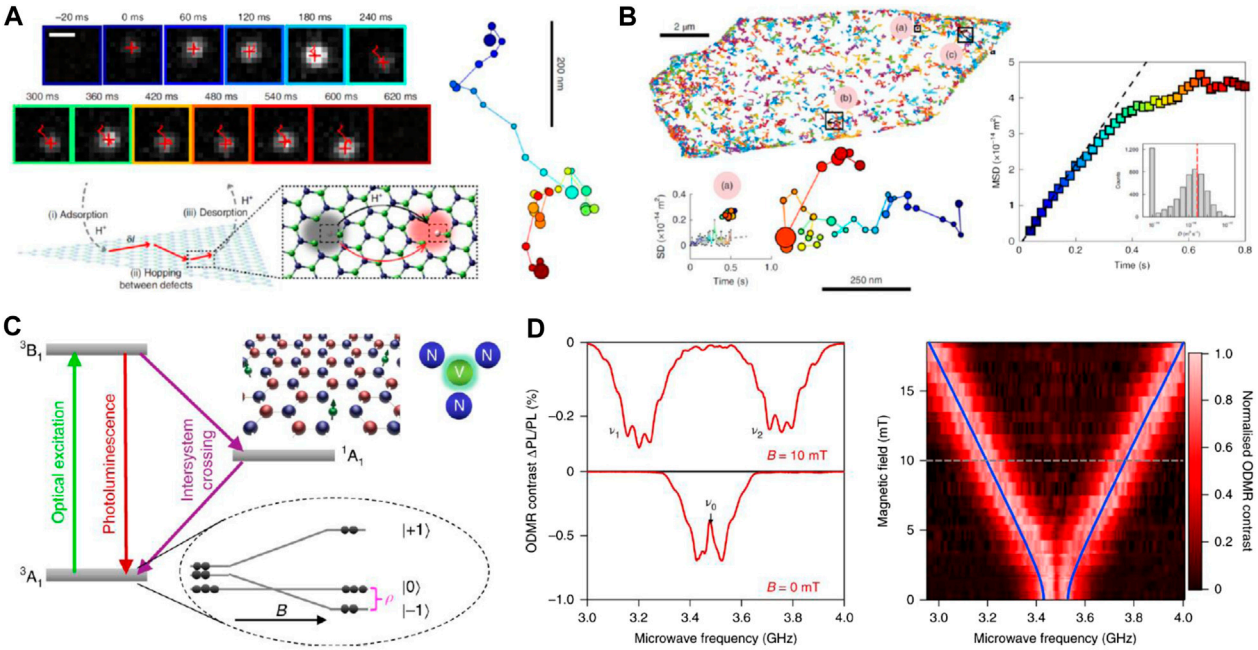

FIGURE 3 | Proton transport and quantum sensing in hBN. **(A)** Top left: time series for spatial migration of luminescence at the surface of the hBN flake, detected with wide-field SMLM (scale bar 500 nm; projected pixel size 100 nm). Right: Reconstructed trajectories showing successive activation of adjacent defects at the surface of the flake and color-coded with increasing time. Localized defects are represented as dots, with the radius corresponding to the localization uncertainty. Bottom left: schematic depicting luminescence migration events, consisting of successive proton adsorption, diffusion and proton desorption from the surface. **(B)** Top left: large-scale mapping of proton trajectories (200 ms) measured at the surface of the hBN flake. Bottom left: representative proton trajectory with the corresponding evolution of the square displacement (SD). Right: variation of the mean square displacement (MSD) as a function of time for the hBN flake. The dashed line is a linear fit from which the averaged diffusion coefficient is extracted $D = 2.8 \times 10^{-14}$ m^2 s^{-1}. Inset: distribution of the diffusion coefficient determined on individual trajectories, with the vertical dashed line being the average value. **(C)** Energy level scheme and atomic structure of the hBN V_B^- center; note the triplet ground state of multiplicity $m_s = 0$ and $m_s = \pm 1$, with a magnetic field B lifting the $m_s = \pm 1$ degeneracy. **(D)** Optically detected magnetic resonance (ODMR) showing manipulation and read out of the spin state. The transitions $m_s = 0 \rightarrow +1$ and $m_s = 0 \rightarrow -1$ are shown by a drop in photoluminescence (ODMR contrast $\Delta PL/PL$) at the corresponding microwave resonant frequency. The dependence of the relative position between $m_s = 0$ and $m_s = \pm 1$ is the basis of quantum sensing applications based on reading out the spin state of the V_B^- center. Figures adapted and reprinted with permission **(A,B)** [142] Copyright Springer Nature 2020 **(C,D)** [56] Copyright Springer Nature 2020.

study, individual atom-like defects with emission wavelength at 670 nm are excited either with a continuous laser at 532 nm or with a pulsed laser at 708 nm (pulses' duration 1 ps). The dependence of the SPEs' photon emission rate as a function of the excitation intensity reveals that excitation with the 708 nm pulsed laser takes place via a two-photon absorption process. In the experiment, large hBN flakes (size ~200 nm) were used, but the technique can be readily extended to smaller hBN nanoparticles (size <10 nm). The results thus demonstrate the possibility of employing nonlinear microscopy of fluorescent hBN nanoprobes as a feasible high-resolution imaging strategy, complementary to super-resolution microscopy.

BEYOND OPTICAL IMAGING

Beyond SRM, hexagonal boron-nitride is showing promise as the hardware material for another class of high-resolution sensing applications at the nanoscale. These are based on monitoring the spin state of individual hBN quantum emitters in response to changes in the surrounding environment. In general, optically active quantum defects can be separated in two categories: single-photon emitters whose photoluminescence corresponds to transitions between well-defined quantum states, and so-called "spin centers" which exhibit coupling between the defects' intrinsic spin and their optical transitions. In other words, spin-centers display photoluminescence which is different depending on which spin state the emitter emits from. An archetype spin-center is the well-known nitrogen-vacancy (NV^-) center in diamond [155].

Spin-centers are sought after as potential qubits for solid-state, room-temperature quantum computation and information technologies [156], but also as ultra-sensitive nanoscale sensors [157]—which is of interest here. This is because their spin state can be manipulated and read out optically, while displaying extreme sensitivity to the local, surrounding environment.

The discovery of spin-centers in hBN is recent [56, 58], with the first identified one being the boron-vacancy center, V_B^-. The defect possesses distinguishable spin-optical transitions (**Figure 3C**). Specifically, the V_B^- has a triplet ($S = 1$) ground state of multiplicity $m_s = 0$ and $m_s = \pm 1$, separated by a zero-field splitting (ZFS) energy $D_{gs} \cong 3.46$ GHz, in Planck's constant units h (Note that, for completeness, the degeneracy

of the $m_s = \pm 1$ states is lifted due to the small off-axial component of the ZFS, $E_{gs} \cong 50$ MHz).

Optical excitation and cycling through the excited state of the defect 'spin-polarize' it in the $m_s = 0$ state, by preferentially populating it (**Figure 3C**). Applying a microwave field resonant with the transitions $m_s = 0 \leftrightarrow \pm 1$ allows manipulating the defect's spin state, which can then be read out, optically—as the excitation-decay cycle from the $m_s = 0$ ground state scatters more photons than the one from the $m_s = \pm 1$ one. These features are the basis of optically detected magnetic resonance (ODMR) in which the spin state of individual point-like defects can be prepared, manipulated, and read out optically at room temperature (**Figure 3D**).

This is relevant for high resolution, quantum sensing applications as the ground state ZFS splitting (D_{gs}, E_{gs}) can vary in response to external stimuli such as e.g., magnetic and electric fields, local chemistry or temperature. These quantities can therefore be measured directly using the V_B^- defect in hBN as nanoprobes, simply by measuring changes in photoluminescence.

Spin defects in three-dimensional materials, such as diamond (e.g., nitrogen vacancy and silicon vacancy centers) [155, 158], silicon carbide (e.g., di-vacancy centers) [159, 160] and rare earth materials (e.g., Yb ions in yttrium orthovanadate hosts) [161, 162] have been extensively used for quantum sensing realizations. Examples include single-spin detection and magnetometry [163, 164], electrometry [165], decoherence microscopy [166], thermometry [167], optical trapping [168] and Forster resonance energy transfer [169, 170]. These exceptional demonstrations raise the question of how hBN V_B^- centers benchmark in this context, especially since—currently—all the realizations involving hBN V_B^- centers have been fundamental rather than practical.

There are several aspects that make spin-defects in hBN particularly attractive for quantum sensing applications. Unlike 3D semiconductor hosts, layered hBN are less prone to having unsaturated dangling bonds. These can act as fluctuating electron spins that generate magnetic noise and degrade the spin coherence—which is crucial for applications in quantum sensing [171].

The 2D nature of hBN confers it several additional, unique features. It allows for extremely high photon-extraction efficiencies. In fact, the out-coupling efficiency of hBN emitters is near-unity, as they are not surrounded by any high refractive index material and are not affected by Fresnel or total internal reflection, scattering and re-absorption [60]. This is desirable for nanoscale sensing applications based on photoluminescence detection, for it increases the signal-to-noise ratio and, thus, signal and/or temporal resolution.

Furthermore, the weak van der Waals forces between layers allow hBN to be readily transferred and integrated with other (hybrid) nanoscale systems made e.g., of 2D materials heterostructures [17, 172–174]. It also allows for the accurate placement of individual nanoprobe with respect to target areas or objects. This was demonstrated in a study that used a fluorescent hBN nanoparticle as an optical nanothermometer—placed deterministically onto a micro-circuit—to measure local temperature and potential hot spots in target areas of the device [175].

Another feature granted by the 2D nature of hBN is the potential close proximity between the emitter-sensors and the object or quantity to be sensed. This can be ~(sub)nm, which is highly desirable as, for instance in magnetometry, dipolar magnetic fields decay as the third inverse power of the distance between sensor and spin [176], which makes their relative separation a critical limiting factor for the sensitivity of the technique.

It should be noted that the field of spin-based quantum sensing, whilst well established in 3D semiconductors such as diamond, is at its absolute infancy in 2D hBN. The spin-addressable properties of the V_B^- have been discovered only recently [56, 57]. In fact, while it has been shown that V_B^- defects can be engineered in hBN via targeted irradiation, the isolation of individual defects is still beyond reach.

The research is certainly very active in the field. Shortly after the report of the V_B^- center, a second and different type of spin-defect has been identified in hBN [58]. The defect is carbon-related (possibly the negatively charged $V_B C_N^-$). It emits with a sharp zero-phonon line wavelength at ~585 nm and is spin-active ($S \geq 1/2$) with a detectable ODMR spectrum. Again, the defect has not been isolated at a single-center level (ODMR has only been observed in ensemble, currently), but there is optimism as emission at ~585 nm from single centers is common in hBN.

CONCLUSION AND OUTLOOK

Two-dimensional materials have garnered a lot of attention in recent years, mostly because their low dimensionality and relative ease of fabrication have allowed the accomplishment of a whole suite of interesting demonstrations difficult to attain with traditional 3D bulk materials. Amongst 2D materials, hexagonal boron-nitride has become object of intense research since 2015, when quantum (single-photon) emission from atom-like defects has been identified [52]. While hBN color centers have—arguably—been trailing behind their well-established counterparts in e.g., diamond and silicon carbide, they are quickly becoming an active field of research in their own right. Their characteristic optical (and recently discovered) spin properties combined with the unique physico-chemical features granted by the low dimensionality of the hBN host make them ideal systems for several fundamental and practical applications—including in high resolution imaging and sensing.

In this review, we have highlighted the role hBN quantum emitters have recently played in the realization of novel super-resolution imaging techniques (RESOLFT and SMLM), as well as their potential impact in advanced spin-based quantum sensing applications. Research geared towards exploiting hBN and its color centers for sensing and imaging is at its infancy. Future endeavors should focus on fully identifying the origin of the defects (besides the V_B^-) and improving material and color centers engineering to move from fundamental demonstrations to practical realizations. In this regard, experiments such as observing single proton transport at the solid/water interface

by hBN-based super-resolution microscopy are encouraging. They show that the material is offering novel capabilities that allow for the exploration of regimes inaccessible with alternative methods.

AUTHOR CONTRIBUTIONS

The author confirms being the sole contributor of this work and has approved it for publication.

REFERENCES

1. Sahl SJ, Hell SW, and Jakobs S Fluorescence nanoscopy in cell biology. *Nat Rev Mol Cel Biol* (2017) 18:685–701. doi:10.1038/nrm.2017.71
2. Hell SW Far-field optical nanoscopy. *Science* (2007) 316:1153–8. doi:10.1126/science.1137395
3. Balzarotti F, Eilers Y, Gwosch KC, Gynnå AH, Westphal V, Stefani FD, et al. Nanometer resolution imaging and tracking of fluorescent molecules with minimal photon fluxes. *Science* (2017) 355:606–12. doi:10.1126/science.aak9913
4. Vicidomini G, Bianchini P, and Diaspro A STED super-resolved microscopy. *Nat Methods* (2018) 15:173–82. doi:10.1038/nmeth.4593
5. Hell SW, and Kroug M Ground-state-depletion fluorscence microscopy: a concept for breaking the diffraction resolution limit. *Appl Phys B* (1995) 60: 495–7. doi:10.1007/bf01081333
6. Gustafsson MGL Surpassing the lateral resolution limit by a factor of two using structured illumination microscopy. SHORT COMMUNICATION. *J Microsc* (2000) 198:82–7. doi:10.1046/j.1365-2818.2000.00710.x
7. Gustafsson MGL Nonlinear structured-illumination microscopy: wide-field fluorescence imaging with theoretically unlimited resolution. *Proc Natl Acad Sci* (2005) 102:13081–6. doi:10.1073/pnas.0406877102
8. York AG, Chandris P, Nogare DD, Head J, Wawrzusin P, Fischer RS, et al. Instant super-resolution imaging in live cells and embryos via analog image processing. *Nat Methods* (2013) 10:1122–6. doi:10.1038/nmeth.2687
9. Rust MJ, Bates M, and Zhuang X Sub-diffraction-limit imaging by stochastic optical reconstruction microscopy (STORM). *Nat Methods* (2006) 3:793–6. doi:10.1038/nmeth929
10. Betzig E, Patterson GH, Sougrat R, Lindwasser OW, Olenych S, Bonifacino JS, et al. Imaging intracellular fluorescent proteins at nanometer resolution. *Science* (2006) 313:1642–5. doi:10.1126/science.1127344
11. Hess ST, Girirajan TPK, and Mason MD Ultra-high resolution imaging by fluorescence photoactivation localization microscopy. *Biophys J* (2006) 91: 4258–72. doi:10.1529/biophysj.106.091116
12. Sharonov A, and Hochstrasser RM Wide-field subdiffraction imaging by accumulated binding of diffusing probes. *Proc Natl Acad Sci* (2006) 103: 18911–6. doi:10.1073/pnas.0609643104
13. Gwosch KC, Pape JK, Balzarotti F, Hoess P, Ellenberg J, Ries J, et al. MINFLUX nanoscopy delivers 3D multicolor nanometer resolution in cells. *Nat Methods* (2020) 17:217–24. doi:10.1038/s41592-019-0688-0
14. Danzl JG, Sidenstein SC, Gregor C, Urban NT, Ilgen P, Jakobs S, et al. Coordinate-targeted fluorescence nanoscopy with multiple off states. *Nat Photon* (2016) 10:122–8. doi:10.1038/nphoton.2015.266
15. Göttfert F, Pleiner T, Heine J, Westphal V, Görlich D, Sahl SJ, et al. Strong signal increase in STED fluorescence microscopy by imaging regions of subdiffraction extent. *Proc Natl Acad Sci U S A* (2017) 114:2125–30. doi:10.1073/pnas.1621495114
16. Pujals S, Feiner-Gracia N, Delcanale P, Voets I, and Albertazzi L Super-resolution microscopy as a powerful tool to study complex synthetic materials. *Nat Rev Chem* (2019) 3:68–84. doi:10.1038/s41570-018-0070-2
17. Geim AK, and Grigorieva IV Van der Waals heterostructures. *Nature* (2013) 499:419–25. doi:10.1038/nature12385
18. Novoselov KS, Mishchenko A, Carvalho A, and Castro Neto AH 2D materials and van der Waals heterostructures. *Science* (2016) 353:aac9439. doi:10.1126/science.aac9439
19. Mak KF, and Shan J Opportunities and challenges of interlayer exciton control and manipulation. *Nat Nanotech* (2018) 13:974–6. doi:10.1038/s41565-018-0301-1
20. Jin C, Ma EY, Karni O, Regan EC, Wang F, and Heinz TF Ultrafast dynamics in van der Waals heterostructures. *Nat Nanotech* (2018) 13:994–1003. doi:10.1038/s41565-018-0298-5
21. Urbaszek B, and Srivastava A Materials in flatland twist and shine, *Nature* (2019) 567:39–40. doi:10.1038/d41586-019-00704-x
22. Qian X, Liu J, Fu L, and Li J Quantum spin Hall effect in two-dimensional transition metal dichalcogenides. *Science* (2014) 346:1344–7. doi:10.1126/science.1256815
23. Ceballos F, Bellus MZ, Chiu H-Y, and Zhao H Ultrafast charge separation and indirect exciton formation in a MoS2-MoSe2 van der Waals heterostructure. *ACS nano* (2014) 8:12717–24. doi:10.1021/nn505736z
24. Gong Y, Lin J, Wang X, Shi G, Lei S, Lin Z, et al. Vertical and in-plane heterostructures from WS2/MoS2 monolayers. *Nat Mater* (2014) 13: 1135–42. doi:10.1038/nmat4091
25. Rivera P, Seyler KL, Yu H, Schaibley JR, Yan J, Mandrus DG, et al. Valley-polarized exciton dynamics in a 2D semiconductor heterostructure. *Science* (2016) 351:688–91. doi:10.1126/science.aac7820
26. Rivera P, Yu H, Seyler KL, Wilson NP, Yao W, and Xu X Interlayer valley excitons in heterobilayers of transition metal dichalcogenides. *Nat Nanotech* (2018) 13:1004–15. doi:10.1038/s41565-018-0193-0
27 Hsu W.-T., Lin B.-H., Lu L.-S., Lee M.-H., Chu M.-W., Li L.-J., et al. Tailoring excitonic states of van der Waals bilayers through stacking configuration, band alignment, and valley spin. *Sci Adv* (2019) 5:eaax7407. doi:10.1126/sciadv.aax7407
28. Liu Y, Rang H, Rasmita A, Zhou Y, Li J, Xiong Q, et al. Room temperature nanocavity laser with interlayer excitons in 2D heterostructures. *Sci Adv* (2019) 5:eaav4506. doi:10.1126/sciadv.aav4506
29. Withers F, Del Pozo-Zamudio O, Mishchenko A, Rooney AP, Gholinia A, Watanabe K, et al. Light-emitting diodes by band-structure engineering in van der Waals heterostructures. *Nat Mater* (2015) 14:301–6. doi:10.1038/nmat4205
30. Gong C, Zhang H, Wang W, Colombo L, Wallace RM, and Cho K, Band alignment of two-dimensional transition metal dichalcogenides: application in tunnel field effect transistors. *Appl Phys Lett* (2013) 103:053513. doi:10.1063/1.4817409
31. Georgiou T, Jalil R, Belle BD, Britnell L, Gorbachev RV, Morozov SV, et al. Vertical field-effect transistor based on graphene-WS2 heterostructures for flexible and transparent electronics. *Nat Nanotech* (2013) 8:100. doi:10.1038/nnano.2012.224
32. Britnell L, Gorbachev RV, Jalil R, Belle BD, Schedin F, Mishchenko A, et al. Field-effect tunneling transistor based on vertical graphene heterostructures. *Science* (2012) 335:947–50. doi:10.1126/science.1218461
33. Aftab S, and Eom J Van der Waals 2D layered-material bipolar transistor. *2D Mater* (2019) 6:035005. doi:10.1088/2053-1583/ab1df2
34. Vu QA, Lee JH, Nguyen VL, Shin YS, Lim SC, Lee K, et al. Tuning carrier tunneling in van der Waals heterostructures for ultrahigh detectivity. *Nano Lett* (2017) 17:453–9. doi:10.1021/acs.nanolett.6b04449
35. Zhou X, Hu X, Zhou S, Song H, Zhang Q, Pi L, et al. Tunneling diode based on WSe2/SnS2 heterostructure incorporating high detectivity and responsivity. *Adv Mater* (2018) 30:1703286. doi:10.1002/adma.201703286
36. Meng J-H, Liu X, Zhang X-W, Zhang Y, Wang H-L, Yin Z-G, et al. Interface engineering for highly efficient graphene-on-silicon Schottky junction solar cells by introducing a hexagonal boron nitride interlayer. *Nano Energy* (2016) 28:44–50. doi:10.1016/j.nanoen.2016.08.028
37. Wang D, Lu Y, Meng J, Zhang X, Yin Z, Gao M, et al. Remote heteroepitaxy of atomic layered hafnium disulfide on sapphire through hexagonal boron nitride. *Nanoscale* (2019) 11:9310–8. doi:10.1039/c9nr01700c
38. Li X, Lin S, Lin X, Xu Z, Wang P, Zhang S, et al. Graphene/h-BN/GaAs sandwich diode as solar cell and photodetector. *Opt Express* (2016) 24: 134–45. doi:10.1364/oe.24.000134
39. Radisavljevic B, Whitwick MB, and Kis A Small-signal amplifier based on single-layer MoS2. *Appl Phys Lett* (2012) 101:043103. doi:10.1063/1.4738986
40. Alem N, Erni R, Kisielowski C, Rossell MD, Gannett W, and Zettl A Atomically thin hexagonal boron nitride probed by ultrahigh-resolution

transmission electron microscopy. *Phys Rev B* (2009) 80:155425. doi:10.1103/PhysRevB.80.155425
41. Elias C, Valvin P, Pelini T, Summerfield A, Mellor CJ, Cheng TS, et al. Direct band-gap crossover in epitaxial monolayer boron nitride. *Nat Commun* (2019) 10:2639. doi:10.1038/s41467-019-10610-5
42. Castelletto S, Inam FA, Sato S-i., and Boretti A Hexagonal boron nitride: a review of the emerging material platform for single-photon sources and the spin-photon interface. *Beilstein J Nanotechnol* (2020) 11:740–69. doi:10.3762/bjnano.11.61
43. Jobst J, van der Torren AJH, Krasovskii EE, Balgley J, Dean CR, Tromp RM, et al. Quantifying electronic band interactions in van der Waals materials using angle-resolved reflected-electron spectroscopy. *Nat Commun* (2016) 7:13621. doi:10.1038/ncomms13621
44. Sponza L, Amara H, Attaccalite C, Latil S, Galvani T, Paleari F, et al. Direct and indirect excitons in boron nitride polymorphs: a story of atomic configuration and electronic correlation. *Phys Rev B* (2018) 98:125206. doi:10.1103/PhysRevB.98.125206
45. Pakdel A, Bando Y, and Golberg D Nano boron nitride flatland. *Chem Soc Rev* (2014) 43:934–59. doi:10.1039/C3CS60260E
46. Kubota Y, Watanabe K, Tsuda O, and Taniguchi T Deep ultraviolet light-emitting hexagonal boron nitride synthesized at atmospheric pressure. *Science* (2007) 317:932–4. doi:10.1126/science.1144216
47. Alem N, Ramasse QM, Seabourne CR, Yazyev OV, Erickson K, Sarahan MC, et al. Subangstrom edge relaxations probed by electron microscopy in hexagonal boron nitride. *Phys Rev Lett* (2012) 109:205502. doi:10.1103/PhysRevLett.109.205502
48. Gibb AL, Alem N, Chen J-H, Erickson KJ, Ciston J, Gautam A, et al. Atomic resolution imaging of grain boundary defects in monolayer chemical vapor deposition-grown hexagonal boron nitride. *J Am Chem Soc* (2013) 135:6758–61. doi:10.1021/ja400637n
49. Zhu W, Wu Z, Foo GS, Gao X, Zhou M, Liu B, et al. Taming interfacial electronic properties of platinum nanoparticles on vacancy-abundant boron nitride nanosheets for enhanced catalysis. *Nat Commun* (2017) 8:15291. doi:10.1038/ncomms15291
50. Cretu O, Lin Y-C, and Suenaga K Evidence for active atomic defects in monolayer hexagonal boron nitride: a new mechanism of plasticity in two-dimensional materials. *Nano Lett* (2014) 14:1064–8. doi:10.1021/nl404735w
51. Sajid A, Reimers JR, and Ford MJ Defect states in hexagonal boron nitride: assignments of observed properties and prediction of properties relevant to quantum computation. *Phys Rev B* (2018) 97:064101. doi:10.1103/PhysRevB.97.064101
52. Tran TT, Bray K, Ford MJ, Toth M, and Aharonovich I Quantum emission from hexagonal boron nitride monolayers. *Nat Nanotech* (2016) 11:37–41. doi:10.1038/nnano.2015.242
53. Abdi M, Chou J-P, Gali A, and Plenio MB Color centers in hexagonal boron nitride monolayers: a group theory and ab initio analysis. *ACS Photon* (2018) 5:1967–76. doi:10.1021/acsphotonics.7b01442
54. Tran TT, Elbadawi C, Totonjian D, Lobo CJ, Grosso G, Moon H, et al. Robust multicolor single photon emission from point defects in hexagonal boron nitride. *ACS Nano* (2016) 10:7331–8. doi:10.1021/acsnano.6b03602
55. Shotan Z, Jayakumar H, Considine CR, Mackoit M, Fedder H, Wrachtrup J, et al. Photoinduced modification of single-photon emitters in hexagonal boron nitride. *ACS Photon* (2016) 3:2490–6. doi:10.1021/acsphotonics.6b00736
56. Gottscholl A, Kianinia M, Soltamov V, Orlinskii S, Mamin G, Bradac C, et al. Initialization and read-out of intrinsic spin defects in a van der Waals crystal at room temperature. *Nat Mater* (2020) 19:540. doi:10.1038/s41563-020-0619-6
57. Ivády V, Barcza G, Thiering G, Li S, Hamdi H, Chou J-P, et al. Ab initio theory of the negatively charged boron vacancy qubit in hexagonal boron nitride. *Npj Comput Mater* (2020) 6:41. doi:10.1038/s41524-020-0305-x
58. Mendelson N, Chugh D, Reimers JR, Cheng TS, Gottscholl A, Long H, et al. Identifying carbon as the source of visible single-photon emission from hexagonal boron nitride. *Nat Mater* (2020). doi:10.1038/s41563-020-00850-y
59. Kianinia M, Regan B, Tawfik SA, Tran TT, Ford MJ, Aharonovich I, et al. Robust solid-state quantum system operating at 800 K. *ACS Photon* (2017) 4:768–73. doi:10.1021/acsphotonics.7b00086
60. Vogl T, Campbell G, Buchler BC, Lu Y, and Lam PK Fabrication and deterministic transfer of high-quality quantum emitters in hexagonal boron nitride. *ACS Photon* (2018) 5:2305–12. doi:10.1021/acsphotonics.8b00127
61. Exarhos AL, Hopper DA, Patel RN, Doherty MW, and Bassett LC Magnetic-field-dependent quantum emission in hexagonal boron nitride at room temperature. *Nat Commun* (2019) 10:222. doi:10.1038/s41467-018-08185-8
62. Xia Y, Li Q, Kim J, Bao W, Gong C, Yang S, et al. Room-temperature giant Stark effect of single photon emitter in van der Waals material. *Nano Lett* (2019) 19:7100–5. doi:10.1021/acs.nanolett.9b02640
63. Nikolay N, Mendelson N, Sadzak N, Böhm F, Tran TT, Sontheimer B, et al. Very large and reversible Stark-shift tuning of single emitters in layered hexagonal boron nitride. *Phys Rev Appl* (2019) 11:041001. doi:10.1103/PhysRevApplied.11.041001
64. Kianinia M, Bradac C, Sontheimer B, Wang F, Tran TT, Nguyen M, et al. All-optical control and super-resolution imaging of quantum emitters in layered materials. *Nat Commun* (2018) 9:874. doi:10.1038/s41467-018-03290-0
65. Comtet J, Glushkov E, Navikas V, Feng J, Babenko V, Hofmann S, et al. Wide-field spectral super-resolution mapping of optically active defects in hexagonal boron nitride. *Nano Lett* (2019) 19:2516–23. doi:10.1021/acs.nanolett.9b00178
66. Shi Y, Hamsen C, Jia X, Kim KK, Reina A, Hofmann M, et al. Synthesis of few-layer hexagonal boron nitride thin film by chemical vapor deposition. *Nano Lett* (2010) 10:4134–9. doi:10.1021/nl1023707
67. Song L, Ci L, Lu H, Sorokin PB, Jin C, Ni J, et al. Large scale growth and characterization of atomic hexagonal boron nitride layers. *Nano Lett* (2010) 10:3209–15. doi:10.1021/nl1022139
68. Yu J, Qin L, Hao Y, Kuang S, Bai X, Chong Y-M, et al. Vertcally aligned boron nitride nanosheets: chemical vapor synthesis, ultraviolet light emission, and superhydrophobicity. *ACS Nano* (2010) 4:414–22. doi:10.1021/nn901204c
69. Xu M, Fujita D, Chen H, and Hanagata N Formation of monolayer and few-layer hexagonal boron nitride nanosheets via surface segregation. *Nanoscale* (2011) 3:2854–8. doi:10.1039/C1NR10294J
70. Lian G, Zhang X, Tan M, Zhang S, Cui D, and Wang Q Facile synthesis of 3D boron nitride nanoflowers composed of vertically aligned nanoflakes and fabrication of graphene-like BN by exfoliation. *J Mater Chem* (2011) 21:9201–7. doi:10.1039/C0JM04503A
71. Han W-Q, Yu H-G, and Liu Z Convert graphene sheets to boron nitride and boron nitride-carbon sheets via a carbon-substitution reaction. *Appl Phys Lett* (2011) 98:203112. doi:10.1063/1.3593492
72. Novoselov KS, Jiang D, Schedin F, Booth TJ, Khotkevich VV, Morozov SV, et al. Two-dimensional atomic crystals. *Proc Natl Acad Sci* (2005) 102:10451–3. doi:10.1073/pnas.0502848102
73. Li LH, Chen Y, Behan G, Zhang H, Petravic M, and Glushenkov AM Large-scale mechanical peeling of boron nitride nanosheets by low-energy ball milling. *J Mater Chem* (2011) 21:11862–6. doi:10.1039/C1JM11192B
74. Pacilé D, Meyer JC, Girit ÇÖ, and Zettl A The two-dimensional phase of boron nitride: few-atomic-layer sheets and suspended membranes. *Appl Phys Lett* (2008) 92:133107. doi:10.1063/1.2903702
75. Liu L, Xiong Z, Hu D, Wu G, Liu B, and Chen P Solid exfoliation of hexagonal boron nitride crystals for the synthesis of few-layer boron nitride nanosheets. *Chem Lett* (2013) 42:1415–6. doi:10.1246/cl.130562
76. Han W-Q, Wu L, Zhu Y, Watanabe K, and Taniguchi T Structure of chemically derived mono- and few-atomic-layer boron nitride sheets. *Appl Phys Lett* (2008) 93:223103. doi:10.1063/1.3041639
77. Warner JH, Rümmeli MH, Bachmatiuk A, and Büchner B Atomic resolution imaging and topography of boron nitride sheets produced by chemical exfoliation. *ACS Nano* (2010) 4:1299–304. doi:10.1021/nn901648q
78. Li X, Hao X, Zhao M, Wu Y, Yang J, Tian Y, et al. Exfoliation of hexagonal boron nitride by molten hydroxides. *Adv Mater* (2013) 25:2200–4. doi:10.1002/adma.201204031
79. Chen X, Dobson JF, and Raston CL Vortex fluidic exfoliation of graphite and boron nitride. *Chem Commun* (2012) 48:3703–5. doi:10.1039/C2CC17611D
80. Meyer JC, Chuvilin A, Algara-Siller G, Biskupek J, and Kaiser U Selective sputtering and atomic resolution imaging of atomically thin boron nitride membranes. *Nano Lett* (2009) 9:2683–9. doi:10.1021/nl9011497

81. Jin C, Lin F, Suenaga K, and Iijima S Fabrication of a freestanding boron nitride single layer and its defect assignments. *Phys Rev Lett* (2009) 102: 195505. doi:10.1103/PhysRevLett.102.195505
82. Jiang X-F, Weng Q, Wang X-B, Li X, Zhang J, Golberg D, et al. Recent progress on fabrications and applications of boron nitride nanomaterials: a review. *J Mat Sci Technol* (2015) 31:589–98. doi:10.1016/j.jmst.2014.12.008
83. Emanet M, Sen Ö, Taşkin IÇ, and Çulha M Synthesis, functionalization, and bioapplications of two-dimensional boron nitride nanomaterials. *Front Bioeng Biotechnol* (2019) 7:363. doi:10.3389/fbioe.2019.00363
84. DeepikaLi LH, Glushenkov AM, Hait SK, Hodgson P, and Chen Y High-efficient production of boron nitride nanosheets via an optimized ball milling process for lubrication in oil. *Sci Rep* (2014) 4:7288. doi:10.1038/srep07288
85. Bari R, Parviz D, Khabaz F, Klaassen CD, Metzler SD, Hansen MJ, et al. Liquid phase exfoliation and crumpling of inorganic nanosheets. *Phys Chem Chem Phys* (2015) 17:9383–93. doi:10.1039/C5CP00294J
86. Smith RJ, King PJ, Lotya M, Wirtz C, Khan U, De S, et al. Large-scale exfoliation of inorganic layered compounds in aqueous surfactant solutions. *Adv Mater* (2011) 23:3944–8. doi:10.1002/adma.201102584
87. Duong NMH, Glushkov E, Chernev A, Navikas V, Comtet J, Nguyen MAP, et al. Facile production of hexagonal boron nitride nanoparticles by cryogenic exfoliation. *Nano Lett* (2019) 19:5417–22. doi:10.1021/acs.nanolett.9b01913
88. Wang Y, Liu Y, Zhang J, Wu J, Xu H, Wen X, et al. Cryo-mediated exfoliation and fracturing of layered materials into 2D quantum dots. *Sci Adv* (2017) 3: e1701500. doi:10.1126/sciadv.1701500
89. Huo B, Liu B, Chen T, Cui L, Xu G, Liu M, et al. One-step synthesis of fluorescent boron nitride quantum dots via a hydrothermal strategy using melamine as nitrogen source for the detection of ferric ions. *Langmuir* (2017) 33:10673–8. doi:10.1021/acs.langmuir.7b01699
90. Bradac C, Gaebel T, Naidoo N, Rabeau JR, and Barnard AS Prediction and measurement of the size-dependent stability of fluorescence in diamond over the entire nanoscale. *Nano Lett* (2009) 9:3555–64. doi:10.1021/nl9017379
91. Bradac C, Gaebel T, Naidoo N, Sellars MJ, Twamley J, Brown LJ, et al. Observation and control of blinking nitrogen-vacancy centres in discrete nanodiamonds. *Nat Nanotech* (2010) 5:345–9. doi:10.1038/nnano.2010.56
92. Nagl A, Hemelaar SR, and Schirhagl R Improving surface and defect center chemistry of fluorescent nanodiamonds for imaging purposes-a review. *Anal Bioanal Chem* (2015) 407:7521–36. doi:10.1007/s00216-015-8849-1
93. Noh G, Choi D, Kim J-H, Im D-G, Kim Y-H, Seo H, et al. Stark tuning of single-photon emitters in hexagonal boron nitride. *Nano Lett* (2018) 18: 4710–5. doi:10.1021/acs.nanolett.8b01030
94. Wang X, Ren X, Kahen K, Hahn MA, Rajeswaran M, Maccagnano-Zacher S, et al. Non-blinking semiconductor nanocrystals. *Nature* (2009) 459:686–9. doi:10.1038/nature08072
95. Bradac C, Gaebel T, Pakes CI, Say JM, Zvyagin AV, and Rabeau JR Effect of the nanodiamond host on a nitrogen-vacancy color-centre emission state. *Small* (2013) 9:132–9. doi:10.1002/smll.201200574
96. Fu K-MC, Santori C, Barclay PE, and Beausoleil RG Conversion of neutral nitrogen-vacancy centers to negatively charged nitrogen-vacancy centers through selective oxidation. *Appl Phys Lett* (2010) 96:121907. doi:10.1063/1.3364135
97. Rondin L, Dantelle G, Slablab A, Grosshans F, Treussart F, Bergonzo P, et al. Surface-induced charge state conversion of nitrogen-vacancy defects in nanodiamonds. *Phys Rev B* (2010) 82:115449. doi:10.1103/physrevb.82.115449
98. Salvetti A, Rossi L, Iacopetti P, Li X, Nitti S, Pellegrino T, et al. In vivobiocompatibility of boron nitride nanotubes: effects on stem cell biology and tissue regeneration in planarians. *Nanomedicine* (2015) 10: 1911–22. doi:10.2217/nnm.15.46
99. Chen X, Wu P, Rousseas M, Okawa D, Gartner Z, Zettl A, et al. Boron nitride nanotubes are noncytotoxic and can be functionalized for interaction with proteins and cells. *J Am Chem Soc* (2009) 131:890–1. doi:10.1021/ja807334b
100. Kıvanç M, Barutca B, Koparal AT, Goncu Y, Boutanci SH, Ay N, et al. Effects of hexagonal boron nitride nanoparticles on antimicrobial and antibiofilm activities, cell viability. *Mater Sci Eng C* (2018) 91:115–24. doi:10.1016/j.msec.2018.05.028
101. Lu T, Wang L, Jiang Y, liu Q, and Huang C Hexagonal boron nitride nanoplates as emerging biological nanovectors and their potential applications in biomedicine. *J Mater Chem B* (2016) 4:6103–10. doi:10.1039/c6tb01481j
102. Lahiri D, Singh V, Benaduce AP, Seal S, Kos L, and Agarwal A Boron nitride nanotube reinforced hydroxyapatite composite: mechanical and tribological performance and *in-vitro* biocompatibility to osteoblasts. *J Mech Behav Biomed Mater* (2011) 4:44–56. doi:10.1016/j.jmbbm.2010.09.005
103. Liu L, Xiao L, Li M, Zhang X, Chang Y, Shang L, et al. Effect of hexagonal boron nitride on high-performance polyether ether ketone composites. *Colloid Polym Sci* (2016) 294:127–33. doi:10.1007/s00396-015-3733-2
104. Ciofani G Potential applications of boron nitride nanotubes as drug delivery systems. *Expert Opin Drug Deliv* (2010) 7:889–93. doi:10.1517/17425247.2010.499897
105. Ciofani G, Ricotti L, Danti S, Menciassi A, Chiellini F, D'Alessandro D, et al. Investigation of interactions between poly-L-lysine-coated boron nitride nanotubes and C2C12 cells: up-take, cytocompatibility, and differentiation. *Ijn* (2010) 5:285–95. doi:10.2147/ijn.s9879
106. Ciofani G, Raffa V, Menciassi A, and Cuschieri A Cytocompatibility, interactions, and uptake of polyethyleneimine-coated boron nitride nanotubes by living cells: confirmation of their potential for biomedical applications. *Biotechnol Bioeng* (2008) 101:850–8. doi:10.1002/bit.21952
107. Ciofani G, Raffa V, Menciassi A, and Cuschieri A Folate functionalized boron nitride nanotubes and their selective uptake by glioblastoma multiforme cells: implications for their use as boron carriers in clinical boron neutron capture therapy. *Nanoscale Res Lett* (2008) 4:113. doi:10.1007/s11671-008-9210-9
108. Horváth L, Magrez A, Golberg D, Zhi C, Bando Y, Smajda R, et al. *In vitro* investigation of the cellular toxicity of boron nitride nanotubes. *ACS Nano* (2011) 5:3800–10. doi:10.1021/nn200139h
109. Li X, Wang X, Zhang J, Hanagata N, Wang X, Weng Q, et al. Hollow boron nitride nanospheres as boron reservoir for prostate cancer treatment. *Nat Commun* (2017) 8:13936. doi:10.1038/ncomms13936
110. Ferreira TH, Silva PRO, Santos RG, and Sousa EMB (2011). A novel synthesis route to produce boron nitride nanotubes for bioapplications. *J Biomat Nanobiotechnol* 2, 426–34. doi:10.4236/jbnb.2011.24052
111. Weng Q, Wang X, Wang X, Bando Y, and Golberg D Functionalized hexagonal boron nitride nanomaterials: emerging properties and applications. *Chem Soc Rev* (2016) 45:3989–4012. doi:10.1039/C5CS00869G
112. Lu F, Wang F, Cao L, Kong CY, and Huang X Hexagonal boron nitride nanomaterials: advances towards bioapplications. *Nanosci Nanotechnol Lett* (2012) 4:949–61. doi:10.1166/nnl.2012.1444
113. Kalay S, Yilmaz Z, Sen O, Emanet M, Kazanc E, and Çulha M Synthesis of boron nitride nanotubes and their applications. *Beilstein J Nanotechnol* (2015) 6:84–102. doi:10.3762/bjnano.6.9
114. Gao Z, Zhi C, Bando Y, Golberg D, and Serizawa T Noncovalent functionalization of boron nitride nanotubes in aqueous media opens application roads in nanobiomedicine. *Nanobiomedicine* (2014) 1:7. doi:10.5772/60000
115. Weng Q, Wang B, Wang X, Hanagata N, Li X, Liu D, et al. Highly water-soluble, porous, and biocompatible boron nitrides for anticancer drug delivery. *ACS nano* (2014) 8:6123–30. doi:10.1021/nn5014808
116. Zhi CY, Bando Y, Terao T, Tang CC, Kuwahara H, and Golberg D Chemically activated boron nitride nanotubes. *Chem Asian J* (2009) 4:1536–40. doi:10.1002/asia.200900158
117. Lin Y, Williams TV, Xu T-B, Cao W, Elsayed-Ali HE, and Connell JW Aqueous dispersions of few-layered and monolayered hexagonal boron nitride nanosheets from sonication-assisted hydrolysis: critical role of water. *J Phys Chem C* (2011) 115:2679–85. doi:10.1021/jp110985w
118. Sainsbury T, Satti A, May P, Wang Z, McGovern I, Gun'ko YK, et al. Oxygen radical functionalization of boron nitride nanosheets. *J Am Chem Soc* (2012) 134:18758–71. doi:10.1021/ja3080665
119. Pakdel A, Bando Y, and Golberg D Plasma-assisted interface engineering of boron nitride nanostructure films. *ACS Nano* (2014) 8:10631–9. doi:10.1021/nn5041729
120. Lee D, Lee B, Park KH, Ryu HJ, Jeon S, and Hong SH Scalable exfoliation process for highly soluble boron nitride nanoplatelets by hydroxide-assisted ball milling. *Nano Lett* (2015) 15:1238–44. doi:10.1021/nl504397h
121. Weng Q, Ide Y, Wang X, Wang X, Zhang C, Jiang X, et al. Design of BN porous sheets with richly exposed (002) plane edges and their application as

TiO2 visible light sensitizer. *Nano Energy* (2015) 16:19–27. doi:10.1016/j.nanoen.2015.06.004
122. Xie S-Y, Wang W, Fernando KAS, Wang X, Lin Y, and Sun Y-P Solubilization of boron nitride nanotubes. *Chem Commun* (2005) 3670–2. doi:10.1039/B505330G
123. Lin Y, Williams TV, and Connell JW Soluble, exfoliated hexagonal boron nitride nanosheets. *J Phys Chem Lett* (2010) 1:277–83. doi:10.1021/jz9002108
124. Ikuno T, Sainsbury T, Okawa D, Fréchet JMJ, and Zettl A Amine-functionalized boron nitride nanotubes. *Solid State Commun* (2007) 142:643–6. doi:10.1016/j.ssc.2007.04.010
125. Liao Y, Chen Z, Connell JW, Fay CC, Park C, Kim J-W, et al. Chemical sharpening, shortening, and unzipping of boron nitride nanotubes. *Adv Funct Mater* (2014) 24:4497–506. doi:10.1002/adfm.201400599
126. Kim D, Nakajima S, Sawada T, Iwasaki M, Kawauchi S, Zhi C, et al. Sonication-assisted alcoholysis of boron nitride nanotubes for their sidewalls chemical peeling. *Chem Commun* (2015) 51:7104–7. doi:10.1039/C5CC00388A
127. Sainsbury T, O'Neill A, Passarelli MK, Seraffon M, Gohil D, Gnaniah S, et al. Dibromocarbene functionalization of boron nitride nanosheets: toward band gap manipulation and nanocomposite applications. *Chem Mater* (2014) 26:7039–50. doi:10.1021/cm503475t
128. Shin H, Guan J, Zgierski MZ, Kim KS, Kingston CT, and Simard B Covalent functionalization of boron nitride nanotubes via reduction chemistry. *ACS Nano* (2015) 9:12573–82. doi:10.1021/acsnano.5b06523
129. Golberg D, Bando Y, Tang CC, and Zhi CY Boron nitride nanotubes. *Adv Mater* (2007) 19:2413–32. doi:10.1002/adma.200700179
130. Zhi C, Bando Y, Tang C, Honda S, Sato K, Kuwahara H, et al. Covalent functionalization: towards soluble multiwalled boron nitride nanotubes. *Angew Chem Int Ed* (2005) 44:7932–5. doi:10.1002/anie.200502846
131. Huang X, Zhi C, Jiang P, Golberg D, Bando Y, and Tanaka T Polyhedral oligosilsesquioxane-modified boron nitride nanotube based epoxy nanocomposites: an ideal dielectric material with high thermal conductivity. *Adv Funct Mater* (2013) 23:1824–31. doi:10.1002/adfm.201201824
132. Ciofani G, Genchi GG, Liakos I, Athanassiou A, Dinucci D, Chiellini F, et al. A simple approach to covalent functionalization of boron nitride nanotubes. *J Colloid Interf Sci* (2012) 374:308–14. doi:10.1016/j.jcis.2012.01.049
133. Bhattacharya A, Bhattacharya S, and Das GP Band gap engineering by functionalization of BN sheet. *Phys Rev B* (2012) 85:035415. doi:10.1103/PhysRevB.85.035415
134. Li X, Zhao J, and Yang J Semihydrogenated BN sheet: a promising visible-light driven photocatalyst for water splitting. *Sci Rep* (2013) 3:1858. doi:10.1038/srep01858
135. Tang C, Bando Y, Huang Y, Yue S, Gu C, Xu F, et al. Fluorination and electrical conductivity of BN nanotubes. *J Am Chem Soc* (2005) 127:6552–3. doi:10.1021/ja042388u
136. Wolters J, Sadzak N, Schell AW, Schröder T, and Benson O Measurement of the ultrafast spectral diffusion of the optical transition of nitrogen vacancy centers in nano-size diamond using correlation interferometry. *Phys Rev Lett* (2013) 110:027401. doi:10.1103/PhysRevLett.110.027401
137. Neuhauser RG, Shimizu KT, Woo WK, Empedocles SA, and Bawendi MG Correlation between fluorescence intermittency and spectral diffusion in single semiconductor quantum dots. *Phys Rev Lett* (2000) 85:3301–4. doi:10.1103/PhysRevLett.85.3301
138. Kobayashi Y, Inose H, Nakagawa T, Gonda K, Takeda M, Ohuchi N, et al. Control of shell thickness in silica-coating of Au nanoparticles and their X-ray imaging properties. *J Colloid Interf Sci* (2011) 358:329–33. doi:10.1016/j.jcis.2011.01.058
139. Deng W, Jin D, Drozdowicz-Tomsia K, Yuan J, Wu J, and Goldys EM Ultrabright Eu-doped plasmonic Ag@SiO2 nanostructures: time-gated bioprobes with single particle sensitivity and negligible background. *Adv Mater* (2011) 23:4649–54. doi:10.1002/adma.201102027
140. Abidi IH, Mendelson N, Tran TT, Tyagi A, Zhuang M, Weng LT, et al. Selective defect formation in hexagonal boron nitride. *Adv Opt Mater* (2019) 7:1900397. doi:10.1002/adom.201900397
141. Feng J, Deschout H, Caneva S, Hofmann S, Lončarić I, Lazić P, et al. Imaging of optically active defects with nanometer resolution. *Nano Lett* (2018) 18:1739–44. doi:10.1021/acs.nanolett.7b04819
142. Comtet J, Grosjean B, Glushkov E, Avsar A, Watanabe K, Taniguchi T, et al. Direct observation of water-mediated single-proton transport between hBN surface defects. *Nat Nanotechnol* (2020) 15:598–604. doi:10.1038/s41565-020-0695-4
143. Schell AW, Tran TT, Takashima H, Takeuchi S, and Aharonovich I Non-linear excitation of quantum emitters in hexagonal boron nitride multiplayers. *APL Photon* (2016) 1:091302. doi:10.1063/1.4961684
144. Sontheimer B, Braun M, Nikolay N, Sadzak N, Aharonovich I, and Benson O Photodynamics of quantum emitters in hexagonal boron nitride revealed by low-temperature spectroscopy. *Phys Rev B* (2017) 96:121202. doi:10.1103/PhysRevB.96.121202
145. Tran TT, Bradac C, Solntsev AS, Toth M, and Aharonovich I Suppression of spectral diffusion by anti-Stokes excitation of quantum emitters in hexagonal boron nitride. *Appl Phys Lett* (2019) 115:071102. doi:10.1063/1.5099631
146. Dertinger T, Colyer R, Iyer G, Weiss S, and Enderlein J Fast, background-free, 3D super-resolution optical fluctuation imaging (SOFI). *Proc Natl Acad Sci U S A* (2009) 106:22287–92. doi:10.1073/pnas.0907866106
147. Wen X, Gong Z, and Li D Nonlinear optics of two-dimensional transition metal dichalcogenides. *InfoMat* (2019) 1:317–37. doi:10.1002/inf2.12024
148. Zhou L, Fu H, Lv T, Wang C, Gao H, Li D, et al. Nonlinear optical characterization of 2D materials. *Nanomaterials* (2020) 10:2263. doi:10.3390/nano10112263
149. Kaiser W, and Garrett CGB Two-photon excitation in CaF2:Eu2+. *Phys Rev Lett* (1961) 7:229–31. doi:10.1103/PhysRevLett.7.229
150. Friedrich DM Two-photon molecular spectroscopy. *J Chem Educ* (1982) 59:472. doi:10.1021/ed059p472
151. Denk W, Strickler J, and Webb W Two-photon laser scanning fluorescence microscopy. *Science* (1990) 248:73–6. doi:10.1126/science.2321027
152. Weissleder R A clearer vision for *in vivo* imaging. *Nat Biotechnol* (2001) 19:316–7. doi:10.1038/86684
153. Doi A, Oketani R, Nawa Y, and Fujita K High-resolution imaging in two-photon excitation microscopy using *in situ* estimations of the point spread function. *Biomed Opt Express* (2018) 9:202–13. doi:10.1364/BOE.9.000202
154. Zhilie T, Chuping Y, Hongjin P, Ruisheng L, and Songhao L Imaging theory and resolution improvement of two-photon confocal microscopy. *Sci China Ser A-Math* (2002) 45:1468–78. doi:10.1007/BF02880042
155. Doherty MW, Manson NB, Delaney P, Jelezko F, Wrachtrup J, and Hollenberg LCL The nitrogen-vacancy colour centre in diamond. *Phys Rep* (2013) 528:1–45. doi:10.1016/j.physrep.2013.02.001
156. Childress L, and Hanson R Diamond NV centers for quantum computing and quantum networks. *MRS Bull* (2013) 38:134–8. doi:10.1557/mrs.2013.20
157. Degen CL, Reinhard F, and Cappellaro P Quantum sensing. *Rev Mod Phys* (2017) 89:035002. doi:10.1103/RevModPhys.89.035002
158. Bradac C, Gao W, Forneris J, Trusheim ME, and Aharonovich I Quantum nanophotonics with group IV defects in diamond. *Nat Commun* (2019) 10:5625. doi:10.1038/s41467-019-13332-w
159. Nagy R, Niethammer M, Widmann M, Chen Y-C, Udvarhelyi P, Bonato C, et al. High-fidelity spin and optical control of single silicon-vacancy centres in silicon carbide. *Nat Commun* (2019) 10:1954. doi:10.1038/s41467-019-09873-9
160. Castelletto S, Johnson BC, Ivády V, Stavrias N, Umeda T, Gali A, et al. A silicon carbide room-temperature single-photon source. *Nat Mater* (2014) 13:151–6. doi:10.1038/nmat3806
161. Zhong M, Hedges MP, Ahlefeldt RL, Bartholomew JG, Beavan SE, Wittig SM, et al. Optically addressable nuclear spins in a solid with a six-hour coherence time. *Nature* (2015) 517:177–80. doi:10.1038/nature14025
162. Kindem JM, Ruskuc A, Bartholomew JG, Rochman J, Huan YQ, and Faraon A Control and single-shot readout of an ion embedded in a nanophotonic cavity. *Nature* (2020) 580:201–4. doi:10.1038/s41586-020-2160-9
163. Grinolds MS, Hong S, Maletinsky P, Luan L, Lukin MD, Walsworth RL, et al. Nanoscale magnetic imaging of a single electron spin under ambient conditions. *Nat Phys* (2013) 9:215–9. doi:10.1038/nphys2543
164. Grinolds MS, Warner M, De Greve K, Dovzhenko Y, Thiel L, Walsworth RL, et al. Subnanometre resolution in three-dimensional magnetic resonance imaging of individual dark spins. *Nat Nanotech* (2014) 9:279–84. doi:10.1038/nnano.2014.30

165. Dolde F, Fedder H, Doherty MW, Nöbauer T, Rempp F, Balasubramanian G, et al. Electric-field sensing using single diamond spins. *Nat Phys* (2011) 7: 459–63. doi:10.1038/nphys1969
166. Cole JH, and Hollenberg LCL Scanning quantum decoherence microscopy. *Nanotechnology* (2009) 20:495401. doi:10.1088/0957-4484/20/49/495401
167. Kucsko G, Maurer PC, Yao NY, Kubo M, Noh HJ, Lo PK, et al. Nanometre-scale thermometry in a living cell. *Nature* (2013) 500:54–8. doi:10.1038/nature12373
168. Geiselmann M, Juan ML, Renger J, Say JM, Brown LJ, de Abajo FJG, et al. Three-dimensional optical manipulation of a single electron spin. *Nat Nanotech* (2013) 8:175–9. doi:10.1038/nnano.2012.259
169. Chen Y-Y, Shu H, Kuo Y, Tzeng Y-K, and Chang H-C Measuring Förster resonance energy transfer between fluorescent nanodiamonds and near-infrared dyes by acceptor photobleaching. *Diamond Relat Mater* (2011) 20:803–7. doi:10.1016/j.diamond.2011.03.039
170. Tisler J, Reuter R, Lämmle A, Jelezko F, Balasubramanian G, Hemmer PR, et al. Highly efficient FRET from a single nitrogen-vacancy center in nanodiamonds to a single organic molecule. *ACS Nano* (2011) 5:7893–8. doi:10.1021/nn2021259
171. Herbschleb ED, Kato H, Maruyama Y, Danjo T, Makino T, Yamasaki S, et al. Ultra-long coherence times amongst room-temperature solid-state spins. *Nat Commun* (2019) 10:3766. doi:10.1038/s41467-019-11776-8
172. Liu Y, Zhang S, He J, Wang ZM, and Liu Z Recent progress in the fabrication, properties, and devices of heterostructures based on 2D materials. *Nano-Micro Lett* (2019) 11:13. doi:10.1007/s40820-019-0245-5
173. Frisenda R, Navarro-Moratalla E, Gant P, Pérez De Lara D, Jarillo-Herrero P, Gorbachev RV, et al. Recent progress in the assembly of nanodevices and van der Waals heterostructures by deterministic placement of 2D materials. *Chem Soc Rev* (2018) 47:53–68. doi:10.1039/C7CS00556C
174. Kim K, Yankowitz M, Fallahazad B, Kang S, Movva HCP, Huang S, et al. van der Waals heterostructures with high accuracy rotational alignment. *Nano Lett* (2016) 16:1989–95. doi:10.1021/acs.nanolett.5b05263
175. Chen Y, Tran TN, Duong NMH, Li C, Toth M, Bradac C, et al. Optical thermometry with quantum emitters in hexagonal boron nitride. *ACS Appl Mater Inter* (2020) 12:25464–70. doi:10.1021/acsami.0c05735
176. Rondin L, Tetienne J-P, Hingant T, Roch J-F, Maletinsky P, and Jacques V Magnetometry with nitrogen-vacancy defects in diamond. *Rep Prog Phys* (2014) 77:056503. doi:10.1088/0034-4885/77/5/056503

Conflict of Interest: The author declares that the research was conducted in the absence of any commercial or financial relationships that could be construed as a potential conflict of interest.

frontiers in Chemistry

REVIEW
published: 20 April 2021
doi: 10.3389/fchem.2021.641330

Shedding New Lights Into STED Microscopy: Emerging Nanoprobes for Imaging

Yanfeng Liu, Zheng Peng, Xiao Peng, Wei Yan*, Zhigang Yang and Junle Qu*

Key Laboratory of Optoelectronic Devices and Systems of Ministry of Education and Guangdong Province, College of Optoelectronic Engineering, Shenzhen University, Shenzhen, China

First reported in 1994, stimulated emission depletion (STED) microscopy has long been regarded as a powerful tool for real-time superresolved bioimaging . However, high STED light power ($10^{1\sim3}$ MW/cm^2) is often required to achieve significant resolution improvement, which inevitably introduces phototoxicity and severe photobleaching, damaging the imaging quality, especially for long-term cases. Recently, the employment of nanoprobes (quantum dots, upconversion nanoparticles, carbon dots, polymer dots, AIE dots, etc.) in STED imaging has brought opportunities to overcoming such long-existing issues. These nanomaterials designed for STED imaging show not only lower STED power requirements but also more efficient photoluminescence (PL) and enhanced photostability than organic molecular probes. Herein, we review the recent progress in the development of nanoprobes for STED imaging, to highlight their potential in improving the long-term imaging quality of STED microscopy and broadening its application scope. We also discuss the pros and cons for specific classes of nanoprobes for STED bioimaging in detail to provide practical references for biological researchers seeking suitable imaging kits, promoting the development of relative research field.

Keywords: STED, nanoprobes, bioimaging, subdiffraction imaging, material science

OPEN ACCESS

Edited by:
Qiuqiang Zhan,
South China Normal University, China

Reviewed by:
Jiong Ma,
Fudan University, China
Fabio Di Nardo,
University of Turin, Italy

****Correspondence:***
Xiao Peng
pengxiao_px@szu.edu.cn
Wei Yan
weiyan@szu.edu.cn

Specialty section:
This article was submitted to Analytical Chemistry, a section of the journal Frontiers in Chemistry

Received: *14 December 2020*
Accepted: *15 February 2021*
Published: *20 April 2021*

Citation:
Liu Y, Peng Z, Peng X, Yan W, Yang Z and Qu J (2021) Shedding New Lights Into STED Microscopy: Emerging Nanoprobes for Imaging. Front. Chem. 9:641330. doi: 10.3389/fchem.2021.641330

INTRODUCTION

Photoluminescence (PL) microscopy imaging has long been a powerful tool in biological research. However, the resolution of conventional far-field fluorescence microscopy was limited to half of the imaging wavelength (~200 nm) by Abbe's optical diffraction-limited theory (Rayleigh, 1896). Such resolution soon became insufficient as the interested events in cytobiological research went smaller in space and faster in timescale. In 1990s, Hell and coworkers put forward and realized the idea of stimulated emission depletion (STED) microscopy (Hell and Wichmann, 1994; Klar and Hell, 1999), which provided the world a state-of-art method to perform imaging beyond the diffraction limit.

The system of STED is based on a modification of the preexisting confocal microscopy. In confocal imaging, the size of point spread function (PSF) is limited by optical diffraction (**Figure 1**). As a result, a number of fluorophores are irradiated at the same time during the acquisition of a single pixel, which leads to a limited resolution. In a STED imaging setup, a donut-like depletion light is applied to suppress the emission of peripheral fluorophores by triggering their stimulated emission (at a red-shifted wavelength), which effectively decreases the size of PSF and thus ensures subdiffraction imaging (see **Figure 1**).

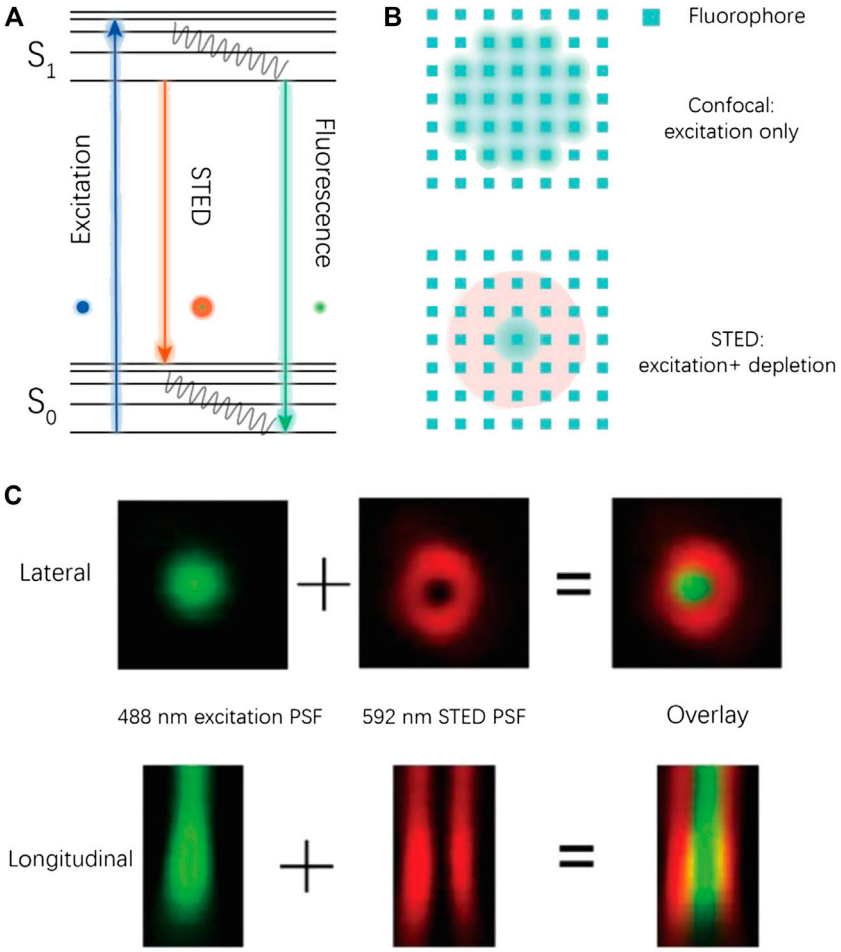

FIGURE 1 | Conceptual illustration for STED imaging. **(A)** The Jablonski diagram for a typical STED process. **(B)** Illustration of the PSF shrinking in STED imaging. **(C)** Experimental PSF in a STED imaging process (Ye et al., 2018).

Compared with other superresolution imaging methods like structure illumination microscopy (SIM) (Gustafsson, 2000; Gustafsson, 2005), photoactivated localization microscopy (PALM) (Betzig et al., 2006), and stochastic optical reconstruction microscopy (STORM) (Rust et al., 2006; Huang et al., 2008), STED is a pure-optical measure that can be applied with a variety of dyes, while being free from complex postimaging calculation. These advantages make STED favorable for superresolution imaging in a real-time mode.

However, the improvement of resolution also comes with a price: depletion of most conventional fluorescent labels, such as molecular probes and fluorescent proteins (FPs), generally requires very high depletion light intensity (Hein et al., 2008; Meyer et al., 2008). As a result, STED bioimaging suffers from severe photobleaching and phototoxicity (Wildanger et al., 2009), thus hampering the development of their long-term imaging applications with live samples. Fortunately, the development of material science has provided a vast menu of photostable fluorescent nanomaterials (Wolfbeis, 2015; Jin et al., 2018). Generally speaking, these nanomaterials are stable and bright and can be more efficiently depleted than molecular dyes, suggesting their potential utility as antibleaching STED probes.

In this article, we first introduce categories of nanoprobes and their brief history in STED applications. Then, we perform a systematic cross-comparison to discuss the pros and cons of different nanoprobes for STED. In addition, we summarize the major challenges for nanoprobes in STED microscopy and propose an outlook on the future development of nanoprobe-based STED imaging.

NANOPARTICLES FOR STED: CATEGORIES AND BRIEF HISTORY

The nanoparticles applied for STED imaging can be divided into two major categories according to their PL origin (**Figure 2**). Nanoparticles with organic PL origin including aggregation-induced emission (AIE) dots, polymer dots (PDots), and

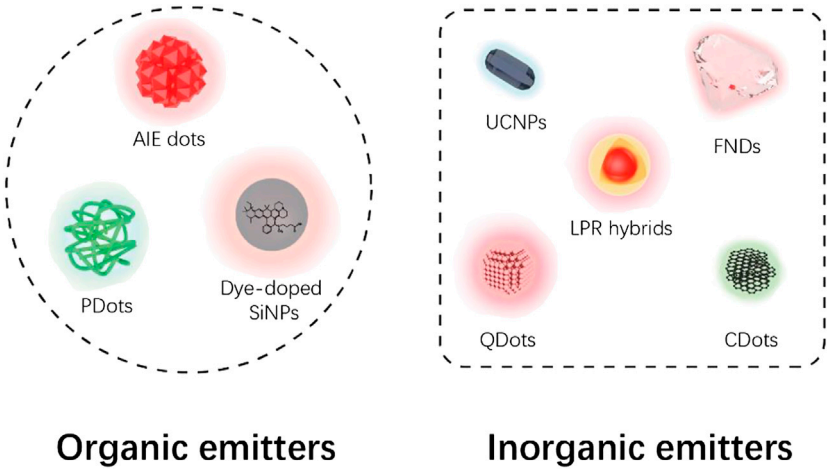

FIGURE 2 | Categories of STED nanoprobes based on current report. Note that dye-doped SiNPs were classified as organic emitters based on their molecular fluorescence origin.

dye-doped silica nanoparticles (SiNPs) have similar emitting mechanism and properties like molecular dyes, but with improved STED performance. Inorganic nanoprobes like fluorescent nanodiamonds (FNDs), localized plasmonic resonance (LPR) hybrids, quantum dots (QDots), upconversion nanoparticles (UCNPs), and carbon dots (CDots) have energy structure and PL properties different from molecular dyes and, in many cases, are more satisfactory emitters with higher depletion efficiencies.

Organic Emitters

Dye-Doped SiNPs

Dye-doped SiNPs are usually classified as organic emitters due to their molecular PL origin, despite their chemical composition with a large amount of inorganic element (Si). For this reason, the basic optical properties of SiNPs such as photostability and depletion efficiency are highly dependent on the character of the doped molecular dyes.

In 2010s, Kraegeloh and coworkers initiated a series of studies on the SiNPs for STED cellular imaging. At the early stage, large SiNPs with diameter exceeding 100 nm were synthesized, which clearly formed discernable aggregates in living cells (Schubbe et al., 2010). Later, SiNPs with smaller particle size were achieved (Schübbe et al., 2012), allowing for a quantitative measurement on their cellular uptake (Peuschel et al., 2015), demonstrating the realistic applicability of these materials. To further synthesize smaller SiNPs with higher brightness, Kraegeloh and coworkers further modified the fabrication technique by applying a dye-conjugated organosilica reagent (Tavernaro et al., 2017). As a result, particles with smaller size (down to 14 nm) and yet higher fluorophore density were fabricated, which showed higher brightness and better photostability for STED imaging with a limiting resolution of 80 nm.

To achieve higher STED resolution, Qu, Liu, and other coworkers designed and synthesized fluorescent SiNPs by hydrothermally treating saline linkers together with dye molecules (Liang et al., 2020; **Figure 3**). These as-synthesized sub-2-nm SiNPs showed outstanding photostability and ultrahigh brightness with a photoluminescence quantum yield (PLQY) of 99%, due to the successful elimination of spin–orbit coupling (SOC) of the fluorescein-derived dye. Furthermore, the SiNPs can be effectively depleted with low STED power, which allowed a resolution of up to 19.2 nm (10-fold improved to confocal results) at <40 mW STED power.

Another success in improving resolution and reducing the STED power requirement was achieved by introducing a nonplanar twist intramolecular charge transfer (TICT) compound DAPF as the emitting core (Man et al., 2019). As a result, a stable and highly efficient STED nanoprobe was fabricated, which achieved a lateral resolution of 60 nm at <1 MW/cm^2 STED intensity (~3 mW in power scale) for cell imaging.

AIE Dots

In 2001, fluorescent molecules with aggregation-induced emission (AIE) feature were first reported by Benzhong Tang and coworkers (Luo et al., 2001). In contrast to conventional aggregation-caused quenching (ACQ) dyes, the AIE fluorophores featured higher emission efficiency in aggregation. Such fascinating character promoted the fast development of the colloidal AIE dots, which have found broad applications in fields of bioimaging, sensing, and theranostics (Hong et al., 2011). According to Tang and coworkers' pioneer work, the AIE materials are more photostable and showed easier depletion by STED than molecular fluorophores (Yu et al., 2015). To further probe the applicability of AIE dots in STED imaging, Tang et al. designed and synthesized silica-hybridized AIE dots from an AIE molecule TTF (Li et al., 2017). The resultant 24-nm particles reached subdiffraction resolution (~30 nm) when depleted with a 775-nm STED light (300 mW) and showed a highly stable and nontoxic effect for cellular imaging.

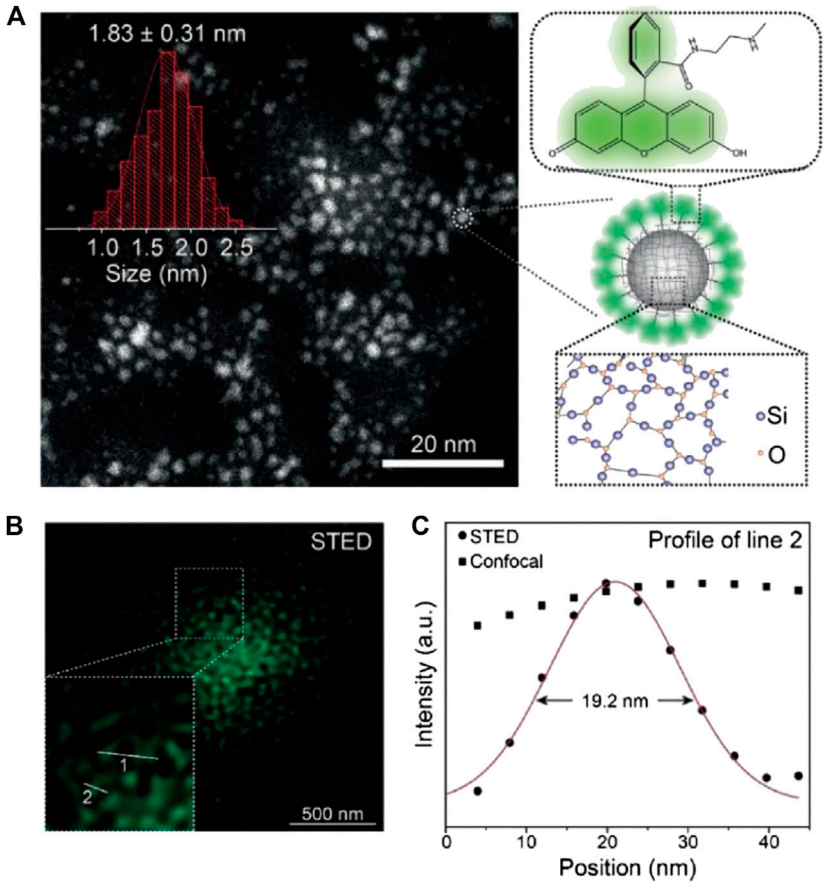

FIGURE 3 | Sub-2-nm dye-doped SiNPs for STED imaging (Liang et al., 2020). **(A)** The morphology and structure illustration of SiNPs. **(B)** The STED microscopy image of dispersed SiNPs. **(C)** The plotfile of signal intensities for confocal and STED images. A resolution of 19.2 nm was calculated from the full width at half maximum (FWHM) of the plotfile.

The potential of AIE dots for subcellular tracking in both fixed and living cells and *in vivo* imaging was further reported (Li et al., 2018; Fang et al., 2017; Xu et al., 2020). Fang and coworkers synthesized carboxylated AIE dots by nanoprecipitation and conjugated them with streptavidin for the STED imaging of microtubules in fixed MCF-7 cells (Fang et al., 2017; **Figure 4**). Li et al. synthesized positively charged AIE dots by direct precipitation of an amphiphilic AIE molecule and used it to label the mitochondria in living cells for STED imaging (Li et al., 2018). Xu et al. synthesized highly biocompatible AIE dots with PEG passivation for *in vitro* and *in vivo* STED bioimaging of living cells and fish-tail microvessels (Xu et al., 2020). The imaging resolution in these works reached 70~100 nm, but the STED power requirement (100~150 mW) was close to that for small molecular probes.

PDots

PDots, an emerging class of nanoparticles derived from fluorescent semiconductor polymers like poly(9, 9-dioctylfluorene-co-benzothiadiazole) (PFBT) and poly(1,4-phenylenevinylene) (PPV), are ideal bioimaging probes with high brightness, photobleaching resistance, and low toxicity (Wu et al., 2010). Despite the scarcity of relative reports, PDots have proven high potential for STED imaging applications. In 2018, Wu and Fang et al. first adopted 40 nm-sized PDots for STED imaging (Wu Y. et al., 2018). As expected, these particles were highly biocompatible and could be facilely conjugated with molecules like biotin. Intriguingly, the PDots showed very low STED power requirement (<3 W for 70 nm resolution) but high photobleaching resistance. In 2020, the potential application of PDots in STED was further explored (Wu et al., 2020). Red and far-red emitting PDots with ~30 nm size were synthesized and used for immunofluorescence staining of subcellular targets including membrane protein CD44, tubulins, and lysosomes (**Figure 5**). Furthermore, a dual-color STED imaging was performed to accomplish the real-time tracking of endosome interactions, which suggested the application potential of these materials as long-term, real-time imaging tags for STED microscopy.

Inorganic Emitters

FNDs

FNDs are one of the inorganic nanomaterials initially applied for STED imaging. The PL of these carbon-based nanoemitters

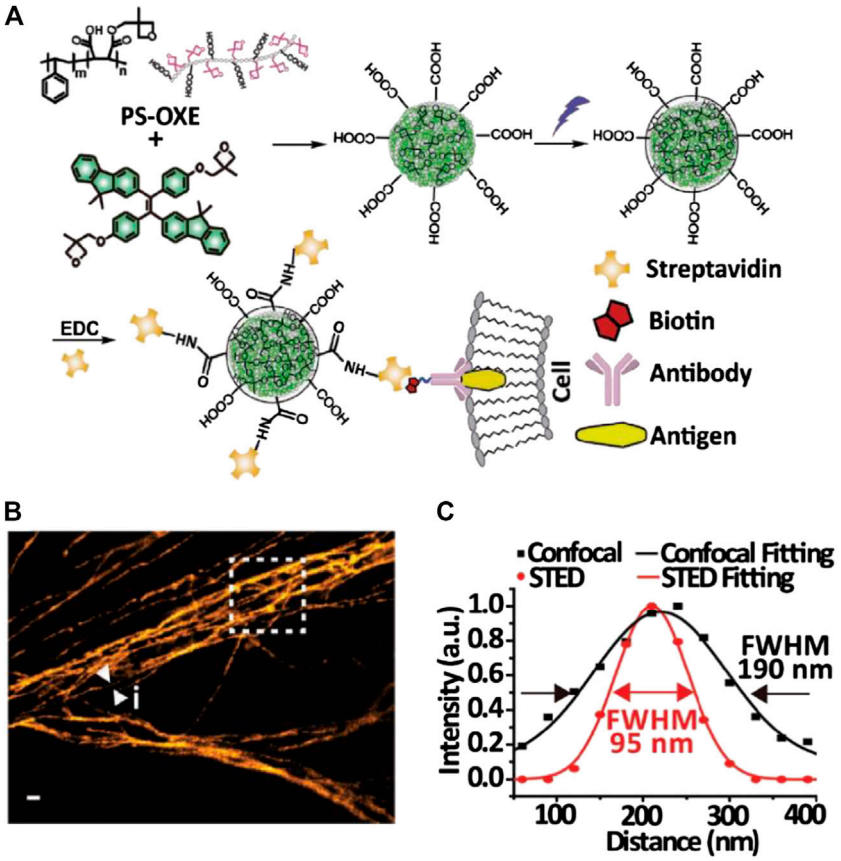

FIGURE 4 | Bioconjugated AIE dots for STED imaging (Fang et al., 2017). **(A)** Synthesis and modification of AIE dots for specific labeling. **(B)** STED microscopy image of microtubules in MCF-7 cells labeled with AIE dots. **(C)** Plotfile for confocal and STED imaging results in the selected area.

comes from defects like nitrogen vacancy centers (NV^-) or nitrogen-vacancy-nitrogen (N-V-N) in the nano-sized sp^3 diamond crystals, which endows them with red or green fluorescence (Hsiao et al., 2016). Unlike organic fluorophores, the NV^- centers are basically non-photobleaching and nonblinking and have longer PL lifetime (~20 ns), promoting their STED applications.

The covalent crystalline nature of FNDs guarantees its outstanding optical stability under harsh physical/chemical conditions. However, such characteristics also cause difficulty in morphology/functionalization control during the synthesis (Yu et al., 2005). Typically, the size of synthesized FNDs ranged from 30 to 100 nm, which still hampers its application as a subdiffraction imaging tag to a certain extent.

Despite the relatively large particle size of FNDs, the fluorescent NV^- centers inside exist at the atomic level, which therefore makes them an ideal target for superresolution imaging. Hell and coworkers first reported the STED imaging with diamond samples with NV^- emitting centers with an ultrahigh resolution of ~6 nm in 2D-STED imaging (Rittweger et al., 2009), a resolution record which was later refreshed to ~2.4 nm (Wildanger et al., 2012). However, such results can only be obtained with an ultrahigh STED power of several GW/cm^2. With a reasonably lowered STED power (~260 mW, considering the endurance of cells), the lateral resolution in STED imaging of dispersed FNDs was ~40 nm (Han et al., 2009); otherwise, with a 100-mW STED power, the lateral and the axial resolution of 3D-STED imaging could reach ~100 nm. On this basis, the potential application of FNDs for STED bioimaging was further explored by Chang and coworkers (Tzeng et al., 2011). To overcome the aggregation tendency of FNDs in physiological environments, Chang et al. modified the FNDs nonconvalently with bovine serum albumin (BSA) to improve their delivery efficiency into HeLa cells for nonspecific labeling. Under a STED power of 180 mW, the lateral resolution of individual FNDs in cells reached 39 nm (**Figure 6**) in accordance with previous results. Similarly, Laporte and Psaltis performed cell imaging with endocytosed green fluorescence FNDs and achieved ~90 nm resolution with 130 MW/cm^2 STED intensity (Laporte and Psaltis, 2016).

QDots

QDots are nano-sized semiconductor particles with quantum confinement-induced photoluminescent features (Michalet, 2005). Compared with molecular fluorophores, QDots feature higher brightness and photostability, better monochromaticity, and continuously tunable emission (determined by particle size), which altogether facilitate their applications as imaging probes.

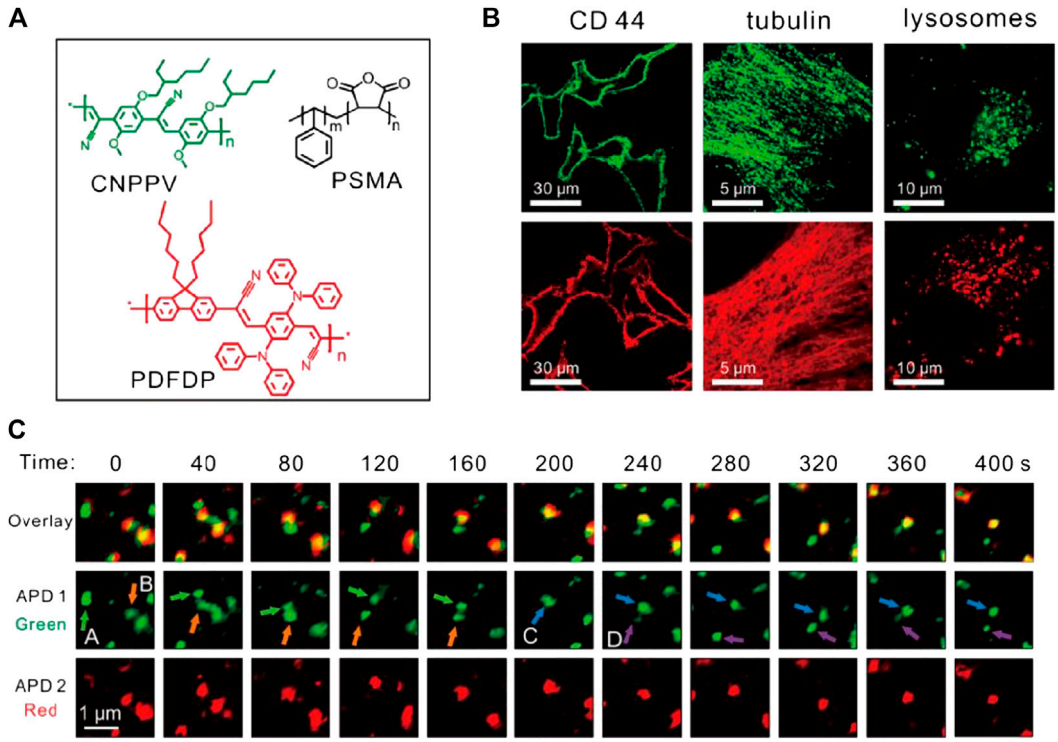

FIGURE 5 | Bioconjugated PDots for STED imaging (Wu et al., 2020). **(A)** Chemical composition of two PDots. **(B)** STED imaging of subcellular structures bonded with PDots through immunofluorescence labeling. **(C)** Application of PDots for real-time tracking of organelle interactions.

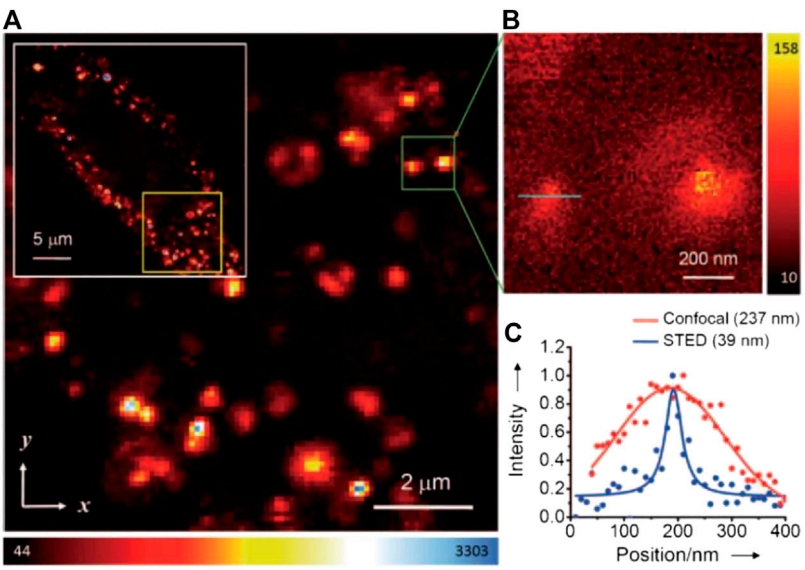

FIGURE 6 | Confocal and STED imaging of HeLa cells labeled with BSA-conjugated FNDs by endocytosis (Tzeng et al., 2011). **(A)** Confocal image of HeLa cells labeled with FNDs. **(B)** STED image of single FNDs. **(C)** Plotfile for confocal and STED imaging results in the region of interest (green line in **B**).

Despite their composition with heavy metal elements (Cd, Pb, etc.), the toxicity of QDots is still proved acceptable for *in vitro* research (Gao et al., 2005). To this day, the technique of immunofluorescence labeling with QDots has been vastly developed, which facilitates their application for superresolution bioimaging.

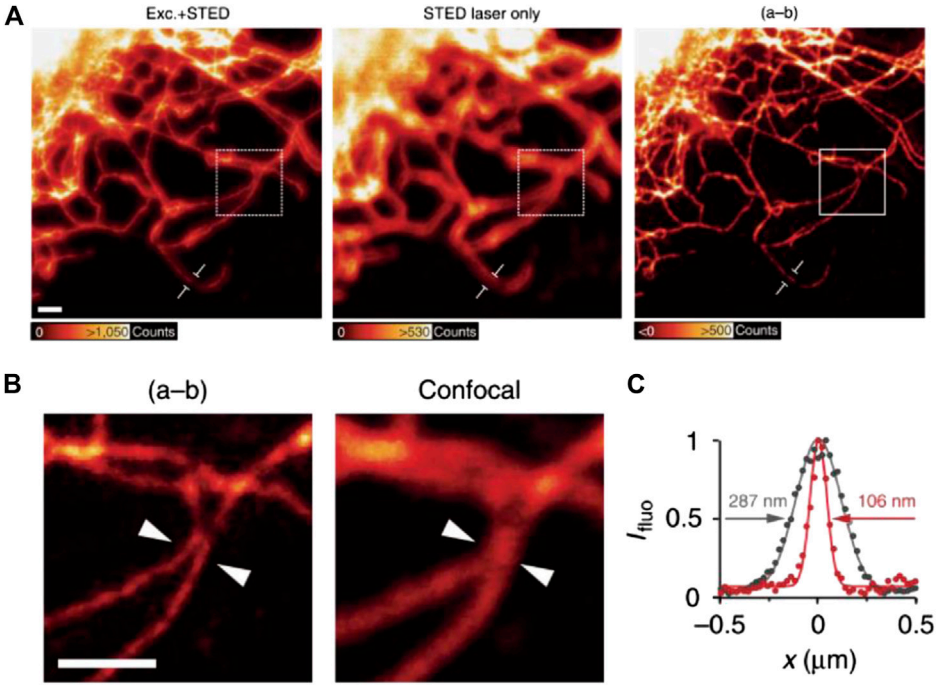

FIGURE 7 | STED imaging of vimentin fibers labeled with commercial QDot705 (Hanne et al., 2015). **(A)** Fluorescence signal acquired by applying excitation + STED, STED light only, and the final image corrected by subtraction. **(B)** The comparison of resolution of corrected STED image and confocal results. **(C)** Plotfile for confocal and corrected STED results in the region of interest.

In brief, QDots have a series of advantages such as small size (generally <20 nm), high brightness, long PL lifetime, and excellent photostability ensuring its potential in superresolution imaging, especially STED imaging where the photostability of probes is always emphasized. However, the application of QDots in STED also enters some challenges due to the unique optical features of these materials. For example, Auger recombination in isolated QDots is known to suppress the stimulated emission of QDots, which lowers the depletion efficiency by STED, especially in smaller dots (Lesoine et al., 2013). Another issue is that the QDots tend to suffer from re-excitation by the STED light, due to their broad absorption and large two-photon absorption cross section, which could cause high background (Larson, 2003).

In 2013, Lesoine et al. reported the first example of STED imaging of individual QDots. To suppress Auger recombination, Lesoine et al. synthesized QDots with a CdS-coated CdSe structure for enhanced biexciton lifetime (Lesoine et al., 2013). An average 40 ± 10 nm resolution was achieved with a 2.0-nJ STED photon power, which was around 10 times improved compared with the confocal resolution (450 ± 90 nm).

In 2015, Hanne and Hell et al. reported the first case of STED imaging with a commercially available CdSe QDot: Qdot705 (Hanne et al., 2015). Despite the significant re-excitation (~26% of the total emission) by 775 nm STED light, subdiffraction resolutions of 54 nm for single particles and ~100 nm for labeled vimentin fibers were achieved by subtracting the re-excitation background through a second scan (**Figure 7**).

It should be noted that the improvement in imaging quality and suppression of anti-Stokes emission background could also be accomplished by optimizing the emission and depletion wavelength. Our group recently reported the successful STED imaging of green-emitted CdSe@ZnS QDots with a resolution of 21 nm (Ye et al., 2020) under the excitation/depletion of commercially available 488/592 nm lasers. In contrast to Hanne et al.'s report, the STED laser did not evoke detectable anti-Stokes emission of the QDots in this case, which might be a result of the far separation of spontaneous emission tail and the STED wavelength.

Apart from the group II~VI semiconductor QDots, the recent-emerging lead-halide perovskite QDots also have shown their potential as STED probes (Ye et al., 2018): in 2018, Ye et al. reported the first example of STED imaging with $CsPbBr_3$ QDots. Impressively, a lateral resolution of 20.6 nm was achieved under 39.8 mW STED power.

CDots

CDots generally refer to a class of sub-10-nm luminescent particles mostly made of carbon and other nonmetal elements. Since the first discovery of these materials in 2006 (Sun et al., 2006), CDots have long been considered as promising PL probes for biological applications because of their excellent biocompatibility, high photostability (Wang et al., 2014), tunable emission (Ding et al., 2018), and high

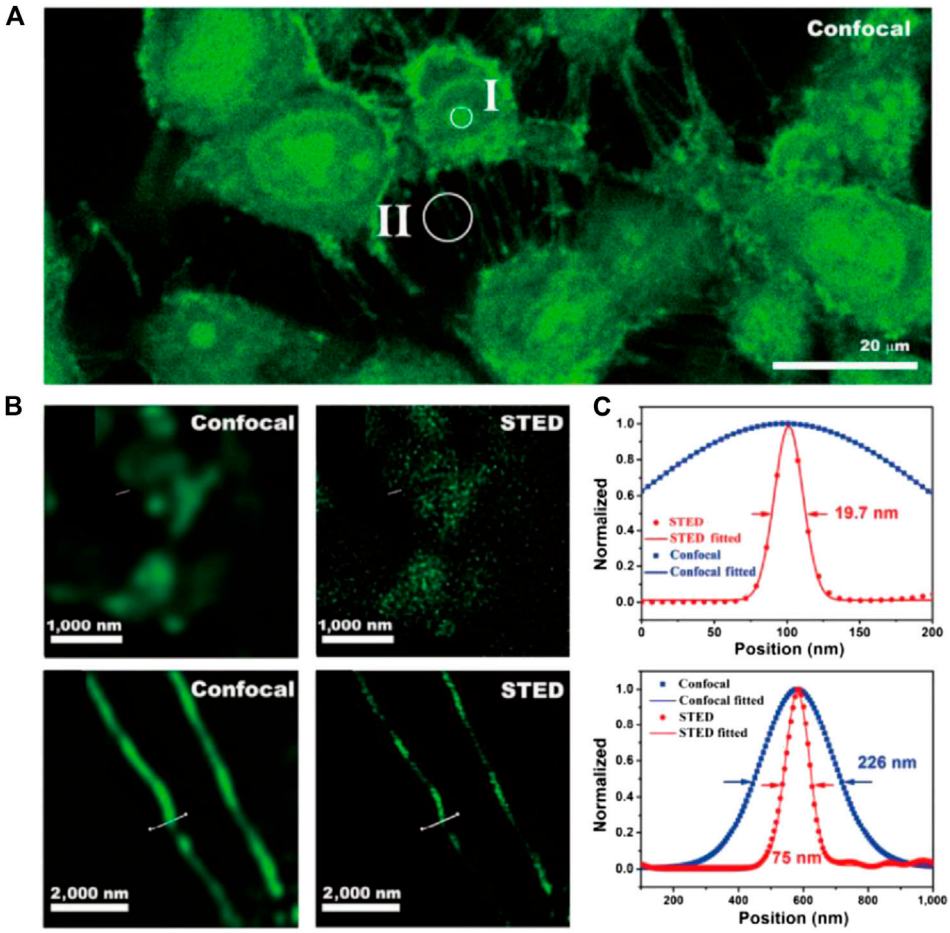

FIGURE 8 | STED imaging of living 4T1 cells stained with CDots (Li et al., 2019). **(A)** Confocal image of 4T1 cells. **(B)** The comparison of STED and confocal images of cells in the nucleus (II) and tunneling nanotubes (II). **(C)** Plotfile for confocal and STED results in both regions of interest.

PLQY (Jia et al., 2019). By virtue of their unique optical and biochemical properties, CDots have found various applications in the fields of bioimaging and theranostics, both for *in vitro* and *in vivo* research.

The first example of CDot-based STED imaging was reported in 2014 by Leménager et al. (2014). Green-emitting CDots with an average diameter of ~5 nm were incubated with MCF-7 cells, to highlight the lysosomal regions. A resolution of ~70 nm (>6-fold improvement compared with confocal) was achieved using a commercial Leica SP8 STED confocal microscopy equipped with a 592 nm depletion laser. Pitifully, this pioneer work did not provide much details on the optical performance of CDots under different experimental conditions.

Compared with other nanoprobes, CDots naturally have very small size, which facilitated their transportation into subcellular regions, especially the nucleus. The first attempt to perform nucleus STED imaging with CDots was reported by Han et al. (2019): a green-emitting CDot was synthesized by oxidizing carbon nanoparticles and modified with para-phenylendiamine and 4-carboxybutyl-triphenylphosphonium (PPh^{3+}) bromide to obtain a cation surface. The resultant materials are highly affinitive to the negatively charged nucleic acids and showed enhanced emission and red-shifting while binding DNA or RNA molecules. Based on that, two-colored confocal and STED imaging was realized using CDots as the only probe. A *z*-stack 3D reconstructed image of the chromosomes was successfully obtained by 3D-STED imaging without severe photobleaching. However, the depletion efficiency, as well as imaging resolution, was not studied in detail. Meanwhile, Hua et al. developed a strategy to synthesis red-emitting carbon dots for cellular nucleus imaging (Hua et al., 2019). A final resolution of ~140 nm was obtained in the nucleus region, with a 660 nm STED laser applied for depletion.

Despite the unique capability of CDots for nucleus STED imaging, the depletion efficiency and imaging resolution of this material are still under investigation. To this end, our group synthesized F,N-codoped CDots with high PLQY and depletion efficiency (Li et al., 2019). N,F-codoped CDots were synthesized molecular precursors through a one-pot hydrothermal process. The resultant material featured high PLQY (56%), low toxicity, chemical inertness, outstanding photostability, and, above all, high depletion efficiency for STED. Despite the intense emission

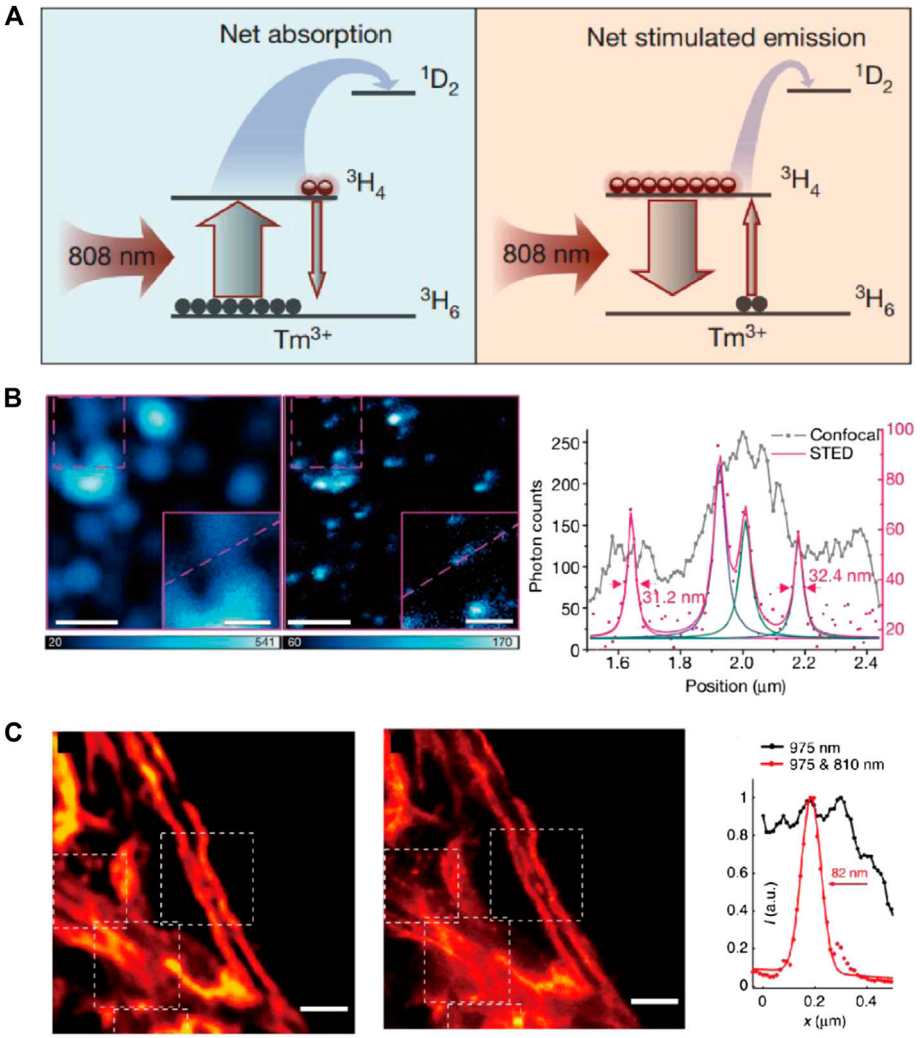

FIGURE 9 | STED performance of UCNPs. **(A)** The diagram of involved energy levels in STED process of Tm-doped UCNPs. **(B)** Particle imaging results and intensity plotfiles of Tm-doped UCNPs with confocal and STED imaging setup (Liu et al., 2017). **(C)** Confocal and STED images of cell skeletons labeled with UCNPs and corresponding plotfiles (Zhan et al., 2017).

induced by 592 and 660 nm STED light, these CDs can be efficiently depleted at 775 nm without re-excitation background. The STED resolution of nucleus structure and tunneling nanotubes of CDot-stained 4T1 cells was 19.7 and 75 nm, respectively (**Figure 8**), and considerably improved compared with confocal imaging results under low STED power (39.6 mW).

Apart from mammal cells, CDs can also be used for the imaging of microorganisms. Yang and coworkers synthesized cation-modified CDots for the labeling of negatively charged *Staphylococcus aureus* bacteria and achieved ~130 nm subdiffraction resolution under STED imaging condition (Yang J. et al., 2016). More recently, Liu et al. visualized *Streptomyces xiamenensis* with internalized CDots, also by adopting a STED imaging setup (Liu S. et al., 2020).

UCNPs

UCNPs generally refer to inorganic nanoparticles containing rare-earth elements and dopants (e.g., Yb/Tm-doped $NaYF_4$). The luminescence of these materials relies on their multiplex excited state energy influenced by the D and F electron orbits of their metallic component, which combines multiple fascinating characters including the upconverting properties, narrow emission bandwidth, and high photobleaching resistance (Haase and Schäfer, 2011). For decades, the potential bioimaging applications of these materials have been widely explored, taking advantage of their long emission lifetime and near-infrared excitation/emission wavelengths (Chen et al., 2014).

The application of UCNPs for STED-like super-resolved microscopy started in 2010s. Subdiffraction imaging was enabled by manipulating the complex intersystem cross with

donut-shaped depletion beams (Kolesov et al., 2011; Wu et al., 2015). However, stimulated emission was not reported in these reports.

The first STED imaging with UCNPs was reported in 2017. Jin and coworkers discovered the amplified stimulated emission in Yb/Tm codoped $NaYF_4$ UCNPs and utilized this phenomenon to depopulate the intermediate excited state and deplete the upconverting emission of UCNPs for the first time (Liang and Liu, 2017; Liu et al., 2017). In this case, the Tm^{3+} dopant played an important role in the STED process by introducing the essential intermediate energy states ($^3H_4$ and $^3H_6$) and enabling the photon-avalanche-like stimulated emission amplification. Unlike most STED setups where the excitation/emission/STED wavelengths each redshift from the left one, the excitation and STED wavelength for UCNPs are shorter than their emission, in order to match the complex energy levels in these inorganic emitters (**Figure 9A**). For potential bioimaging applications, 13 nm UCNPs were synthesized and imaged with 980 nm excitation and 800 nm depletion light. As a result, a resolution of ~28 nm (~1/35 of the excitation wavelength) was reached at 7.5 MW/cm^2 STED intensity (**Figure 9B**).

The same year, He, Zhan, and coworkers also independently established results similar to STED imaging with Tm-doped UCNPs (Zhan et al., 2017). He et al. pointed out that the complex cross relaxation in Tm/Tb-doped UCNPs is essential to initiate the STED process, which could be readily enhanced by increasing the content of rare-earth dopants (in accordance with Jin et al.'s conclusion). Different from Jin, He et al. believe the population inversion happened at a higher energy level ($^1D_2$) and assigned the stimulated emission of UCNPs under 810 nm (STED laser) irradiation to the $^1D_2 \rightarrow {}^3F_2$ transition. A resolution of ~66 nm was achieved in single-particle STED imaging with 17.7 MW/cm^2 STED light intensity. For bioimaging applications, the UCNPs were conjugated with antibodies and used for immunofluorescence labeling of cytoskeleton protein in living HeLa cells, which achieved a resolution of 82 nm (**Figure 9C**).

To further overcome the slow imaging speed [~4 ms per pixel (Liu et al., 2017)] due to the slow emission transients of UCNPs, Zhan et al. further developed a fast imaging method based on the previous work (Peng et al., 2019). Herein, the content of sensitizer (Yb^{3+}) was increased to enhance the emission intensity and accelerate emission kinetics simultaneously, which successfully narrowed down the average pixel dwell time for UCNPs-STED to 10 μs, the same as typical STED scanning speed for molecular probes. Besides the most studied Tm/Yb-doped materials, other UCNPs also showed potential for STED imaging, but with a lower depletion efficiency (Krause et al., 2019): Krause and coworkers tested the STED performance of Dy^{3+}- and Eu^{3+}-doped $NaYF_4$ UCNPs with a resolution of 90 nm at 320 MW/cm^2 depletion intensity.

Despite the outstanding performance of UCNPs for STED imaging, it should be noted that irremovable re-emission backgrounds occur due to the upconversion excitation, which limits the STED resolution of UCNPs under higher STED laser power. Fortunately, the intensity of such irreversible background amounts to less than 10% of the total emission (Liu et al., 2017; Zhan et al., 2017) and therefore has little influence compared with other issues like particle size and achievable laser power.

LPR Hybrids

The LPR effect of noble metal nanoparticles (Au/Ag) has long been adopted as a powerful tool for PL enhancement (Kneipp et al., 1997; Tovmachenko et al., 2006). In 2012, Sivan et al. first established a theoretical research on the possibility of utilizing LPR of metallic nanomaterial to enhance STED imaging quality (Sivan et al., 2012). In this design, the dye was wrapped in a structured gold nanoshell, which had a LPR absorption tuned to the STED wavelength, that is, red-shifted from the emission of dyes. Such structure benefited the STED applications for several reasons: first, the core–shell structure ensured substantial field enhancement in the center, which enhanced the depletion efficiency of the dye by a factor Γ (that is, reduced the required STED power by Γ^{-1}). Second, the singlet and triplet excited state decay rates were enhanced due to the metallic shell, which alleviated the photobleaching effect. Third, as a result of the first and second effects, it would be possible to apply higher excitation and depletion power for imaging, leading to improvement in the resolution and signal-to-noise ratio of STED. For demonstration, Sivan and coworkers studied a 26 nm gold particle with 10 nm dye-capsuled silica core as a standard model. The calculated resolution of this nanoparticle-assisted STED method (named NP-STED by Sivan et al.) showed a striking 7 times improvement compared with the conventional STED method. Furthermore, theoretical calculation indicated that the performance of this NP-STED method can be further improved by increasing the thickness of the metallic shell. That being said, NPs with smaller particle size have more potential in realistic applications, considering the intrinsic goal of precise localization in STED imaging. In a following research, Sivan further completed the model of NP-STED with different STED pulse durations (including continuous wave STED), in different time-gating conditions (Sivan, 2012). The abovementioned pioneer works on the concept of NP-STED with plasmon-assisted resolution improvement feature were acknowledged and reviewed by Balzarotti and Stefani, who pointed out that compared with nanoshells, metallic nanorods might be more simple and realistic in practice (Balzarotti and Stefani, 2012). Balzarotti and Stefani envisioned a nanorod particle with two LPR peaks (corresponding to transverse and the longitudinal dipolar modes, respectively) that can be adjusted to amplify both the excitation and STED light by near-field effect. Ideally, the fluorescent probe should be attached near the center of this rod for maximal improvement in the STED resolution and signal-to-noise ratio.

In 2014, applicability of the conceptual NP-STED method was finally supported by solid experimental results (Sonnefraud et al., 2014). Herein, Sonnefraud, Sivan, and other coworkers managed to synthesize batches of uniformed hybrid nanoparticles with 60 nm fluorescent cores and 20-nm-thick gold shells. This composite gives a 670-nm emission peak and a 780-nm LPR absorption, the latter of which efficiently overlapped with the STED wavelength. In this case, the depletion efficiency was enhanced by ~4 times ($\Gamma = 3.8 \pm 0.8$). The reason for the

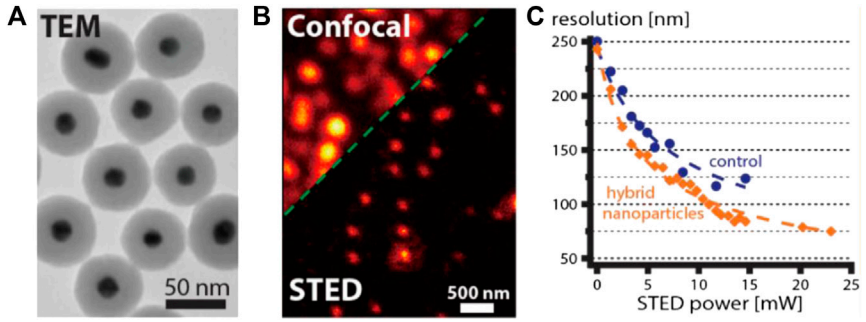

FIGURE 10 | STED performance of typical LPR hybrids (Urban et al., 2018). **(A)** The transmission electronic microscopy (TEM) image of LPR hybrids synthesized by Urban et al. **(B)** Confocal and STED imaging results of single LPR hybrid particles. **(C)** The comparison of resolution enhancement for dye-doped particles with and without (control) LPR effect under different STED powers.

small Γ value might be due to the existence of background fluorescence of metallic components, which was not considered in the theoretical model. In the experimental work by Cortés, Sivan, and other coworkers, they further improved the results of NP-STED by using gold nanorods instead of shell structures (Cortés et al., 2016). Compared with the former strategy, conjugating dyes onto the rods avoided unwanted quenching of fluorophors nearby the metal, and the overall metal usage was also reduced owing to the more effective LPR effect. As a result, the enhancement of STED can be further facilitated, and the parasitic background of gold luminescence clearly reduced. The confluence of multiple positive effects gives a doubled Γ value of ~8.5. However, the final imaging resolution of two studies for dispersed particles is only slightly higher than that of the confocal diffraction limits (~200 nm).

Clearly, further improvement in resolution is required to promote realistic applications of NP-STED in bioimaging. To this end, Hell and Sivan et al. further developed 50 nm LPR hybrid particles with gold core and a silica shell doped with molecular dye Atto488. Such structure led to a variable-field enhancement effect within the particle that decayed as the distance from metallic core increased. As a result, the overall near-field enhancement level is expected to be lower than that of the gold shell or nanorod particles. Interestingly, despite the lower Γ value predicted by calculation (~1.34 for average particles), the overall performance of this new material actually exceeded the previously reported ones (Urban et al., 2018). Specifically, a final resolution of 75 nm was achieved with a STED power of ~20 mW (**Figure 10**), which equaled to a 3.3-fold improvement in resolution with respect to the diffraction limit of confocal microscopy. Meanwhile, the power requirement was ~1.75 times lower than that needed for the standard dye (8.1~10 MW/cm^2).

It is also worth noting that the LPR field enhancement effect is a versatile tool that not only amplifies STED effect but also modulates the excitation-emission dynamics and, in some cases, entirely alters the characteristics of the original spontaneous fluorescence. A good example was given by the surface plasmon laser (spaser) technique, in which surface plasmon of noble metals was used to induce the lasing emission of fluorophores in hybrid nanoparticles (Galanzha et al., 2017). The resultant emissions are highly efficient, monochromatic, and stable, which all benefit their potential bioimaging applications. Recently, Kang and coworkers demonstrated the first example of spaser-based STED (Gao et al., 2020). Similar to the conventional STED process, the depletion of spaser emission power under increasing STED laser power corresponds well with the typical square root law. However, the role of metallic plasmon in this case is quite different from that of the NP-STED model. As depicted in **Figure 11**, the plasmonic cavity facilitates the spaser emission from the T2 energy level, while the depletion by STED happened on the S1 level (which corresponds to the spontaneous fluorescence of the bare dyes without spaser construction). Such configuration is quite the opposite of most STED processes but yields similar resolution improvement. With a 300-mW STED power, the spaser probe proved a ~74-nm resolution, together with an ultranarrow emission bandwidth of ~10 nm.

PROS AND CONS OF STED NANOPROBES: SYSTEMATIC COMPARISON

To further illustrate the advantages and disadvantages of different STED nanoprobes, herein we systematically cross-compare these materials with molecular STED probes in terms of morphology and functionalization, optical performance, and STED bioimaging utility.

Morphology and Functionalization

Particle Size

The currently reported STED nanoprobes have different sizes ranging from ~2 nm to slightly over 100 nm (see **Table 1**; **Figure 12A**). The larger size of these materials compared with molecular probes (mostly <1 nm) raised several issues, which may interfere with the STED imaging quality. For example, the labeling density of nanoparticles is inevitably lower than that of molecules, due to their larger size (**Figure 12B**; Wu et al., 2020). Furthermore, nanoparticles beyond ~30 nm suffer from

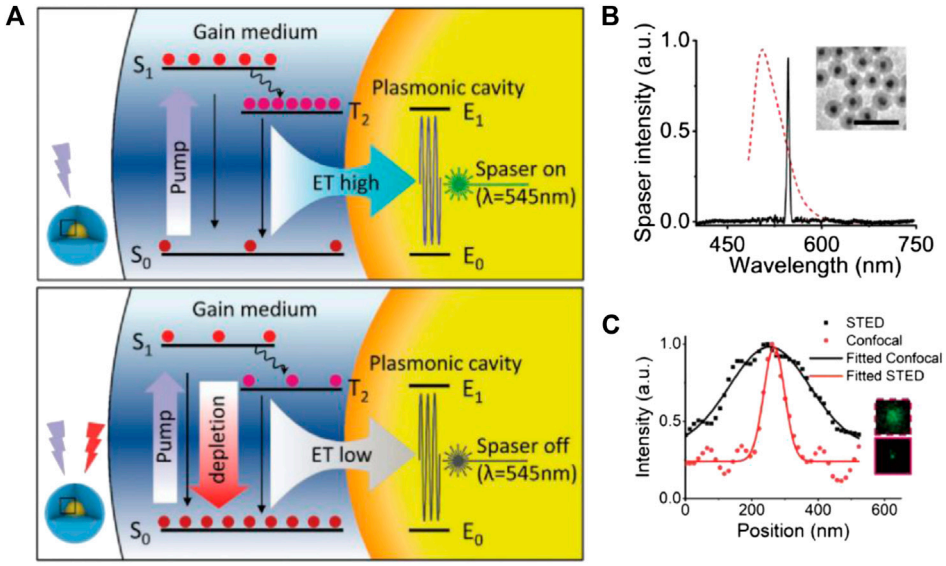

FIGURE 11 | STED performance of spaser nanoprobe (Gao et al., 2020). **(A)** The energy diagram of spaser in STED; notice that the energy of STED light is higher than the spontaneous emission energy. **(B)** Typical emission spectra of spaser (black solid) and the original dye (red dotted). **(C)** Resolution enhancement from confocal to STED imaging and the corresponding plot files.

TABLE 1 | Summary of the particle sizes and surface functionalizing methods for STED probes.

Categories	Size	Functionalizing methods	References
Molecular dyes and FPs	<1 nm		Hein et al. (2008), Meyer et al. (2008), Wildanger et al. (2009)
Dye-doped SiNPs	Tunable from 30 to 100 nm; smallest size <2 nm	Through silane linkers	Schubbe et al. (2010), Schübbe et al. (2012), Peuschel et al. (2015), Tavernaro et al. (2017), Man et al. (2019), Liang et al. (2020)
AIE dots	10~50 nm	Amidation (NHS-EDC)	Yu et al. (2015), Fang et al. (2017), Li et al. (2017), Li et al. (2018), Xu et al. (2020)
PDots	25~50 nm	Amidation (NHS-EDC)	Wu et al. (2018b), Wu et al. (2020)
FNDs	35~70 nm	Noncovalent passivation	Han et al. (2009), Rittweger et al. (2009), Tzeng et al. (2011), Prabhakar et al. (2013), Laporte and Psaltis, (2016)
QDots	10~20 nm	Ligands + amidation (NHS-EDC)	Lesoine et al. (2013), Hanne et al. (2015), Yang et al. (2016b), Ye et al. (2018), Ye et al. (2020)
CDots	3~7 nm	Amidation (NHS-EDC/ $SOCl_2$)	Leménager et al. (2014), Yang et al. (2016a), Han et al. (2019), Hua et al. (2019), Li et al. (2019), Liu et al. (2020b)
UCNPs	10~30 nm	Ligand + amidation (NHS-EDC)	Liu et al. (2017), Zhan et al. (2017), Peng et al. (2019)
LPR hybrids	25~100 nm	Streptavidin–biotin binding	Sonnefraud et al. (2014), Cortés et al. (2016), Urban et al. (2018), Gao et al. (2020)

insufficient transportation into and within cells, which might lead to poor targeting ability in bioimaging (Schübbe et al., 2012). Particles with even a larger size might induce an unneglectable steric effect, which severely interferes with subcellular targeting and may cause potential cellular damage, and meanwhile also put a physical limitation on the resolution (Schubbe et al., 2010; Prabhakar et al., 2013).

Fortunately, the size control method of most colloidal materials is mature nowadays, and sub-30-nm-sized NPs, including UCNPs (Liu et al., 2017; Zhan et al., 2017), SiNPs (Liang et al., 2020), AIE dots (Fang et al., 2017; Li et al., 2017; Li et al., 2018), PDots (Wu et al., 2020), and QDots (Lesoine et al., 2013; Hanne et al., 2015; Ye et al., 2018; Zhao et al., 2019), have all been successfully fabricated for STED applications, some of which are even commercially available (Hanne et al., 2015; Zhao et al., 2019). CDots (Leménager et al., 2014; Wang et al., 2017; Han et al., 2019; Hua et al., 2019; Li et al., 2019), on the contrary, are naturally nano-sized (<10 nm) and are well known for their fast transport dynamics across membranes (Lu et al., 2019). For FNDs and LPR nanohybrid particles, the smallest particle size in reported STED imaging cases is 40~50 nm (Tzeng et al., 2011; Urban et al., 2018). However, such limitations could be overcome, as the synthesis of smaller particles has also been reported (Liu P. et al., 2020; Ma et al., 2020).

In this sense, despite a few cases, the disadvantages of large particle size have been well addressed for most STED nanoprobes. Subsequently, synthesizing sub-5-nm-sized nanoparticles (Hua et al., 2019; Liang et al., 2020) should be the next target, as they in

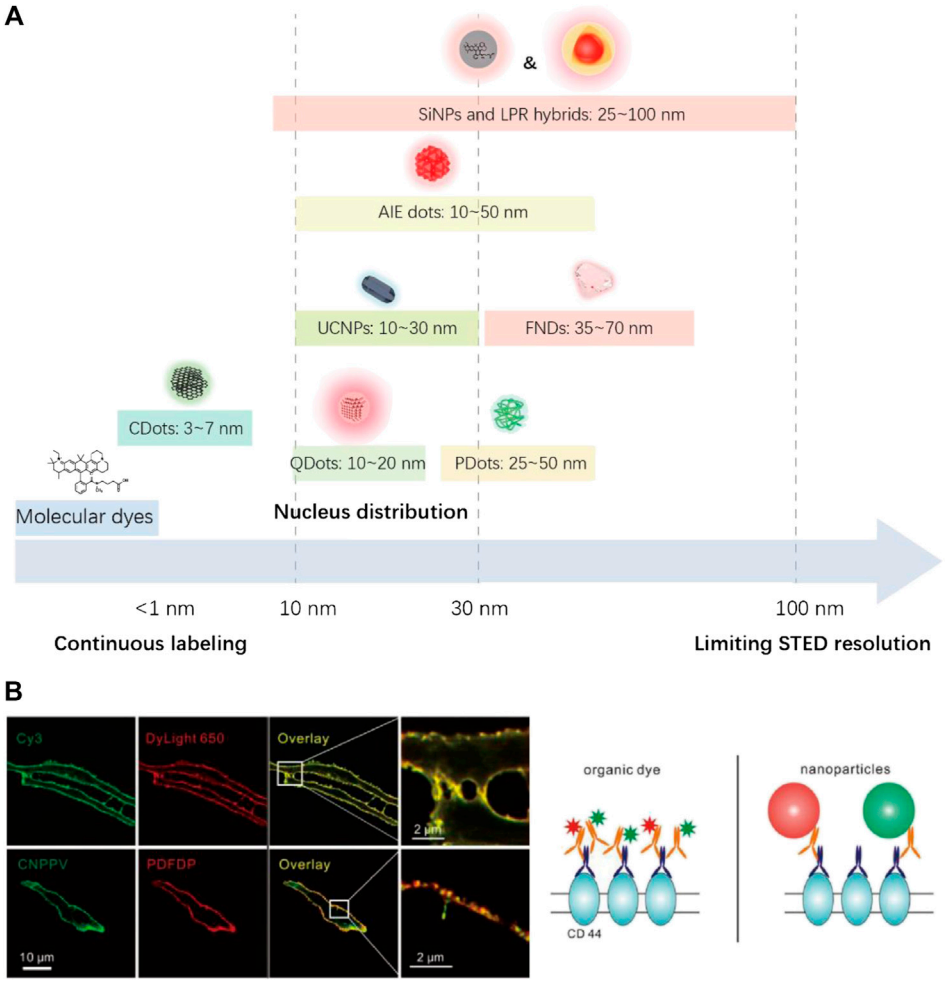

FIGURE 12 | (A) Size distribution of reported STED nanoprobes (also see **Table 1**). **(B)** The observation of discontinuous labeling of nanoparticles due to steric effect (Wu et al., 2020).

principle could provide a better biological and optical performance without losing the ultrafine targeting ability of molecular probes.

Functionalizing Methods

Compared with molecular dyes or FPs, the modification of nanoparticles faces more challenges due to significant steric effects. Still, many applicable functionalizing methods have been put forward, and some have proved applicable for the modification of STED nanoprobes (see **Table 1**).

Nanoparticles with full organic composition (AIE dots and PDots) usually consist of highly carboxylated surficial structures (Fang et al., 2017; Wu Y. et al., 2018; Wu et al., 2020). Such characters enable the facile functionalization of these particles with aminated molecules or proteins through the highly efficient amidation catalyzed by N-hydroxysuccinimide (NHS) and 1-(3-dimethylaminopropyl)-3-ethylcarbodiimide (EDC). For carbon materials like FNDs or CDots, surficial carboxyl groups can be induced by chemical oxidation (Tzeng et al., 2011; Han et al., 2019). Despite that, FNDs still suffer from severe aggregation tendency and have only been successfully passivated by a noncovalent method, due to their large size (Tzeng et al., 2011). Comparatively, nano-sized CDots can be more easily functionalized by chemical methods, utilizing either their carboxyl (Han et al., 2019) or amine groups for modification (Yang J. et al., 2016). Such strategies have been adopted to produce CDot probes for the targeting of different organelles in living cells (Wu X. et al., 2018), which might play important roles in STED imaging.

By contrast, nanoprobes with inorganic surface undergo more complicated functionalization routes. For SiNPs, their surficial Si-OH groups are not very reactive with most linkage groups (carboxyl, amine, etc.). Therefore, the functionalization of SiNPs is mostly performed through silane linkers like APTES before further modification with functional molecules by amidation (Schubbe et al., 2010; Schübbe et al., 2012; Man et al., 2019). This might lead to an increase in particle size during the modification, altering the biodistribution of these probes, especially for smaller particles.

TABLE 2 | Summary of photostability and saturation intensities for STED probes.

Categories	Photostability	I_{sat}	References
Molecular dyes and FPs	Very poor, bleachable within tens of STED scans	$10^{1\sim2}$ MW/cm^2	Hein et al. (2008), Meyer et al. (2008), Wildanger et al. (2009)
Dye-doped SiNPs	Poor [<50% intensity remains after 15 min of continuous scanning; exception: (Man et al. (2019)]	~$10^{-1\sim2}$ MW/cm^2 depending on dyes Lowest reported value: 0.18~0.188 MW/cm^2 (Man et al. (2019), Liang et al. (2020)	Schubbe et al. (2010), Schübbe et al. (2012), Peuschel et al. (2015), Tavernaro et al. (2017), Man et al. (2019), Liang et al. (2020)
AIE dots	Robust (>50% intensity remains after 30 min of continuous STED scanning)	~$10^{1\sim2}$ MW/cm^2 (estimated)	Yu et al. (2015), Fang et al. (2017), Li et al. (2017), Li et al. (2018), Xu et al., 2020)
PDots	Robust (>50% intensity remains after 2 h of continuous STED scanning)	~10^{-1} MW/cm^2 (estimated)	Wu et al. (2018b), Wu et al. (2020)
FNDs	Non-photoleaching	0.7~6.6 MW/cm^2	Han et al. (2009), Rittweger et al. (2009), Tzeng et al. (2011), Prabhakar et al. (2013), Laporte and Psaltis, (2016)
QDots	Robust (>50% intensity remains after 2~3 h of continuous STED scanning or thousands of scans)	0.129~0.192 MW/cm^2	Lesoine et al. (2013), Hanne et al. (2015), Yang et al. (2016b), Ye et al. (2018), Ye et al. (2020)
CDots	Robust (no significant bleaching after ~1000 continuous scans)	0.226 MW/cm^2 Li et al. (2019)	Leménager et al. (2014), Yang et al. (2016a), Han et al. (2019), Hua et al. (2019), Li et al. (2019), Liu et al. (2020b)
UCNPs	Robust (no significant bleaching after ~200 min of continuous STED scaning)	0.19~0.849 MW/cm^2	Liu et al. (2017), Zhan et al. (2017), Peng et al. (2019)
LPR hybrids	Improved compared with molecular dyes or SiNPs	4.6~5.8 MW/cm^2	(Sonnefraud et al. (2014), Cortés et al. (2016), Urban et al. (2018), Gao et al. (2020)

Inorganic emitters with metal element on their surface (QDots and UCNPs) can be functionalized with ligands that introduce active functional groups, which further enable the fabrication of bioconjugates for immunofluorescence label (Hanne et al., 2015; Zhan et al., 2017). At present, such strategies have been fully developed and utilized in commercially available QD probes. Meanwhile, gold-shelled LPR hybrids can be directly modified with streptavidin and further bound with biotinylated structures (Cortés et al., 2016).

Optical Performance

The optical performance of different nanoparticles can be compared in the following different dimensions (see **Table 2**).

Photostability

Generally speaking, nanoparticle probes, compared with molecular probes, are more stable against photobleaching, which benefits their applications in long-term and 3D-STED imaging (Han et al., 2009; Ye et al., 2018; Han et al., 2019). The increased photostability of nanoparticles can be explained in several ways. First, the compact nanostructure of these materials separated the photoluimincent centers from environmental oxygen, thus effectively alleviating the photo-oxidation effect, which causes permanent bleaching of fluorophores. Second, the compact fluorophores and/or solid media provide additional intramolecular relaxation pathways, which also help alleviate photobleaching.

Inorganic emitters like QDots, UCNPs, and FNDs perform well under intense irradiation (×$10^{1\sim2}$ MW/cm^2) for ~1 h (Han et al., 2009; Rittweger et al., 2009; Lesoine et al., 2013; Hanne et al., 2015; Laporte and Psaltis, 2016; Zhan et al., 2017; Ye et al., 2020), due to the high stability of inorganic crystalline structures compared with linear covalent bonds. Specifically, FNDs are highly stable to extremely high STED power (several GW/cm^2), which allows nanoscale STED resolution comparable to electronic microscopy (Rittweger et al., 2009; Wildanger et al., 2012).

CDots are usually considered as highly photostable materials that endure tens of MW/cm^2 STED power (Leménager et al., 2014; Wang et al., 2014; Li et al., 2019), but there are also evidence that some of the CDots are not as stable as typical inorganic nanomaterials (still, more stable than molecular fluorophores) (Hua et al., 2019), which suggests that their fluorescence might be related to embedded fluorophores rather than crystalline carbon cores (Qu and Sun, 2020).

Condensed organic nanoparticles like AIE dots and PDots are also resistant to photobleaching and can typically perform continuous STED imaging for up to 1~2 h with over 50% fluorescence intensities remaining (Li et al., 2017; Wu Y. et al., 2018; Wu et al., 2020). Compared with other nanoparticles, dye-doped SiNPs suffer most from photobleaching, as their fluorescence originates from dispersed molecular emitters (Tavernaro et al., 2017). This issue can be addressed by either introducing metallic LPR structures (Sivan et al., 2012) or eliminating SOC by material engineering (Liang et al., 2020), which enhances their photostability to an acceptable level, similar to other nanoparticles.

Saturation Intensity

Saturation intensity is another crucial property of STED nanoprobes. In a typical STED imaging setup, the resolution is given as

$$\delta_{STED} = \frac{\lambda}{2NA\sqrt{1 + I_{STED}/I_{sat}}} \quad (1)$$

where I_{STED} and I_{sat} are the applied STED power and the saturation power of the materials, respectively. Considering the resolution limit for confocal imaging,

$$\delta_{confocal} = \frac{\lambda}{2NA} \quad (2)$$

For most molecular and protein STED probes, their I_{sat} values range from $10^{1\sim2}$ MW/cm^2 (Hein et al., 2008; Bianchini et al., 2012). In this sense, the STED power required to achieve ~100 nm resolution (approximately 2~4 times improved from the limiting resolution of confocal imaging) easily exceeded 100 MW/cm^2, which causes potential cellular damage and severe photobleaching. Apparently, lowering the I_{sat} value could help reducing the STED power requirement and improve the STED imaging quality. According to Schrof and Hell et al. (Schrof et al., 2011), the saturation intensity of a STED probe is determined by

$$I_{sat} = \frac{h\nu}{\sigma\tau} \quad (3)$$

with $h\nu$ being the photon energy, σ the cross section for stimulated emission, and τ the PL lifetime. Compared with the dispersed molecular emitters, the compact nanoemitters typically show higher brightness and larger optical cross sections, which contribute to a lower saturation intensity or, equally, higher depletion efficiency. Furthermore, inorganic emitters like UCNPs and QDots typically have a longer PL lifetime (×10 ns), which also contribute to their low saturation intensity values. To this day, nanoprobes like UCNPs (Liu et al., 2017; Liang and Liu, 2017), QDots (Ye et al., 2020; Ye et al., 2018), CDots (Li et al., 2019), and SiNPs (Liang et al., 2020; Man et al., 2019) have been reported with an ultralow saturation intensity of 10^{-1} MW/cm^2, which are 2~3 magnitude lower than that of typical molecular STED probes. For FNDs, the lowest reported saturation intensity for N-V and N-V-N defects was 1 MW/cm^2 (Han et al., 2009) and 2.5 MW/cm^2 (Laporte and Psaltis, 2016), respectively, slightly lower than that of molecular probes.

It should be noted that compared with other materials, the saturation intensities of SiNPs may vary a lot according to the specific type of dyes used for doping. For example, SiNPs doped with the Atto647N dye showed STED power requirement (100~400 MW/cm^2) similar to that of the bare dyes (Tavernaro et al., 2017). Meanwhile, SiNPs doped with specially designed fluorophores (non-SOC (Liang et al., 2020) or non-ACQ (Man et al., 2019)) showed an ultralow I_{sat} of ~10^{-1} MW/cm^2.

The exact saturation intensity values of AIE dots and PDots are absent from the literature, which can be estimated according to their power requirement for STED imaging. For AIE dots, their saturation intensities are estimated to be in the range of $10^{1\sim2}$ MW/cm^2, judged from both the STED power requirement for imaging (>100 mW) (Fang et al., 2017; Li et al., 2017; Li et al., 2018; Xu et al., 2020) and the comparison of their depletion efficiency with molecular probes like coumarin (Yu et al., 2015). Although their depletion efficiency is similar to that of molecular dyes, the achievable resolution has been improved (Li et al., 2017) due to their higher endurance to STED photons. For PDots, the saturation intensities are estimated to be ~10^{-1} MW/cm^2.

LPR hybrids have smaller saturation intensity values than the original dyes used in the hybrid, which are determined by

$$I_{sat'} = \frac{I_{sat}}{\Gamma} \quad (4)$$

where $I_{sat'}$ is the effective saturation intensity of LPR hybrid, I_{sat} is the saturation intensity value of the dyes, and Γ is the factor describing the enhancement of depletion effect induced by LPR. So far, the reported $I_{sat'}$ of LPR hybrids is still limited to ~5 MW/cm^2 (Sonnefraud et al., 2014; Urban et al., 2018), partially due to the high I_{sat} value of the molecular dyes used in the hybrids.

Excitation/Emission Features

Basic excitation/emission features of the probes, such as PLQY, fluorescence lifetime, and potential re-excitation, play important roles in the STED bioimaging.

PLQY values indicate how efficient the fluorescent probe converts excitation light into emission signals. Probes with higher PLQY may provide a better signal-to-noise ratio in imaging similar excitation and depletion conditions. Herein, the reported PLQY values of different nanoprobes for STED imaging are summarized, as shown in **Table 3**. FNDs and QDs showed highest average quantum yield above ~70%, followed by CDots, PDots, and AIE dots, whose PLQY varied between 10 and 60% depending on the specific materials. The PLQY of SiNPs and LPR hybrids is highly dependent on the doped dyes and may reach a near-unity level with optimized condition (Liang et al., 2020). As for UCNPs, although their PLQY was not provided in relative research, the values are estimated to be <5% according to relative research on similar materials (Chen et al., 2012). The relative low-emitting efficiency however can be compensated by applying higher excitation power [1 mW (Liu et al., 2017) or 700 kW/cm^2 (Zhan et al., 2017)], which has been performed in STED imaging.

In terms of PL lifetime, most STED nanoprobes including organic emitters (AIE dots, PDots, and dispersed dye molecules) (Li et al., 2017; Liang et al., 2020), FNDs (Rittweger et al., 2009), QDots (Ye et al., 2020), and CDots (Li et al., 2019) have short PL lifetime ranging from 1 to 20 ns, which allows fast scanning speed and similar time-gating setup similar to molecular probes for the improvement in STED imaging quality (Wang et al., 2018). The pixel dwell times of these nanoprobes are therefore typically shorter than 1 ms. The only exception was FNDs (1~10 ms per pixel), which required longer pixel dwell times to compensate for the low signal intensities under extreme STED power. UCNPs however have much longer lifetimes scale up to μs due to complex intersystem relaxation (Liu et al., 2017), which leads to a much longer dwell time per pixel (typically 1~10 ms) than other probes. Although increasing the content of sensitizer ion may accelerate the emission kinetics (Peng et al., 2019), it might also increase the power requirement for STED imaging, as suggested in **Eq. 3**.

The re-excitation in STED imaging refers to a situation where the STED light alone induces unneglectable emission of

TABLE 3 | Summary of excitation/emission features for different STED nanoprobes.

Categories	PLQY	Lifetime	Pixel dwell times	Re-excitation	References
Dye-doped SiNPs	Depending on dyes, up to 99% Liang et al. (2020)	1~10 ns	~10 μs	Not mentioned	Schubbe et al. (2010), Schübbe et al. (2012), Peuschel et al. (2015), Tavernaro et al. (2017), Man et al. (2019), Liang et al. (2020)
AIE dots	20~30%	1~5 ns	Not mentioned	No in most cases (exception: Li et al. (2017))	Yu et al. (2015), Fang et al. (2017), Li et al. (2017), Li et al. (2018), Xu et al. (2020)
PDots	20~50%	\	0.5~1 ms	No	Wu et al. (2018b), Wu et al. (2020)
FNDs	70~95%	~12 ns (N-V defects) /27 ns (N-V-N defects)	1~10 ms	No	Han et al. (2009), Rittweger et al. (2009), Tzeng et al. (2011), Prabhakar et al. (2013), Laporte and Psaltis, (2016)
QDots	64~90.5%	8~10 ns	10~100 μs	Yes (3~26%) Can be avoided	Lesoine et al. (2013), Hanne et al. (2015), Yang et al. (2016b), Ye et al. (2018), Ye et al. (2020)
CDots	14.5~56%	~5 ns	Not mentioned	Yes, can be avoided	Leménager et al. (2014), Yang et al. (2016a), Han et al. (2019), Hua et al. (2019), Li et al. (2019), Liu et al. (2020b)
UCNPs	\	~$10^{0\sim1}$ μs	Typically, 1~10 ms. shortest reported value: 10 μs Peng et al. (2019)	Yes (<10%)	Liu et al. (2017), Zhan et al. (2017), Peng et al. (2019)
LPR hybrids	\	~0.9 ns	10~100 μs	Yes	Sonnefraud et al. (2014), Cortés et al. (2016), Urban et al. (2018), Gao et al. (2020)

the probes. In this case, a parasitic background fluorescence always exists and even enhances in the donut-shaped STED light irradiated region, which leads to dim halos in the image and prevent the further improvement in resolution (**Figure 7**). So far, nanoprobes including QDots, CDots, UCNPs, and LPR hybrids have witness re-excitation in their STED applications (see **Table 3**). For QDots, the re-excitation intensity might reach up to 26% of the total emission, which clearly damaged the imaging resolution and signal-to-noise ratio (Hanne et al., 2015). This issue however can be facilely addressed by rationally selecting a longer STED wavelength located apart from the tail of QDots' emission (Ye et al., 2020). Similarly, the re-excitation of CDots could also be avoided by using STED light with a longer wavelength (Li et al., 2019). The re-excitation of UCNPs, on the other hand, is difficult to avoid, due to their multiplex energy levels that pick up anti-Stokes excitations easily. Luckily, the re-excitation observed in UCNPs is not very intense (<10% as reported in (Liu et al., 2017) and <4% as reported in (Zhan et al., 2017)) and therefore can be omitted during the imaging. The re-excitation of LPR hybrids originates from their metallic fluorescence, which can be distinguished from the fluorescence of doped dyes by time-gating (Sonnefraud et al., 2014). Meanwhile, PDots, AIE dots, and FNDs are mostly free from re-excitation due to their relatively large Stokes shift (>100 nm), apart from occasional exceptions (Li et al., 2017).

Besides the careful selection of STED wavelength, the re-excitation can also be eliminated by other experimental or instrumental methods. For example, by applying STEDD (stimulated emission double depletion) imaging with two depletion pulses, the re-excitation background can be effectively subtracted (Gao and Ulrich Nienhaus, 2017). In other situations, the anti-Stokes emission background evoked by depletion laser generally has a shorter PL lifetime compared with the down-converted fluorescence, which therefore allows time-related background subtraction by gated STED or STED-FLIM technology (Wang et al., 2018; Ma and Ha, 2019). Another known solution is to apply adaptive STED illumination, aka the DyMIN (Dynamic intensity MINimum) method, which not only eliminates re-excitation but also alleviates photobleaching at the same time (Li et al., 2020). Still, the abovementioned methods pose high instrumental requirements that might not be satisfied by most STED devices.

STED Bioimaging Utility

The actual STED bioimaging utility of nanoparticles is determined by multiple factors, including the biocompatibility, targeting, real-time tracking ability, and power requirement.

Biocompatibility

To meet the requirements of bioimaging, especially for living cells and long-term applications, the nanoprobes must be biocompatible and nontoxic in usage. The cytotoxicity of all nanoprobes applied for STED has been extensively studied (Soenen et al., 2011; Luo et al., 2013; Wolfbeis, 2015; Reisch and Klymchenko, 2016). The conclusion can be summarized as follows:

In terms of chemical composition, materials like SiNPs, AIE dots, PDots, FNDs, and CDots that consist of nonmetal elements are generally biocompatible and nearly nontoxic with a concentration of several tens of μg/mL, which is normally 5~10 times higher than the working concentration used in imaging. Still, it should be noted that materials with large size (~100 nm) and/or aggregation tendency might induce cellular damage in long-term studies. This particularly limits the usage of bare SiNPs and FNDs, as their surface composition is hydrophobic and might form agglomerates under physiological conditions (Schubbe et al., 2010; Tzeng et al., 2011). Meanwhile, inorganic nanoparticles like QDots, UCNPs, and LPR hybrids

TABLE 4 | Summary of representative works on STED nanoprobes for bioimaging.

Categories	STED power	Resolution	Bioimaging applications	References
Dye-doped SiNPs	\	88 ± 4 nm	Cellular intake quantification	Peuschel et al. (2015)
	18~38 mW (6.27 ~13.23 MW/cm^2)	19.2 nm (particles, 38 mW) 43.6 (*in vitro*, 18 mW)	Nonspecific cell imaging	Liang et al. (2020)
	0.89 MW/cm^2	61~65 nm (particles and *in vitro*)	Nonspecific cell imaging	Man et al. (2019)
AIE dots	100 MW/cm^2	95 nm	Specific labeling (microtubule)	Fang et al. (2017)
	150 mW	74.37 nm	Specific labeling (mitochondria)	Li et al. (2018)
	144 mW	~100 nm	Nonspecific cell imaging	Xu et al. (2020)
PDots	3 mW or 10 MW/cm^2	78 nm	Specific labeling, real-time tracking, dual-color STED	Wu et al. (2020)
	3 mW or 10 MW/cm^2	68 nm		
FNDs	180 mW	39 nm	Nonspecific cell imaging	Tzeng et al. (2011)
	130 MW/cm^2	90 nm	Nonspecific cell imaging	Laporte and Psaltis, (2016)
QDots	150 mW	54 nm	Specific labeling (vimentin fiber)	Hanne et al. (2015)
	200 mW	85 nm	Specific labeling (microtubule)	Yang et al. (2016b)
	39.6 mW	21 nm	Nonspecific cell imaging	Ye et al. (2020)
	27.5 mW	20.6 nm	Nonspecific plant cell imaging	Ye et al. (2018)
CDots	\	71 (±25) nm	Lysosome imaging	Leménager et al. (2014)
	\	~130 nm	Bacteria imaging	Yang et al. (2016a)
	39.6 mW	22.1 nm	Nucleus/tunneling nanotubes imaging	Li et al. (2019)
UCNPs	\	66 nm (particles)/82 nm (cellular skeleton)	Specific labeling (cellular skeleton)	Zhan et al. (2017)
LPR hybrids	0.5~1.5 MW/cm^2	20~50% improved from confocal results*	Specific labeling (actin)	Cortés et al., (2016)

**The specific imaging resolution was not provided.*

contain heavy metal elements, resulting in potential long-term toxicity, especially for *in vivo* imaging. Fortunately, since the toxicity of inorganic nanoparticles can be largely alleviated by bioconjugation and the dosages required for imaging are generally low, the toxicity of these materials for cellular imaging has proved acceptable (Gao et al., 2005).

Another important issue however is the phototoxicity of nanomaterials. This concern comes from two major aspects. First, a number of nanomaterials have been applied in photodynamic therapies (Cheng et al., 2014), suggesting their toxicity under continuous irradiation. Second, under the continuous irradiation of STED light, some nanoprobes such as LPR hybrids showed a considerable photothermal effect (Cortés et al., 2016) that might damage the living samples, which should be taken into account in the toxicity assessment of STED nanoprobes. However, little work has been applied, except for individual reports on the low phototoxicity of PDots (Wu et al., 2020).

Specific Targeting

There are two major strategies to create specific-targeting nanoparticles. The first one is the immunofluorescence method, which is a universal method that allows the specific targeting of interested subcellular structures such as microtubules. Small-sized (<30 nm) particles like AIE dots, PDots, ligand-modified QDots, and UCNPs have all been demonstrated for subcellular targeting by the immunofluorescence method (Fang et al., 2017; Wu et al., 2020; Hanne et al., 2015; Zhan et al., 2017; Urban et al., 2018) (see **Table 4**). However, the immunofluorescence method in most cases is adapted for fixed cell, as the transportation of antibodies across the membrane requires enhanced permeability. Another problem with immunofluorescence staining is that the steric effect of nanoparticles might induce discontinuous label, which might lead to a false-dotted signal, especially when higher imaging resolutions are achieved (Wu et al., 2020). It is also worth noting that the ability of immunofluorescence labeling is also limited by the size and dispersibility of materials, as silica particles and FNDs with aggregation tendency under physiological environments have proved not to be suitable for specific targeting so far (Schubbe et al., 2010; Schübbe et al., 2012; Prabhakar et al., 2013; Prabhakar et al., 2018).

As the other option, active targeting in living cells is mostly facilitated by introducing charge and hydrophobicity/hydrophilicity through material design. For example, introducing hydrophobic cation structures might endow CDots and PDots with mitochondrial targeting ability (Li et al., 2018; Geng et al., 2019), while strong positive charge on an overall hydrophilic material might introduce affinity toward nucleic acids (Han et al., 2019). In some cases, the targeting of lysosomes or endosomes can also be achieved by utilizing the retention tendency of nanomaterials in these organelles (Leménager et al., 2014; Wu et al., 2020).

Real-Time Tracking

Bioconjugated PDots have been applied to label endosomes with different caveolins and study their interaction in real time (Wu et al., 2020). Meanwhile, CDots and AIE dots with engineered

surface charge have been used to perform real-time tracking on nucleus (Han et al., 2019) and mitochondrial (Li et al., 2018) activities (see **Table 4**).

The real-time tracking ability of STED nanoprobes is highly influenced by their imaging speed. Generally, a dwell time of <10 μs per pixel or several seconds per frame is considered acceptable for real-time tracking applications (Peng et al., 2019). For nanoparticles, two issues might decrease imaging speed and reduce their real-time tracking abilities. Firstly, STED light alone could excite the probes in some cases, which severely slows down the imaging acquisition as a second-time scanning, and thus, calculation is required to remove the background noise (Hanne et al., 2015). Fortunately, such inconvenience can be avoided by either selecting suitable STED wavelengths (Ye et al., 2020) or applying time-resolved methods for background elimination (Castello et al., 2017; Wang et al., 2018; Ma and Ha, 2019). The second issue that interferes with the STED imaging efficiency is the prolonged dwell time due to longer PL lifetime of materials. This is particularly significant for UCNPs, whose PL lifetime scales up to μs and leads to ultralong dwell time per pixel exceeding 1 ms (Liu et al., 2017). For the time being, this issue can only be addressed by accelerating emission kinetics through adjusting the material composition (Peng et al., 2019).

Resolution and Power Requirement

The resolution of STED nanoprobes is limited by three major factors, namely, the size of particles, the depletion efficiency, and endurable imaging power. As discussed above, most reported STED nanoprobes have reached the size below 30 nm, providing little limit in the resolution of imaging (typically 30~200 nm). The only exception was FNDs, which have achieved a higher resolution than particle size limitations (Rittweger et al., 2009; Wildanger et al., 2012). Still, considering the endurance of imaging samples toward STED irradiation, the bioimaging resolution was limited to ~40 nm with a 180 mW STED power (Tzeng et al., 2011).

The power requirement and single-particle resolution of nanoprobes are basically determined by their saturation intensities. Materials like QDots, CDots, SiNPs, and UCNPs have achieved saturation intensities below 0.25 MW/cm^2, allowing ~30 nm single particle resolution with a low STED power of <50 mW or intensity <20 MW/cm^2. As for AIE dots and LPR hybrid NPs, the power requirement for STED is typically 2~4 times higher (100~200 mW), while the overall resolutions are limited (~70 nm), except for individual cases with ultrahigh STED power (312.5 mW, ~30 nm) (Li et al., 2017). In comparison, the currently reported PDots for bioimaging typically require a very low STED power of <5 mW, while providing a final resolution of ~70 nm (Wu Y. et al., 2018; Wu et al., 2020) (see **Table 4**).

Multicolor STED Imaging

Multicolor STED imaging is a powerful tool for the study of nanoscale interactions in living organisms (Meyer et al., 2008). The successful multicolor STED imaging depends on two major conditions. First, the emission spectra of different probes should be distinguishable with minimal crosstalk. Secondly, identical STED and excitation wavelength should be applied for multicolor imaging if possible, in order to avoid locating error. For the first requirement, the emitting bandwidth of probes should be as narrow as possible (ideally <20 nm), which might be resolved by materials like QDs (Ye et al., 2018), UCNPs (Zhan et al., 2017), and some LPR hybrids (spaser) (Gao et al., 2020). The second requirement asks for large Stokes shifts, which can effectively avoid re-excitation and allow the application of a single STED wavelength for probes with different emissions. So far, this requirement has only been fulfilled by PDots (Wu et al., 2020), which however typically has a broad emission band.

CONCLUSIONS AND OUTLOOK

Developing nanoprobes for STED imaging provides a valuable view on improving the STED imaging quality from a material perspective. These materials showed overall high brightness, photostability, and depletion efficiency. Furthermore, a variety of nanoprobes have demonstrated their applicability in realistic bioimaging of subdiffraction biostructures, both in fixed and living cells. Despite the abovementioned success, the steric effect, potential toxicity, and difficulties in modification of these materials still propose concern in their future development.

In order to reach the full potential of nanoprobe-based STED microscopy, the most important issue to address is perhaps their particle sizes. A reasonable future target for STED nanoprobes would be synthesizing particles with 2~5 nm lateral size. The importance of the size might be important for STED imaging and could be explained as follows: first, considering the current single particle resolution limit of ~20 nm, sub-5-nm particles in principle could have avoided significant discontinuous labeling in bioimaging. Second, it has been proved that sub-5-nm particles could be efficiently cleared from organisms after imaging (Soo Choi et al., 2007), which makes them safer imaging probes regardless of chemical composition. Third, smaller particles have a relatively larger surface area, which provides sufficient modifying spots for the tuning of their targeting ability. Meanwhile, it is also true that due to the size effect, particles smaller than 2 nm might become highly active and are hard to fabricate, stabilize, or modify. Also, the emission wavelength of particles like QDots and CDots is highly dependent on their size, and particles below 2 nm in diameter might show highly blue-shifted spectra, which would cause a higher phototoxicity in bioimaging.

Currently speaking, the development of STED nanoprobes is still in a primitive stage, where different types of nanomaterials are manufactured, tested, and measured in STED microscopy. However, introducing nanoprobes into STED should go beyond supplementing the library of fluorescent probe. Taking the unique chemical/physical properties of nanomaterials into account, we believe the vast potential of these materials in STED microscopy is yet to be fully realized.

Exploring Imaging Applications for Microorganisms

Considering the growing concern on human health crisis caused by microorganisms, such as the occurrence of superbacteria with antibiotic resistance and the recent outbreak of coronavirus, real-

time and superresolution bioimaging of microorganisms is becoming more and more important. STED imaging might provide crucial tools for systematic study of their behavior, infecting mechanism and potential cure, and the application of nanoprobes in this scenario is worth expecting. Currently, only CDots have been applied for bacteria STED imaging (Yang J. et al., 2016; Liu S. et al., 2020), and the potential of STED nanoprobes for microorganism imaging still needs further exploration.

Utilizing Nanoprobes as Multifunctional Theranostic Platform

Compared with small molecules, nanoparticles are considered as more of platforms than fluorescent tags in their nature. Their microscopic size, large surface area, and improved stability are all in favor of creating multifunctional hybrid materials for theranostics applications (Kelkar and Reineke, 2011). It is promising to cooperate the subdiffraction STED imaging ability with mass delivery, catalysis, energy conversion, and photochemical functions which could allow *in situ* and real-time observation of the physical/chemical process, especially during a classical theranostic process with nanomaterials. The knowledge of biophysics at nanoscale acquired with this tool might deepen our understanding on the actual performance of nanomedicine and how to achieve better therapeutic effects.

Nanoprobes for Multimode Superresolution Imaging

Subdiffraction imaging methods including STED, PALM, STORM, and SIM together with electronic microscopy provide an individual tool to achieve nanoscale resolution. However, cooperating different methods might provide further structural information of the interested biotargets. Many STED nanoprobes can also be utilized in other superresolution imaging methods (Dertinger et al., 2009; Yang X. et al., 2016; Chen et al., 2017; Zhi et al., 2018), which in principle allow multimode superresolution imaging with the same material (Denkova et al., 2019). Furthermore, inorganic nanomaterials like FNDs provide high contrast in TEM, which have enabled the cooperation of STED and TEM for cellular research (Prabhakar et al., 2018).

From STED to Beyond

The STED imaging method itself undergoes fast development and has become very mature nowadays, as the resolution, imaging speed, and photon efficiency have greatly improved (Heine et al., 2017; Eilers et al., 2018). Meanwhile, novel imaging methods specifically applicable for nanoprobes relying on STED or STED-like imaging setups have been developed, most of which can be assigned to the concept of reversible saturable optical fluorescence transition (RESOLFT) imaging proposed by Hell et al. (Hofmann et al., 2005). By triggering fluorescence depletion through other saturation pathways (e.g., by exciting the fluorophore into a metastable dark state), the shrinking of PSF can be realized, in many cases, with much lower saturation intensities (1~2 magnitude lower than the corresponding STED I_{sat}). For many nanoprobes like QDots (Irvine et al., 2008; Xu et al., 2014; Kianinia et al., 2018), FNDs (Han et al., 2010), UCNPs (Kolesov et al., 2011; Wu et al., 2015), and CDots (Khan et al., 2015), such pathways have been discovered, and some were even utilized for STED-like subdiffraction imaging.

Another idea to perform STED-like imaging was to get rid of the central excitation beam and using the donut-shaped beam as the only excitation/saturation source. Resultantly, dark spot in a circle of dim light occurs, indicating the location of nanoparticles (Chen et al., 2018). Furthermore, the idea of STED-like microscopy can be broadened beyond fluorescence imaging, such as the suppression of scattering imaging (SUSI) method with plasmonic gold nanoparticles (Xu et al., 2018).

With all the abovementioned success, we firmly believe that the mutual development of nanomaterials and STED/STED-like imaging technique shall continuously provide new perspectives in achieving superresolved imaging both in space and time, shedding new lights into the subdiffraction bioimaging.

AUTHOR CONTRIBUTIONS

All authors listed have made a substantial, direct, and intellectual contribution to the work and approved it for publication.

FUNDING

This work has been partially supported by the National Basic Research Program of China (2017YFA0700500), National Natural Science Foundation of China (61975127/61525503/81727804), Key Project of Department of Education of Guangdong Province (2016KCXTD007), Guangdong Natural Science Foundation (2020A1515010679/2019A1515110380), Shenzhen Basic Research Project (JCYJ20180305125304883/JCYJ20170818100153423), Shenzhen International Cooperation Project (GJHZ20180928161811821), and China Postdoctoral Science Foundation (2019M663050).

REFERENCES

Balzarotti, F., and Stefani, F. D. (2012). Plasmonics meets far-field optical nanoscopy. *ACS Nano* 6, 4580–4584. doi:10.1021/nn302306m

Betzig, E., Patterson, G. H., Sougrat, R., Lindwasser, O. W., Olenych, S., Bonifacino, J. S., et al. (2006). Imaging intracellular fluorescent proteins at nanometer resolution. *Science* 313, 1642–1645. doi:10.1126/science.1127344

Bianchini, P., Harke, B., Galiani, S., Vicidomini, G., and Diaspro, A. (2012). Single-wavelength two-photon excitation-stimulated emission depletion (SW2PE-STED) superresolution imaging. *Proc. Natl. Acad. Sci. U.S.A.* 109, 6390–6393. doi:10.1073/pnas.1119129109

Castello, M., Tortarolo, G., Coto Hernández, I., Deguchi, T., Diaspro, A., and Vicidomini, G. (2017). Removal of anti-Stokes emission background in STED microscopy by FPGA-based synchronous detection. *Rev. Sci. Instrum.* 88, 053701. doi:10.1063/1.4983082

Chen, C., Wang, F., Wen, S., Su, Q. P., Wu, M. C. L., Liu, Y., et al. (2018). Multi-photon near-infrared emission saturation nanoscopy using upconversion nanoparticles. *Nat. Commun.* 9, 3290. doi:10.1038/s41467-018-05842-w

Chen, G., Qiu, H., Prasad, P. N., and Chen, X. (2014). Upconversion nanoparticles: design, nanochemistry, and applications in Theranostics. *Chem. Rev.* 114, 5161–5214. doi:10.1021/cr400425h

Chen, G., Shen, J., Ohulchanskyy, T. Y., Patel, N. J., Kutikov, A., Li, Z., et al. (2012). (α-NaYbF4:Tm(3+))/CaF2 core/shell nanoparticles with efficient near-infrared to near-infrared upconversion for high-contrast deep tissue bioimaging. *ACS Nano* 6, 8280–8287. doi:10.1021/nn302972r

Chen, X., Li, R., Liu, Z., Sun, K., Sun, Z., Chen, D., et al. (2017). Small photoblinking semiconductor polymer dots for fluorescence nanoscopy. *Adv. Mater. Weinheim* 29, 1604850. doi:10.1002/adma.201604850

Cheng, L., Wang, C., Feng, L., Yang, K., and Liu, Z. (2014). Functional nanomaterials for phototherapies of cancer. *Chem. Rev.* 114, 10869–10939. doi:10.1021/cr400532z

Choi, H., Liu, W., Misra, P., Tanaka, E., Zimmer, J. P., Itty Ipe, B., et al. (2007). Renal clearance of quantum dots. *Nat. Biotechnol.* 25, 1165–1170. doi:10.1038/nbt1340

Cortés, E., Huidobro, P. A., Sinclair, H. G., Guldbrand, S., Peveler, W. J., Davies, T., et al. (2016). Plasmonic nanoprobes for stimulated emission depletion nanoscopy. *ACS Nano* 10, 10454–10461. doi:10.1021/acsnano.6b06361

Denkova, D., Ploschner, M., Das, M., Parker, L. M., Zheng, X., Lu, Y., et al. (2019). 3D sub-diffraction imaging in a conventional confocal configuration by exploiting super-linear emitters. *Nat. Commun.* 10, 3695. doi:10.1038/s41467-019-11603-0

Dertinger, T., Colyer, R., Iyer, G., Weiss, S., and Enderlein, J. (2009). Fast, background-free, 3D super-resolution optical fluctuation imaging (SOFI). *Proc. Natl. Acad. Sci. U.S.A.* 106, 22287–22292. doi:10.1073/pnas.0907866106

Ding, H., Wei, J.-S., Zhang, P., Zhou, Z.-Y., Gao, Q.-Y., and Xiong, H.-M. (2018). Solvent-controlled synthesis of highly luminescent carbon dots with a wide color gamut and narrowed emission peak widths. *Small* 14, 1800612. doi:10.1002/smll.201800612

Eilers, Y., Ta, H., Gwosch, K. C., Balzarotti, F., and Hell, S. W. (2018). MINFLUX monitors rapid molecular jumps with superior spatiotemporal resolution. *Proc. Natl. Acad. Sci. U.S.A.* 115, 6117–6122. doi:10.1073/pnas.1801672115

Fang, X., Chen, X., Li, R., Liu, Z., Chen, H., Sun, Z., et al. (2017). Multicolor photo-crosslinkable AIEgens toward compact nanodots for subcellular imaging and STED nanoscopy. *Small* 13, 1702128. doi:10.1002/smll.201702128

Galanzha, E. I., Weingold, R., Nedosekin, D. A., Sarimollaoglu, M., Nolan, J., Harrington, W., et al. (2017). Spaser as a biological probe. *Nat. Commun.* 8, 15528. doi:10.1038/ncomms15528

Gao, P., and Nienhaus, G. (2017). Precise background subtraction in stimulated emission double depletion nanoscopy. *Opt. Lett.* 42, 831. doi:10.1364/OL.42.000831

Gao, X., Yang, L., Petros, J. A., Marshall, F. F., Simons, J. W., and Nie, S. (2005). *In vivo* molecular and cellular imaging with quantum dots. *Curr. Opin. Biotechnol.* 16, 63–72. doi:10.1016/j.copbio.2004.11.003

Gao, Z., Wang, J. H., Song, P., Kang, B., Xu, J. J., and Chen, H. Y. (2020). Spaser nanoparticles for ultranarrow bandwidth STED super-resolution imaging. *Adv. Mater.* 32, 1907233. doi:10.1002/adma.201907233

Geng, X., Sun, Y., Li, Z., Yang, R., Zhao, Y., Guo, Y., et al. (2019). Retrosynthesis of tunable fluorescent carbon dots for precise long-term mitochondrial tracking. *Small* 15, 1901517. doi:10.1002/smll.201901517

Gustafsson, M. G. L. (2000). Surpassing the lateral resolution limit by a factor of two using structured illumination microscopy. *J. Microsc.* 198, 82–87. doi:10.1046/j.1365-2818.2000.00710.x

Gustafsson, M. G. L. (2005). Nonlinear structured-illumination microscopy: wide-field fluorescence imaging with theoretically unlimited resolution. *Proc. Natl. Acad. Sci. U.S.A,* 102, 13081–13086. doi:10.1073/pnas.0406877102

Haase, M., and Schäfer, H. (2011). Upconverting nanoparticles. *Angew. Chem. Int. Ed. Engl.* 50, 5808–5829. doi:10.1002/anie.201005159

Han, G., Zhao, J., Zhang, R., Tian, X., Liu, Z., Wang, A., et al. (2019). Membrane-penetrating carbon quantum dots for imaging nucleic acid structures in live organisms. *Angew. Chem. Int. Ed. Engl.* 58, 7087–7091. doi:10.1002/anie.201903005

Han, K. Y., Kim, S. K., Eggeling, C., and Hell, S. W. (2010). Metastable dark states enable ground state depletion microscopy of nitrogen vacancy centers in diamond with diffraction-unlimited resolution. *Nano Lett.* 10, 3199–3203. doi:10.1021/nl102156m

Han, K. Y., Willig, K. I., Rittweger, E., Jelezko, F., Eggeling, C., and Hell, S. W. (2009). Three-dimensional stimulated emission depletion microscopy of nitrogen-vacancy centers in diamond using continuous-wave light. *Nano Lett.* 9, 3323–3329. doi:10.1021/nl901597v

Hanne, J., Falk, H. J., Görlitz, F., Hoyer, P., Engelhardt, J., Sahl, S. J., et al. (2015). STED nanoscopy with fluorescent quantum dots. *Nat. Commun.* 6, 7127. doi:10.1038/ncomms8127

Hein, B., Willig, K. I., and Hell, S. W. (2008). Stimulated emission depletion (STED) nanoscopy of a fluorescent protein-labeled organelle inside a living cell. *Proc. Natl. Acad. Sci. U.S.A.* 105, 14271–14276. doi:10.1073/pnas.0807705105

Heine, J., Reuss, M., Harke, B., D'Este, E., Sahl, S. J., and Hell, S. W. (2017). Adaptive-illumination STED nanoscopy. *Proc. Natl. Acad. Sci. U.S.A.* 114, 9797–9802. doi:10.1073/pnas.1708304114

Hell, S. W., and Wichmann, J. (1994). Breaking the diffraction resolution limit by stimulated emission: stimulated-emission-depletion fluorescence microscopy. *Opt. Lett.* 19, 780. doi:10.1364/ol.19.000780

Hofmann, M., Eggeling, C., Jakobs, S., and Hell, S. W. (2005). Breaking the diffraction barrier in fluorescence microscopy at low light intensities by using reversibly photoswitchable proteins. *Proc. Natl. Acad. Sci. U.S.A.* 102, 17565–17569. doi:10.1073/pnas.0506010102

Hong, Y., Lam, J. W., and Tang, B. Z. (2011). Aggregation-induced emission. *Chem. Soc. Rev.* 40, 5361–5388. doi:10.1039/c1cs15113d

Hsiao, W. W., Hui, Y. Y., Tsai, P. C., and Chang, H. C. (2016). Fluorescent nanodiamond: a versatile tool for long-term cell tracking, super-resolution imaging, and nanoscale temperature sensing. *Acc. Chem. Res.* 49, 400–407. doi:10.1021/acs.accounts.5b00484

Hua, X. W., Bao, Y. W., Zeng, J., and Wu, F. G. (2019). Nucleolus-targeted red emissive carbon dots with polarity-sensitive and excitation-independent fluorescence emission: high-resolution cell imaging and *in vivo* tracking. *ACS Appl. Mater. Inter.* 11, 32647–32658. doi:10.1021/acsami.9b09590

Huang, B., Wang, W., Bates, M., and Zhuang, X. (2008). Three-dimensional super-resolution imaging by stochastic optical reconstruction microscopy. *Science* 319, 810–813. doi:10.1126/science.1153529

Irvine, S. E., Staudt, T., Rittweger, E., Engelhardt, J., and Hell, S. W. (2008). Direct light-driven modulation of luminescence from Mn-doped ZnSe quantum dots. *Angew. Chem. Int. Ed. Engl.* 47, 2685–2688. doi:10.1002/anie.200705111

Jia, H., Wang, Z., Yuan, T., Yuan, F., Li, X., Li, Y., et al. (2019). Electroluminescent warm white light-emitting diodes based on passivation enabled bright red bandgap emission carbon quantum dots. *Adv. Sci. (Weinh)* 6, 1900397. doi:10.1002/advs.201900397

Jin, D., Xi, P., Wang, B., Zhang, L., Enderlein, J., and Van Oijen, A. M. (2018). Nanoparticles for super-resolution microscopy and single-molecule tracking. *Nat. Methods* 15, 415–423. doi:10.1038/s41592-018-0012-4

Kelkar, S. S., and Reineke, T. M. (2011). Theranostics: combining imaging and therapy. *Bioconjug. Chem.* 22, 1879–1903. doi:10.1021/bc200151q

Khan, S., Verma, N. C., Gupta, A., and Nandi, C. K. (2015). Reversible photoswitching of carbon dots. *Sci. Rep.* 5, 11423. doi:10.1038/srep11423

Kianinia, M., Bradac, C., Sontheimer, B., Wang, F., Tran, T. T., Nguyen, M., et al. (2018). All-optical control and super-resolution imaging of quantum emitters in layered materials. *Nat. Commun.* 9, 874. doi:10.1038/s41467-018-03290-0

Klar, T. A., and Hell, S. W. (1999). Subdiffraction resolution in far-field fluorescence microscopy. *Opt. Lett.* 24, 954. doi:10.1364/ol.24.000954

Kneipp, K., Wang, Y., Kneipp, H., Perelman, L. T., Itzkan, I., Dasari, R. R., et al. (1997). Single molecule detection using surface-enhanced Raman scattering (SERS). *Phys. Rev. Lett.* 78, 1667–1670. doi:10.1103/PhysRevLett.78.1667

Kolesov, R., Reuter, R., Xia, K., Stöhr, R., Zappe, A., and Wrachtrup, J. (2011). Super-resolution upconversion microscopy of praseodymium-doped yttrium aluminum garnet nanoparticles. *Phys. Rev. B.* 84, 153413. doi:10.1103/PhysRevB.84.153413

Krause, S., Liisberg, M. B., Lahtinen, S., Soukka, T., and Vosch, T. (2019). Lanthanide-doped nanoparticles for stimulated emission depletion nanoscopy. *ACS Appl. Nano Mater.* 2, 5817–5823. doi:10.1021/acsanm.9b01272

Laporte, G., and Psaltis, D. (2016). STED imaging of green fluorescent nanodiamonds containing nitrogen-vacancy-nitrogen centers. *Biomed. Opt. Express* 7, 34. doi:10.1364/BOE.7.000034

Larson, D. R., Zipfel, W. R., Williams, R. M., Clark, S. W., Bruchez, M. P., Wise, F. W., et al. (2003). Water-soluble quantum dots for multiphoton fluorescence imaging *in vivo*. *Science* 300, 1434–1436. doi:10.1126/science.1083780

Leménager, G., De Luca, E., Sun, Y. P., and Pompa, P. P. (2014). Super-resolution fluorescence imaging of biocompatible carbon dots. *Nanoscale* 6, 8617–8623. doi:10.1039/C4NR01970A

Lesoine, M. D., Bhattacharjee, U., Guo, Y., Vela, J., Petrich, J. W., and Smith, E. A. (2013). Subdiffraction, luminescence-depletion imaging of isolated, giant, CdSe/CdS nanocrystal quantum dots. *J. Phys. Chem. C.* 117, 3662–3667. doi:10.1021/jp312231k

Li, C., Li, Y., Han, Y., Zhang, Z., Li, Y., Wang, W., et al. (2020). Pulsed saturated absorption competition microscopy on nonbleaching nanoparticles. *ACS Photon.* 7, 1788–1798. doi:10.1021/acsphotonics.0c00456

Li, D., Ni, X., Zhang, X., Liu, L., Qu, J., Ding, D., et al. (2018). Aggregation-induced emission luminogen-assisted stimulated emission depletion nanoscopy for super-resolution mitochondrial visualization in live cells. *Nano Res.* 11, 6023–6033. doi:10.1007/s12274-018-2118-5

Li, D., Qin, W., Xu, B., Qian, J., and Tang, B. Z. (2017). AIE nanoparticles with high stimulated emission depletion efficiency and photobleaching resistance for long-term super-resolution bioimaging. *Adv. Mater. Weinheim* 29, 1703643. doi:10.1002/adma.201703643

Li, H., Ye, S., Guo, J., Wang, H., Yan, W., Song, J., et al. (2019). Biocompatible carbon dots with low-saturation-intensity and high-photobleaching-resistance for STED nanoscopy imaging of the nucleolus and tunneling nanotubes in living cells. *Nano Res.* 12, 3075–3084. doi:10.1007/s12274-019-2554-x

Liang, L., and Liu, X. (2017). STED nanoscopy goes low power. *Chem.* 2, 331–333. doi:10.1016/j.chempr.2017.02.016

Liang, L., Yan, W., Qin, X., Peng, X., Feng, H., Wang, Y., et al. (2020). Designing sub-2 nm organosilica nanohybrids for far-field super-resolution imaging. *Angew. Chem. Int. Ed. Engl.* 59, 746–751. doi:10.1002/anie.201912404

Liu, P., Wang, Y., Liu, Y., Tan, F., Li, J., and Li, N. (2020). S-nitrosothiols loaded mini-sized Au@silica nanorod elicits collagen depletion and mitochondrial damage in solid tumor treatment. *Theranostics* 10, 6774–6789. doi:10.7150/thno.42661

Liu, S., Yi, X., Wu, X., Li, Q., and Wang, Y. (2020). Internalized carbon dots for enhanced extracellular electron transfer in the dark and light. *Small* 16, 2004194. doi:10.1002/smll.202004194

Liu, Y., Lu, Y., Yang, X., Zheng, X., Wen, S., Wang, F., et al. (2017). Amplified stimulated emission in upconversion nanoparticles for super-resolution nanoscopy. *Nature* 543, 229–233. doi:10.1038/nature21366

Lu, D., Yang, X., Zhang, Q., Wang, R., Zhou, S., Yang, G., et al. (2019). Tracking the single-carbon-dot transmembrane transport by force tracing based on atomic force microscopy. *ACS Biomater. Sci. Eng.* 5, 432–437. doi:10.1021/acsbiomaterials.8b01363

Luo, J., Xie, Z., Lam, J. W., Cheng, L., Chen, H., Qiu, C., et al. (2001). Aggregation-induced emission of 1-methyl-1,2,3,4,5-pentaphenylsilole. *Chem. Commun. (Camb)* 18, 1740–1741. doi:10.1039/b105159h

Luo, P. G., Sahu, S., Yang, S. T., Sonkar, S. K., Wang, J., Wang, H., et al. (2013). Carbon "quantum" dots for optical bioimaging. *J. Mater. Chem. B.* 1, 2116–2127. doi:10.1039/c3tb00018d

Ma, X., Liu, X., Li, Y., Xi, X., Yao, Q., and Fan, J. (2020). Influence of crystallization temperature on fluorescence of n-diamond quantum dots. *Nanotechnology* 31, 505712. doi:10.1088/1361-6528/abb72d

Ma, Y., and Ha, T. (2019). Fight against background noise in stimulated emission depletion nanoscopy. *Phys. Biol.* 16, 051002. doi:10.1088/1478-3975/ab255c

Man, Z., Lv, Z., Xu, Z., Cui, H., Liao, Q., Zheng, L., et al. (2019). Organic nanoparticles with ultrahigh stimulated emission depletion efficiency for low-power STED nanoscopy. *Nanoscale* 11, 12990–12996. doi:10.1039/c9nr02781e

Meyer, L., Wildanger, D., Medda, R., Punge, A., Rizzoli, S. O., Donnert, G., et al. (2008). Dual-color STED microscopy at 30-nm focal-plane resolution. *Small* 4, 1095–1100. doi:10.1002/smll.200800055

Michalet, X., Pinaud, F. F., Bentolila, L. A., Tsay, J. M., Doose, S., Li, J. J., et al. (2005). Quantum dots for live cells, *in Vivo* imaging, and diagnostics. *Science* 307, 538–544. doi:10.1126/science.1104274

Peng, X., Huang, B., Pu, R., Liu, H., Zhang, T., Widengren, J., et al. (2019). Fast upconversion super-resolution microscopy with 10 μs per pixel dwell times. *Nanoscale* 11, 1563–1569. doi:10.1039/C8NR08986H

Peuschel, H., Ruckelshausen, T., Cavelius, C., and Kraegeloh, A. (2015). Quantification of internalized silica nanoparticles via STED microscopy. *Biomed. Res. Int.* 2015, 961208–961216. doi:10.1155/2015/961208

Prabhakar, N., Näreoja, T., von Haartman, E., Karaman, D. Ş., Jiang, H., Koho, S., et al. (2013). Core-shell designs of photoluminescent nanodiamonds with porous silica coatings for bioimaging and drug delivery II: Application. *Nanoscale* 5, 3713–3722. doi:10.1039/c3nr33926b

Prabhakar, N., Peurla, M., Koho, S., Deguchi, T., Näreoja, T., Chang, H. C., et al. (2018). STED-TEM correlative microscopy leveraging nanodiamonds as intracellular dual-contrast markers. *Small* 14, 1701807. doi:10.1002/smll.201701807

Qu, D., and Sun, Z. (2020). The formation mechanism and fluorophores of carbon dots synthesized via a bottom-up route. *Mater. Chem. Front.* 4, 400–420. doi:10.1039/C9QM00552H

Rayleigh, L. (1896). XV.On the theory of optical images, with special reference to the microscope. *Lond. Edinb. Dublin Philosophical Mag. J. Sci.* 42, 167–195. doi:10.1080/14786449608620902

Reisch, A., and Klymchenko, A. S. (2016). Fluorescent polymer nanoparticles based on dyes: seeking brighter tools for bioimaging. *Small* 12, 1968–1992. doi:10.1002/smll.201503396

Rittweger, E., Han, K. Y., Irvine, S. E., Eggeling, C., and Hell, S. W. (2009). STED microscopy reveals crystal colour centres with nanometric resolution. *Nat. Photon* 3, 144–147. doi:10.1038/nphoton.2009.2

Rust, M. J., Bates, M., and Zhuang, X. (2006). Sub-diffraction-limit imaging by stochastic optical reconstruction microscopy (STORM). *Nat. Methods* 3, 793–795. doi:10.1038/nmeth929

Schrof, S., Staudt, T., Rittweger, E., Wittenmayer, N., Dresbach, T., Engelhardt, J., et al. (2011). STED nanoscopy with mass-produced laser diodes. *Opt. Express* 19, 8066. doi:10.1364/oe.19.008066

Schübbe, S., Cavelius, C., Schumann, C., Koch, M., and Kraegeloh, A. (2010). STED microscopy to monitor agglomeration of silica particles inside A549 cells. *Adv. Eng. Mater.* 12, 417–422. doi:10.1002/adem.201000093

Schübbe, S., Schumann, C., Cavelius, C., Koch, M., Müller, T., and Kraegeloh, A. (2012). Size-dependent localization and quantitative evaluation of the intracellular migration of silica nanoparticles in Caco-2 cells. *Chem. Mater.* 24, 914–923. doi:10.1021/cm2018532

Sivan, Y., Sonnefraud, Y., Kéna-Cohen, S., Pendry, J. B., and Maier, S. A. (2012). Nanoparticle-assisted stimulated-emission-depletion nanoscopy. *ACS Nano* 6, 5291. doi:10.1063/1.473531910.1021/nn301082g

Sivan, Y., Sonnefraud, Y., Kéna-Cohen, S., Pendry, J. B., and Maier, S. A. (2012). Nanoparticle-assisted stimulated-emission-depletion nanoscopy. *ACS Nano* 6, 5291–5296. doi:10.1021/nn301082g

Soenen, S. J., Rivera-Gil, P., Montenegro, J.-M., Parak, W. J., De Smedt, S. C., and Braeckmans, K. (2011). Cellular toxicity of inorganic nanoparticles: common aspects and guidelines for improved nanotoxicity evaluation. *Nano Today* 6, 446–465. doi:10.1016/j.nantod.2011.08.001

Sonnefraud, Y., Sinclair, H. G., Sivan, Y., Foreman, M. R., Dunsby, C. W., Neil, M. A., et al. (2014). Experimental proof of concept of nanoparticle-assisted STED. *Nano Lett.* 14, 4449–4453. doi:10.1021/nl5014103

Sun, Y. P., Zhou, B., Lin, Y., Wang, W., Fernando, K. A., Pathak, P., et al. (2006). Quantum-sized carbon dots for bright and colorful photoluminescence. *J. Am. Chem. Soc.* 128, 7756–7757. doi:10.1021/ja062677d

Tavernaro, I., Cavelius, C., Peuschel, H., and Kraegeloh, A. (2017). Bright fluorescent silica-nanoparticle probes for high-resolution STED and confocal microscopy. *Beilstein J. Nanotechnol.* 8, 1283–1296. doi:10.3762/bjnano.8.130

Tovmachenko, O. G., Graf, C., van den Heuvel, D. J., van Blaaderen, A., and Gerritsen, H. C. (2006). Fluorescence enhancement by metal-core/silica-shell nanoparticles. *Adv. Mater.* 18, 91–95. doi:10.1002/adma.200500451

Tzeng, Y. K., Faklaris, O., Chang, B. M., Kuo, Y., Hsu, J. H., and Chang, H. C. (2011). Superresolution imaging of albumin-conjugated fluorescent nanodiamonds in cells by stimulated emission depletion. *Angew. Chem. Int. Ed. Engl.* 50, 2262–2265. doi:10.1002/anie.201007215

Urban, N. T., Foreman, M. R., Hell, S. W., and Sivan, Y. (2018). Nanoparticle-assisted STED nanoscopy with gold nanospheres. *ACS Photon.* 5, 2574–2583. doi:10.1021/acsphotonics.7b00833

Wang, L., Chen, B., Yan, W., Yang, Z., Peng, X., Lin, D., et al. (2018). Resolution improvement in STED super-resolution microscopy at low power using a phasor plot approach. *Nanoscale* 10, 16252–16260. doi:10.1039/c8nr03584a

Wang, L., Wang, Y., Xu, T., Liao, H., Yao, C., Liu, Y., et al. (2014). Gram-scale synthesis of single-crystalline graphene quantum dots with superior optical properties. *Nat. Commun.* 5, 5357. doi:10.1038/ncomms6357

Wang, Y., Bai, Z., Wang, Q., and Wang, G. (2017). Experimental investigations on fluorescence excitation and depletion of carbon dots. *J. Fluoresc.* 27, 1435–1441. doi:10.1007/s10895-017-2082-6

Wildanger, D., Medda, R., Kastrup, L., and Hell, S. W. (2009). A compact STED microscope providing 3D nanoscale resolution. *J. Microsc.* 236, 35–43. doi:10.1111/j.1365-2818.2009.03188.x

Wildanger, D., Patton, B. R., Schill, H., Marseglia, L., Hadden, J. P., Knauer, S., et al. (2012). Solid immersion facilitates fluorescence microscopy with nanometer resolution and sub-ångström emitter localization. *Adv. Mater. Weinheim* 24, OP309–13. doi:10.1002/adma.201203033

Wolfbeis, O. S. (2015). An overview of nanoparticles commonly used in fluorescent bioimaging. *Chem. Soc. Rev.* 44, 4743–4768. doi:10.1039/C4CS00392F

Wu, C., Schneider, T., Zeigler, M., Yu, J., Schiro, P. G., Burnham, D. R., et al. (2010). Bioconjugation of ultrabright semiconducting polymer dots for specific cellular targeting. *J. Am. Chem. Soc.* 132, 15410–15417. doi:10.1021/ja107196s

Wu, R., Zhan, Q., Liu, H., Wen, X., Wang, B., and He, S. (2015). Optical depletion mechanism of upconverting luminescence and its potential for multi-photon STED-like microscopy. *Opt. Express* 23, 32401. doi:10.1364/oe.23.032401

Wu, X., Ma, L., Sun, S., Jiang, K., Zhang, L., Wang, Y., et al. (2018). A versatile platform for the highly efficient preparation of graphene quantum dots: photoluminescence emission and hydrophilicity-hydrophobicity regulation and organelle imaging. *Nanoscale* 10, 1532–1539. doi:10.1039/C7NR08093J

Wu, Y., Ruan, H., Dong, Z., Zhao, R., Yu, J., Tang, X., et al. (2020). Fluorescent polymer dot-based multicolor stimulated emission depletion nanoscopy with a single laser beam pair for cellular tracking. *Anal. Chem.* 92, 12088–12096. doi:10.1021/acs.analchem.0c02821

Wu, Y., Ruan, H., Zhao, R., Dong, Z., Li, W., Tang, X., et al. (2018). Ultrastable fluorescent polymer dots for stimulated emission depletion bioimaging. *Adv. Opt. Mater.* 6, 1800333. doi:10.1002/adom.201800333

Xu, J., Fan, Q., Mahajan, K. D., Ruan, G., Herrington, A., Tehrani, K. F., et al. (2014). Micelle-templated composite quantum dots for super-resolution imaging. *Nanotechnology* 25, 195601. doi:10.1088/0957-4484/25/19/195601

Xu, J., Zhang, T., Yang, S., Feng, Z., Li, H., Hu, D., et al. (2018). Plasmonic nanoprobes for multiplexed fluorescence-free super-resolution imaging. *Adv. Opt. Mater.* 6, 1800432. doi:10.1002/adom.201800432

Xu, Y., Zhang, H., Zhang, N., Wang, X., Dang, D., Jing, X., et al. (2020). Deep-red fluorescent organic nanoparticles with high brightness and photostability for super-resolution *in vitro* and *in vivo* imaging using STED nanoscopy. *ACS Appl. Mater. Inter.* 12, 6814–6826. doi:10.1021/acsami.9b18336

Yang, J., Zhang, X., Ma, Y. H., Gao, G., Chen, X., Jia, H. R., et al. (2016). Carbon dot-based platform for simultaneous bacterial distinguishment and antibacterial applications. *ACS Appl. Mater. Inter.* 8, 32170–32181. doi:10.1021/acsami.6b10398

Yang, X., Zhanghao, K., Wang, H., Liu, Y., Wang, F., Zhang, X., et al. (2016b). Versatile application of fluorescent quantum dot labels in super-resolution fluorescence microscopy. *ACS Photon.* 3, 1611–1618. doi:10.1021/acsphotonics.6b00178

Ye, S., Guo, J., Song, J., and Qu, J. (2020). Achieving high-resolution of 21 nm for STED nanoscopy assisted by CdSe@ZnS quantum dots. *Appl. Phys. Lett.* 116, 041101. doi:10.1063/1.5133427

Ye, S., Yan, W., Zhao, M., Peng, X., Song, J., and Qu, J. (2018). Low-saturation-intensity, high-photostability, and high-resolution STED nanoscopy assisted by CsPbBr3 quantum dots. *Adv. Mater.* 30, 1800167. doi:10.1002/adma.201800167

Yu, J., Sun, X., Cai, F., Zhu, Z., Qin, A., Qian, J., et al. (2015). Low photobleaching and high emission depletion efficiency: the potential of AIE luminogen as fluorescent probe for STED microscopy. *Opt. Lett.* 40, 2313. doi:10.1364/OL.40.002313

Yu, S. J., Kang, M. W., Chang, H. C., Chen, K. M., and Yu, Y. C. (2005). Bright fluorescent nanodiamonds: No photobleaching and low cytotoxicity. *J. Am. Chem. Soc.* 127, 17604–17605. doi:10.1021/ja0567081

Zhan, Q., Liu, H., Wang, B., Wu, Q., Pu, R., Zhou, C., et al. (2017). Achieving high-efficiency emission depletion nanoscopy by employing cross relaxation in upconversion nanoparticles. *Nat. Commun.* 8, 1058. doi:10.1038/s41467-017-01141-y

Zhao, M., Ye, S., Peng, X., Song, J., and Qu, J. (2019). Green emitted CdSe@ZnS quantum dots for FLIM and STED imaging applications. *J. Innov. Opt. Health Sci.* 12, 1940003. doi:10.1142/S1793545819400030

Zhi, B., Cui, Y., Wang, S., Frank, B. P., Williams, D. N., Brown, R. P., et al. (2018). Malic acid carbon dots: from super-resolution live-cell imaging to highly efficient separation. *ACS Nano* 12, 5741–5752. doi:10.1021/acsnano.8b01619

Conflict of Interest: The authors declare that the research was conducted in the absence of any commercial or financial relationships that could be construed as a potential conflict of interest.

frontiers in Chemistry

MINI REVIEW
published: 29 April 2021
doi: 10.3389/fchem.2021.655324

Probing Biosensing Interfaces With Single Molecule Localization Microscopy (SMLM)

Xiaoyu Cheng[1]* *and Wei Yin*[2]

[1] State Key Laboratory for Modern Optical Instrumentations, National Engineering Research Center of Optical Instrumentation, College of Optical Science and Engineering, Zhejiang University, Hangzhou, China, [2] Core Facilities, School of Medicine, Zhejiang University, Hangzhou, China

Far field single molecule localization microscopy (SMLM) has been established as a powerful tool to study biological structures with resolution far below the diffraction limit of conventional light microscopy. In recent years, the applications of SMLM have reached beyond traditional cellular imaging. Nanostructured interfaces are enriched with information that determines their function, playing key roles in applications such as chemical catalysis and biological sensing. SMLM enables detailed study of interfaces at an individual molecular level, allowing measurements of reaction kinetics, and detection of rare events not accessible to ensemble measurements. This paper provides an update to the progress made to the use of SMLM in characterizing nanostructured biointerfaces, focusing on practical aspects, recent advances, and emerging opportunities from an analytical chemistry perspective.

Keywords: biosensors, interfaces, single molecules, super-resolution imaging, fluorescence imaging

OPEN ACCESS

Edited by:
Fan Wang,
University of Technology Sydney, Australia

Reviewed by:
Leiting Pan,
Nankai University, China
Yongtao Liu,
University of Technology Sydney, Australia

***Correspondence:**
Xiaoyu Cheng
xiaoyu.cheng@zju.edu.cn

Specialty section:
This article was submitted to Analytical Chemistry, a section of the journal Frontiers in Chemistry

Received: *18 January 2021*
Accepted: *16 March 2021*
Published: *29 April 2021*

Citation:
Cheng X and Yin W (2021) Probing Biosensing Interfaces With Single Molecule Localization Microscopy (SMLM). Front. Chem. 9:655324. doi: 10.3389/fchem.2021.655324

INTRODUCTION

At the heart of measurement science lies the need to find answers to the following questions: 1. What is in the sample? 2. In what amount? The same questions are being asked repeatedly in applications including (but not limited to) drug discovery, environmental monitoring, cancer diagnostics, and SARS-COVID19 testing etc., all of which have broad social impacts on a global scale. However, asking questions is easy, finding answers to them are often hard, especially when the concentration of analytes is low and signals difficult to detect.

Single Molecule Localization Microscopy (SMLM) represents a class of fluorescent super-resolution imaging technique capable of detecting individual molecules with resolution at least a magnitude lower than the diffraction limit of conventional light microscopy. First demonstrated in 2006 and winning the Nobel Prize in Chemistry in 2014 (Dickson et al., 1997; Betzig et al., 2006; Rust et al., 2006; Moerner, 2015a,b), the elegant and robust design of SMLM allows direct observation of fluorescent molecules with resolution at molecular length scale using a standard bench-top microscope. The typical lateral resolution of SMLM is around 20 nm, and the axial resolution is below 100 nm (von Diezmann et al., 2017; Pan et al., 2018, 2019). Being a far field technique which can rely on large field-of-view detectors (Huang et al., 2011; Long et al., 2012; Ma et al., 2013), SMLM enables the probing of millions of single molecules simultaneously, which is hard to achieve with near-field scanning techniques. This has made SMLM an ideal tool for studying biosensing interfaces such that rare events can be detected and sample heterogeneity

studied to enable building quantitative relationships inaccessible to ensemble studies (Titus and Willets, 2013a,b; Blythe et al., 2014; Nicovich et al., 2017; Pan et al., 2018; Cheng et al., 2019; Xing et al., 2019). Here, we provide a short account on the advances of using SMLM in the study of biosensors, focusing on application aspects, and recent progresses in the past several years.

BASICS OF SMLM

The foundations of SMLM have been reviewed thoroughly elsewhere, therefore they are only covered briefly due to the limited scope of this mini review (Moerner, 2015a,b). Fundamentally speaking, there are two building blocks to the mainstream SMLM techniques: scholastically photo-switching single molecules, and super-reconstruction. Briefly speaking, the process work via (1) accurate localization of point spread function (PSF) from single emitters, and (2) using various methods to allow only a limited number of emitters to be in the "ON" state so that (1) can be applied to each image plane to allow super-reconstruction, such as an early demonstration shown by Betzig et al. (2006) (**Figure 1**).

Typical Methods to Induce Single Molecule Blinking

As a fluorescence technique, one of the requirements of SMLM is to observe probe molecules randomly switch between fluorescent "ON" and "OFF" states. After first observation of such phenomena in fluorescent proteins at room temperature in the late 1990s (Dickson et al., 1997), the past two decades have seen numerous SMLM probes developed and methods to blinking control (Li and Vaughan, 2018). Usually, fluorophores are more likely to stay in the fluorescent "ON" state. In practice, the challenge is often to find ways to extend the length of the "OFF," or dark state, and to develop methods to reduce labeling density. Among the various approaches reported, three approaches have been established, and are the most frequently used in the today's mainstream SMLM.

The first is direct photos-switching of immobilized fluorophores in a buffered environment (Nahidiazar et al., 2016) (**Figure 2**, top). This is the most commonly used approach in SMLM, with many examples demonstrated represented with dSTORM, STORM, PALM, etc. (van de Linde et al., 2011). A carefully designed buffer environment requires: (1) an oxygen-removing reaction, which typically involves glucose oxidation and this also reduces photo bleaching. (2) A reducing agent, such as β-mercaptoethanol or Tris(2-carboxyethyl)phosphine (TCEP), is often added to drive the fluorophores into the dark states (Vaughan et al., 2013), typically with the Alexa fluorophore family (e.g., Alexa 647). (3) Additional reagents, such as the enzyme horseradish peroxidase was used to reduce the amount of hydrogen peroxide, a radical generator. This is the most widely adopted approach to induce photo-switching for SMLM, and numerous studies have been reported in literature (Sauer and Heilemann, 2017).

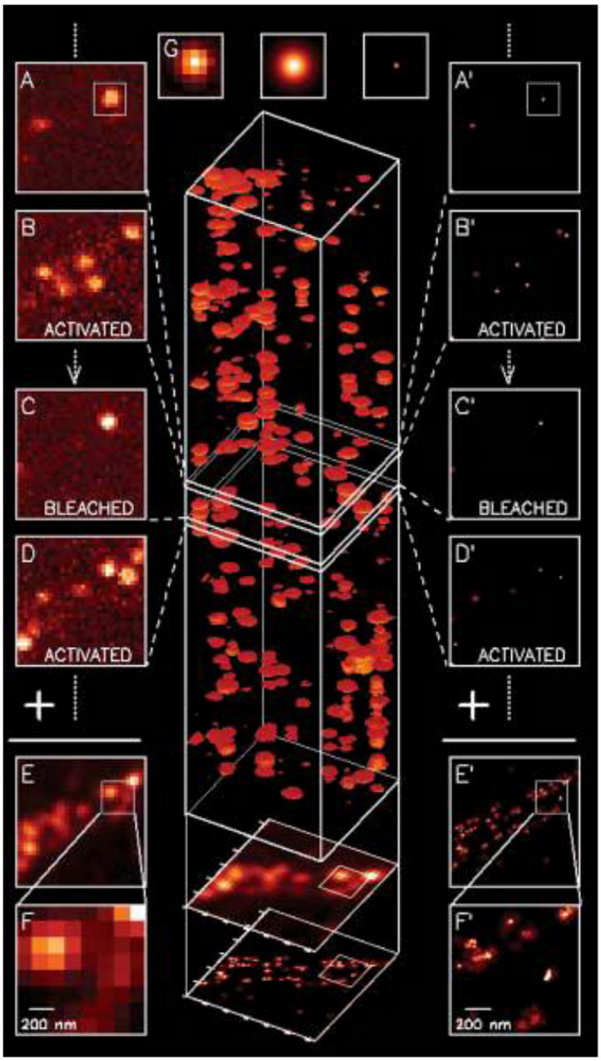

FIGURE 1 | The first SMLM demonstrated with fluorescent proteins in 2006 (Betzig et al., 2006). A series of diffraction limited images were acquired, and to each image PSF for single emitters were localized with accuracy typically below ~20 nm and image reconstructed to form the final image. Copyright with permission from Science.

The second group of methods is PAINT (Jungmann et al., 2014, 2016; Schnitzbauer et al., 2017; Stehr et al., 2019) (**Figure 2**, bottom). PAINT stands for points accumulation for imaging nanoscale topography. As a different method to the direct photo-switching methods mentioned above, PAINT does not rely on photo-switching of immobilized fluorophores in the imaging plane. Instead, fluorophores labeled imaging species, usually single stranded DNA, diffuse in the imaging buffer and bind transiently to the surface bound species to produce the fluorescent "ON" signal (Peterson et al., 2016b; Morris et al., 2018; Lackey et al., 2020). e.g., By controlling the length of the

Abbreviations: GFP, Green Fluorescent Protein; dSTORM, Direct Stochastic Optical Reconstruction Microscopy; GSDIM, Ground State Depletion with Individual Molecular Return; PALM, Photo-activated Localization Microscopy; PAINT, Points Accumulation for Imaging Nanoscale Topography; SMLM, Single Molecule Localization Microscopy; STED, Stimulated Emission Depletion Microscopy; STORM, Stochastic Optical Reconstruction Microscopy; TIRF, Total Internal Reflection Fluorescence.

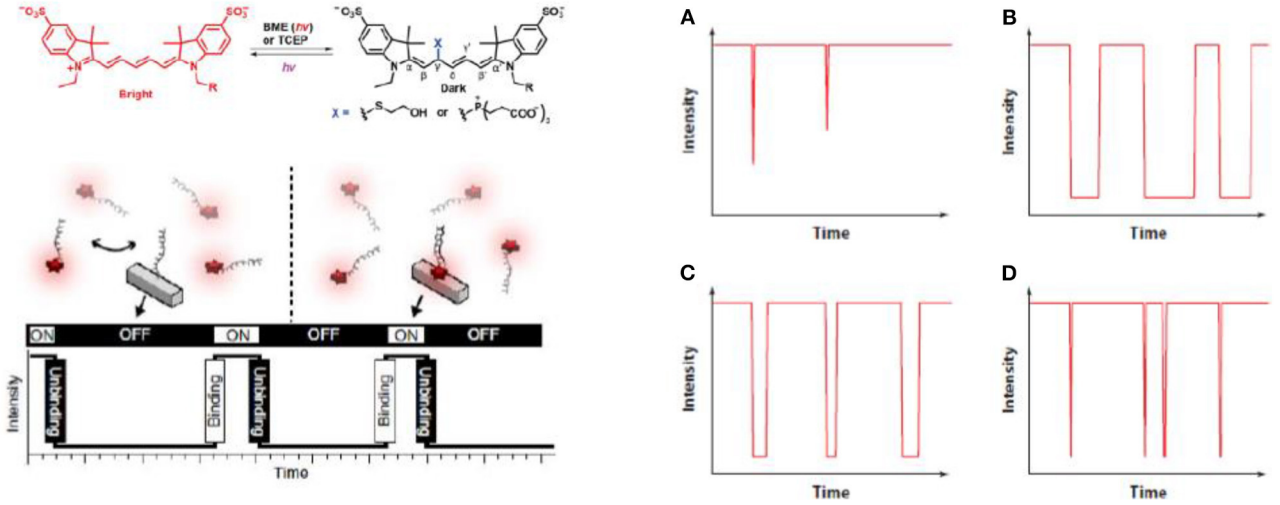

FIGURE 2 | Three typical methods to introduce single molecule blinking. A carefully designed buffer environment extends the length of the "OFF" state (van de Linde et al., 2011; Sauer and Heilemann, 2017; Li and Vaughan, 2018) (Top). In PAINT, blinking control is achieved by transient adsorption of the imaging strand to the binding strand immobilized on the substrate (Jungmann et al., 2010; Stein et al., 2019) (Bottom). Triplet mediated blinking can be controlled in the gas phase without the use of solution environment once oxygen is removed and lifetime of triplet state extended (Ha and Tinnefeld, 2012; Blythe and Willets, 2016; Cheng et al., 2019) (Right). **(A)** Without oxygen removal. **(B)** Oxygen removed. **(C)** With an inefficient triplet quencher. **(D)** With an efficient triplet quencher. Copyright with permission from the American Chemical Society and Nature Publishing Group.

matching strand pairs, stochastic blinking of single molecular fluorophores can be achieved, and the lateral spatial resolution can be lowered down to ∼5 nm (Dai et al., 2016). The very high resolution is possible because localization precision is related to the inverse square of the photon count, and in PAINT, high photon counts can be obtained when a longer stranded DNA is used, although to some extend the speed of imaging has to be compromised (Dai et al., 2016). A feature with PAINT is that multiple contact between probes and their target enables a higher total number of photons, hence higher resolution to the technique.

The third approach does not require a solution environment, but can be performed in the gas phase, as seen in **Figure 2**, right (Ha and Tinnefeld, 2012; Blythe and Willets, 2016; Cheng et al., 2019). In gas phase SMLM, fluorescent photons are observed as fluorophores cycling between singlet excited state and the ground state, with a small chance to enter the triplet state. The triplet state is non-emissive because electrons are parallel and spin-forbidden, the lifetime of which is significantly longer than the singlet state ("ON" state), e.g., millisecond to second. Hence, once a fluorophore enters the triplet state, it can remain in the dark for a long time, as long as oxygen is removed because oxygen is a triplet quencher (Blythe et al., 2015a,b; Blythe and Willets, 2016; Cheng et al., 2019). An advantage of triplet quenching induced SMLM is its good performance in an epi set-ups without buffer environment, which is hard to achieve with PAINT or dSTORM when the imaging strands freely diffuse, so typically objective based TIRF set-ups are used.

Super Reconstruction: The Importance for Fiducial Correction

SMLM relies on stacking many images of blinking fluorophores into the same region of interest. Hence, the second building block to SMLM is super-reconstruction (Sage et al., 2015). Overall, the aim of super reconstruction is to develop methods to obtain images below the diffraction limit efficiently and accurately. Roughly speaking, this process involves three separate steps: the first is drift correction, the second single emitter localization and third image reconstruction. The past decade has seen rapid advances in our understanding of emission patterns of single emitters, namely point spread function (PSF), and now higher order PSF fittings are available to enable 3D super-resolution imaging (Hao et al., 2013; von Diezmann et al., 2017; Li et al., 2020). Higher order drift correction methods, such as 3D drift control, has been shown to work efficiently

Due to the limited length of this mini review, more commonly used methods for drift correction after imaging acquisition are not the focus of this article, which were reviewed thoroughly elsewhere (Mockl and Moerner, 2020).

Apart from PSF engineering, a recent development in super reconstruction is the realization of the importance of drift correction (**Figure 3**). In the past, attentions have been focused on PSF engineering so that advanced imaging concepts, e.g., high speed 3D imaging, can be done, in some cases close to video rate (Huang et al., 2013). Since images of SMLM were acquired over an extended period of time (e.g., *tens to hundreds of seconds*), the physical movement of the sample stage could induce significant aberrations. Solving this issue leads to SMLM microscopy with superior performance. In a recent study by Coelho et al. (2020), it was shown that actively stabilizing the microscope sample stage over the imaging process frame by frame could reduce the spatial drift down to ∼1 nm (Coelho et al., 2020). Rapid repositioning of the samples using self-calibrated piezostage and anti-shaking algorithms were shown to reduce drift far below the photon-limited localization precision and improved the spatial resolution, and this does not require complex algorithms or

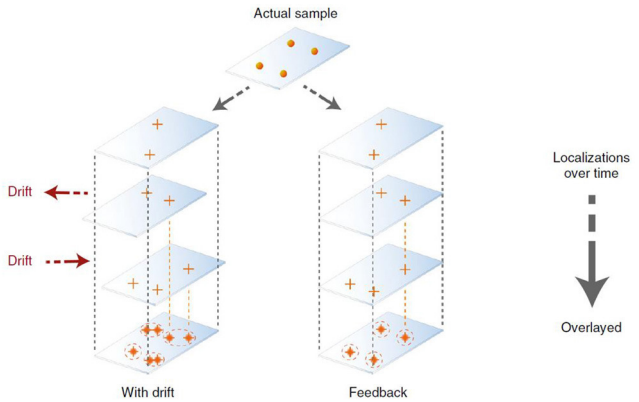

FIGURE 3 | Active SMLM is achieved with better drift correction to improve the resolution without PSF engineering or change of fluorophores (Coelho et al., 2020, 2021). It was shown that using an actively stabilizing microscope, the lateral spatial drift could be reduced down to ~1 nm using self-calibrated piezostage and anti-shaking algorithms. This can be done without relying on complicated hardware and the entire process can be completed in 2 weeks. Copyright with permission from Nature Publishing Group.

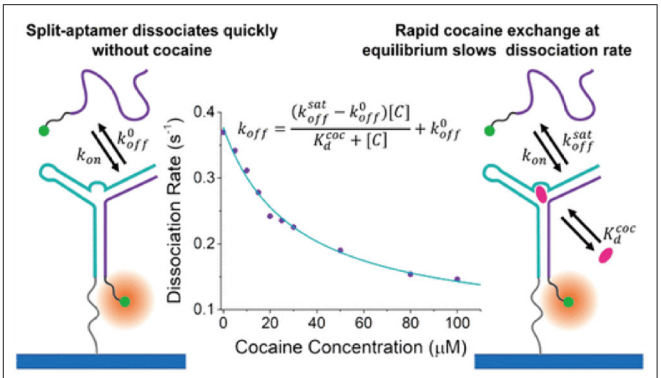

FIGURE 4 | Measurement of single molecular binding kinetics with PAINT. Initially developed as an imaging tool, PAINT has been established as a method to measure binding affinities between biomolecules including DNA, peptides, and small molecular drug targets. Shown above as an example of measuring dissociation constant between cocaine and single stranded DNA split aptamer (Morris et al., 2018). Copyright with permission from the American Chemical Society.

hardware to achieve (Coelho et al., 2020). This is important because this technique can be applied without using a second laser beam, as seen in the single molecule depletion imaging via non-linear optical properties of the probes (Balzarotti et al., 2017).

APPLICATION TOWARD QUANTITATIVE BIOANALYSIS

Initially established as an advanced imaging tool to probe biological structures (Tuson and Biteen, 2015), the applications of SMLM is advancing rapidly into the field of surface analysis including catalysis and biosensors (Sambur et al., 2016; Chen et al., 2017). Here we focus on the latter topic due to the very few reviews available to this topic at the moment, here three types of applications are addressed: PAINT for single molecule kinetic measurements; quantitative single molecule sensors with counting; and the emerging use of SMLM for predictive chromatography separations.

PAINT: From Imaging to Kinetic Measurement

As mentioned earlier, PAINT represents a subtype of SMLM techniques that relies on transient binding of biomolecules onto a surface immobilized molecule to induce photo-switching. Since the time each molecule resides on the imaging plane is related to the binding affinity between the molecular pairs at chemical equilibrium, important kinetic information, such as dissociation and/or association constant, namely K_d or K_a, can be extracted by analyzing the fluorescent "ON" period in relation to the "OFF" period in the single molecular time trace (Jungmann et al., 2010). e.g., A series of studies by Harris's group showed measurement of molecular binding kinetics could be studied at single molecular level with PAINT, demonstrated by several examples with e.g., biotin-avidin, structure-switching aptamer, peptides, and small molecular targets etc. (Fox et al., 2009; Wayment and Harris, 2009; Heider et al., 2011; Peterson et al., 2016a; Morris et al., 2018; Peterson and Harris, 2018; Lackey et al., 2020) as seen in **Figure 4**.

The success of PAINT in studying molecular interactions at a single entity level is inspiring (**Figure 4**). PAINT is distinct to conventional methods for probing molecular interactions at biointerfaces, such as surface plasmon resonance sensors which typically relies on change of local dielectric environment therefore an ensemble measurement tool (Jiang et al., 2016, 2017). A clear advantage is that PAINT is capable of detecting rare events and sample heterogeneity, a distinct feature to single molecule tools. Saying this, due to the weak binding between single stranded DNAs, the robustness of DNA PAINT in response to the influences of environmental factors, such as salt concentration and temperature is yet to be explored, which could vary significantly in complex sensing environments, such as blood or serum. Another factor to consider is that PAINT remains as a fluorescent technique, but in many applications, the candidate molecule are non-fluorescent hence it is unlikely for PAINT to completely replace current methods in the near future.

Counting Single Molecules on Biosensing Interfaces

Single molecule counting is another topic currently attracting broad attentions. From a quantitative biology perspective, knowing the exact number of molecules, especially proteins, in complex biological environments such as cells is of enormous importance and interest. This is because such knowledge will not only produce insights to how cells function and communicate, but could establish completely new ways of studying biological systems when information is gathered from single events instead of ensemble approaches currently being used (Zanacchi et al., 2017). In other words, single molecule counting allows SMLM to be treated as a bottom-up bioanalytical tool to generate discrete signal response, instead of simply an imaging tool to break the

diffraction limit of light microscopy whose mechanism has been well-appreciated (Gooding and Gaus, 2016; Lu et al., 2017; Liu et al., 2018). This marks a conceptual recent advance of SMLM, and it is most relevant to the analytical science community.

Though it sounds attractive, counting the absolute number of single molecules is by no means a trivial task. This is especially true for cellular imaging, in which counting accuracy is impaired by difficulties in controlling labeling density of the probes or complex photophysics of the blinking fluorophores. e.g., Some probes can remain in the dark and never switch "ON," others could all switch randomly at different rates. Fluorescence is a process reflecting electrons transferring between ground/excited states to emit photons. Electrons within different bands are fermions and follow rules of Boltzmann's distribution, photons are Boson particles in nature and follow Poisson's distribution, the complex origins governing the single molecular blinking imposes significant challenges to build mathematical relationships, even empirical ones.

For biosensors, challenges to the labeling issue can be partially resolved, because the density of surface epitopes can be controlled at the interface. From an analytical chemistry point of view, this is important because in principle quantification can be done directly without amplification of the analytes or accumulation of the signal. This is a distinct advantage of SMLM sensors to other single molecule assays such as digital polymerase chain reaction, or single molecule optical arrays (Wu et al., 2019).

One example was demonstrated by Lu et al. (2017). In a recent report, it was shown that images of SMLM could be obtained using fluorophore labeled antigens immobilized onto substrate modified by self-assembled monolayers with density of probes well-controlled (**Figure 5**) (Lu et al., 2017). An evident quantitative relationship was found when an increasing amount of antibodies was added. This study was important because it demonstrated the first proof-of-concept quantitative immunobiosensors with SMLM. Though it sounds straightforward, absolute counting of single molecules on biosensing interfaces is not a trivial task. In practice, counting usually relies on preliminary knowledge of the blinking behavior of molecular targets, or calibration toward a reference (Jungmann et al., 2010). Common issues include: 1. A blinking fluorophore can enter the dark state due to various reasons including photobleaching, reacting with the reducing agent, or entering triplet state, each with a significantly different lifetimes. 2. A fraction of fluorophore may never turn "ON." All of which can lead to over counting or under counting issues (Lee et al., 2012).

To date, absolute counting of single molecules with SMLM is still difficult to achieve, especially when biological samples are used when calibration can be difficult and target molecules tend to cluster together while the sample is heterogeneous. Additional challenges are associated with issues such as data interpretation and linking (Lee et al., 2017). Saying this, some successes have been achieved. e.g., In a recent study, combining SMLM to fluorescent correlation produces localization-based fluorescence correlation spectroscopy, or lbFCS (Stein et al., 2019). Essentially, the method might be the first to allow absolute counting of single molecules using SMLM, but due to the relatively complicated multimodal system it depends on, which is off-putting to non-experts, to what extent the technique can be widely used is still to be explored.

Application to Analytical Bioseparation

Chromatography separation is a basic technique used in many industrial chemical production processes such as antibody drug developments. Bringing a new biopharmaceutical product into the market is both time consuming and cost ineffective, and during this process, nearly half of the effort is spent on the separation and purifications (Calabrase et al., 2020). Conventional analytical chromatography relies heavily on empirical trials and currently there is only very limited ability to predict their outcomes (Kisley and Landes, 2015). Due to the complexity of protein structures and significant sample heterogeneity (e.g., size, charge, structure), large amount of resources are being spent to optimize column separation efficiency. At the moment, methods to improve the performance of protein chromatography techniques are in urgent need.

Single molecule optical methods may point to a possible direction to potentially solve this issue. In principle, SMLM allows quantification of protein-substrate interactions at a single molecular level. This has enabled improvements in the random theory of chromatography, with the aim of making it more quantitative and predictive (**Figure 6**) (Calabrase et al., 2020) e.g., in the recent works, it was shown that rapid imaging with time resolved single molecule detection, and combining fluorescence correlation spectroscopy and fluctuation imaging can be applied to the study of proteins diffusing through porous materials (Calabrase et al., 2020). Although strictly speaking this is still not an SMLM technique, it was shown that rare events that interfere with efficient protein separations could be identified and several quantitative relationships proposed by studying them. These developments were inspiring, because they represent a possible route for predictive chromatography single molecule technique design, hence a possible direction for applications of SMLM.

CHALLENGES AND EMERGING DIRECTIONS

Mass Transport and Target Enrichment

Mass transport is a fundamental process that describes the motion of analytes within their environments, which has been studied extensively in the field of electrochemistry and often the discussion is centered around Butler-Volmer equation. e.g., The focus is often centered on whether electron transfer or mass transport dominates the signal response (Wen et al., 2013). In the context of single molecular biosensors, mass transport is addressed by the insufficient interactions between the target molecule and sensing interface, especially when the analyte is present at low concentrations and Brownian motion inadequate. e.g., Studies with nanopores sensors suggested it could take over 10 min for the analyte to diffuse through the pore when the concentration is very low (Ying and Long, 2019) (e.g., <pM). In other words, even with a *sCMOS* with single molecular

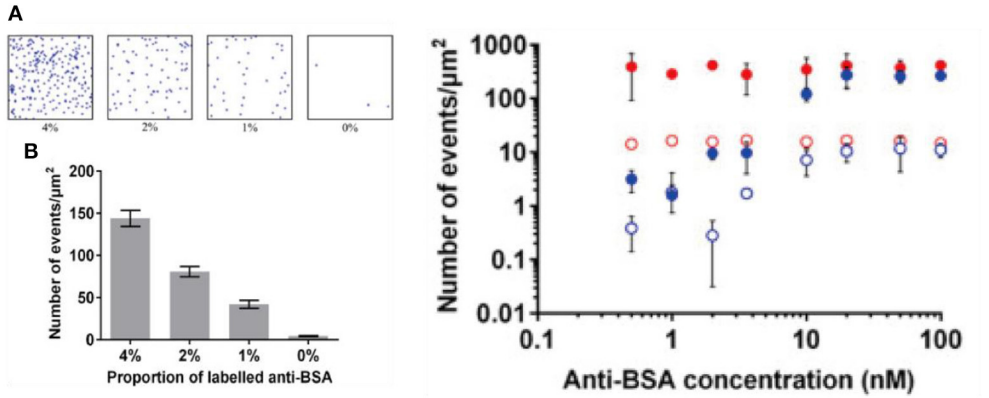

FIGURE 5 | Toward immuno-biosensors with SMLM. Shown above: (Left) **(A)** raw images of bovine serum albumin proteins immobilized on glass coverslips with self-assembled monolayer on transparent conducting oxide substrate. **(B)** A quantitative relationship is built with increased amount of labeled proteins on the surface (Right) adding an increasing amount of antibody results in an increasing number of counting per image area (Lu et al., 2017). Copyright with permission from Elsevier.

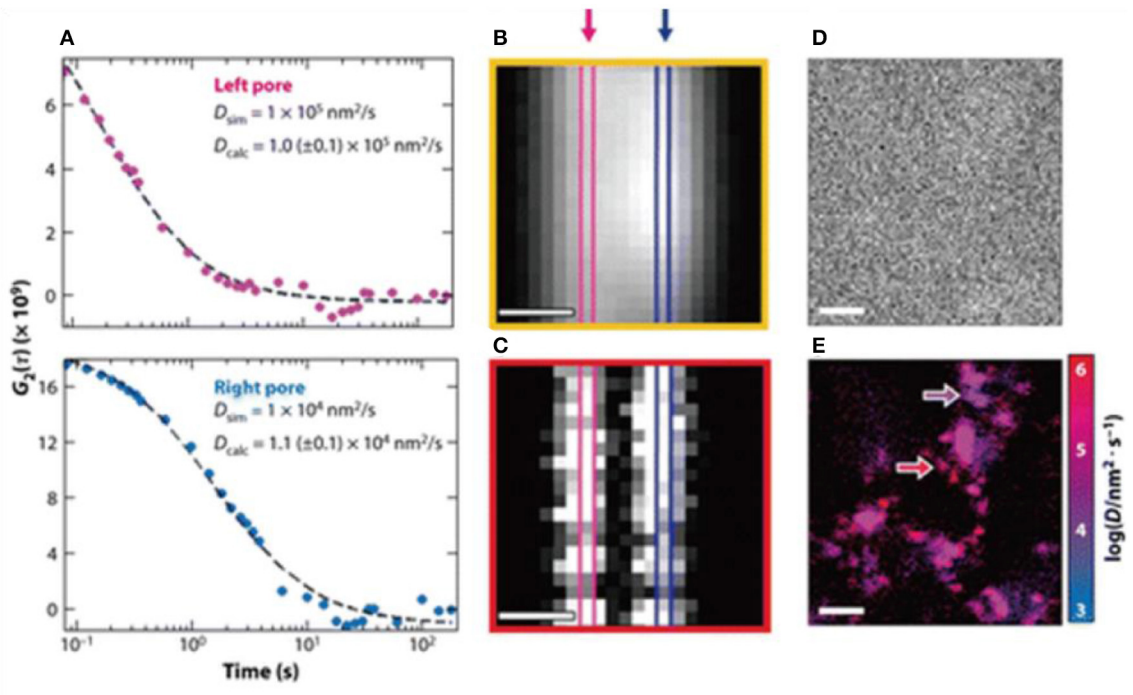

FIGURE 6 | (A–E) Toward predictive protein chromatography via SMLM. It was shown that time resolved super-resolution imaging techniques and combining fluorescence correlation to fluctuation could help build new theoretical frameworks to expand the current understanding of the protein separations in column chromatography. Shown above as an example of using dual mode correlation spectroscopy and fluctuation imaging, so that heterogeneous diffusion behavior of proteins could be resolved and parameters derived (Moringo et al., 2018). Copyright with permission from American Chemical Society.

resolution, in practice the testing cycle could be hours, and therefore impractical (Wu et al., 2019).

One simple solution to this issue is magnetic enrichment, as shown in **Figure 7**. It has been shown that incorporating magnetic nanoparticles into the analysis could substantially reduce the limit of detection and also reduce non-specific effects via target enrichment (Tavallaie et al., 2018), as discussed in a recent review (Gloag et al., 2019). Currently, there are still limited studies on the use of magnetic nanoparticles for such uses in SMLM, so a clear opportunity exists. Saying this, caution is still needed, because magnetic nanoparticles are often coated with gold because of its well-established surface chemistry (Rosi and Mirkin, 2005). It is known that at this length scale, gold nanoparticles exhibit plasmonic effects, which are coherent oscillation of conducting *d* band electrons in response to the incident light (Willets et al., 2017). In the context of SMLM,

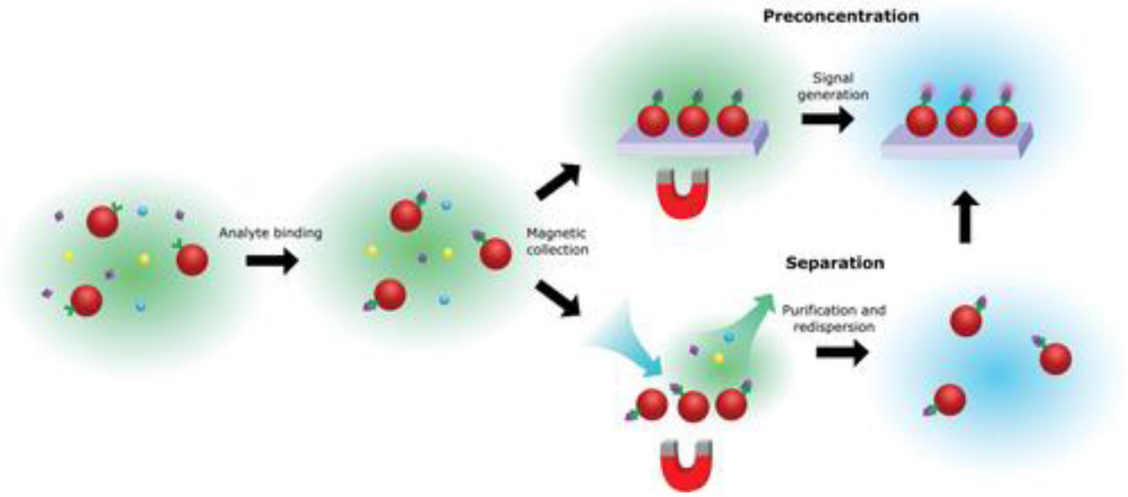

FIGURE 7 | Basic principles of magnetic enrichment. Being a "hero" in solving the mass transport issue for ultrasensitive biosensors, the use of magnetic nanoparticles can be used for pre-concentration and/or separation of the analyte, while at the same time reducing non-specific effects (Gloag et al., 2019). Copyright with permission from Wiley.

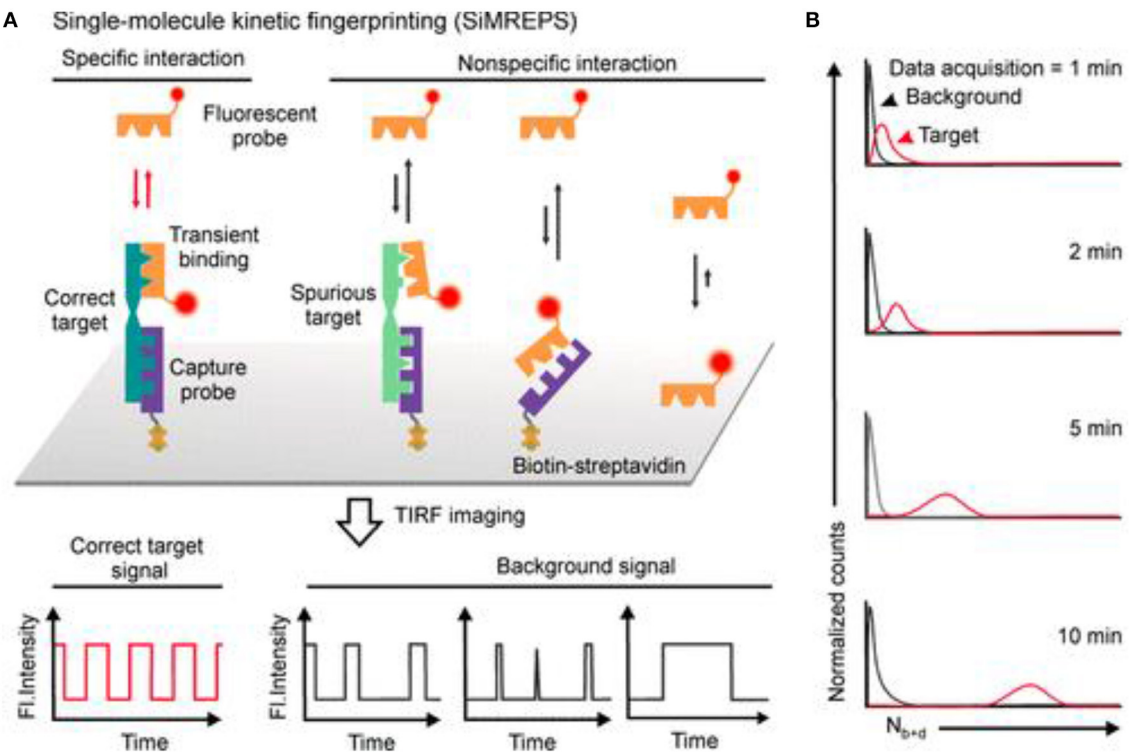

FIGURE 8 | Using SMLM to differentiate specific vs. non-specific effects with PAINT. In SiMREPS, **(A)** using carefully designed molecular probes, specific interactions are associated with single molecule blinking signals that are homogeneous over time, while non-specific events are seen as heterogeneous blinking events. **(B)** Over time, better separation between specific and non-specific events are expected (Mandal et al., 2020). Copyright with permission from the American Chemical Society.

plasmonic effects can potentially produce two outcomes, the first is that the emitting center can be shifted by the complex plasmon-molecular interactions (Xia et al., 2019), shrinking the images, and this is not favored (Cheng et al., 2019). The second is that it could produce significant signal enhancement which leads to higher localization precision, and is hence preferred. Hence, whether in this context, working with plasmonic metal is necessary or not is yet to be determined (Baiyasi et al., 2019).

Non-specific vs. Specific Interactions

For biosensors to operate in complex environments, such as blood or serum, a key aspect to consider is non-specific interactions (Jiang et al., 2020). e.g., Nucleic acid analysis and immuno-biosensors typically rely on the specific binding of biomolecules on the sensing interface to induce an optical or electrical response. For such sensors, a non-specific effect is usually undesired and should be minimized. Typically, reducing non-specificity requires the use of a chemical antifouling layer or nanostructured interface, e.g., polyethylene glycol, zwitterionic layer, or mesoporous surfaces, etc. (del Rio et al., 2019; Jiang et al., 2020).

Recently, SMLM has been shown to be able to differentiate specific and non-specific interactions by exploring the single molecule time traces, as seen in **Figure 8**. e.g., In a recent development, an amplification-free approach, named single-molecule recognition through equilibrium Poisson sampling (SiMREPS) has been shown to be able to detect miRNA with LOD close to 1 fM (Johnson-Buck et al., 2015, 2019; Chatterjee et al., 2020; Li J. M. et al. et al., 2020). In SiMREPS, specific and non-specific interactions are resolved by inspecting different kinetic time traces at a single molecular level. e.g., Specific interactions produce homogeneous blinking events, while non-specific events generate single molecular signals that are more random and heterogeneous. This development is important, because it is one of the first examples of using SMLM to differentiate specific and non-specific binding, which is pivotal to nearly all biosensors.

CONCLUSIONS

First demonstrated in 2006, it has been 15 years since the first demonstration of SMLM. Numerous methods of SMLM techniques have been developed, and now it is finding more applications in ultrasensitive bioanalysis. The realization of drift correction in SMLM is significant because it could potentially make sub-5 nm optical microscopy a routine technique without high-end engineering expertise and this is the length scale of a fluorescent protein. Kinetic measurement with PAINT, quantitative single molecule sensors and application to separation science are just three examples of emerging research frontiers brought about by SMLM. In the context of ultrasensitive sensing, to solve the mass transport issue for low abundance analyte detection, magnetic enrichment may present a viable solution, but caution is needed when a plasmonic system is used. Specificity is a fundamental issue to many bioanalytical devices operating in complex sensing environments, SMLM could lead to new knowledge to it and potentially offer a solution. Overall, the past years have witnessed rapid advances of using SMLM to probe biosensing interfaces. It is expected that the relevant field will continue to develop in an accelerated rate.

AUTHOR CONTRIBUTIONS

All authors listed have made a substantial, direct and intellectual contribution to the work, and approved it for publication.

FUNDING

This work was supported by the National Science Foundation of China (61905211 and 61474100), the Natural Science Foundation of Zhejiang Province (LY21B050002), Fundamental Research Funds for the Central Universities (No. 511308*172210191), the Science and Technology Department of Zhejiang Province (LGC19H090001), and the Department of Education of Zhejiang Province (Y202045700).

REFERENCES

Baiyasi, R., Jebeli, S. A. H., Zhang, Q. F., Su, L., Hofkens, J., Uji-i, H., et al. (2019). PSF distortion in dye-plasmonic nanomaterial interactions: friend or foe? *Acs Photon.* 6, 699–708. doi: 10.1021/acsphotonics.8b01576

Balzarotti, F., Eilers, Y., Gwosch, K. C., Gynna, A. H., Westphal, V., Stefani, F. D., et al. (2017). Nanometer resolution imaging and tracking of fluorescent molecules with minimal photon fluxes. *Science* 355, 606–612. doi: 10.1126/science.aak9913

Betzig, E., Patterson, G. H., Sougrat, R., Lindwasser, O. W., Olenych, S., Bonifacino, J. S., et al. (2006). Imaging intracellular fluorescent proteins at nanometer resolution. *Science* 313, 1642–1645. doi: 10.1126/science.1127344

Blythe, K. L., Titus, E. J., and Willets, K. A. (2014). Triplet-state-mediated super-resolution imaging of fluorophore-labeled gold nanorods. *Chemphyschem* 15, 784–793. doi: 10.1002/cphc.201300767

Blythe, K. L., Titus, E. J., and Willets, K. A. (2015a). Effects of tuning fluorophore density, identity, and spacing on reconstructed images in super-resolution imaging of fluorophore-labeled gold nanorods. *J. Phys. Chem. C* 119, 28099–28110. doi: 10.1021/acs.jpcc.5b08364

Blythe, K. L., Titus, E. J., and Willets, K. A. (2015b). Comparing the accuracy of reconstructed image size in super-resolution imaging of fluorophore-labeled gold nanorods using different fit models. *J. Phys. Chem. C* 119, 19333–19343. doi: 10.1021/acs.jpcc.5b04993

Blythe, K. L., and Willets, K. A. (2016). Super-resolution imaging of fluorophore-labeled DNA bound to gold nanoparticles: a single-molecule, single-particle approach. *J. Phys. Chem. C* 120, 803–815. doi: 10.1021/acs.jpcc.5b08534

Calabrase, W., Bishop, L. D., Dutta, C., Misiura, A, Landes, C. F., and Kisley, L. (2020). Transforming separation science with single-molecule methods. *Anal. Chem*. 92, 13622–13629. doi: 10.1021/acs.analchem.0c02572

Chatterjee, T., Li, Z., Khanna, K., Montoya, K., Tewari, M., Walter, N. G., et al. (2020). Ultraspecific analyte detection by direct kinetic fingerprinting of single molecules. *Trac.-Trend Anal. Chem*. 123:115764. doi: 10.1016/j.trac.2019.115764

Chen, T., Dong, B., Chen, K. C., Zhao, F., Cheng, X. D., Ma, C. B., et al. (2017). Optical super-resolution imaging of surface reactions. *Chem. Rev*. 117, 7510–7537. doi: 10.1021/acs.chemrev.6b00673

Cheng, X. Y., Anthony, T. P., West, C. A., Hu, Z. W., Sundaresan, V., McLeod, A. J., et al. (2019). Plasmon heating promotes ligand reorganization on single gold nanorods. *J. Phys. Chem. Lett*. 10, 1394–1401. doi: 10.1021/acs.jpclett.9b00079

Coelho, S., Baek, J., Graus, M. S., Halstead, J. M., Nicovich, P. R., Feher, K., et al. (2020). Ultraprecise single-molecule localization microscopy enables in situ distance measurements in intact cells. *Sci. Adv*. 6:eaay8271. doi: 10.1126/sciadv.aay8271

Coelho, S., Baek, J., Walsh, J., Gooding, J. J., and Gaus, K. (2021). 3D active stabilization for single-molecule imaging. *Nat. Protoc*. 16, 497–515. doi: 10.1038/s41596-020-00426-9

Dai, M. J., Jungmann, R., and Yin, P. (2016). Optical imaging of individual biomolecules in densely packed clusters. *Nat. Nanotechnol.* 11, 798–807. doi: 10.1038/nnano.2016.95

del Rio, J. S., Henry, O., Jolly, P., and Ingber, D. E. (2019). An antifouling coating that enables affinity-based electrochemical biosensing in complex biological fluids. *Nat. Nanotechnol.* 14, 1143–1149. doi: 10.1038/s41565-019-0566-z

Dickson, R. M., Cubitt, A. B., Tsien, R. Y., and Moerner, W. E. (1997). On/off blinking and switching behaviour of single molecules of green fluorescent protein. *Nature* 388, 355–358. doi: 10.1038/41048

Fox, C. B., Wayment, J. R., Myers, G. A., Endicott, S. K., and Harris, J. M. (2009). Single-molecule fluorescence imaging of peptide binding to supported lipid bilayers. *Anal. Chem.* 81, 5130–5138. doi: 10.1021/ac9007682

Gloag, L., Mehdipour, M., Chen, D. F., Tilley, R. D., and Gooding, J. J. (2019). Advances in the application of magnetic nanoparticles for sensing. *Adv. Mater.* 31:e1904385. doi: 10.1002/adma.201904385

Gooding, J. J., and Gaus, K. (2016). Single-molecule sensors: challenges and opportunities for quantitative analysis. *Angew Chem. Int. Edit.* 55, 11354–11366. doi: 10.1002/anie.201600495

Ha, T., and Tinnefeld, P. (2012). Photophysics of fluorescent probes for single-molecule biophysics and super-resolution imaging. *Annu. Rev. Phys. Chem.* 63, 595–617. doi: 10.1146/annurev-physchem-032210-103340

Hao, X., Kuang, C. F., Gu, Z. T., Wang, Y. F., Li, S. A., Ku, Y. L., et al. (2013). From microscopy to nanoscopy via visible light. *Light-Sci. Appl.* 2:e108. doi: 10.1038/lsa.2013.64

Heider, E. C., Peterson, E. M., Barhoum, M., Gericke, K. H., and Harris, J. M. (2011). Quantitative fluorescence microscopy to determine molecular occupancy of phospholipid vesicles. *Anal. Chem.* 83, 5128–5136. doi: 10.1021/ac200129n

Huang, F., Hartwich, T. M., Rivera-Molina, F. E., Lin, Y., Duim, W. C., Uchil, P. D., et al. (2013). Video-rate nanoscopy using sCMOS camera-specific single-molecule localization algorithms. *Nat. Methods* 10, 653–658. doi: 10.1038/nmeth.2488

Huang, Z. L., Zhu, H. Y., Long, F., Ma, H. Q., Qin, L. S., Liu, Y. F., et al. (2011). Localization-based super-resolution microscopy with an sCMOS camera. *Opt. Express.* 19, 19156–19168. doi: 10.1364/OE.19.019156

Jiang, C., Wang, G. X., Hein, R., Liu, N. Z., Luo, X. L., and Davis, J. J. (2020). Antifouling strategies for selective in vitro and in vivo sensing. *Chem. Rev.* 120, 3852–3889. doi: 10.1021/acs.chemrev.9b00739

Jiang, L., Zeng, S., Xu, Z., Ouyang, Q., Zhang, D.-H., Chong, P. H. J., et al. (2017). Multifunctional hyperbolic nanogroove metasurface for submolecular detection. *Small* 13:1700600. doi: 10.1002/smll.201700600

Jiang, L., Zhao, X. Y., Fei, Y., Yu, D. D., Qian, J., Tong, J. G., et al. (2016). The effects of magnetic fields exposure on relative permittivity of saline solutions measured by a high resolution SPR system. *Sci. Rep.* 6:25111. doi: 10.1038/srep25111

Johnson-Buck, A., Li, J. M., Tewari, M., and Walter, N. G. (2019). A guide to nucleic acid detection by single-molecule kinetic fingerprinting. *Methods* 153, 3–12. doi: 10.1016/j.ymeth.2018.08.002

Johnson-Buck, A., Su, X., Giraldez, M. D., Zhao, M. P., Tewari, M., and Walter, N. G. (2015). Kinetic fingerprinting to identify and count single nucleic acids. *Nat. Biotechnol.* 33, 730–732. doi: 10.1038/nbt.3246

Jungmann, R., Avendano, M. S., Dai, M. J., Woehrstein, J. B., Agasti, S. S., Feiger, Z., et al. (2016). Quantitative super-resolution imaging with qPAINT. *Nat. Methods* 13, 439–442. doi: 10.1038/nmeth.3804

Jungmann, R., Avendano, M. S., Woehrstein, J. B., Dai, M. J., Shih, W. M., and Yin, P. (2014). Multiplexed 3D cellular super-resolution imaging with DNA-PAINT and Exchange-PAINT. *Nat. Methods* 11, 313–318. doi: 10.1038/nmeth.2835

Jungmann, R., Steinhauer, C., Scheible, M., Kuzyk, A., Tinnefeld, P., and Simmel, F. C. (2010). Single-molecule kinetics and super-resolution microscopy by fluorescence imaging of transient binding on DNA origami. *Nano Lett.* 10, 4756–4761. doi: 10.1021/nl103427w

Kisley, L., and Landes, C. F. (2015). Molecular approaches to chromatography using single molecule spectroscopy. *Anal. Chem.* 87, 83–98. doi: 10.1021/ac5039225

Lackey, H. H., Peterson, E. M., Harris, J. M., and Heemstra, J. M. (2020). Probing the mechanism of structure-switching aptamer assembly by super-resolution localization of individual DNA molecules. *Anal. Chem.* 92, 6909–6917. doi: 10.1021/acs.analchem.9b05563

Lee, A., Tsekouras, K., Calderon, C., Bustamante, C., and Presse, S. (2017). Unraveling the thousand word picture: an introduction to super-resolution data analysis. *Chem. Rev.* 117, 7276–7330. doi: 10.1021/acs.chemrev.6b00729

Lee, S. H., Shin, J. Y., Lee, A., and Bustamante, C. (2012). Counting single photoactivatable fluorescent molecules by photoactivated localization microscopy (PALM). *Proc. Natl. Acad. Sci. U. S. A.* 109, 17436–17441. doi: 10.1073/pnas.1215175109

Li, C. K., Le, V., Wang, X. N., Hao, X., Liu, X., and Kuang, C. F. (2020). Resolution enhancement and background suppression in optical super-resolution imaging for biological applications. *Laser Photonics Rev.* 15:1900084. doi: 10.1002/lpor.201900084

Li, H. L., and Vaughan, J. C. (2018). Switchable fluorophores for single-molecule localization microscopy. *Chem. Rev.* 118, 9412–9454. doi: 10.1021/acs.chemrev.7b00767

Li, J. M., Zhang, L. Y., Johnson-Buck, A., and Walter, N. G. (2020). Automatic classification and segmentation of single-molecule fluorescence time traces with deep learning. *Nat. Commun.* 11:5833. doi: 10.1038/s41467-020-19673-1

Liu, W. J., Toussaint, K. C., Okoro, C., Zhu, D. Z., Chen, Y. H., Kuang, C. F., et al. (2018). Breaking the axial diffraction limit: a guide to axial super-resolution fluorescence microscopy. *Laser Photonics Rev.* 12:1700333. doi: 10.1002/lpor.201700333

Long, F., Zeng, S. Q., and Huang, Z. L. (2012). Localization-based super-resolution microscopy with an sCMOS camera Part II: experimental methodology for comparing sCMOS with EMCCD cameras. *Opt. Express* 20, 17741–17759. doi: 10.1364/OE.20.017741

Lu, X., Nicovich, P. R., Gaus, K., and Gooding, J. J. (2017). Towards single molecule biosensors using super-resolution fluorescence microscopy. *Biosensors Bioelectronics* 93, 1–8. doi: 10.1016/j.bios.2016.10.048

Ma, H. Q., Kawai, H., Toda, E., Zeng, S. Q., and Huang, Z. L. (2013). Localization-based super-resolution microscopy with an sCMOS camera part III: camera embedded data processing significantly reduces the challenges of massive data handling. *Opt. Lett.* 38, 1769–1771. doi: 10.1364/OL.38.001769

Mandal, S., Li, Z., Chatterjee, T., Khanna, K., Montoya, K., Dai, L., et al. (2020). Direct kinetic fingerprinting for high-accuracy single-molecule counting of diverse disease biomarkers. *Accounts Chem. Res.* 54, 388–402. doi: 10.1021/acs.accounts.0c00621

Mockl, L., and Moerner, W. E. (2020). Super-resolution microscopy with single molecules in biology and beyond-essentials, current trends, and future challenges. *J. Am. Chem. Soc.* 142, 17828–17844. doi: 10.1021/jacs.0c08178

Moerner, W. E. (2015a). Nobel lecture: single-molecule spectroscopy, imaging, and photocontrol: foundations for super-resolution microscopy. *Rev. Mod. Phys.* 87:1183. doi: 10.1103/RevModPhys.87.1183

Moerner, W. E. (2015b). Single-molecule spectroscopy, imaging, and photocontrol: foundations for super-resolution microscopy (nobel lecture). *Angew Chem. Int. Edit.* 54, 8067–8093. doi: 10.1002/anie.201501949

Moringo, N. A., Shen, H., Bishop, L., Wang, W., and Landes, C. F. (2018). Enhancing analytical separations using super-resolution microscopy. *Annu. Rev. Phys. Chem.* 69, 353–375. doi: 10.1146/annurev-physchem-052516-045018

Morris, F. D., Peterson, E. M., Heemstra, J. M., and Harris, J. M. (2018). Single-molecule kinetic investigation of cocaine-dependent split-aptamer assembly. *Anal. Chem.* 90, 12964–12970. doi: 10.1021/acs.analchem.8b03637

Nahidiazar, L., Agronskaia, A. V., Broertjes, J., van den Broek, B., and Jalink, K. (2016). Optimizing imaging conditions for demanding multi-color super resolution localization microscopy. *PLoS ONE* 11:e158884. doi: 10.1371/journal.pone.0158884

Nicovich, P. R., Owen, D. M., and Gaus, K. (2017). Turning single-molecule localization microscopy into a quantitative bioanalytical tool. *Nat. Protoc.* 12, 453–460. doi: 10.1038/nprot.2016.166

Pan, L. T., Yan, R., Li, W., and Xu, K. (2018). Super-resolution microscopy reveals the native ultrastructure of the erythrocyte cytoskeleton. *Cell Rep.* 22, 1151–1158. doi: 10.1016/j.celrep.2017.12.107

Pan, L. T., Zhang, P., Hu, F., Yan, R., He, M. N., Li, W., et al. (2019). Hypotonic stress induces fast, reversible degradation of the vimentin cytoskeleton via intracellular calcium release. *Adv. Sci.* 6:7416. doi: 10.1101/607416

Peterson, E. M., and Harris, J. M. (2018). Identification of individual immobilized DNA molecules by their hybridization kinetics using single-molecule fluorescence imaging. *Anal. Chem.* 90, 5007–5014. doi: 10.1021/acs.analchem.7b04512

Peterson, E. M., Manhart, M. W., and Harris, J. M. (2016a). Competitive assays of label-free DNA hybridization with single-molecule fluorescence imaging detection. *Anal. Chem*. 88, 6410–6417. doi: 10.1021/acs.analchem.6b00992

Peterson, E. M., Manhart, M. W., and Harris, J. M. (2016b). Single-molecule fluorescence imaging of interfacial DNA hybridization kinetics at selective capture surfaces. *Anal. Chem*. 88, 1345–1354. doi: 10.1021/acs.analchem.5b03832

Rosi, N. L., and Mirkin, C. A. (2005). Nanostructures in biodiagnostics. *Chem. Rev*. 105, 1547–1562. doi: 10.1021/cr030067f

Rust, M. J., Bates, M., and Zhuang, X. W. (2006). Sub-diffraction-limit imaging by stochastic optical reconstruction microscopy (STORM). *Nat. Methods* 3, 793–795. doi: 10.1038/nmeth929

Sage, D., Kirshner, H., Pengo, T., Stuurman, N., Min, J., Manley, S., et al. (2015). Quantitative evaluation of software packages for single-molecule localization microscopy. *Nat. Methods* 12, 717–737. doi: 10.1038/nmeth.3442

Sambur, J. B., Chen, T. Y., Choudhary, E., Chen, G. Q., Nissen, E. J., Thomas, E. M., et al. (2016). Sub-particle reaction and photocurrent mapping to optimize catalyst-modified photoanodes. *Nature* 530, 77–80. doi: 10.1038/nature16534

Sauer, M., and Heilemann, M. (2017). Single-molecule localization microscopy in eukaryotes. *Chem. Rev*. 117, 7478–7509. doi: 10.1021/acs.chemrev.6b00667

Schnitzbauer, J., Strauss, M. T., Schlichthaerle, T., Schueder, F., and Jungmann, R. (2017). Super-resolution microscopy with DNA-PAINT. *Nat. Protoc*. 12, 1198–1228. doi: 10.1038/nprot.2017.024

Stehr, F., Stein, J., Schueder, F., Schwille, P., and Jungmann, R. (2019). Flat-top TIRF illumination boosts DNA-PAINT imaging and quantification. *Nat. Commun*. 10:1268. doi: 10.1038/s41467-019-09064-6

Stein, J., Stehr, F., Schueler, P., Blumhardt, P., Schueder, F., Mucksch, J., et al. (2019). Toward absolute molecular numbers in DNA-PAINT. *Nano Lett*. 19, 8182–8190. doi: 10.1021/acs.nanolett.9b03546

Tavallaie, R., McCarroll, J., Le Grand, M., Ariotti, N., Schuhmann, W., Bakker, E., et al. (2018). Nucleic acid hybridization on an electrically reconfigurable network of gold-coated magnetic nanoparticles enables microRNA detection in blood. *Nat. Nanotechnol.* 13, 1066–1071. doi: 10.1038/s41565-018-0232-x

Titus, E. J., and Willets, K. A. (2013a). Superlocalization surface-enhanced raman scattering microscopy: comparing point spread function models in the ensemble and single-molecule limits. *ACS Nano* 7, 8284–8294. doi: 10.1021/nn403891t

Titus, E. J., and Willets, K. A. (2013b). Accuracy of superlocalization imaging using gaussian and dipole emission point-spread functions for modeling gold nanorod luminescence. *ACS Nano* 7, 6258–6267. doi: 10.1021/nn4022845

Tuson, H. H., and Biteen, J. S. (2015). Unveiling the inner workings of live bacteria using super-resolution microscopy. *Anal. Chem*. 87, 42–63. doi: 10.1021/ac5041346

van de Linde, S., Loschberger, A., Klein, T., Heidbreder, M., Wolter, S., Heilemann, M., et al. (2011). Direct stochastic optical reconstruction microscopy with standard fluorescent probes. *Nat. Protoc*. 6, 991–1009. doi: 10.1038/nprot.2011.336

Vaughan, J. C., Dempsey, G. T., Sun, E., and Zhuang, X. W. (2013). Phosphine quenching of cyanine dyes as a versatile tool for fluorescence microscopy. *J. Am. Chem. Soc*. 135, 1197–1200. doi: 10.1021/ja3105279

von Diezmann, A., Shechtman, Y., and Moerner, W. E. (2017). Three-dimensional localization of single molecules for super resolution imaging and single-particle tracking. *Chem. Rev*. 117, 7244–7275. doi: 10.1021/acs.chemrev.6b00629

Wayment, J. R., and Harris, J. M. (2009). Biotin-avidin binding kinetics measured by single-molecule imaging. *Anal. Chem*. 81, 336–342. doi: 10.1021/ac80 1818t

Wen, Y. L., Liu, G., Pei, H., Li, L. Y., Xu, Q., Liang, W., et al. (2013). DNA nanostructure-based ultrasensitive electrochemical microRNA biosensor. *Methods* 64, 276–282. doi: 10.1016/j.ymeth.2013.07.035

Willets, K. A., Wilson, A. J., Sundaresan, V., and Joshi, P. B. (2017). Super-resolution imaging and plasmonics. *Chem. Rev*. 117, 7538–7582. doi: 10.1021/acs.chemrev.6b00547

Wu, Y. F., Tilley, R. D., and Gooding, J. J. (2019). Challenges and solutions in developing ultrasensitive biosensors. *J. Am. Chem. Soc*. 141, 1162–1170. doi: 10.1021/jacs.8b09397

Xia, J., Tang, J. W., Bao, F. L., Evans, J., and He, S. L. (2019). Channel competition in emitter-plasmon coupling. *Opt. Express*. 27, 30893–30908. doi: 10.1364/OE.27.030893

Xing, F. L., Hu, F., Yang, J. Y., Pan, L. T., and Xu, J. J. (2019). Structural and functional studies of erythrocyte membrane-skeleton by single-cell and single-molecule techniques. *J. Innov. Opt. Heal. Sci*. 12:1830004. doi: 10.1142/S1793545818300045

Ying, Y. L., and Long, Y. T. (2019). Nanopore-based single-biomolecule interfaces: from information to knowledge. *J. Am. Chem. Soc*. 141, 15720–15729. doi: 10.1021/jacs.8b11970

Zanacchi, F. C., Manzo, C., Alvarez, A. S., Derr, N. D., Garcia-Parajo, M. F., and Lakadamyali, M. (2017). A DNA origami platform for quantifying protein copy number in super-resolution. *Nat. Methods* 14, 789–792. doi: 10.1038/nmeth.4342

Conflict of Interest: The authors declare that the research was conducted in the absence of any commercial or financial relationships that could be construed as a potential conflict of interest.

frontiers in Chemistry

ORIGINAL RESEARCH
published: 30 April 2021
doi: 10.3389/fchem.2021.640519

Application of SNAP-Tag in Expansion Super-Resolution Microscopy Using DNA Oligostrands

Longfang Yao[1†], *Li Zhang*[2†], *Yiyan Fei*[1], *Liwen Chen*[1], *Lan Mi*[1*] and *Jiong Ma*[1,2,3*]

[1] Department of Optical Science and Engineering, Shanghai Engineering Research Center of Ultra-Precision Optical Manufacturing, Key Laboratory of Micro and Nano Photonic Structures (Ministry of Education), Green Photoelectron Platform, Fudan University, Shanghai, China, [2] Shanghai Engineering Research Center of Industrial Microorganisms, The Multiscale Research Institute of Complex Systems, School of Life Sciences, Fudan University, Shanghai, China, [3] Insititute of Biomedical Engineering and Technology, Academy for Engineering and Technology, Fudan University, Shanghai, China

Expansion super-resolution technology is a new technology developed in recent years. It anchors the dye on the hydrogel and the dye expands with the expansion of the hydrogel so that a super-resolution map can be obtained under an ordinary microscope. However, by labeling the target protein with a first antibody and secondary antibody, the distance between the fluorescent group and the actual target protein is greatly increased. Although fluorescent proteins can also be used for expansion super-resolution to reduce this effect, the fluorescent protein is often destroyed during sample preparation. To solve this problem, we developed a novel label system for expansion microscopy, based on a DNA oligostrand linked with a fluorescent dye, acrylamide group (linker), and benzoylguanine (BG, a small substrate molecule for SNAP-tag). This protocol greatly reduced the error between the position of fluorescent group and the actual target protein, and also reduced loss of the fluorescent group during sample preparation.

Keywords: expansion super-resolution, DNA oligostrand, SNAP, F-actin, nuclear pore complex

OPEN ACCESS

Edited by:
Hongyan Sun,
City University of Hong Kong, Hong Kong

Reviewed by:
Markus Sauer,
Julius Maximilian University of Würzburg, Germany
Huatang Zhang,
Guangdong University of Technology, China

***Correspondence:**
Lan Mi
lanmi@fudan.edu.cn
Jiong Ma
jiongma@fudan.edu.cn

[†] *These authors have contributed equally to this work*

Specialty section:
This article was submitted to Analytical Chemistry, a section of the journal Frontiers in Chemistry

Received: *11 December 2020*
Accepted: *12 April 2021*
Published: *30 April 2021*

Citation:
Yao L, Zhang L, Fei Y, Chen L, Mi L and Ma J (2021) Application of SNAP-Tag in Expansion Super-Resolution Microscopy Using DNA Oligostrands. Front. Chem. 9:640519. doi: 10.3389/fchem.2021.640519

INTRODUCTION

The optical microscope has been an important tool for biomedical research for a long time, because of its advantages of non-contact and no damage to the specimen. However, the diffraction limit, ∼200–300 nm in the lateral direction, is comparable to or larger than many subcellular structures. Super-resolution fluorescence microscopy overcomes this limitation and provides an unprecedented tool for life science research (Huang et al., 2009). Stimulated emission depletion (STED) microscopy was the first super-resolution far-field optical microscopy technology; it utilizes a laser to suppress the fluorescence emission from the fluorophores located at the periphery of the excitation using stimulated emissions (Hell, 2015). STED microscopy can realize immunofluorescence imaging at 20 nm resolution and fluorescent protein imaging at 50–70 nm (Willig et al., 2006; Hein et al., 2008; Rankin et al., 2008). Single-molecule localization microscopy (SMLM) is based on the localization of individual fluorescent molecules. Typical examples of this kind of technology are photoactivated localization microscopy and stochastic optical reconstruction microscopy (STORM) (Betzig et al., 2006; Rust et al., 2006). Another method to improve the spatial resolution of optical microscope is structured illumination microscopy (SIM), which applies a patterned illumination field to the sample to obtain multiple images with illumination patterns of different phases and directions, thus reconstructing high-resolution

images with a lateral resolution of ∼100 nm and axial resolution of ∼300 nm (Gustafsson, 2000; Gustafsson et al., 2008; Schermelleh et al., 2008). However, these three technologies have their own disadvantages. STED technology causes a large amount of light damage to the sample; SMLM technology has slow imaging speed and requires special fluorescent molecular markers; SIM technology has fast imaging speed, but lower resolution improvement.

In 2015, the Boyden group invented expansion super-resolution technology (Chen et al., 2015). This technology does not make changes to the microscope hardware but puts the fluorescently labeled biological sample in the swellable hydrogel so that the sample can be enlarged evenly as the polyacrylamide hydrogel swells. In this way, a super-resolution image can be obtained using ordinary microscope equipment. Combining expansion technology with traditional super-resolution optical imaging technology greatly increases the resolution, allowing observation of subtle structures and phenomena that were previously unobservable. For example, in 2018, expansion stimulated emission depletion microscopy (ExSTED), combined expansion microscopy and STED together, achieved super-resolution images with a resolution of <10 nm, which is 30 times higher than traditional microscopy techniques (Gao et al., 2018). In addition, the combination of expansion and STORM has also achieved good results. Using this technology in mouse spermatocytes achieved a resolution of 10–20 nm and showed a detailed structural view of the meiotic chromosome axis (Xu et al., 2019). The combination of extension and SIM can also increase the spatial resolution to 30 nm. Furthermore, ExFEAST, which combines fluctuation-enhanced Airyscan technology (FEAST) and sample expansion microscopy, improves the lateral resolution to ∼26 nm (Wang et al., 2020). Its advantages of simple operation and fast but powerful functions provide great convenience for the research of fixed biological specimens and even more biological systems (Halpern et al., 2017).

At present, there are two main fluorescent labeling methods used in expansion super-resolution. One is to use a primary antibody to connect a fluorescently-coupled secondary antibody (Kunz et al., 2020). The other is to use a fluorescent protein fused to the target protein (Tillberg et al., 2016). After expansion, the fluorescence signal can be lost owing to various reasons. Under normal circumstances, the luminous efficiency, brightness, and anti-quenching ability of antibodies are much stronger than fluorescent proteins. Therefore, even if the fluorescent signal is lost during the preparation of the expanded sample, information from the sample can be obtained based on the remaining fluorescent signal. However, the disadvantage of antibody labeling is that their large size leads the luminescent group to be far away from the target protein. In addition, only a few kinds of antibodies are available, limiting their practicability. In non-expanded samples, this size of an antibody is ∼20 nm, which does not cause a large error, but after expansion, the size of antibody can often reach more than 80 nm (Mikhaylova et al., 2015; Zwettler et al., 2020). Antibody size is a critical factor that limits further resolution improvement in expansion microscopy (Li et al., 2018). The advantage of labeling the target protein with fluorescent protein is that the distance error is small, but the loss of fluorescent protein during preparation of the expanded sample is relatively large. Therefore, significant information is often missing (Tillberg et al., 2016). To improve this situation, one method is to expand the sample first and then label. For example, a biotin-conjugated antibody is used to identify the target protein before expansion, and dye-labeled streptavidin is used to identify the biotin after expansion (Li et al., 2018). Compared to using antibodies before expansion, this method can reduce the distance between the luminescent group and the target protein and reduce the loss of fluorescent signal. However, additional methods are still needed to reduce the distance between the fluorescent dye and the target protein.

To solve this problem, we developed a novel labeling system suitable for expansion microscopy. The system is based on SNAP-tag and a DNA oligostrand. SNAP-tag, a small mutant of the DNA repair protein O6-alkylguanine-DNA alkyltransferase (20 kD, <5 nm), can be covalently modified using O6-benzylguanine substrates (BG) (Juillerat et al., 2003; Nieves et al., 2019). The DNA oligostrand that we designed is a double-stranded DNA of 20 bp modified with BG, Acrydite, and dye at both ends of the DNA oligostrand. Fluorescent dyes can be taken to the target protein through the connection between SNAP and BG, and Acrydite can participate in the polymerization process of hydrogels to reduce the loss of the fluorescent group. In addition, since the DNA oligostrand, still intact after proteolysis, is not enlarged with the hydrogel, we can achieve our goal to reduce the distance between the fluorescent group and the target protein after expansion. We applied this method to observe the structure of F-actin and the nuclear pore complex (NPC), and found that these structures could be seen more delicately, indicating that it has the potential for application in a variety of fields.

MATERIALS AND METHODS

Materials

Vector pEGFP-N1 was used to create the plifeAct-SNAP-EGFP, plifeAct-SNAP, and pNup153-SNAP plasmids. After restriction digestion to generate an empty backbone, the appropriate fragments were inserted into pEGFP-N1.

Modification and Synthesis of DNA Oligostrand

We designed the DNA single strands according to Chen et al. (2015) with some modification. The sequences of the single-stranded DNAs are as follows: 5′-Alexa647-GACGATGTATGCTTAGGGTCT-Acrydite-3′; 5′-Alexa488-GACGATGTATGCTTAGGGTCT-Acrydite-3′; and 5′-BG-GACCCTAAGCATACATCGTCTT-3′. The modified DNA single strands were synthesized by the Beijing Genomics Institution (Beijing, China). Using the annealing program of the thermocycler, the DNA oligostrands were formed by the polymerization of single-stranded DNA. DNA oligostrands synthesized from different single strands were named BG-dsDNA-Alexa647 and BG-dsDNA-Alexa488.

Cell Culture

HeLa and U2OS cells were grown in DMEM containing 1 g/L glucose (Gibco/Invitrogen) supplemented with 10% fetal bovine serum and 100 U/mL penicillin-streptomycin in a 37°C tissue culture incubator. Before transfection, cells were cultured in chambered cover glasses overnight to 60–80% confluence. The cells were transfected with constructs for 24 h using Lipofectamine 3000 (ThermoFisher) according to the manufacturer's protocol. After transfection, cells were then seeded on a #1.0/18 mm diameter round cover glass (Menzel) for use.

Labeling With DNA Oligostrand in Fixed Cells

For fixed cell labeling, cells expressing SNAP-tags were harvested at 60–80% confluence and rinsed twice with phosphate buffered saline (PBS) to remove dead cells and debris. After fixing with 4% paraformaldehyde (157-8, Electron Microscopy Sciences) and 0.1% glutaraldehyde for 15 min at 25°C, cells were permeabilized with PBS supplemented with 0.3% Triton-X100 for 3 min and rinsed with PBS three times. DNA oligostrands were incubated with fixed cells at a final concentration of 1 μM in PBS supplemented with 5% bovine serum albumin and 1 mM DL-dithiothreitol (DTT) for 2 h.

Labeling of Live Cells With DNA Oligostrands

Coverslips covered in an ∼60–80% confluent layer of HeLa and U2OS cells were transfected with related constructs, incubated in 37°C prewarmed 40 μg/mL digitonin (Cat#D141; Sigma Aldrich) in import buffer (20 mM Hepes, 110 mM KOAC, 5 mM NaOAC, 2 mM MgOAC, 1 mM EGTA, pH 7.3) for 15 s for F-actin and 3 min for NPC, and then rinsed twice with 1.5% polyvinylpyrrolidone (PVP) in import buffer. The cells were stained with DNA oligostrands at a final concentration of 1 μM in 1.5% polyvinylpyrrolidone supplemented with 1 mM DTT for 5 min. Cells were then fixed with 4% paraformaldehyde and 0.1% glutaraldehyde (A600875-0025, BBI Life Sciences, Shanghai, China) for 15 min at 25°C, rinsed with PBS, and mounted in ProLong Glass Antifade Mountant (P36980, Invitrogen, Thermo Fisher Scientific). In this study, for plifeact-SNAP-EGFP, DNA oligostrand BG-dsDNA-Alexa647 was used. For plifeAct-SNAP and pNup153-SNAP, DNA oligostrand BG-dsDNA-Alexa488 was used.

Expansion Microscopy

Expansion microscopy was performed as previously described (Chozinski et al., 2016) with slight modifications. To form a gel, stained and fixed cells were incubated with a monomer solution containing 8.625% sodium acrylate (w/w) (408220, Sigma-Aldrich), 2.5% acrylamide (w/w) (A4058, Sigma-Aldrich), 0.15% *N, N*, -methylenebisacrylamide (w/w) (M7279, Sigma-Aldrich), 2 M NaCl (S5886, Sigma), and 1× PBS at room temperature and supplemented with fresh 0.2% (w/w) ammonium persulfate (APS, 17874, Thermo Fisher Scientific, Waltham, MA) and 0.2% (w/w) tetramethylethylenediamine (TEMED, 17919, Thermo Fisher Scientific, Waltham, MA) when used. Polymerization was performed for 2 h. The diameter of the gelated samples was measured to calculate the expansion ratio. A total of 8 U/mL proteinase K (EO0491, Thermo Fisher Scientific, Waltham, MA) in digestion buffer (50 mM Tris pH 8.0, 1 mM EDTA, 0.5% Triton X-100, 0.8 M guanidine HCl) was added to the gelated samples to digest cells. The digested cells were then expanded in ddH_2O, and the water was changed every 30 min until the gel size no longer changed. The diameter of the gel was measured to calculate the expansion factor with dimensions before expansion. The expanded gels were stored in ddH_2O at 4°C until use. For imaging, the gel was fixed with 3% low melting point agarose near the corner of the gel.

Imaging

Unexpanded and expanded specimens in 35 mm glass bottom dishes were fixed as described in the previous protocol. Wide-field fluorescent images were collected onto an EMCCD camera (Evolve 512, Delta Photometrics) with an oil-immersed objective (150×/1.45, Olympus), yielding a pixel size of 106 nm. Emissions were collected through an objective and filtered by a 520 nm band-pass filter (FF01-520/35-25, Semrock) for Alexa488 or by a 655 nm band-pass filter (FF02-655/40-25, Semrock) for Alexa647. Airyscan imaging was performed using a commercial microscope (ZEISS, LSM880, Germany) with an additional Airy FAST detector module (Zeiss), equipped with a Plan-Apochromat 63×/1.4NA oil objective (Zeiss; Plan-Apochromat 63×/1.4 Oil DIC M27). Samples stained with BG-dsDNA-Alexa488 were excited using a 488 nm laser. Emissions were collected through a 495–550 nm band-pass filter, 570 nm long-pass filter, and a 1.25 airy unit (∼60 μm) pinhole onto a 32 GaAsP detector element. Pictures were obtained using ZEN software (Zeiss; black edition) and pixel size was set to ∼40 nm in the x and y directions. SIM imaging was performed using a commercial microscope (NIKON, A1&SIM&STORM, Japan) with a SIM model equipped with a 100×/1.49NA oil objective (Nikon; CFI Apo TIRF 100×/1.49 Oil), and the 488 laser was selected.

Image Processing and Analysis

Airyscan images were processed using ZENs Airyscan processing with automatic deconvolution parameters. Fluorescence images were analyzed using ImageJ and Origin software. A total of 300 images obtained by Airyscan mode were used to achieve reconstruction using the NanoJ-SRRF plug in ImageJ FEAST image (Gustafsson et al., 2016; Wang et al., 2020). SIM reconstruction was automatically constructed by Nikon software. According to the size changes before and after the expansion of the hydrogel, we determined that the expansion coefficient was 4.10 ± 0.05.

RESULTS

Design of DNA Oligostrands

The BG molecule is a ligand of the SNAP protein; they can combine with each other in the cell to form a stable covalent bond (**Figures 1A,B,D**). To reduce the distance between the fluorescent group and the target protein, we designed DNA oligostrands of 20 bp. It is not only small in size (∼6.8 nm),

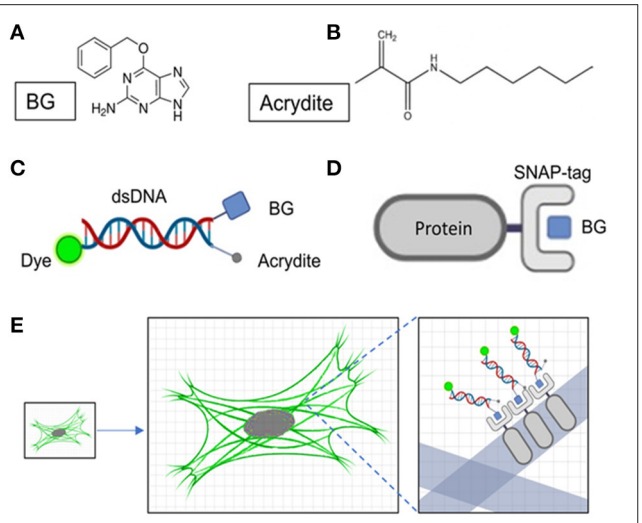

FIGURE 1 | Design of DNA oligostrands and schematic diagram of SNAP-benzoylguanine (BG) staining. **(A)** Molecular formula of BG. **(B)** Molecular formula of Acrydite. **(C)** Schematic diagram of the designed DNA oligostrands. **(D)** Schematic diagram of SNAP-tag protein binding to BG. **(E)** Staining and expansion of the DNA oligostrand.

but also not enlarged as the hydrogel enlarges, for it cannot be degraded by proteinase K. The main body is a double-stranded DNA, modified with a BG molecule, fluorescent group, and Acrydite at the ends (**Figure 1C**). For the target protein to be labeled with the designed DNA oligostrand, we needed to express the target protein by fusion with SNAP, a small tag that can also reduce the distance between the target protein and the fluorescent signal after expansion to a certain degree. Through binding between BG and SNAP, the DNA oligostrand chain can bring the fluorescent group to the vicinity of the target protein. Acrydite connects the sample to the gel by participating in the polymerization process of hydrogels. DNA oligostrands can be designed with different fluorescent groups according to different experimental requirements. To perform experiments, we only need to transfect the relevant plasmid and wait for it to be expressed in the cell, and then incubate with the designed DNA oligostrands to stain the cell. Next, by following the protocol of sample expansion, we can achieve amplification of the target protein in the cell (**Figure 1E**). For this research, Alexa647 and Alexa488 were utilized. Alexa647 was chosen to distinguish from EGFP-labeled F-actin. Alexa488 was chosen for subsequent expansion super-resolution technology because it retains more signal after expansion than Alexa647 (Tillberg et al., 2016).

Cell Staining After Fixation

Since the DNA oligostrand is essentially a piece of double-stranded DNA, it cannot directly penetrate the cell membrane and bind to the SNAP-tag protein expressed inside the cell, thus, making it impossible to directly stain the target protein. Regarding how to use the DNA oligostrand to stain the SNAP-labeled target protein, we devised a fixed cell staining method described below (Nieves et al., 2019). First, cells were incubated with 4% paraformaldehyde for 15 min, then permeabilized with Triton X-100 and stained with dye (**Figure 2A**). We first used the plifeact-SNAP -EGFP plasmid to transfect cells at a confluence between 60 and 80% and incubated them for 24 h to allow expression of the fusion protein. Next, we used the designed DNA oligostrand with Alexa647 to stain F-actin in the cells. At the same time, we used genetic engineering methods to label F-actin with EGFP to help verify the accuracy of the DNA dye-labeled site. From the light emitted by the DNA oligostrand and EGFP, we observed that the light-emitting areas of the two overlapped strongly and both stained F-actin (**Figure 2C**). **Figure 2D** is a simulation effect diagram of two channel co-localization, and the Pearson correlation coefficient (PCC) was 0.75. The distribution of the correlation scatter plot of the two channels is shown in **Figure 2E**. The staining results showed that the DNA oligostrand stained F-actin in the cell after cell fixation. However, the status of F-actin in the whole cell was not good, and the pseudopodia of the cell was not clear (**Figure 2C**). The results showed that a large number of microfilaments were depolymerized during the entire sample preparation process, and the cell morphology could not be well-maintained. Although this dyeing method can label F-actin, the result is not satisfactory. For this reason, we explored a new method.

Optimization of the Staining Method

The new dyeing method is based on the properties of PVP, which can prevent osmotic swelling of cells. The method involves staining the cells while the cells are alive before fixation. **Figure 2B** shows the operation parameters. We first treated the cells with digitonin for 15 s to form small holes in the cell membrane, quickly incubated the cells with the DNA oligostrand in PVP for a short time, and then fixed the cells. Pore damage caused by digitonin to the cells is minimal, and cells are always in an environment with PVP; therefore, the cells remain alive during the short processing time (Ma and Yang, 2010). Since BG binds to SNAP very quickly, only a short incubation is sufficient to stain the cells. The stain results are shown in **Figure 2F**. With this new method, F-actin in the cells was stained and the cell morphology was relatively complete. The details were well-preserved, and the pseudopodia of the cells were clearly visible (**Figure 2F**). The PCC of the two channels was 0.81(**Figure 2G**), and its correlation was also greater than the stained image after fixation. The distribution of the correlation scatter plot of the two channels is shown in **Figure 2H**. The corresponding line-scanning profile from the images (**Figures 2C,F**) shows that the signal-to-noise ratio of the improved dyeing method is better than the previous dyeing method (**Figure 2I**). Compared with the staining method after fixation, now the F-actin structure of cells was better preserved.

Expansion Super-Resolution

To observe whether our method was suitable for expansion super-resolution, we performed expansion experiments after dyeing. For F-actin, more pseudopod details were observed after expansion. Comparing the results before and after expansion, we found that more pseudopods were formed by the aggregation of several bundles of fiber filaments (**Figures 3A,C**). **Figures 3B,D**

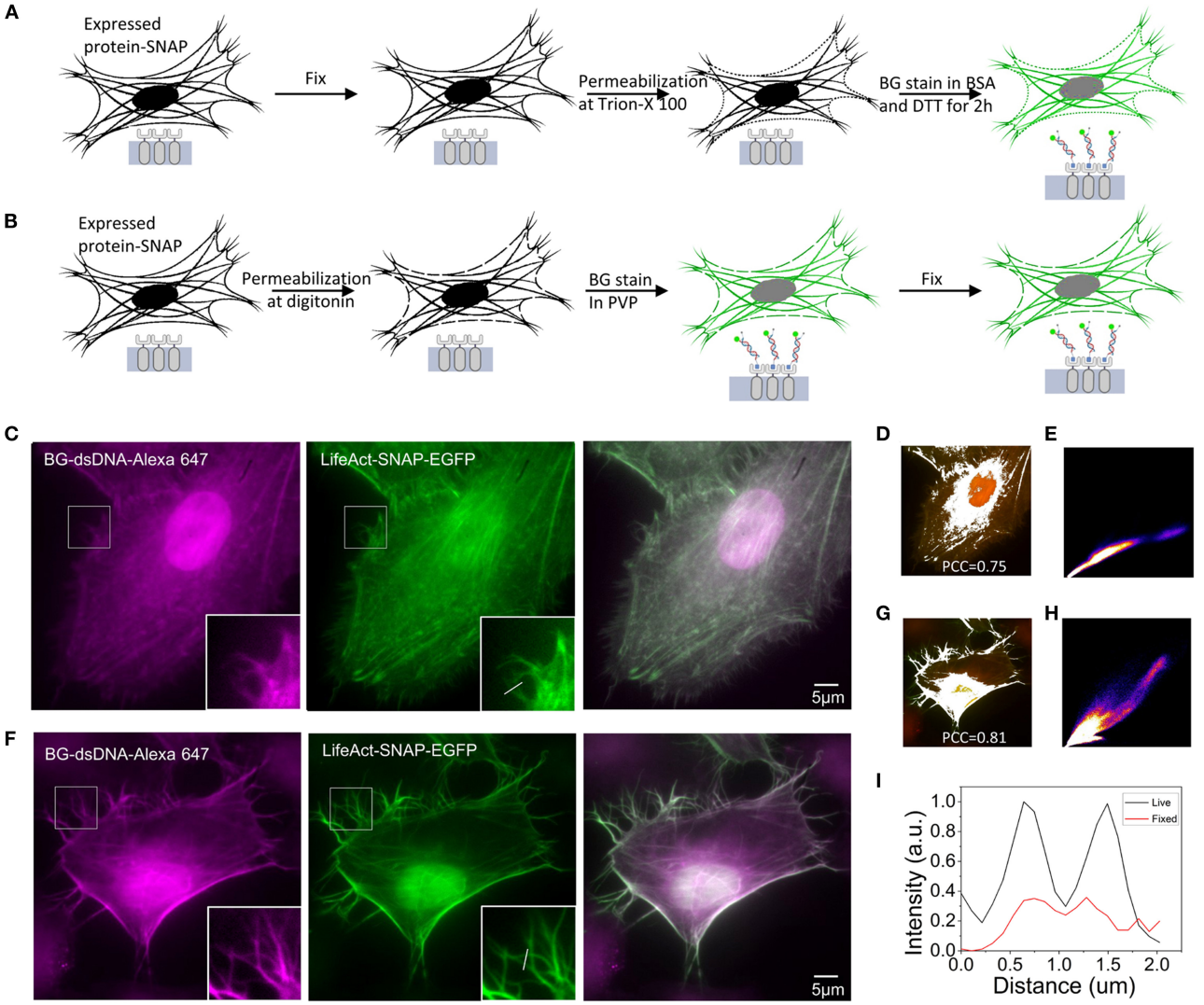

FIGURE 2 | Comparison of F-actin staining using two methods in Hela **(A)** Schematic diagram of the process of staining after cell fixation. **(B)** Schematic diagram of the process of staining and then fixing cells. **(C)** Staining of F-actin with benzoylguanine (BG)-dsDNA-Alexa647 after fixation. **(D)** Simulation effect diagram of the co-location of the two channels in **(C)**. The Pearson correlation coefficient (PCC) is 0.75. **(E)** Distribution of the correlation scatter plot of the two channels in **(C)**. **(F)** Staining of F-actin with BG-dsDNA-Alexa647 before fixation. **(G)** Simulation effect diagram of the co-location of the two channels in **(F)** The Pearson correlation coefficient (PCC) is 0.81. **(H)** Distribution of the correlation scatter plot of the two channels in **(F)**. **(I)** Corresponding line-scanning profile from the images **(C,F)**. Scale bars, 5 μm.

are enlarged details of **Figures 3A,C**. Fitting the cross-sectional (**Figure 3B**) section of F-actin before expansion to a Gaussian peak, we determined the full width at half maximum (FWHM) to be 426 nm (**Figure 3E**). Similarly, we determined the FWHM in **Figure 3D** after rescaling by the expansion ratio after expansion to be 188 nm, which is smaller than pre-expansion (**Figure 3E**). The resolution barrier inherent in light microscopy restricts the ability to differentiate between objects closer than 300 nm (Thorley et al., 2014). However, after expansion, we could observe structures with a bifurcation of <300 nm in the pseudopodia under a wide field of view. The results obtained in the experiment show that the improved resolution after expansion allowed us to see more of the local structure of F-actin. To further test its application in analysis of different cellular structures, we next performed imaging of the NPC, which has great challenges for high-resolution structural research (Grossman et al., 2012). In our experiment, we imaged the organization of Nup153, a stable component of the NPC (Winterflood and Ewers, 2014). According to the results shown in **Figure 3F**, the nuclear pores before expansion were densely distributed, but were relatively sparsely distributed after expansion (**Figure 3H**). Fitting the cross-sectional (**Figures 3G,I**) section of the NPC before and after expansion to a Gaussian peak, we obtained the FWHM after rescaling by the expansion ratio after

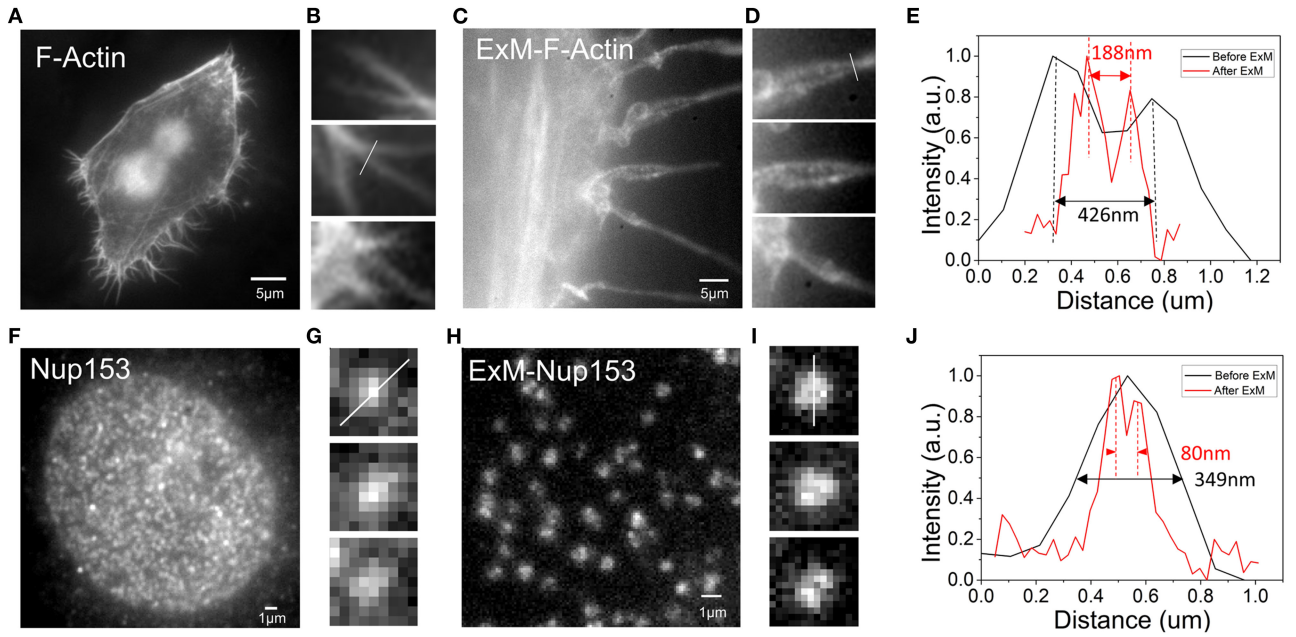

FIGURE 3 | Comparison of the results of F-actin in Hela and NPC in U2OS before and after expansion **(A)** F-actin stained with benzoylguanine (BG)-dsDNA-Alexa488 before expansion. **(B)** Enlargement of part of picture **(A)**. **(C)** F-actin stained with BG-dsDNA-Alexa488 after expansion. **(D)** Enlargement of part of picture **(C)**. **(E)** Intensity distribution plot along arrows in **(B,D)**. **(F)** nNup153 stained with BG-dsDNA-Alexa488 before expansion. **(G)** Zoomed in view of **(F)**. **(H)** nNup153 stained with BG-dsDNA-Alexa488 after expansion. **(I)** Zoomed in views of **(H)**. **(J)** Line profiles of selected nuclear pore complexes in **(G,I)**. Scale bar: 5 μm in **(A,C)**, 1 μm in **(F,H)**.

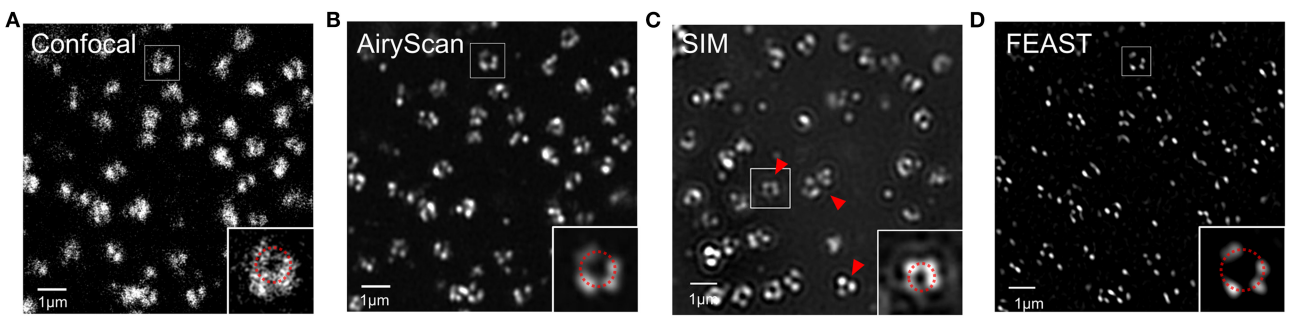

FIGURE 4 | Combination of expansion super-resolution and other super-resolution technologies **(A)** nNup153 taken in confocal mode after expansion. **(B)** nNup153 taken in Airyscan mode after expansion. **(C)** Image of nNup153 after structured illumination microscopy reconstruction. **(D)** Image of nNup153 after fluctuation-enhanced Airyscan technology reconstruction. Scale bars, 1 μm.

expansion to be 80 nm, which is smaller than the 349 nm determined before expansion (**Figure 3J**). Note that the image scale bars for expanded specimens in this report have not been divided by their respective measured expansion factors of 4.10 ± 0.05, but the data processing distances refer to pre-expansion dimensions.

Analysis of the NPC

Combining expansion super-resolution technology with other super-resolution technologies enabled us to further analyze the structure of the NPC. For the same field of view, we used confocal and Airyscan modes to photograph and SRRF to process the images taken by Airyscan to obtain a FEAST image. We also used SIM mode to photograph and reconstruct the NPC. In the picture taken in confocal mode, we found that the hollow structures of most NPCs were faintly visible (**Figure 4A**). In the picture taken in Airyscan mode, the hollow structure of most NPCs was clearer than in the confocal picture (**Figure 4B**). In the SIM mode, we also observed the hollow structure of the NPC (**Figure 4C**). However, we found some arc artifacts in the SIM reconstruction image (red arrow in **Figure 4C**) but not in other images. The FEAST image was the clearest (**Figure 4D**). The resolution of the NPC image processed by FEAST was higher than that of the other three. In addition, based on the statistics of 100 nuclear hole diameters processed by FEAST, the average diameter of the Nup153 ring was ∼102 nm (**Supplementary Figure 1**),

comparable to a previously reported measurement of Nup153 (Winterflood and Ewers, 2014). It is also comparable to that of other NPC components, such as Nup96 (Szymborska et al., 2013) and Nup133 (Li et al., 2018).

DISCUSSION

Expansion super-resolution technology has become popular tin recent years. Because of its simple operation and low instrument requirements, it can be quickly applied to various fields (Düring et al., 2019; Gambarotto et al., 2019; Götz et al., 2020). However, the shortcomings of expansion super-resolution technology are slowly being identified. Part of the signal can be lost during the formation of the hydrogel, and as the hydrogel expands, the distance error caused by commonly used antibody markers is amplified by the same multiple (Li et al., 2018; Zwettler et al., 2020). Therefore, a method with less signal loss and a small size is needed. We designed a new 20 bp DNA oligostrand BG-dsDNA-dye based on the characteristics of high specific binding between BG and SNAP and their small size. We used the DNA oligostrand to stain living cells, which is suitable for expansion super-resolution technology. Acrydite connected to the BG-dsDNA-dye can directly participate in the formation process of the hydrogel, thus reducing signal loss during the expansion process. Although other three functional linkers have been reported, this linker is very suitable for small molecule targeting of fluorophores (Wen et al., 2020). However, only some of the structures could be labeled well with small-molecules or antibodies. Our three function linker with genetic SNAP tag should be applicable for most proteins. The size of SNAP and BG-dsDNA-dye is also smaller than the size of most antibodies; therefore, the distance error between the fluorescent signal and the target protein can be reduced. A wider range of proteins than antibodies can be labeled by genetic engineering. Only a small number of proteins have their mature antibodies. Many antibodies would cause complex backgrounds as their unspecific binding problem. Using this method combined with expansion super-resolution, we have obtained a more detailed structure of F-actin and the NPC. The results show that the designed DNA oligostrands are suitable for expansion super-resolution technology and have wide applications.

Current super-resolution microscopy technology has improved the range of optical resolution from ∼250 to ∼10 nm, providing us with a powerful tool for studying the details of matter (Galbraith and Galbraith, 2011). When using antibodies to label the target protein, the resolution can be accurate to tens of nanometers. However, with the improvement of resolution, the influence of errors caused by the size of the antibody itself also increases. The accuracy of the location of the target protein is also greatly reduced. In expansion super-resolution technology, errors caused by the size of the antibody owing to swelling of the hydrogel are also amplified, which can be as high as 80 nm (Zwettler et al., 2020). Therefore, it is necessary to develop new labeling technology to reduce the labeling errors. Labeling after expansion is a way to reduce labeling errors since the antibody will not be enlarged with the enlargement of the hydrogel (Li et al., 2018; Zwettler et al., 2020). In addition, labeling errors can be directly reduced by reducing the size of the marker. In our method, the distance between the luminescent group and the target protein is determined by the size of the SNAP and the length of the DNA oligostrand. We obtained a reduction ratio of 1.09 through the relative molecular mass ratio of EGFP (26 kD) and SNAP (20 kD) (Deng et al., 2011). By referring to the size of EGFP (3.5 nm), we obtained an estimated SNAP diameter of 3.2 nm based on the reduction ratio. A 20 bp DNA double strand can form approximately two helices with an average pitch of 3.4 nm, so the size of the DNA oligostrand size is ∼6.8 nm. The orientation between SNAP and DNA oligostrand is uncertain. When the relationship between SNAP and DNA oligostrand is vertical, the distance between the target protein and the luminescent group is the shortest. When the relationship between SNAP and DNA oligostrand is parallel, the distance between the target protein and the luminescent group is the longest. Therefore, the distance between the target protein and the luminescent group before expansion is in the range of 7.5–10 nm. After expansion, the size of SNAP is stretched four times to as large as 12.8 nm owing to digestion with proteinase K. The size of the DNA oligostrand remains unchanged at 6.8 nm because the DNA oligostrand is not digested by proteinase K. Therefore, the distance between the target protein and the luminescent group after expansion is in the range of 14.5–19.6 nm. Before or after expansion, the distance error caused by labeling in this study is smaller than the error in conventional antibody labeling. Therefore, the method in this study is not only suitable for expansion super-resolution technology, but also has fewer labeling errors.

Although our method labels F-actin and NPC well, the labeling efficiency we found was not as remarkable as expected according to the results of the NPC. NPC is a macromolecular assembly of eight-fold symmetrical arrangement of protein subcomplexes (Grossman et al., 2012). The pictures revealed that not all Nup153 molecules could be equally recognized by the marker. This may be due to the existence of endogenous Nup153 which causes not all Nup153 could be recognized by DNA oligostrands. Further work should be carried out to increase the labeling efficiency. As far as the scope of application is concerned, our method is suitably applied to the study of the subcellular structure, while not for the research of rapid cell activities. For the time-consuming activities that cell can be fixed in each state, our method still has reference significance. In addition, it is uncertain whether the results obtained in this study remain the same when the experimental conditions such as cell types or growth conditions are changed. However, it is still a good marking method to reduce errors and signal loss in expansion super-resolution technology. It helps to improve the localization accuracy of expanded samples and provides a technical basis for subsequent studies of the expansion super-resolution technology. The strategies developed in this work can also be used to combine expansion super-resolution microscopy with other imaging techniques.

CONCLUSIONS

In summary, since the advent of the expansion super-resolution technology in 2015, it has been widely used in biology and other fields because of its simple operation and low equipment requirements. However, because the commonly used antibody labeling technology and fluorescent protein labeling technology have shortcomings, such as large size of the marker after expansion or loss of signal when used in expansion super-resolution technology. We designed a DNA oligostrand, and connected BG, Acrydite, and a fluorescent dye to the ends of the oligostrand. The DNA oligostrand is brought to the vicinity of the target protein by specific binding between BG and SNAP. Expansion super-resolution microscopy in combination with other super-resolution techniques showed that the DNA oligostrands are suitable for expansion super-resolution technology. The use of oligostrands in expansion super-resolution also achieved a better resolution of the structures of F-actin and the NPC. Compared with antibodies, DNA oligostrands have several advantages, including simple operation, suitability for expansion, smaller distance errors, and wide application feasibility.

DATA AVAILABILITY STATEMENT

The original contributions presented in the study are included in the article/**Supplementary Material**, further inquiries can be directed to the corresponding authors.

AUTHOR CONTRIBUTIONS

LY and JM conceived the project. LY designed the experiments and performed the imaging processing and data analysis. LY and LZ completed the experiment together and wrote the manuscript. LY, LZ, LM, and JM participated in revising the manuscript. All authors contributed to the article and approved the submitted version.

FUNDING

This work was financially supported by the National Natural Science Foundation of China (NSFC) (grant No. 11574056, 61575046), Ministry of science and technology of the People's Republic of China (China-Serbia bilateral project SINO-SERBIA2018002), Fudan University-CIOMP Joint Fund (FC2017-007, FC2018-001), and Pioneering Project of Academy for Engineering and Technology, Fudan University (gyy2018-001, gyy2018-002), Shanghai Natural Science Foundation (grant No. 20ZR1405100, 20ZR1403700), Science and Technology Research Program of Shanghai (grant No. 19DZ2282100), Shanghai key discipline construction plan (2020–2022) (grant No. GWV-10.1-XK01), Shanghai Engineering Technology Research Center of Hair Medicine (grant No. 19DZ2250500).

ACKNOWLEDGMENTS

The authors wish to thank LC for the help in experiment and Baoju Wang, Yueyue Jing for the help in revising the manuscript. The authors would like to thank Editage (www.editage.cn) for English language editing.

SUPPLEMENTARY MATERIAL

The Supplementary Material for this article can be found online at: https://www.frontiersin.org/articles/10.3389/fchem.2021.640519/full#supplementary-material

Supplementary Figure 1 | Diameters of Nup153 ring measured in FEAST images.

REFERENCES

Betzig, E., Patterson, G. H., Sougrat, R., Lindwasser, O. W., Olenych, S., Bonifacino, J. S., et al. (2006). Imaging intracellular fluorescent proteins at nanometer resolution. *Science* 313, 1642–1645. doi: 10.1126/science.1127344

Chen, F., Tillberg, P. W., and Boyden, E. S. (2015). Optical imaging. Expansion microscopy. *Science* 347, 543–548. doi: 10.1126/science.1260088

Chozinski, T. J., Halpern, A. R., Okawa, H., Kim, H. J., Tremel, G. J., Wong, R. O. L., et al. (2016). Expansion microscopy with conventional antibodies and fluorescent proteins. *Nat. Methods* 13, 485–488. doi: 10.1038/nmeth.3833

Deng, C., Huang, D., and Song, F. (2011). Green fluorescence protein and its application. *China Biotechnol.* 31, 96–102. doi: 10.13523/j.cb.20110118

Düring, D. N., Rocha, M. D., Dittrich, F., Gahr, M., and Hahnloser, R. H. R. (2019). Expansion light sheet microscopy resolves subcellular structures in large portions of the songbird brain. *Front. Neuroanat.* 13:2. doi: 10.3389/fnana.2019.00002

Galbraith, C. G., and Galbraith, J. A. (2011). Super-resolution microscopy at a glance. *J. Cell Sci.* 124(Pt 10), 1607–1611. doi: 10.1242/jcs.080085

Gambarotto, D., Zwettler, F. U., Le Guennec, M., Schmidt-Cernohorska, M., Fortun, D., Borgers, S., et al. (2019). Imaging cellular ultrastructures using expansion microscopy (U-ExM). *Nat. Methods* 16, 71–74. doi: 10.1038/s41592-018-0238-1

Gao, M., Maraspini, R., Beutel, O., Zehtabian, A., Eickholt, B., Honigmann, A., et al. (2018). Expansion stimulated emission depletion microscopy (ExSTED). *ACS Nano* 12, 4178–4185. doi: 10.1021/acsnano.8b00776

Götz, R., Panzer, S., Trinks, N., Eilts, J., Wagener, J., Turrà, D., et al. (2020). Expansion microscopy for cell biology analysis in fungi. *Front. Microbiol.* 11:574. doi: 10.3389/fmicb.2020.00574

Grossman, E., Medalia, O., and Zwerger, M. (2012). Functional architecture of the nuclear pore complex. *Annu. Rev. Biophys.* 41, 557–584. doi: 10.1146/annurev-biophys-050511-102328

Gustafsson, M. G. (2000). Surpassing the lateral resolution limit by a factor of two using structured illumination microscopy. *J. Microsc.* 198, 82–87. doi: 10.1046/j.1365-2818.2000.00710.x

Gustafsson, M. G., Shao, L., Carlton, P. M., Wang, C. J., Golubovskaya, I. N., Cande, W. Z., et al. (2008). Three-dimensional resolution doubling in wide-field fluorescence microscopy by structured illumination. *Biophys. J.* 94, 4957–4970. doi: 10.1529/biophysj.107.120345

Gustafsson, N., Culley, S., Ashdown, G., Owen, D. M., Pereira, P. M., and Henriques, R. (2016). Fast live-cell conventional fluorophore nanoscopy with imagej through super-resolution radial fluctuations. *Nat. Commun.* 7:12471. doi: 10.1038/ncomms12471

Halpern, A. R., Alas, G. C. M., Chozinski, T. J., Paredez, A. R., and Vaughan, J. C. (2017). Hybrid structured illumination expansion microscopy

reveals microbial cytoskeleton organization. *ACS Nano* 11, 12677–12686. doi: 10.1021/acsnano.7b07200

Hein, B., Willig, K. I., and Hell, S. W. (2008). Stimulated emission depletion (STED) nanoscopy of a fluorescent protein-labeled organelle inside a living cell. *Proc. Natl. Acad. Sci. U.S.A.* 105, 14271–14276. doi: 10.1073/pnas.0807705105

Hell, S. W. (2015). Strategy for far-field optical imaging and writing without diffraction limit. *Phys. Lett. A* 326, 140–145. doi: 10.1016/j.physleta.2004.03.082

Huang, B., Bates, M., and Zhuang, X. (2009). Super-resolution fluorescence microscopy. *Annu. Rev. Biochem.* 78, 993–1016. doi: 10.1146/annurev.biochem.77.061906.092014

Juillerat, A., Gronemeyer, T., Keppler, A., Gendreizig, S., Pick, H., Vogel, H., et al. (2003). Directed evolution of O6-alkylguanine-DNA alkyltransferase for efficient labeling of fusion proteins with small molecules *in vivo*. *Chem. Biol.* 10, 313–317. doi: 10.1016/S1074-5521(03)00068-1

Kunz, T. C., Götz, R., Gao, S., Sauer, M., and Kozjak-Pavlovic, V. (2020). Using expansion microscopy to visualize and characterize the morphology of mitochondrial cristae. *Front. Cell Dev. Biol.* 8:617. doi: 10.3389/fcell.2020.00617

Li, R., Chen, X., Lin, Z., Wang, Y., and Sun, Y. (2018). Expansion enhanced nanoscopy. *Nanoscale* 10, 17552–17556. doi: 10.1039/C8NR04267E

Ma, J., and Yang, W. (2010). Three-dimensional distribution of transient interactions in the nuclear pore complex obtained from single-molecule snapshots. *Proc. Nat. Acad. Sci. U.S.A.* 107, 7305–7310. doi: 10.1073/pnas.0908269107

Mikhaylova, M., Cloin, B. M., Finan, K., van den Berg, R., Teeuw, J., Kijanka, M. M., et al. (2015). Resolving bundled microtubules using anti-tubulin nanobodies. *Nat. Commun.* 6:7933. doi: 10.1038/ncomms8933

Nieves, D. J., Hilzenrat, G., Tran, J., Yang, Z., MacRae, H. H., Baker, M. A. B., et al. (2019). tagPAINT: covalent labelling of genetically encoded protein tags for DNA-PAINT imaging. *R. Soc. Open Sci.* 6:191268. doi: 10.1098/rsos.191268

Rankin, B. R., Kellner, R. R., and Hell, S. W. (2008). Stimulated-emission-depletion microscopy with a multicolor stimulated-Raman-scattering light source. *Opt. Lett.* 33, 2491–2493. doi: 10.1364/OL.33.002491

Rust, M. J., Bates, M., and Zhuang, X. (2006). Sub-diffraction-limit imaging by stochastic optical reconstruction microscopy (STORM). *Nat. Methods* 3, 793–795. doi: 10.1038/nmeth929

Schermelleh, L., Carlton, P. M., Haase, S., Shao, L., Winoto, L., Kner, P., et al. (2008). Subdiffraction multicolor imaging of the nuclear periphery with 3D structured illumination microscopy. *Science* 320, 1332–13366. doi: 10.1126/science.1156947

Szymborska, A., de Marco, A., Daigle, N., Cordes, V. C., Briggs, J. A., and Ellenberg, J. (2013). Nuclear pore scaffold structure analyzed by super-resolution microscopy and particle averaging. *Science* 341, 655–658. doi: 10.1126/science.1240672

Thorley, J. A., Pike, J., and Rappoport, J. Z. (2014). "Super-resolution microscopy," in *Fluorescence Microscopy*, eds A. Cornea and P. M Conn (Cambridge, MA: Academic Press), 199–212.

Tillberg, P. W., Chen, F., Piatkevich, K. D., Zhao, Y., Yu, C. C., English, B. P., et al. (2016). Protein-retention expansion microscopy of cells and tissues labeled using standard fluorescent proteins and antibodies. *Nat. Biotechnol.* 34, 987–992. doi: 10.1038/nbt.3625

Wang, B., Yao, L., Jing, Y., Fei, Y., and Ma, J. (2020). Multicomposite super-resolution microscopy: enhanced airyscan resolution with radial fluctuation and sample expansions. *J. Biophotonics* 13:e2419. doi: 10.1002/jbio.201960211

Wen, G., Vanheusden, M., Acke, A., Valli, D., Neely, R. K., Leen, V., et al. (2020). Evaluation of direct grafting strategies via trivalent anchoring for enabling lipid membrane and cytoskeleton staining in expansion microscopy. *ACS Nano* 28, 7860–7867. doi: 10.1021/acsnano.9b09259

Willig, K. I., Rizzoli, S. O., Westphal, V., Jahn, R., and Hell, S. W. (2006). STED microscopy reveals that synaptotagmin remains clustered after synaptic vesicle exocytosis. *Nature* 440, 935–939. doi: 10.1038/nature04592

Winterflood, C. M., and Ewers, H. (2014). Single-molecule localization microscopy using mCherry. *ChemphysChem* 15, 3447–3451. doi: 10.1002/cphc.201402423

Xu, H., Tong, Z., Ye, Q., Sun, T., Hong, Z., Zhang, L., et al. (2019). Molecular organization of mammalian meiotic chromosome axis revealed by expansion storm microscopy. *Proc. Nat. Acad. Sci. U.S.A.* 116, 18423–18428. doi: 10.1073/pnas.1902440116

Zwettler, F. U., Reinhard, S., Gambarotto, D., Bell, T. D. M., Hamel, V., Guichard, P., et al. (2020). Molecular resolution imaging by post-labeling expansion single-molecule localization microscopy (Ex-SMLM). *Nat. Commun.* 11:3388. doi: 10.1038/s41467-020-17086-8

Conflict of Interest: The authors declare that the research was conducted in the absence of any commercial or financial relationships that could be construed as a potential conflict of interest.

Advantages of publishing in Frontiers

OPEN ACCESS
Articles are free to read for greatest visibility and readership

FAST PUBLICATION
Around 90 days from submission to decision

HIGH QUALITY PEER-REVIEW
Rigorous, collaborative, and constructive peer-review

TRANSPARENT PEER-REVIEW
Editors and reviewers acknowledged by name on published articles

Frontiers
Avenue du Tribunal-Fédéral 34
1005 Lausanne | Switzerland

Visit us: www.frontiersin.org
Contact us: frontiersin.org/about/contact

REPRODUCIBILITY OF RESEARCH
Support open data and methods to enhance research reproducibility

DIGITAL PUBLISHING
Articles designed for optimal readership across devices

FOLLOW US
@frontiersin

IMPACT METRICS
Advanced article metrics track visibility across digital media

EXTENSIVE PROMOTION
Marketing and promotion of impactful research

LOOP RESEARCH NETWORK
Our network increases your article's readership